

ABSTRACT

Title of dissertation: X-RAY TIME AND SPECTRAL VARIABILITY
AS PROBES OF ULTRALUMINOUS
X-RAY SOURCES

Dheeraj Ranga Reddy Pasham,
Doctor of Philosophy, 2014

Dissertation directed by: Professor Coleman Miller
Department of Astronomy

A long-standing debate in the field of ultraluminous X-ray sources (ULXs: luminosities $\gtrsim 3 \times 10^{39}$ ergs s $^{-1}$) is whether these objects are powered by stellar-mass black holes (mass range of 3-25 M_{\odot}) undergoing hyper-accretion/emission or if they host the long-sought after class of intermediate-mass black holes (mass range of a few 100-1000 M_{\odot}) accreting material at sub-Eddington rates. We present X-ray time and energy spectral variability studies of ULXs in order to understand their physical environments and accurately weigh their compact objects.

A sample of ULXs exhibit quasi-periodic oscillations (QPOs) with centroid frequencies in the range of 10-200 mHz. The nature of the power density spectra (PDS) of these sources is qualitatively similar to stellar-mass black holes when they exhibit the so-called type-C low-frequency QPOs (frequency range of 0.2-15 Hz). However, the crucial difference is that the characteristic frequencies within the PDS of ULXs, viz., the break frequencies and the centroid frequencies of the QPOs, are scaled down by a factor of ≈ 10 -100 compared to stellar-mass black holes. It has thus been argued

that the ULX mHz QPOs are the type-C low-frequency QPO analogs of stellar-mass black holes and that the observed difference in the frequencies (a few $\times 0.01$ Hz compared with a few Hz) is due to the presence of intermediate-mass black holes ($M_{\text{ULX}} = (QPO_{\text{stellar-mass black hole}}/QPO_{\text{ULX}}) \times M_{\text{stellar-mass black hole}}$, where M and QPO are the mass and the QPO frequency, respectively) within these ULXs. We analyzed all the archival *XMM-Newton* X-ray data of ULXs NGC 5408 X-1 and M82 X-1 in order to test the hypothesis that the ULX mHz QPOs are the type-C analogs by searching for a correlation between the mHz QPO frequency and the energy spectral power-law index as type-C QPOs show such a dependence. From our multi-epoch timing and spectral analysis of ULXs NGC 5408 X-1 and M82 X-1, we found that the mHz QPOs of these sources vary in frequency by factors of ≈ 4 and 6, respectively. However, we did not find evidence for changes in their energy-spectral indices. The apparent lack of a correlation—unlike the type-C QPOs—implies that either the ULX mHz QPOs are fundamentally different compared to the stellar-mass black hole low-frequency QPOs or they are indeed analogous to the low-frequency QPOs but with the observed dependence corresponding to the saturated portion of the correlation seen in stellar-mass black holes.

We analyzed all the archival *Swift* data of ULX NGC 5408 X-1 and found evidence for a 243 ± 23 day X-ray period. Based on its variation profile, energy dependence and transient nature, we argue that this period represents the orbital period of the black hole binary. We revisit the previously reported 62 day X-ray period of M82 X-1 and found evidence that the accretion disk’s flux varies with this period’s phase and also noted that the period’s phase changed unusually fast during

a certain epoch. Based on this we argue that this period might not be orbital but instead be due to a precessing accretion disk.

By combining and averaging all the archival *RXTE*/PCA data of M82 we detect stable, 3:2 frequency ratio QPOs ($>4.7\sigma$ statistical significance) which we argue represent the high-frequency QPO analogs of stellar-mass black holes. Unlike the low-frequency QPOs, the high-frequency QPOs of stellar-mass black holes are stable, often occur in frequency ratios of 3:2 and scale inversely with black hole mass. Using the most recent mass estimates of stellar-mass black holes which show high-frequency QPOs and the detected 3:2 pair frequencies of 3.32 ± 0.06 and 5.07 ± 0.06 Hz from M82 X-1, we were able to accurately weigh its black hole to $428\pm 105 M_{\odot}$. This detection presents a unique technique to weigh the black holes in variable ULXs. Similar oscillations in other ULXs should be detectable with future X-ray observatories.

Finally, we conclude by discussing our preliminary results from the first X-ray – optical reverberation mapping of a ULX and also describe future prospects of detecting intermediate-mass black holes using tidal disruption flares and by searching for high-frequency QPOs in ULXs.

X-RAY TIME AND SPECTRAL VARIABILITY AS PROBES OF
ULTRALUMINOUS X-RAY SOURCES

by

Dheeraj Ranga Reddy Pasham

Dissertation submitted to the Faculty of the Graduate School of the
University of Maryland, College Park in partial fulfillment
of the requirements for the degree of
Doctor of Philosophy
2014

Advisory Committee:
Professor Coleman Miller, Chair/Advisor
Dr. Tod Strohmayer, Co-Advisor
Professor Richard Mushotzky
Professor Sylvain Veilleux
Professor Thomas Cohen

© Copyright by
Dheeraj Ranga Reddy Pasham
2014

Preface

The contents of this thesis are part of the following six journal articles, five of which have already been published and one of which has recently been accepted for publication. The bibliographic references to these articles are as follows:

- A Multi-epoch Timing and Spectral Study of the Ultraluminous X-Ray Source NGC 5408 X-1 with *XMM-Newton* (Chapter 2)
Pasham R. Dheeraj, Tod E. Strohmayer 2012, *ApJ*, 753, 139
- On the Nature of the mHz X-Ray Quasi-periodic Oscillations from Ultraluminous X-Ray Source M82 X-1: Search for Timing-Spectral Correlations (Chapter 3)
Dheeraj R. Pasham, Tod E. Strohmayer 2013, *ApJ*, 771, 101
- Discovery of a 7 mHz X-Ray Quasi-periodic Oscillation from the most Massive Stellar-mass Black Hole IC 10 X-1 (Chapter 4)
Dheeraj R. Pasham, Tod E. Strohmayer, Richard F. Mushotzky 2013, *ApJL*, 771, L44
- Evidence for Quasi-periodic X-Ray Dips from an Ultraluminous X-Ray Source: Implications for the Binary Motion (Chapter 5)
Dheeraj R. Pasham, Tod E. Strohmayer 2013, *ApJ*, 764, 93
- Can the 62 Day X-Ray Period of ULX M82 X-1 Be Due to a Precessing Accretion Disk? (Chapter 6)
Dheeraj R. Pasham, Tod E. Strohmayer 2013, *ApJL*, 774, L16
- A 400 Solar Mass Black Hole in the M82 Galaxy (Chapter 7)
Dheeraj R. Pasham, Tod E. Strohmayer, Richard F. Mushotzky 2014, *Nature*, accepted

All the data used in this thesis were acquired by the X-ray observatories *XMM-Newton*, *RXTE* and *Swift*. The data presented in Chapters 2 & 4 were acquired through the *XMM-Newton* guest observer program during cycles 4, 6, 9 & 11 (PI: Strohmayer). Some of the monitoring observations used in Chapter 5 were obtained as part of an approved *Swift* Cycle 4 program (PI: Strohmayer). The rest of the data were acquired from the publicly available *HEASARC* archive.

Dedication

To my mother, father, brother and significant other

Acknowledgments

I owe my gratitude to all the people in the Department of Astronomy at the University of Maryland College park including graduate students (former graduates), faculty, research associates, postdocs (former postdocs) and the staff members who have helped me with both technical and non-technical issues throughout my graduate career. I would also like to thank the people at Goddard with whom I have had valuable scientific discussions and especially those who have been an integral part of this thesis. Finally, I would like to thank the members of the CRESST team for facilitating work with Goddard researchers.

Table of Contents

List of Tables	viii
List of Figures	ix
List of Abbreviations	xi
1 Introduction	1
1.1 Ultraluminous X-ray sources (ULXs)	6
1.2 Probing the nature of ULXs	13
1.3 Basic Physical Picture to Describe the X-ray Variations	15
1.4 Thesis outline	20
2 A Search for Timing-Spectral Correlations in the ULX NGC 5408 X-1	24
2.1 Introduction & Background	24
2.2 <i>XMM-Newton</i> Observations	28
2.3 Timing Analysis	31
2.4 Energy Spectral Analysis	44
2.5 Timing - Spectral Correlations	52
2.6 Discussion	57
2.7 Summary	61
3 On the Nature of the mHz X-ray QPOs from ULX M82 X-1: Search for Timing-Spectral Correlations	63
3.1 Introduction	63
3.2 <i>XMM-Newton</i> observations and surface brightness modeling	64
3.3 Results	70
3.3.1 Timing analysis	70
3.3.1.1 Origin of the mHz QPOs	75
3.3.2 Spectral analysis: Energy-dependent surface brightness modeling	76
3.3.3 Timing-Spectral correlations	79
3.4 Discussion	79

4	Discovery of a 7 mHz X-ray Quasi-periodic Oscillation from the most Massive Stellar-mass Black Hole IC 10 X-1	86
4.1	Introduction	86
4.2	<i>XMM-Newton</i> observations	88
4.3	Results	90
4.3.1	Search for a power spectral break	94
4.4	Discussion	95
5	Evidence for Quasi-periodic X-ray Dips from an Ultraluminous X-ray Source: Implications for the Binary Motion	102
5.1	Introduction & Background	102
5.2	<i>Swift</i> /XRT Observations	107
5.3	Results: Timing Analysis	109
5.3.1	X-ray Light Curve	110
5.3.2	Timing Evidence for weakening of the 115 day modulation	111
5.3.3	Dip distribution and the folded light curve	113
5.3.4	Energy dependence of the X-ray modulations	114
5.3.4.1	Energy-dependent quasi-sinusoidal modulation	114
5.3.4.2	Energy independent or dependent sharp dips?	117
5.4	Results: Spectral analysis	117
5.4.1	Spectral evidence for a change in the absorption	119
5.4.2	Spectra during the sharp dips versus elsewhere	125
5.5	Discussion	128
5.5.1	Roche Lobe Accretion: Eccentric accretion disk and stream-disk interaction	131
5.5.2	Alternative Scenarios	136
5.6	Summary	137
6	Can the 62 day X-ray Period of the Ultraluminous X-ray Source M82 X-1 be due to a Precessing Accretion Disk?	138
6.1	Introduction	138
6.2	Data Primer	139
6.3	Results	140
6.3.1	Timing Analysis	140
6.3.2	Energy Spectral Analysis	143
6.4	Discussion	148
6.5	Orbital Scenario and caveats	151
7	Evidence for a 3:2 High Frequency QPO Pair in an Ultraluminous X-ray Source: a 400 Solar Mass Black Hole in M82	153
7.1	Introduction	153
7.2	<i>RXTE</i> /PCA observations	155
7.3	Results	157
7.4	Discussion	162

8	Conclusions & Future Work	170
8.1	X-ray–Optical Reverberation Mapping of ULXs: Search for and Measure X-ray – Optical Time Lags	171
8.2	Searches for Tidal Disruption Signatures of a Star by an intermediate-mass black hole	173
8.2.1	Expected Results: Coordinated <i>Swift</i> and Ground-based UV/Optical/IR Observations	177
8.3	ULX High-Frequency QPOs using <i>NICER</i>	180
8.3.1	Expected results with <i>NICER</i>	180
	Bibliography	182

List of Tables

2.1	Summary of the <i>XMM-Newton</i> observations of NGC 5408 X-1	28
2.2	Summary of the best-fitting model parameters for the power density spectra of the ULX NGC 5408 X-1	38
2.3	Summary of the best-fitting model parameters for the power density spectra of ULX NGC 5408 X-1	42
2.4	Summary of the energy spectral modeling of NGC 5408 X-1	43
2.5	Summary of the energy spectral modeling of NGC 5408 X-1	46
2.6	Power spectral properties of NGC 5408 X-1 and stellar-mass black holes with type-C QPOs	51
2.7	Mass estimate of the black hole in NGC 5408 X-1	62
3.1	Resolved X-ray count rates of M82 X-1 and source 5	65
3.2	Summary of the 3-10 keV power spectral modeling of M82	74
3.3	Summary of energy-dependent surface brightness modeling	81
4.1	Summary of power spectral modeling of IC 10 X-1	93
5.1	Summary of the best-fitting model parameters of the X-ray modulation profiles of NGC 5408 X-1	118
5.2	Summary of the spectral modeling of NGC 5408 X-1	121
6.1	Summary of the phase-resolved energy spectral modeling of M82 . . .	147

List of Figures

1.1	Sample power density spectra of stellar-mass black holes showing their extremely fast and coherent X-ray variability	2
1.2	Orbital tracks of stars around our Galactic center	4
1.3	Black hole mass-stellar velocity dispersion relation ($M - \sigma$) of super-massive black holes	6
1.4	Black hole mass-Luminosity relation ($M - L$) of super-massive black holes	7
1.5	Comparing the disk luminosity versus temperature of ULXs with stellar-mass black holes	10
1.6	X-ray energy spectrum of a ULX showing the high-energy break . . .	12
1.7	Predicted versus observed power spectral break frequencies of stellar-mass and super-massive black holes	14
1.8	The observed correlation between the X-ray power spectral break frequency and the QPO frequency	16
1.9	Disk-Corona schematic of a black hole system	17
1.10	Schematic showing physical locations of some X-ray oscillations . . .	21
2.1	Good time intervals and light curves of NGC 5408 X-1	30
2.2	Good time intervals and light curves of NGC 5408 X-1	33
2.3	Power density spectra of NGC 5408 X-1	35
2.4	Power density spectra of NGC 5408 X-1	36
2.5	QPO RMS amplitude versus centroid frequency	40
2.6	A sample X-ray energy spectrum of NGC 5408 X-1	47
2.7	Timing-Spectral correlations	54
2.8	Timing-Spectral correlations using the BMC-model	56
3.1	EPIC-MOS1 surface brightness contour maps of M82	68
3.2	EPIC-pn 3-10 keV power density spectra of M82 X-1	71
3.3	EPIC-pn and MOS power density spectra of M82 X-1	72
3.4	Origin of the mHz QPOs of M82	77
3.5	Timing-Spectral correlations	80
4.1	EPIC-pn X-ray (0.3-10.0 keV) image of IC 10 X-1	89

4.2	X-ray light curve of IC 10 X-1	92
4.3	Power density spectra and the RMS amplitude of the QPO as a function of the bandpass	96
4.4	Combined MOS PDS of IC 10 X-1 in various energy bands	98
5.1	<i>Swift</i> /XRT X-ray light curve of the ULX NGC 5408 X-1 in the 0.3-8.0 keV energy band	107
5.2	The first and the second half of the entire light curve and their respective periodograms	110
5.3	Histogram of the sharp dips as a function of their phase	112
5.4	The epoch folded X-ray (0.3-8.0 keV) light curve of NGC 5408 X-1	113
5.5	The epoch folded light curves of NGC 5408 X-1 in varying energy bands	116
5.6	Energy dependence of the fractional variability amplitude	122
5.7	Time history of the X-ray hardness ratio	124
5.8	The <i>Swift</i> /XRT spectra of NGC 5408 X-1 in the energy range 0.5-8.0 keV	126
5.9	Confidence contours that represent the variable spectral parameters	129
5.10	An idealized depiction of a possible accretion geometry for NGC 5408 X-1	133
6.1	Complete <i>RXTE</i> /PCA binned X-ray (3-15 keV) light curve of M82	140
6.2	Epoch folded light curves of M82 showing the sudden phase jump	142
6.3	Demonstrating the phase jump using various periods within the error bar reported by Kaaret & Feng (2007)	144
6.4	The phase-resolved X-ray disk and power-law fluxes	146
7.1	Sample 128-second <i>RXTE</i> /PCA X-ray (3-13 keV) light curves and their corresponding power spectra of M82	156
7.2	Six-year average X-ray (3-13 keV) power density spectrum of M82	159
7.3	Relativistic precession model analysis of M82 X-1	166
8.1	Simultaneous X-ray and optical light curve of NGC 5408 X-1	173
8.2	UV and Optical light curve of tidal disruption flare PS1-10jh	174
8.3	Expected tidal disruption rates per galaxy as a function of black hole mass and X-ray light curve of Swift J1644+57	178

List of Abbreviations

AGN	Active Galactic Nuclei
EPIC	European Photon Imaging Camera
FWHM	Full Width Half Maximum
GTI	Good Time Interval
HLX	Hyper Luminous X-ray source
MOS	Metal Oxide Semi-conductor
PCA	Proportional Counter Array
PDS	Power Density Spectrum
PSF	Point Spread Function
QPO	Quasi-Periodic Oscillation
RMS	Root Mean Square
RPM	Relativistic Precession Model
RXTE	Rossi X-ray Timing Explorer
SAS	Science Analysis System
SED	Spectral Energy Density
S/N	Signal-to-Noise Ratio
TDE	Tidal Disruption Event
TT	Terrestrial Time
ULX	UltraLuminous X-ray source
UTC	Universal Coordinated Time
VLA	Very Large Array
XRT	X-Ray Telescope

Chapter 1: Introduction

Black holes are among the most exotic and mysterious objects in the Universe, serving as one-way portals for matter, light, or anything else that gets too close. Our modern conception of black holes stems directly from Albert Einstein’s theory of gravity, the general theory of relativity, proposed in 1915. However, it was not until the 1970s that evidence emerged that these objects not only exist, but actually power the brightest objects in the Universe (Bolton 1972; Webster & Murdin 1972).

It is now established that there are at least two classes of black holes: (1) the so-called “stellar-mass” black holes that weigh about 3-15 times the mass of our Sun (M_{\odot}) (McClintock & Remillard 2006) and (2) “super-massive” black holes with masses in the range of a few $\times 10^{5-10} M_{\odot}$ (Magorrian et al. 1998; Ferrarese & Ford 2005).

Evidence for the existence of the former class comes mainly from two lines of reasoning. Firstly, fast and coherent variations in the X-ray flux (~ 0.01 s: McClintock & Remillard 2006; see Figure 1.1) of some objects indicate that they are extremely compact¹. Secondly, the mass measurements of these objects indicate

¹This is based on the fact that in order for a source to vary coherently on these short timescales, all the points within its emitting region must be causally connected, i.e., size of the emitting region $<$ speed of light \times variability timescale (≈ 0.01 s) = 3000 km (for comparison, the radius of the Sun is 6.95×10^5 km).

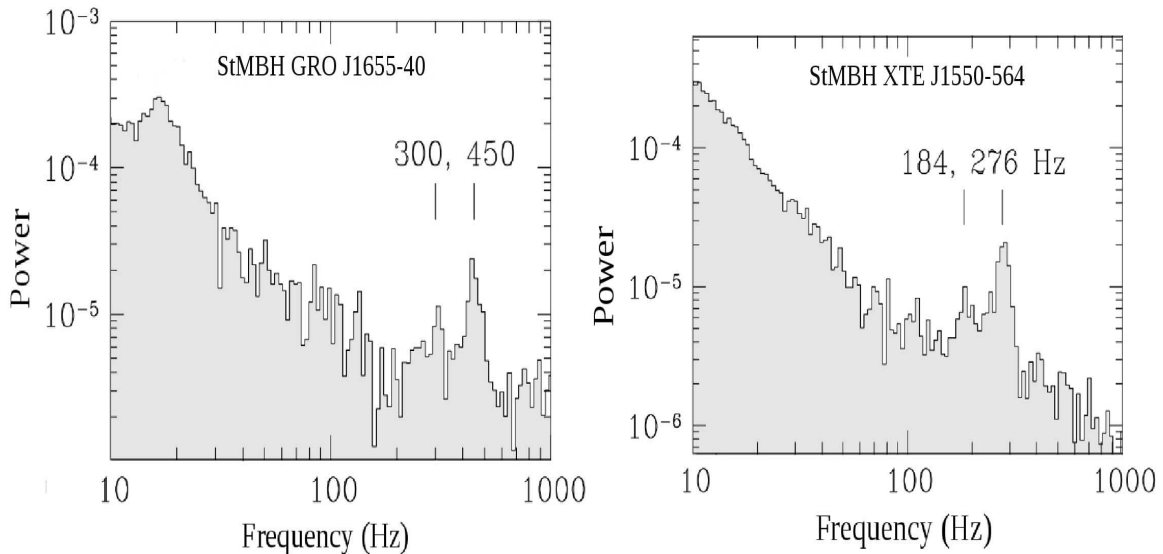


Figure 1.1: Power density spectra of two stellar-mass black holes GRO J1655-40 (left panel) and XTE J1550-564 (right panel) showing the 3:2 high-frequency oscillations on timescales faster than 0.01 s (McClintock & Remillard 2006).

that they are heavier than $3M_{\odot}$, a value well above the generally accepted upper limit for a neutron star or a white dwarf. A natural description for such an object, under the interpretation of the theory of general relativity, is a black hole. The most direct way to weigh them is via a dynamical mass measurement technique, which involves tracking the binary motion of their companion stars through their radial velocity measurements. The equation for the minimum mass of the black hole, defined as the mass function $f(M)$, can be derived from Newton's laws and is given by

$$f(M) = \frac{(M_{BH} \sin i)^3}{(M_{star} + M_{BH})^2} = \frac{M_{BH} \sin^3 i}{(1 + q)^2} = \frac{PK_{Star}^3}{2\pi G} \quad (1.1)$$

where M_{star} and M_{BH} are the masses of the companion star and the black

hole, respectively, and $q = M_{star}/M_{BH}$ is their ratio. The remaining quantities, i , P and K_{star} are the inclination of the binary, the orbital period and the radial velocity semi-amplitude of the donor star, respectively, and G is the gravitational constant. The above equation applies for circular orbits; if the companion is a low-mass star it will donate mass via Roche lobe overflow in which case the system circularizes rapidly. Such measurements have confirmed over twenty stellar-mass black holes with masses in the range of 3-15 M_{\odot} (Orosz 2003). Roughly another twenty objects have been classified as black hole candidates based on the similarity of their X-ray spectral and variability characteristics with confirmed black holes (Table 4.3 of McClintock & Remillard 2006).

On the other hand, the strongest evidence for super-massive black holes residing at the centers of massive galaxies stems from direct imaging in the optical and the radio bands where (1) tracking of the proper motions of stars in close orbits around our Galactic center indicates the presence of an object of mass $\approx 4 \times 10^6 M_{\odot}$ confined within a radius of $\lesssim 60$ astronomical units (Figure 1.2; Ghez et al. 2008), and (2) more recent high spatial resolution radio observations using the event horizon telescope have resolved the central point sources in M87 and the Galactic center to less than 10 Schwarzschild radii, again suggesting a massive object in a small volume (Doeleman et al. 2012; Lu et al. 2014). Moreover, many massive galaxies appear to produce large amounts of energy emanating from compact regions in their centers—presumably by accretion of matter on to a super-massive black hole (Ferrarese & Ford 2005).

Although we understand that stellar-mass black holes are produced by the

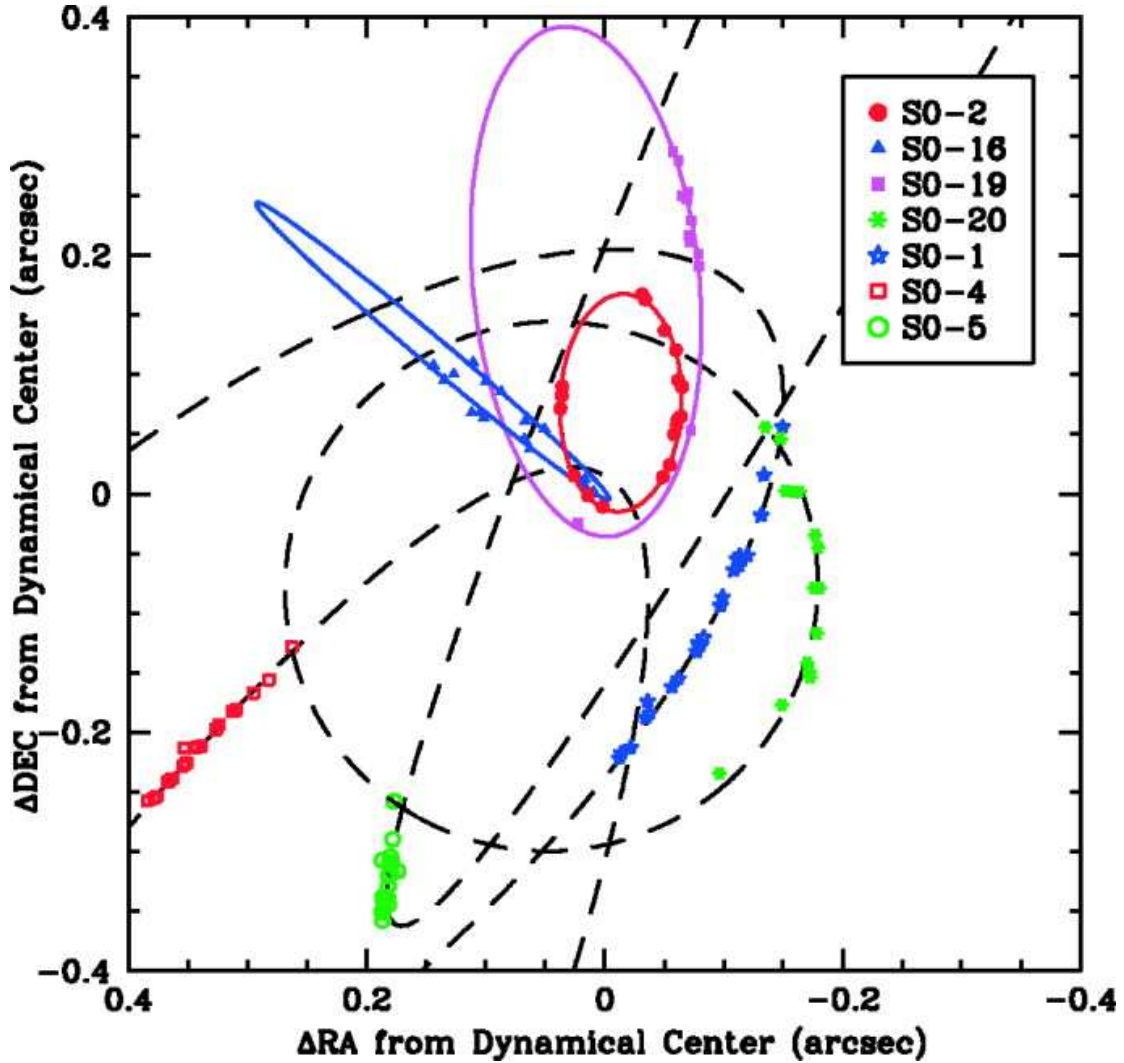


Figure 1.2: Orbital tracks of stars around the Galactic center observed between 1995-2003 (Ghez et al. 2005). The solid lines indicate the orbits of stars that have enabled constraints on the black hole mass while the dashed lines are other stars orbits. The stars S0-1, S0-2, and S0-16 have their orbits in the clockwise direction while the rest have counterclockwise motion (S0-4, S0-5, S0-19, and S0-20).

spectacular deaths of the heaviest stars, the formation and growth of super-massive black holes that are responsible for shaping the nature of many galaxies is still a mystery. Understanding the formation of super-massive black holes holds a key to understanding the growth of galaxies that are the building blocks of the Universe. Current evidence indicates that super-massive black holes might have grown by

accumulation of matter onto middle-weight black holes that are a few hundred to a thousand times more massive than the Sun and formed when the Universe was only $\approx 5\%$ of its current age (Madau & Rees 2001; Volonteri et al. 2003). Such intermediate-mass black holes are also expected to play a key role in the dynamics of many massive star clusters, as studies of the evolution of such clusters suggest that in $\sim 10\%$ of them intermediate-mass black holes should form via runaway mergers of massive stars (Miller & Hamilton 2002). In addition, intermediate-mass black holes are important targets for gravitational wave searches by ground-based laser interferometers such as LIGO and Virgo. These are most sensitive in the frequency range of 10-1000 Hz and are best suited for detecting gravitational wave emission from the final stages of coalescing intermediate-mass black hole – intermediate-mass black hole and intermediate-mass black hole – compact object (neutron star or a stellar-mass black hole) binaries (e.g., Amaro-Seoane et al. 2009). Finally, the well-known $M - \sigma$ and $M - L$ (Figures 1.3 & 1.4; black hole mass – galaxy bulge stellar velocity dispersion and black hole mass – host galaxy luminosity) relations—which suggest that the growth of super-massive black holes is inherently tied to the evolution of their host galaxies—is only calibrated between black hole masses of a few $\times 10^{6-9} M_{\odot}$ (e.g., Gebhardt et al. 2000; Ferrarese & Merritt 2000; Gültekin et al. 2009). Intermediate-mass black holes are a missing link in this evolutionary chain. In spite of such essential importance intermediate-mass black hole searches over the past few decades have yielded only limited success.

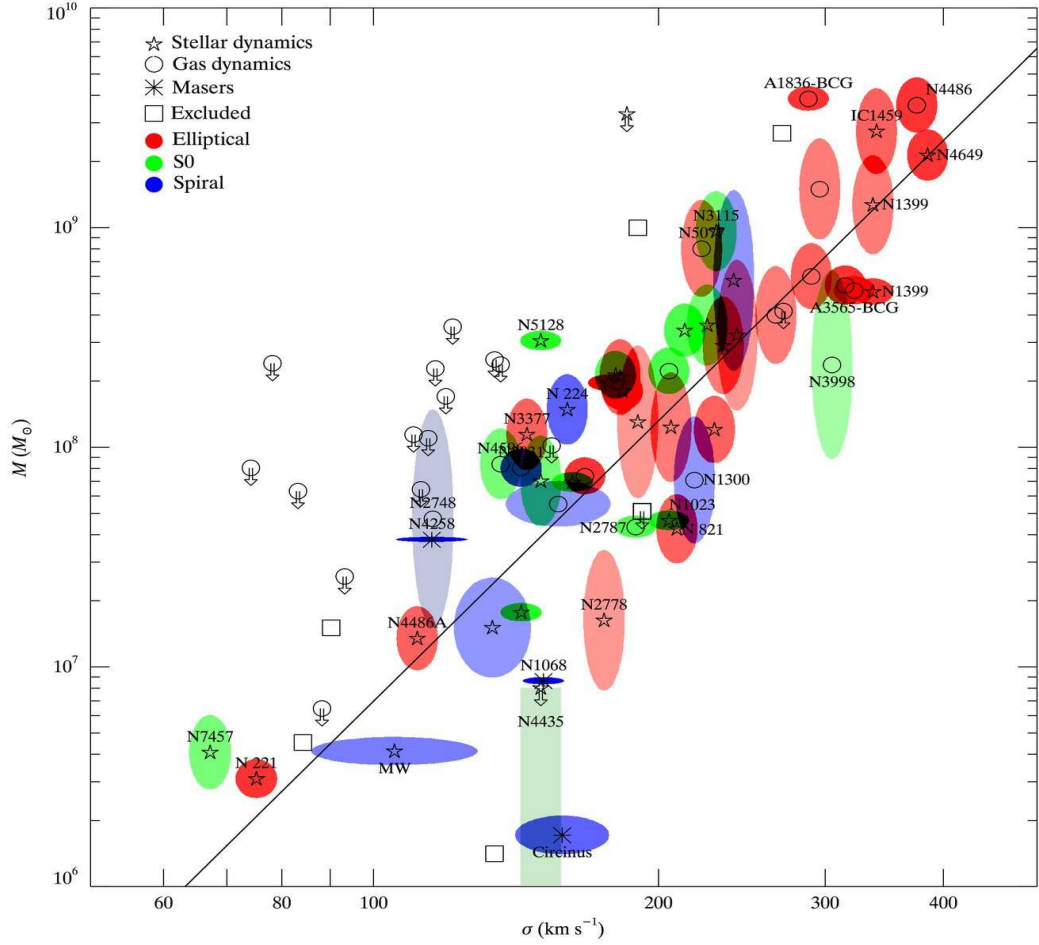


Figure 1.3: Black hole mass – host-galaxy bulge stellar velocity dispersion relation for black holes with dynamical mass measurements (Gültekin et al. 2009). The symbols indicate the mass measurement technique used. The color of the error ellipse indicates the Hubble type of the host galaxy: elliptical (red), S0 (green), and spiral (blue). The color saturation is inversely proportional to the area of the ellipse in each case.

1.1 Ultraluminous X-ray sources (ULXs)

In the early 1980s the *Einstein* X-ray observatory discovered a class of extragalactic X-ray sources whose apparent isotropic luminosities exceeded the Eddington

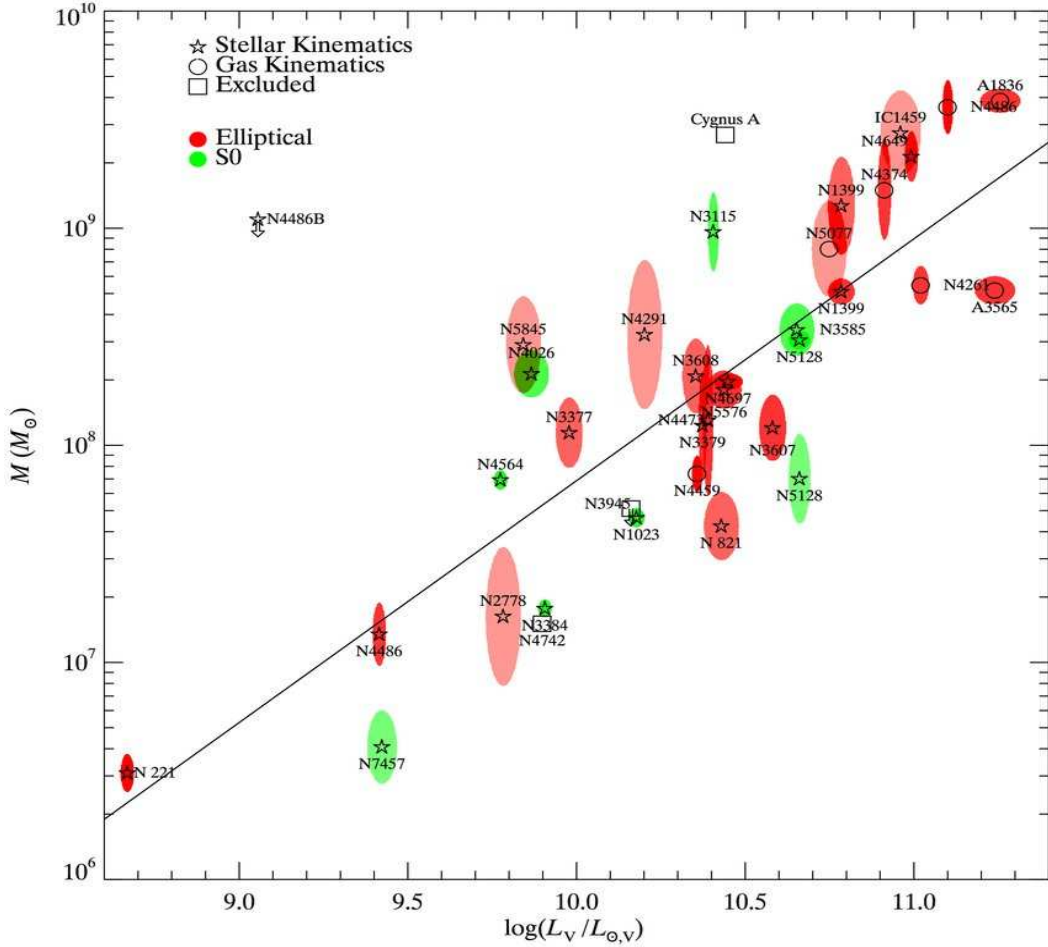


Figure 1.4: Black hole mass – host galaxy luminosity relation for super-massive black holes with dynamical mass measurements (Gültekin et al. 2009). Similar to Figure 1.3 the symbols indicate the mass measurement technique used. The ellipses are indicative of the errors and the color saturation is inversely proportional to the area of the ellipse. The best-fit model is also shown (solid line).

limit² of a $25 M_{\odot}$ stellar-mass black hole³, i.e., luminosities $\gtrsim 3 \times 10^{39} \text{ erg s}^{-1}$ (Fabiano 1989). Such sources are referred to as ultraluminous X-ray sources (ULXs)⁴.

Rapid X-ray variability of some of these sources (known to vary on timescales of

²The luminosity beyond which matter accreting isotropically onto a black hole would be driven away by radially outward radiation forces

³ $25 M_{\odot}$ is a conservative upper limit for the mass of a stellar-mass black hole

⁴Within the context of this thesis the term ULX only refers to black holes and does not include the X-ray bright supernovae (Immler & Lewin 2003) which have sometimes been referred to as ULXs in the literature

the order of a few minutes as will be discussed later in this thesis) suggests they are compact. Follow-up higher spatial resolution observations revealed that these sources are offset from their host galactic nuclei (e.g., Matsumoto et al. 2001) ruling them out as candidates for super-massive black holes. Given the ages of their host galaxies, if they were super-massive black holes, they should have sunk to the centers of their galaxies due to dynamical friction (Miller & Colbert 2004). Clearly, this is not the case. This argument combined with the fact that they are too bright to be powered by sub-Eddington accretion on to stellar-mass black holes makes them some of the strongest intermediate-mass black hole candidates to-date.

For a standard accretion disk—geometrically thin, optically thick and radiatively efficient—the mass accretion rate (assuming cosmic composition of hydrogen and only electron scattering), the isotropic⁵ luminosity (L) and the mass of the central black hole (M) are related and can be expressed as

$$L_{iso} \approx \frac{1.38 \times 10^{38}}{b} \dot{m} \left(\frac{M}{M_{\odot}} \right) \text{ ergs } s^{-1} \quad \dot{m} \lesssim 1 \quad (1.2)$$

where \dot{m} is the dimensionless mass accretion rate normalized by the Eddington rate (Eddington 1924; Feng & Soria 2011; Shakura & Sunyaev 1973) and b is the beaming factor⁶. The theoretical form of the equation changes if the accretion rate is either close to or above the Eddington limit. An estimate due to Poutanen et al. (2007) is given by

⁵(Observed flux) $\times 4\pi r^2$ where r is the distance to the source

⁶Beaming factor b is defined as the ratio of the opening solid angle of the X-ray emission and 4π ($b \leq 1$)

$$L \approx \frac{1.38 \times 10^{38}}{b} \left(1 + \frac{3}{5} \ln(\dot{m})\right) \left(\frac{M}{M_{\odot}}\right) \text{ ergs s}^{-1} \quad 1 \lesssim \dot{m} \lesssim 100 \quad (1.3)$$

It should be noted that at super-Eddington accretion rates the luminosity of the source is dictated by two physical effects, advection and radiation pressure driven outflows. In one extreme when the flow is advection-dominated most of the gas reaches the black hole but the released gravitational energy reaches the hole via advection (Poutanen et al. 2007). Inside this advection zone the radiative flux scales as R^{-2} (R is the radial distance) and thus the luminosity—which is an integral over $4\pi R$ —scales as the logarithm of the mass accretion rate. On the other hand, when outflows are dominant in expelling gas through strong radiation pressure-driven winds, accretion depends linearly on the radius. Again in this case, the radiative flux scales as R^{-2} and hence the logarithmic scaling factor.

It is clear from the above two equations that the apparent high luminosities of ULXs (10^{39-41} ergs s^{-1}) can be explained under the standard disk paradigm using one or a combination of the following three solutions: (1) high beaming (King et al. 2001; Begelman 2002), (2) high mass accretion rate (e.g., Poutanen et al. 2007; Gladstone et al. 2009) or (3) an intermediate-mass black hole (Colbert & Mushotzky 1999; mass range of a few \times (100-1000) M_{\odot}). The strong beaming solution ($1/b \gg 1$) has serious problems owing to the following reason. It predicts that for every ULX at a high luminosity there should be a larger number of low-luminosity sources. For example, for every ULX at 10^{40} ergs s^{-1} it predicts that there should be ≈ 30 sources

with luminosities greater than 10^{39} ergs s^{-1} . Empirical studies, however, find that this number is significantly lower by a factor of $\approx 3-6$ (5-10 sources: Walton et al. 2011; Swartz et al. 2004; Grimm et al. 2003).

Therefore, currently, the biggest debate regarding ULXs is whether they are stellar-mass black holes accreting close-to or above the Eddington limit or if they are intermediate-mass black holes accreting at sub-Eddington rates.

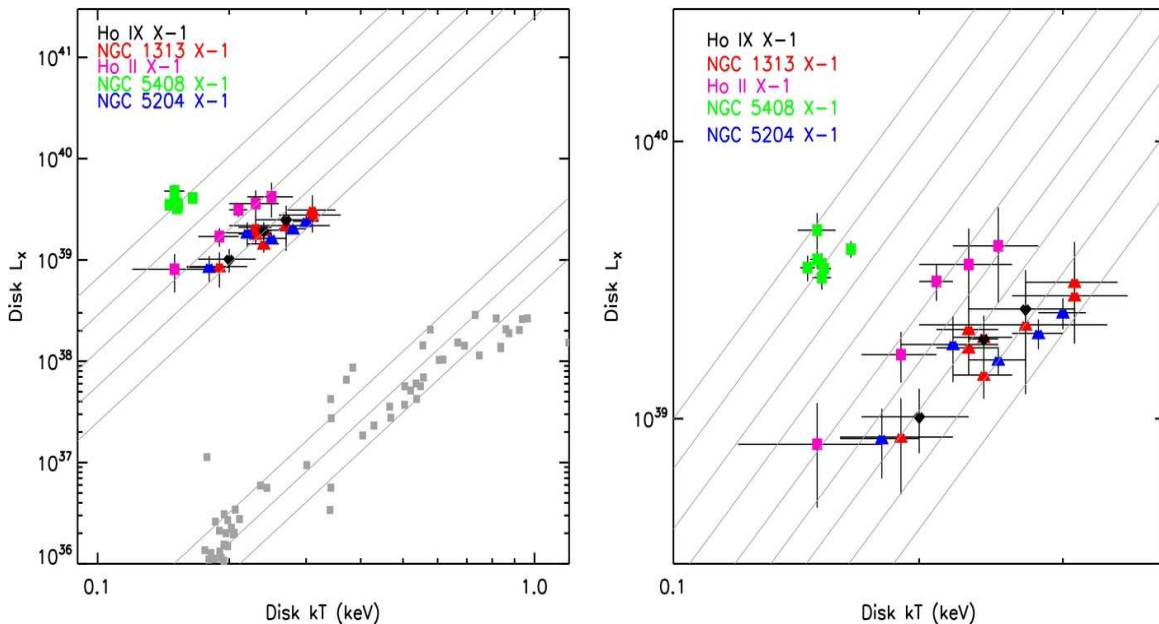


Figure 1.5: Comparing the disk luminosity versus the disk temperature of ULXs (colored points) with stellar-mass black holes (gray data points; Reynolds & Miller 2013). Only the brightest ULXs ($\gtrsim 10^{40}$ ergs s^{-1}) are shown here. The diagonal gray lines represent the $L \propto T^4$ law with varying normalizations. The right panel is the same as the left panel except that the scale has been changed to highlight the ULX region of the left panel.

In addition to the high luminosity argument, modeling of the high-quality *Chandra* and *XMM-Newton* X-ray (0.3-10.0 keV) spectra of some of the brightest ULXs shows evidence for the presence of cooler accretion disks ($\sim 0.1-0.2$ keV) compared to the hot accretion disks of stellar-mass black holes ($\sim 1-2$ keV; Miller et

al. 2004, 2013). For a standard accretion disk (geometrically thin, optically thick, radiatively-efficient disk) extending to the innermost stable orbit, the inner disk temperature T_{in} is related to the black hole mass M and total luminosity L as

$$T_{in} = 1.2 \left(\frac{\xi}{0.41} \right)^{1/2} \left(\frac{\kappa}{1.7} \right) \alpha^{-1/2} \left(\frac{L}{L_{Edd}} \right)^{1/4} \left(\frac{M}{10M_{\odot}} \right)^{-1/4} \text{ keV} \quad (1.4)$$

where α is a spin-dependent factor with a value of 1 for a maximally spinning black hole and 1/6 for a non-spinning hole. ξ is a correction factor that takes into account the no-torque boundary condition at the innermost orbit, κ is the spectral hardening factor (Makishima 2000) and L_{Edd} is the Eddington luminosity of the black hole. It is evident from the above expression that for a given Eddington ratio the effective disk temperature scales inversely with the mass of the black hole as $T \propto M^{-1/4}$ (Shakura & Sunyaev 1973). The presence of such cool disks combined with high X-ray luminosities therefore suggests that some ULXs may host intermediate-mass black holes. This is demonstrated in Figure 1.5 where the ULXs occupy a distinct phase space in the disk temperature – luminosity plot compared to stellar-mass black holes (Miller et al. 2004, 2013).

On the other hand, proponents of super-Eddington accretion onto stellar-mass black holes have argued that the X-ray spectra of ULXs are fundamentally different (Gladstone et al. 2009). Using more physically-motivated models consisting of a disk plus a Comptonized corona they show that the ULX corona are in general optically thick (optical depth, $\tau \sim 5-30$) compared to stellar-mass black holes where the model-fit coronae have optical depths of ~ 1 . It has thus been argued that this

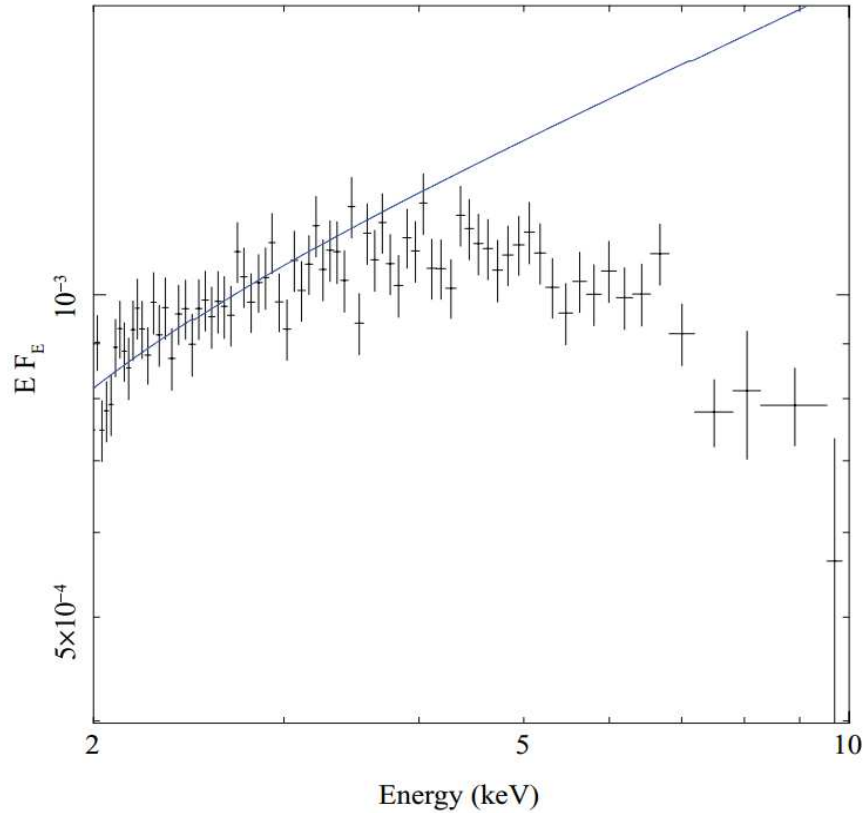


Figure 1.6: *XMM-Newton* X-ray (2-10 keV) energy spectrum of NGC 1313 X-2 (crosses). The data was first fit with a broken power-law. The solid line is an extension of the pre-break power-law index to higher energies (> 5 keV) and clearly highlights that there is a break beyond 3 keV (Gladstone et al. 2009).

dense ULX corona masks the innermost (hot) accretion disk from an observer who in-effect only sees the cooler X-ray photons from the disk outside the corona. The evidence for this is a strong break in the energy spectra at higher energies (2-8 keV) which has been argued arises from this cool, optically thick corona. An example of this is shown in Figure 1.6 where the break is clearly apparent. It has also been shown that the corona-corrected disk temperatures fall well-within the usual stellar-mass black hole regime with values ~ 1 keV (Gladstone et al. 2009). At present, the debate between super-Eddington versus sub-Eddington is far from resolved. The

X-ray spectra alone cannot rule out either scenario.

1.2 Probing the nature of ULXs

Much of our inability to learn about these sources is because they are extragalactic and thus significantly fainter than the relatively nearby galactic stellar-mass black holes or the far away but more luminous active galactic nuclei (AGN). The most direct method to resolve the ULX mass question is by identifying an absorption/emission line from a companion star in orbit around the central black hole in order to track its radial velocity to measure a dynamical mass (Eq 1.1). There have been a handful of such attempts (e.g., Roberts et al. 2011; Liu et al. 2012; Cseh et al. 2013) but without any success. This is primarily because, (1) the orbital periods of these systems are not known, and (2) the inability to correctly identify the origin of the spectroscopic lines or to conclusively associate the identified lines with a companion star. In some cases it is ambiguous if there is even a companion star in the first place. Under such circumstances one has to resort to indirect methods that have been well-calibrated against stellar-mass and super-massive black holes.

For example, it is now known that certain characteristic timescales in accreting black hole systems scale with the mass of the black hole. For instance, McHardy et al. (2006) have established that in soft-state stellar-mass black holes and AGN, the break timescale of the X-ray power density spectrum (PDS), the mass of the black hole and the luminosity are strongly correlated. This is shown in Figure 1.7. This result was further extended to the hard-state, stellar-mass black holes by K rding

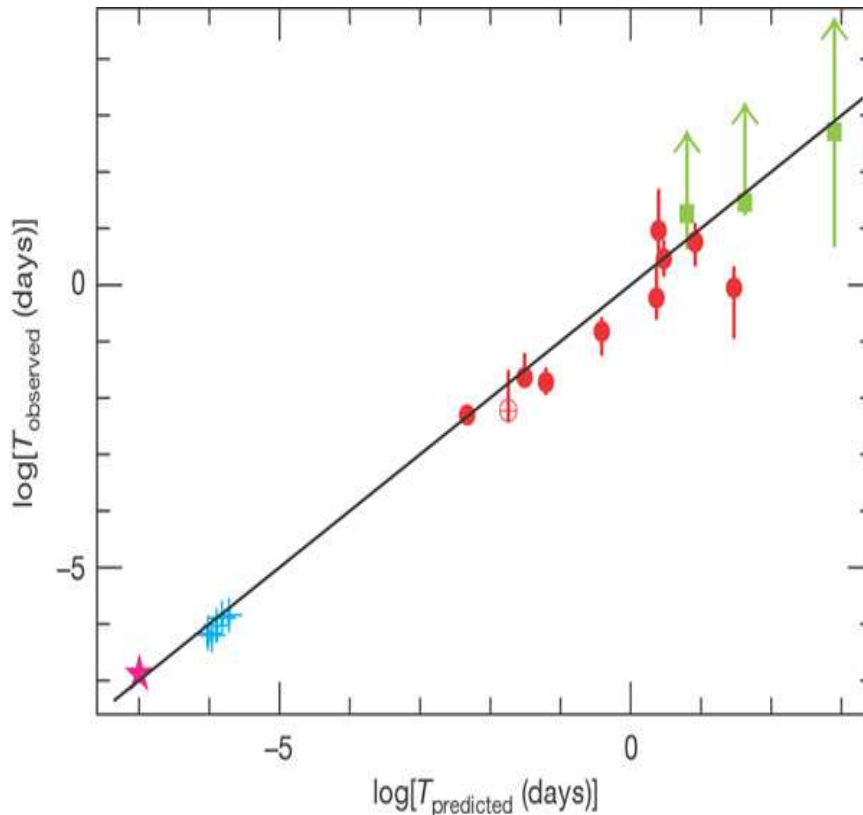


Figure 1.7: Observed power spectral break timescale ($T_{observed}$ in days) versus the predicted break timescale ($T_{predicted}$) by fitting the relation $\text{Log}(T_{predicted}) = 2.1 \times \text{Log}(M_{BH}) - 0.98 \times \text{Log}(L_{bol}) - 2.32$ to stellar-mass and super-massive black holes (McHardy et al. 2006). M_{BH} and L_{bol} are the mass and the bolometric luminosity of the black hole. The shapes and the colors of the data points are used to indicate the various types of AGN and stellar-mass black holes and are irrelevant to the current discussion.

et al. (2007). Furthermore, it is known that in stellar-mass black holes the break frequency/timescale of the power spectrum strongly correlates with the centroid frequency of the strongest type-C (see Chapter 2 for more discussion) quasi-periodic oscillation (QPO) (Wijnands & van der Klis 1999; see Figure 1.8). Therefore, if one can clearly identify the type-C analogs of stellar-mass black holes in a ULX a reliable mass estimate can be made (Chapters 2, 3 & 4). Such studies have strongly demonstrated that certain physical timescales of accreting compact objects

scale directly with the mass of the compact source applicable over seven orders of magnitude. Therefore, timing studies can play a key role in extracting valuable information about the mass of the compact source.

In addition, periodic/quasi-periodic variations in the X-ray flux on longer timescales of hours to years have been detected from various accreting X-ray binaries (both neutron star and stellar-mass black hole binaries; e.g., Parmar & White 1988; Armitage & Livio 1998) which have been extremely valuable in mapping their accretion geometries. If similar modulations can be detected in ULXs we can probe their environments in an analogous way (Chapter 5 & 6).

1.3 Basic Physical Picture to Describe the X-ray Variations

Our current understanding of accreting stellar-mass black hole systems comes from studies of twenty or so confirmed black hole binaries, a majority of which accrete material via Roche lobe overflow of their low-mass companion stars. As the gas flowing through the L_1 Lagrange point has non-zero specific angular momentum, it cannot directly accrete onto the black hole, and therefore, forms an accretion disk in which the matter moves in circular orbits with Keplerian angular frequencies given by $\sqrt{GM/R^3}$ (Here G , M , and R are the Gravitational constant, the black hole mass and the radius within the accretion disk, respectively). The dissipative viscous forces operating between the successive radii of the accretion disk drive the angular momentum outwards which allows the material to flow inwards all the way until the last stable circular orbit (which is $6R_g$ for a non-spinning black hole and

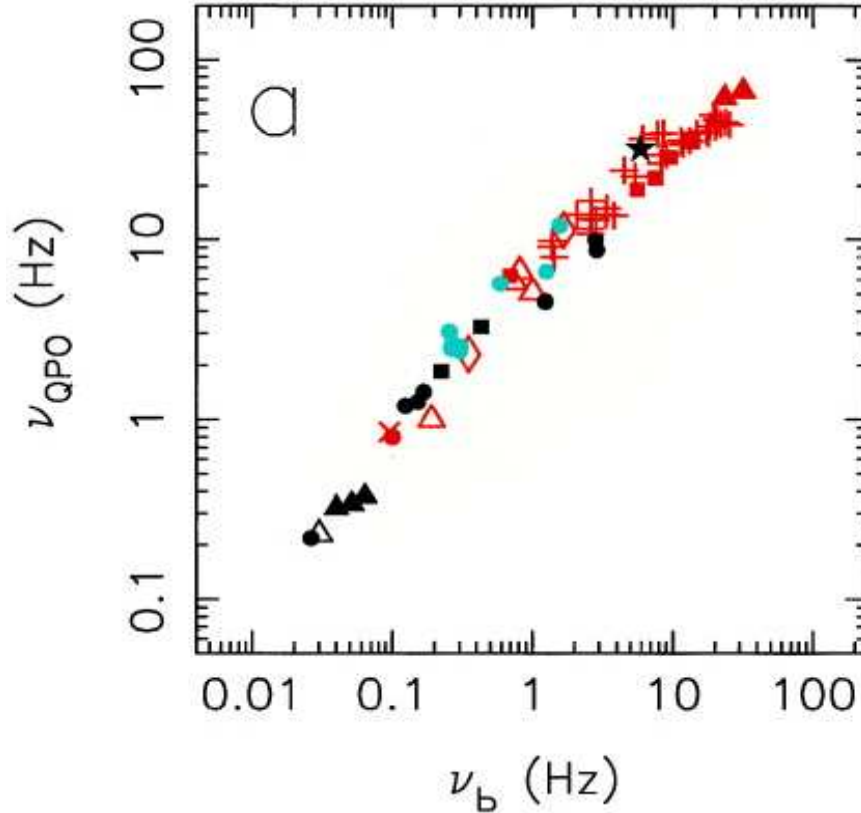


Figure 1.8: The break frequency (X-axis) of the power density spectra of accreting X-ray binaries (both neutron star and black hole binaries) versus their QPO frequency (Y-axis). These quantities are clearly correlated (Wijnands & van der Klis 1999). The various colors and shapes of the data points represent the various neutron star and black hole sources and are not relevant to the current discussion.

R_g for a maximally spinning hole, where $R_g = GM/c^2$ is the so-called gravitational radius). Moreover, the energy liberated from viscous dissipation is emitted locally and promptly, increasing the local disk temperature. In fact, most of this energy is released within the inner few gravitational radii, for instance, 90% of the energy is released within the inner $20R_g$. This assumption of local thermal equilibrium is the basis for the so-called thin accretion disk which has been used as a theoretical standard for decades (Shakura & Sunyaev 1973).

For stellar-mass black holes it is expected that the disk temperature peaks in

the range of 1-2 keV (depending on the exact black hole mass). Observationally, X-ray spectra of various stellar-mass black holes show evidence for this thermal disk component⁷ with the maximum disk temperatures in the expected range of 1-2 keV (McClintock & Remillard 2006). In addition, depending on the mass accretion rate, these systems also show a non-thermal spectral component which is often characterized by a simple power-law. The physical origin of this component is currently unclear but it is plausible that it originates from Comptonization (Compton up-scattering) of the accretion disk's thermal photons in a hot but tenuous cloud/layer of electrons which is referred to as a corona. A schematic of this disk-corona paradigm is shown in Figure 1.9.

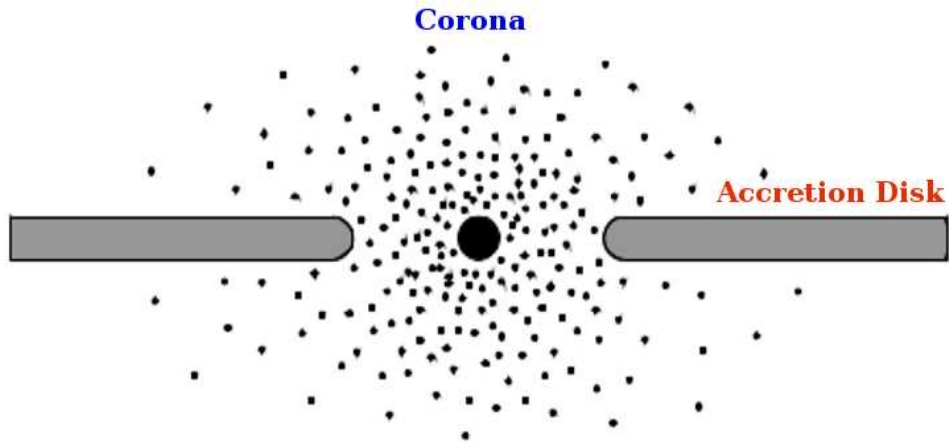


Figure 1.9: Schematic showing the two-component model for an accreting black hole. The corona is represented by dots while the accretion disk by the horizontal bars (McClintock & Remillard 2006). The exact location and properties of the corona is still unclear but is often represented as a tenuous cloud/layer of electrons.

⁷Each radius within the accretion disk is presumed to be emitting like a black body at a given temperature. The final energy spectrum of the source is thus a composite of these individual black body/thermal spectra.

The observed relative strengths of these two spectral components has also been used as a basis for classification of black hole X-ray accretion states. While there are various classification schemes proposed in the literature, here we only discuss the one proposed by McClintock & Remillard (2006) which we also adopt in this thesis (Chapter 2). This classification scheme, which uses both the energy and the power spectra in the 2-20 keV X-ray bandpass, suggests three principal X-ray states for accreting black holes. (1) The low/hard state during which the source's energy spectrum is dominated by the non-thermal, coronal component, and the power spectra by strong (up to roughly 50% rms) broadband timing noise. The power spectrum during the low/hard state can be described by flat-topped noise at the lowest frequencies breaking into a power-law with low-frequency QPOs (0.2-15 Hz) on the power-law portion. (2) During the high/soft state the soft/thermal component dominates and is accompanied by a weak power-law timing noise. (3) Finally, the so-called very high state has approximately equal power-law and thermal contributions and strong 3-12 Hz QPOs on top of a strong power-law like noise. For precise values that demarcate one state from the other see McClintock et al. (2009).

The X-ray variability of accreting black holes can be understood within this physical framework consisting of an accretion disk, a corona, and a companion star. Relevant to this thesis are the low-frequency QPOs (such as the Type-C QPOs referred to above), the high-frequency QPOs, and the orbital & the super-orbital periods. Starting at the farthest radial distance from the black hole, one can have coherent X-ray variability on an orbital period timescale. Periodic X-ray variability can arise from regular obscuration of the X-ray source by intervening material (see

Chapter 5) between the X-ray source and the observer. This intervening material can be the companion star itself when the system is highly inclined (referred to as eclipsing), or an accretion disk–accretion stream interaction hot-spot (e.g., White 1995), or even a focused wind in the case where the companion is a massive Wolf-Rayet star with strong winds (e.g., Feng & Cui 2002). Periods longer than the orbital period are usually referred to as super-orbital periods and they are very likely associated with precession of the accretion disk (Charles et al. 2008). While the exact mechanism that drives the disk precession is still controversial, the change in the projected area of the accretion disk as it precesses is believed to cause the observed periodic X-ray variability. In stellar-mass black holes, super-orbital periods range from a few tens to hundreds of days (see, e.g., Kotze et al. 2011).

The underlying physical mechanisms for the low-frequency (0.2-15 Hz) and the high-frequency QPOs (100-450 Hz) are still unclear. Given the diversity of the low-frequency QPO complex, viz., their wide frequency range of 0.2-15 Hz (McClintock & Remillard 2006), rms amplitude range of 2-15% (Casella et al. 2005), presence over varying source luminosity (e.g., Reig et al. 2000) and their dependence on energy spectral properties (e.g., Sobczak et al. 2002; Vignarca et al. 2003), currently there is no single model that can explain all these observed properties. Some of the models in the literature include the global disk oscillations (Titarchuk & Osherovich 2000), radial oscillations of the accretion shock fronts (Chakrabarthi & Manickam 2000), a precessing ring model (Schnittman et al. 2006), etc. The main issue with low-frequency QPOs is the fact that they appear to be slower than the relevant Keplerian orbital periods. For example, for a $10 M_{\odot}$ black hole, the orbital radius

that corresponds to 3 Hz is $100R_g$, while most of the X-ray emission is expected from 1-10 R_g (McClintock & Remillard 2006). Most of the current models suggest that the low-frequency QPOs originate from less than a few 100 R_g . The high-frequency QPOs on the other hand seem to be conceptually simpler, in the sense that they are much faster with stable frequencies in the range of 100-450 Hz and rms amplitudes of a few percent (Belloni et al. 2011). Because their frequencies are comparable to the Keplerian orbital frequencies in the inner few gravitational radii of the accretion disk and they are relatively stable for a given source, many corresponding models propose a general relativistic origin with these oscillations arising from within the inner few R_g (e.g., Abramowicz et al. 2004; Wagoner 1999, etc). In Figure 1.10 we show a schematic with plausible locations for the origin of these four X-ray modulations.

1.4 Thesis outline

The main goal of this thesis is to probe the nature of ULXs, not limited to their black hole masses, using their time and energy spectral variability. The idea is to understand the observed variability properties of ULXs within the context of what is already known from the well-studied accreting X-ray binaries. A brief outline of this thesis is described below:

- Chapter 2) I test the hypothesis that the mHz QPOs of ULX NGC 5408 X-1 are of type-C by searching for a correlation between its variable QPO centroid frequency and the energy spectral power-law index using all the archival *XMM-Newton* data

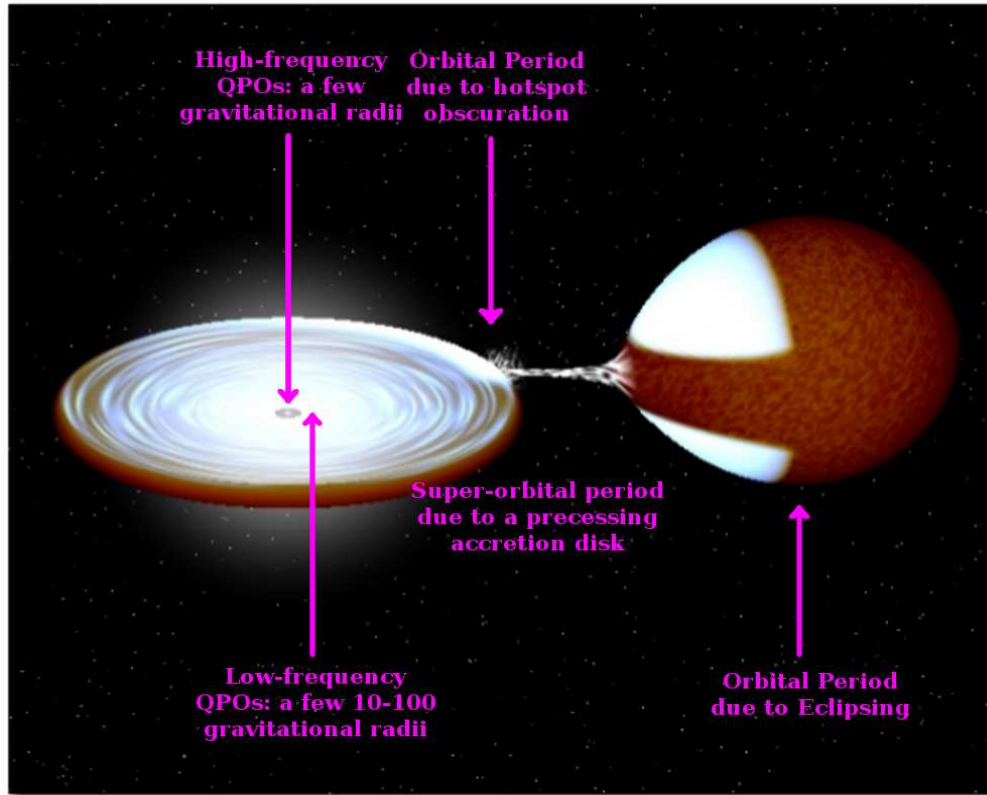


Figure 1.10: Schematic showing the rough locations of the origin of some of the oscillations commonly observed from black hole binaries.

of this source. Establishing the mHz QPOs as type-C will validate the mass-scaling methodology and thus ascertain it as an intermediate-mass black hole (Dheeraj & Strohmayer 2012).

- Chapter 3) I test the same hypothesis for the ULX M82 X-1 using all of its archival data. However, due to dense clustering of X-ray point sources in the innermost regions of this galaxy the analysis involves carefully modeling the surface brightness of the images in order to estimate the hardness ratio (count rate in the hard X-rays/count rate in the soft X-rays) of M82 X-1. The hardness ratio was used as a proxy for the energy spectral power-law index (Pasham & Strohmayer 2013b).

- Chapter 4) Current measurements of IC 10 X-1 suggest it hosts a stellar-mass black hole with an estimated mass in the range of $23\text{-}34M_{\odot}$ (Prestwich et al. 2007; Silverman & Filippenko 2008). We discovered a low frequency 7 mHz pulsation in its X-ray light curve. Using this example we demonstrate the perils of direct scaling of QPO frequencies with black hole mass (Pasham, Strohmayer & Mushotzky 2013).
- Chapter 5) I analyze ≈ 1240 days of *Swift/XRT* X-ray (0.3-8 keV) monitoring data of the ULX NGC 5408 X-1 and detect a 243 day quasi-period in addition to the 115.5 day period earlier reported (Strohmayer 2009). Based on the various properties of these two periods, viz., their energy dependence, their variation profile and the phase separation, etc, we propose an accretion geometry for the ULX (Pasham & Strohmayer 2013a).
- Chapter 6) I revisit the 62 day X-ray period of M82 X-1 using a data set with a temporal baseline twice as long as previous studies and find that the period changes its phase suddenly. When the phase-resolved X-ray energy spectra of this source are modeled with a disk and a power-law model the disk flux appears to modulate with phase. We argue that these two lines of evidence indicate that the period is due to a precessing accretion disk (Pasham & Strohmayer 2013c).
- Chapter 7) I co-add all the power density spectra of M82 X-1 taken over a time span of ≈ 5.5 years and detect stable 3:2 frequency ratio pulsations that we argue are similar to the so-called high-frequency QPOs of stellar-mass black holes, where it is known that the frequency scales directly with the black hole mass (McClintock & Remillard 2006). Our result indicates that the black hole in M82 X-1 is $\approx 400M_{\odot}$ and provides some of the strongest quantitative evidence to-date for a few hundred

solar mass black hole.

- Chapter 8) I conclude with an outlook where I present preliminary results from the first ever attempt of an X-ray – optical reverberation mapping of a ULX. I also discuss the future prospects of detecting intermediate-mass black holes using the phenomenon of tidal disruption flares and by searching for the 3:2 high-frequency QPO analogs using NASA’s Neutron star Interior Composition Explorer (*NICER*).

Chapter 2: A Search for Timing-Spectral Correlations in the ULX NGC 5408 X-1

2.1 Introduction & Background

Within the context of stellar-mass black holes, the so-called low-frequency QPOs (those in the frequency range of 0.1-15 Hz) are broadly classified into three categories based on their properties and the overall nature of their power density spectra (Casella et al. 2005). A power density spectrum with type-A and B QPOs is characterized by weak red noise (noise at the low frequency end of the power density spectrum) with the type-A QPOs occurring with relatively low coherence (quality factor, $Q = \text{centroid frequency}/\text{width (FWHM)}, \lesssim 3$) compared to the type-B ($Q \gtrsim 6$). Finally, one has the type-C QPOs which are most relevant to the present work. The power density spectra accompanying these QPOs in stellar-mass black hole systems can be described by a flat-topped, band-limited noise breaking to a power law with the QPOs evident on the power-law portion of the spectrum, close to the break.

Further, the type-C QPOs are fairly coherent with the quality factor, Q from 5-15 and amplitudes (% rms) ranging from 2-20. In stellar-mass black holes, they are

known to occur in the frequency range from ≈ 0.1 -15 Hz. In light of the work unifying the stellar-mass and the super-massive black holes, if some ULXs were to host intermediate-mass black holes then the qualitative behavior of their power density spectra should be comparable to stellar-mass black holes with the characteristic variability times scaling according to the mass of the putative intermediate-mass black hole. This idea has been explored by a number of authors to search for the “QPO analogs” in ULXs; and QPOs have now been detected in a handful of them. The QPOs detected in M82 X-1 (Strohmayer & Mushotzky 2003), NGC 5408 X-1 (Strohmayer et al. 2007) and NGC 6946 X-1 (Rao et al. 2010) resemble the type-C QPOs, while those detected in the M82 source X42.3+59 more closely resemble the type-A or -B QPOs (Feng et al. 2010). The crucial difference here is that the QPO centroid frequencies of the ULX sources appear to be scaled down by a factor of a few \times (10 - 100) (\sim few mHz) compared to the low-frequency QPOs in stellar-mass black holes.

Under the assumption that the ULX mHz QPOs are analogs of the low-frequency QPOs in stellar-mass black holes, it is reasonable to assume that their characteristic timescales/frequencies (e.g., QPO centroid frequencies, power density spectral break frequencies) scale with the mass of the accreting source and vice versa. However, the type-C QPOs occur with a wide range of centroid frequencies (0.1 – 15 Hz) in stellar-mass black hole systems. Therefore, timing information alone is not sufficient to accurately estimate ULX masses in this way, but combining timing and spectral information has proven to be a valuable tool. For example, in stellar-mass black hole systems, the power-law photon index and disk flux are correlated with

the QPO centroid frequency. The general trend is an increase in the power-law photon index and the disk flux with the QPO centroid frequency (e.g., Sobczak et al. 2000a; Vignarca et al. 2003; Shaposhnikov & Titarchuk 2009), with evidence for saturation (constancy of the power-law photon index and the disk flux with a further increase in the QPO centroid frequency) beyond a certain frequency.

Using a reference stellar-mass black hole system with a measured QPO centroid frequency – photon-index relation, one can then scale the QPO centroid frequencies detected in ULX systems at a given power-law spectral index to get an estimate of the mass. For example, with archival *XMM-Newton* data from M82 X-1, Dewangan et al. (2006) extracted the energy and the power spectra of the source. The power spectrum was strikingly reminiscent of a stellar-mass black hole with type-C QPOs, i.e., flat-top noise breaking to a power-law with QPOs on the power-law portion of the spectrum. However, the respective timescales were scaled down by a factor of ~ 10 . The QPO in this case was centered around a frequency of ~ 114 mHz and the energy spectrum had a power law photon index of ~ 2.0 . Using the QPO frequency - photon index correlations from two stellar-mass black hole reference sources, GRS 1915+105 and XTE J1550-564, they estimated the mass of the ULX in M82 X-1 by scaling its QPO centroid frequency (~ 114 mHz) at the given photon index (~ 2.0). They estimated the mass of the black hole to be in the range $25\text{-}520M_{\odot}$. Similar scaling arguments were used by Rao et al. (2010) to estimate the mass of the black hole in the ULX NGC 6946 X-1 to be in the range $(1\text{-}4) \times 1000 M_{\odot}$. Based on both the power density spectrum and the energy spectrum of NGC 5408 X-1, Strohmayer & Mushotzky (2009) argued that the source behavior was consistent with the steep

power-law state often seen in stellar-mass black holes. They compared the available data from NGC 5408 X-1 to five different stellar-mass black hole reference sources and estimated the mass of the black hole to be a few $1000 M_{\odot}$. Feng et al. (2010) detected 3-4 mHz QPOs from the ULX X42.3+59 in M82 and identified them as either type A/B analogs of stellar-mass black holes. They estimated the mass of the black hole to be in the range $12,000-43,000 M_{\odot}$ by scaling the QPO frequency to that of the type A/B QPOs in stellar-mass black holes.

It is important to note that the above scaling arguments have several caveats. First, the mass estimates were established under the assumption that the mHz QPOs detected from these ULX systems are analogous to a particular type of low-frequency QPO detected in stellar-mass black hole systems, i.e., A, B or C. These identifications were based on the qualitative nature of the power spectrum alone in some cases and both the power spectrum and the energy spectrum in the case of NGC 5408 X-1. Second, in the case of the ULX mHz QPOs, the observed range of QPO centroid frequencies and photon indices has been limited. To gain a more secure identification one would like to see the QPO frequencies and photon spectral indices *correlate* in a similar fashion as for the stellar-mass black holes.

In this chapter, we further explore these issues using extensive new observations of NGC 5408 X-1 with *XMM-Newton*. We describe the properties of the mHz QPOs over a wider range of centroid frequencies than previous data allowed. More specifically, we study the nature of the mHz QPOs from NGC 5408 X-1 through a systematic search for timing – spectral correlations similar to those seen in the stellar-mass black holes. The chapter is arranged as follows. In §2.2 we describe

Table 2.1: Summary of the *XMM-Newton* observations of NGC 5408 X-1

ObsID	T_{obs}^1 (ksecs)	Net Count rate ² (counts s ⁻¹)	Effective Exposure ³ (ksecs)
0302900101 (2006)	132.25	1.26 ± 0.04	99.94
0500750101 (2008)	115.69	1.19 ± 0.04	48.55
0653380201 (2010A)	128.91	1.46 ± 0.04	80.68
0653380301 (2010B)	130.88	1.40 ± 0.04	110.0
0653380401 (2011A)	121.02	1.34 ± 0.07	107.75
0653380501 (2011B)	126.37	1.31 ± 0.07	98.66

¹The total observation time.

²The average *pn+MOS* count rate.

³After accounting for flaring background and good time intervals. See §2 and §3 for details on filtering.

the data used for the present study. In §2.3 we show the results from our timing analysis, while in §2.4 we give details of the energy spectral analysis. In §2.5 we describe our search for timing - spectral correlations similar to those seen in accreting stellar-mass black hole systems. The search is conducted using two different spectral models, a phenomenological model of a *multi-colored disk + power-law* and then with a model describing Comptonization by bulk motion (Titarchuk et al. 1997) that has been used previously to derive black hole masses from QPO scaling arguments (Shaposhnikov & Titarchuk 2009). Finally, in §2.6 we discuss the implications of our results on the mass of the black hole in NGC 5408 X-1.

2.2 *XMM-Newton* Observations

XMM-Newton has now observed NGC 5408 X-1 on multiple occasions. We use

data from six of these observations (~ 100 ksecs each) spread over a time span of five years (2006-2011). The details of the observations are outlined in Table 2.1. Results from the first two observations (in 2006 and 2008, respectively) were summarized in Strohmayer et al. (2007) & Strohmayer & Mushotzky (2009). Using the 2006 data, Strohmayer et al. (2007) reported the first detection of quasi-periodic variability from this source. Strohmayer & Mushotzky (2009)'s analysis of the 2008 observation again showed evidence for the presence of quasi-periodic oscillations. However, the most prominent QPO during the 2008 observation was at a lower frequency (QPO at ~ 10 mHz compared to 20 mHz in 2006). Further, Strohmayer & Mushotzky (2009) noted that the disk contribution to the total flux and the power-law index of the energy spectrum decreased slightly compared to its state in 2006. This is analogous to a trend often seen in stellar-mass black hole systems where the disk flux and the power law index of the energy spectrum positively correlate with the centroid frequency of the most dominant QPO (e.g., Viagnarca et al. 2003, Sobczak et al. 2000a). These findings were used to propose additional observations with *XMM-Newton*, with the goal of detecting QPOs over a range of frequencies and hence to further explore for correlations between timing and energy spectral properties. A large program was approved for Cycle 9 (PI: Strohmayer), and four observations (~ 100 ksecs each) were made under this program. Two of the observations were carried out in 2010 (2010a & 2010b) and the rest in 2011 (2011a & 2011b). Here we present results from these new observations as well as a reanalysis of the earlier pointings, so as to facilitate a consistent comparison of all the available data.

For the present work, we use the data acquired by the European photon imag-

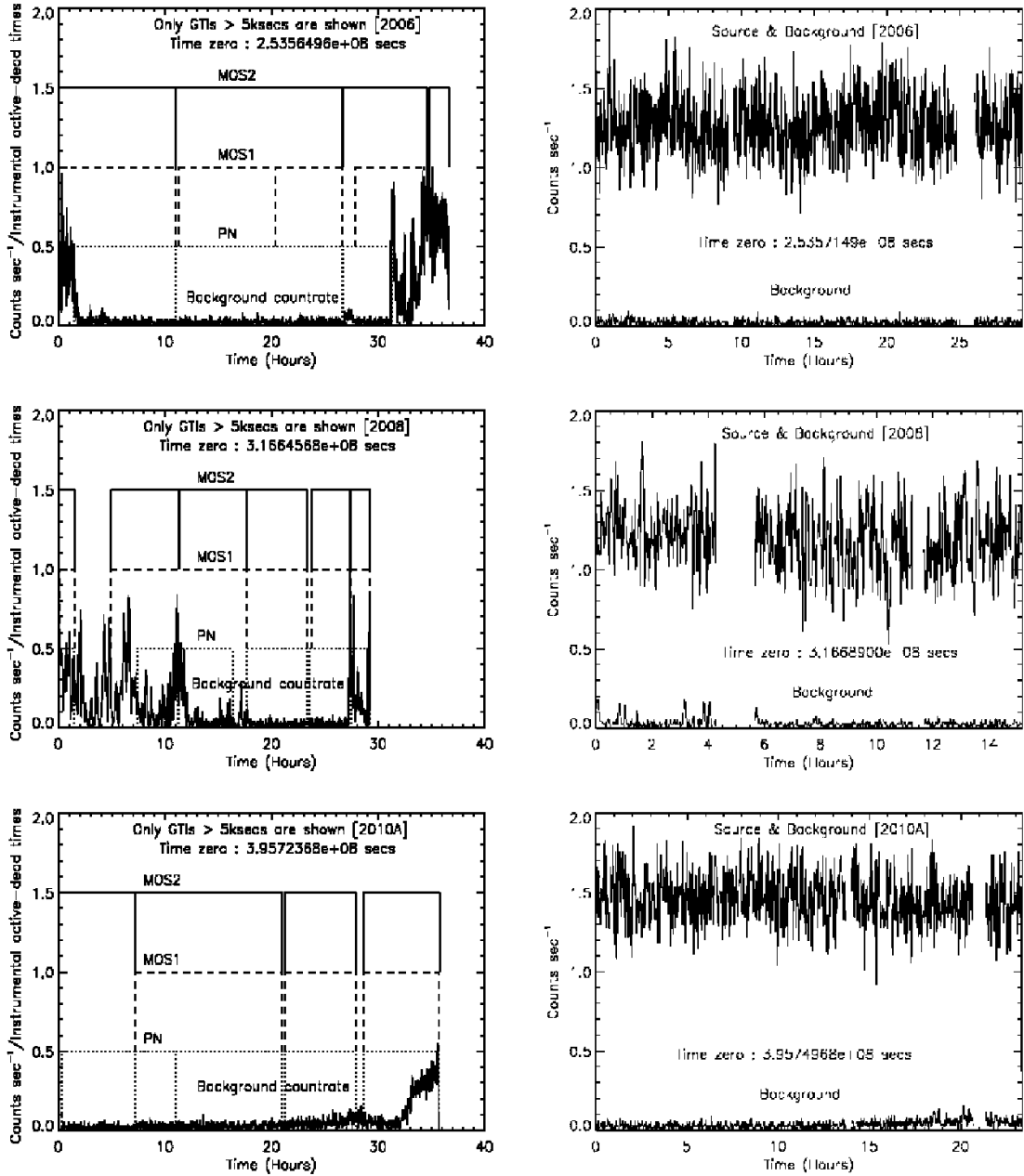


Figure 2.1: *Left Panels:* Good time intervals (>5 ksecs) from EPIC-pn, MOS1 & 2 onboard *XMM-Newton*. For a given instrument, at a given time (X-axis), a finite value on the y-axis implies the instrument was *continuously* active for at least 5 ksecs. Also shown is a combined background (pn+MOS1+MOS2) light curve with flaring evident in some cases. The observation year is indicated at the top of each plot (Shown here are **2006**, **2008** & **2010A** data: see Table 2.1). Time zero is indicated in secs since 1998.0 TT. *Right Panels:* Filtered light curves (pn+MOS1+MOS2) accounting for both instrumental dead times and flaring. The power spectra were derived from these cleaned light curves. These light curves were extracted using photons in the energy range of 0.3-10.0 keV.

ing camera (EPIC), i.e., both the *pn* and *MOS* to get a higher signal-to-noise ratio in the power and energy spectra. We used the standard SAS version 11.0.0 to reduce the images and filtered event-lists from all the EPIC data. The standard filter with (*PATTERN* ≤ 4), to include only single and double pixel events, was applied to the event-lists and events only in the energy range 0.3-12.0 keV were considered for further analysis. Background flaring was prominent for brief periods during certain observations. The power and energy spectra were carefully extracted taking into account both the background flaring and the instrumental dead time effects (specific details in the next sections). In all the observations the source was easily detectable and we did not face any source confusion problems. We extracted source events from a region of radius 32'' centered around the source. This particular value was chosen to roughly include 90% of the light from the source (estimated from the fractional encircled energy of the EPIC instruments). A background region, free of other sources, was extracted in a nearby region. The size of the background region was chosen to be consistent with the source region. Further, the size of the source and the background region was chosen to be consistent for all the six observations (i.e., 32''). We present the specific details of the timing and spectral analysis in the following sections.

2.3 Timing Analysis

We produced the source and the background light curves to assess the quality of the data. Shown in the left panels of Figure 2.1 and 2.2 are the background count

rates ($pn+MOS1+MOS2$) for each of the six observations. Overlaid are the time intervals during which a given instrument ($pn, MOS1/2$) was continuously active for more than 5 ksecs, i.e., all the instrumental good time intervals (GTIs) longer than 5 ksecs. For a given instrument, a horizontal line (offset to an arbitrary value for each instrument) indicates the active time, while a vertical line marks the beginning or the end of a continuous data interval. Such an insight is important as we are using both the pn and the MOS data to achieve higher count rates compared to, say, the pn alone. In other words, this ensures that the combined pn and MOS event-lists contain only events corresponding to the times during which all the three instruments were active. Furthermore, inspection of the light curves reveals background flaring at either the beginning or the end, or both, of all the observations. Therefore, the final combined ($pn+MOS1+MOS2$) light curves were extracted by taking into account the GTIs of all the instruments and excluding the periods of background flaring. The filtered light curves (100s bins) of the source and the non-flaring background in the energy range 0.3 - 12.0 keV are shown in the right panels of Figures 2.1 and 2.2. The combined mean count rates (0.3-12.0 keV) during each observation are listed in Table 2.1. Notice that the gaps in the data are either due to exclusion of background flaring times, dead time intervals or the absence of GTIs longer than 5 ksecs.

It is evident from the light curves (right panels of Figure 2.1 and 2.2) that the source varies significantly during all the observations. To quantify the variability, we construct a power density spectrum from each of the light curves. To achieve higher signal-to-noise in the power density spectra, we break the GTIs into shorter

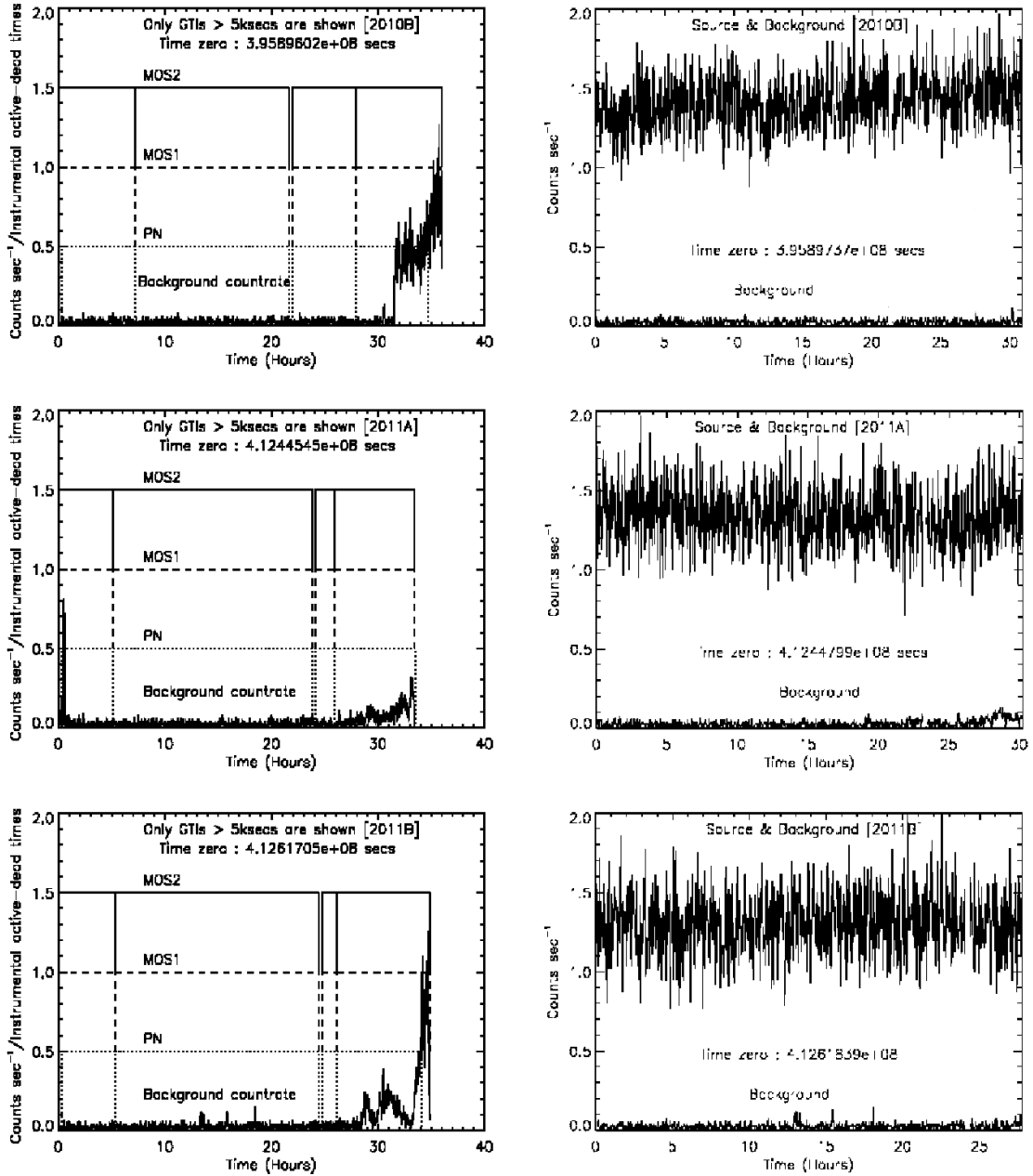


Figure 2.2: *Left Panels:* Good time intervals (>5 ksecs) from EPIC-pn, MOS1 & 2 onboard *XMM-Newton*. For a given instrument, at a given time (X-axis), a finite value on the y-axis implies the instrument was *continuously* active for at least 5 ksecs. Also shown is a combined background (pn+MOS1+MOS2) light curve with flaring evident in some cases. The observation year is indicated at the top of each plot (Shown here are **2010B**, **2011A** & **2011B** data: Refer to Table 2.1). Time zero is indicated in secs since 1998.0 TT. *Right Panels:* Filtered light curves (pn+MOS1+MOS2) accounting for both instrumental dead times and flaring. The power spectra were derived from these cleaned light curves. These light curves were extracted using photons in the energy range of 0.3-10.0 keV.

segments ($S/N \propto \sqrt{\text{Number of individual spectra}}$, e.g., Van der klis 1989) and derive an average power spectrum. For a given observation, the size and the number of such segments are shown in the first row of Table 2.2. Figures 2.3 and 2.4 show the power density spectra and the best-fitting model (*thick solid line*) for each of the six observations in two different energy bands. Shown in the left panel is a power density spectrum in an energy band in which a QPO is detected with high statistical significance and in the right panel is a power density spectrum derived from photons in the energy band of 1.0-10.0 keV (the reason for constructing power spectra in two different energy bands is discussed in the next paragraph). All the power spectra shown here use the so-called Leahy normalization, with the Poisson noise level being 2 (Leahy et al. 1983). Clearly, in each spectrum the power rises below ~ 0.1 Hz with evidence for a QPO in the range of 10-40 mHz and essentially Poisson noise at higher frequencies.

To quantify this behavior, we fit a bending power law to the continuum and a Lorentzian to model the QPO (Belloni et al. 2002). The model fits well with the reduced $\chi^2 \approx 1$ (last row of Tables 2.2 & 2.3) in three cases (2008, 2011A, 2011B) and gives acceptable fits with the reduced χ^2 in the range 1.3-1.5 (last row of Tables 2.2 & 2.3) in the other three cases (2006, 2010A, 2010B). A careful analysis of the residuals in the latter three cases indicates that multiple weak features contribute significantly to increase the overall χ^2 . For example in the case of the power density spectrum derived from the 2010A data (bottom two panels of Figure 2.3), the weak QPO-like feature at ~ 55 mHz and the excess at ~ 0.2 Hz contribute about 30 to the total χ^2 . However, their individual statistical significance is rather

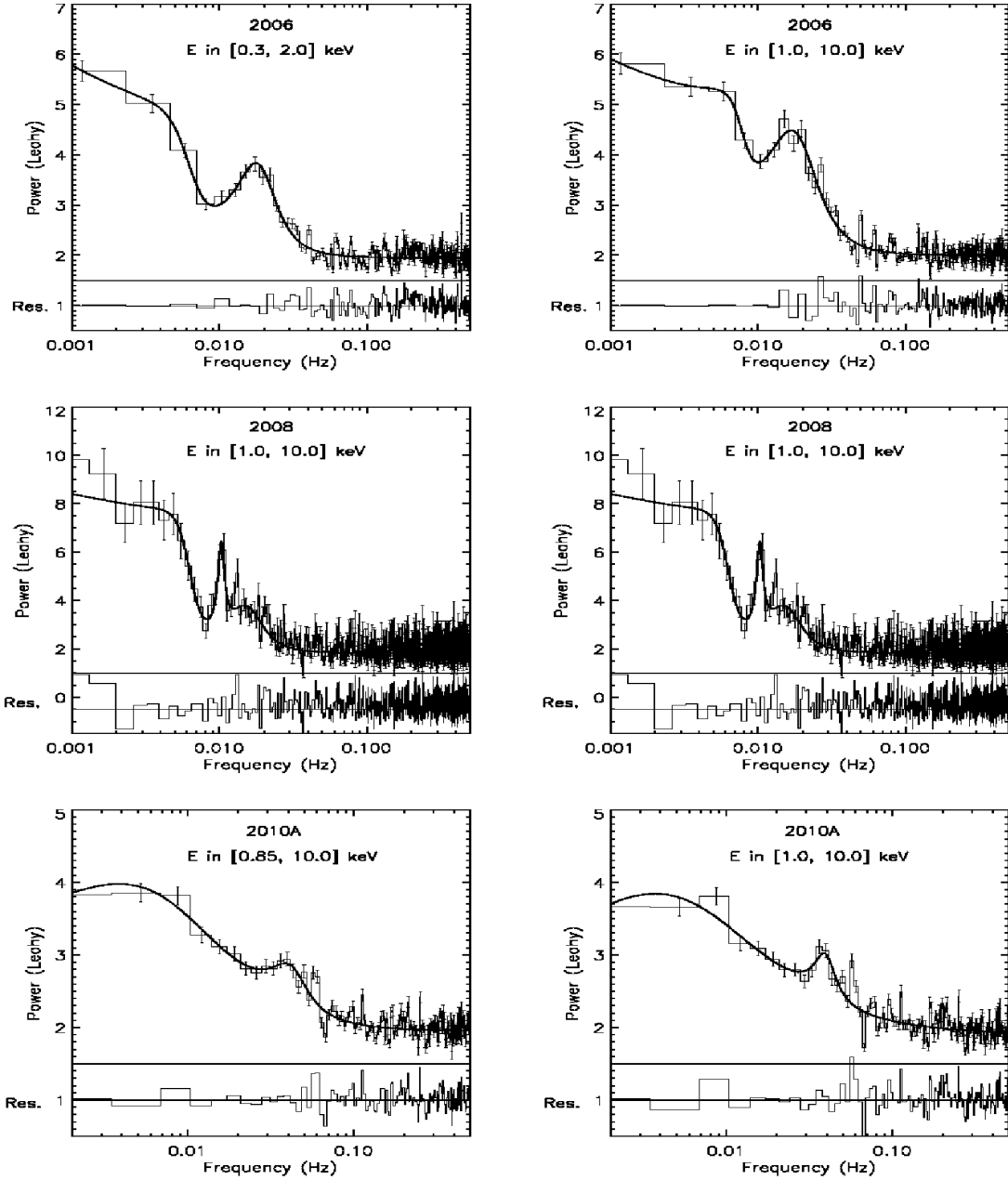


Figure 2.3: Shown are the power spectra derived from the first three of the six *XMM-Newton* observations (**2006**, **2008**, **2010A**: Table 2.1). For a given power spectrum the strength of a QPO is dependent on the energy band under consideration. *Left Panels*: The power spectrum using an energy band (shown at the top of each plot) in which the QPO is clearly detected. Also shown are the error bars and the residuals (Data-Model) offset to an arbitrary value in each case. *Right Panels*: Same as the plots on the left panel. However, here we choose a fixed energy range of 1.0-10.0 keV. A consistent energy band across all the power spectra is required to unambiguously assess the behavior (especially, rms amplitude versus QPO centroid frequency: Fig.3) of these QPOs.

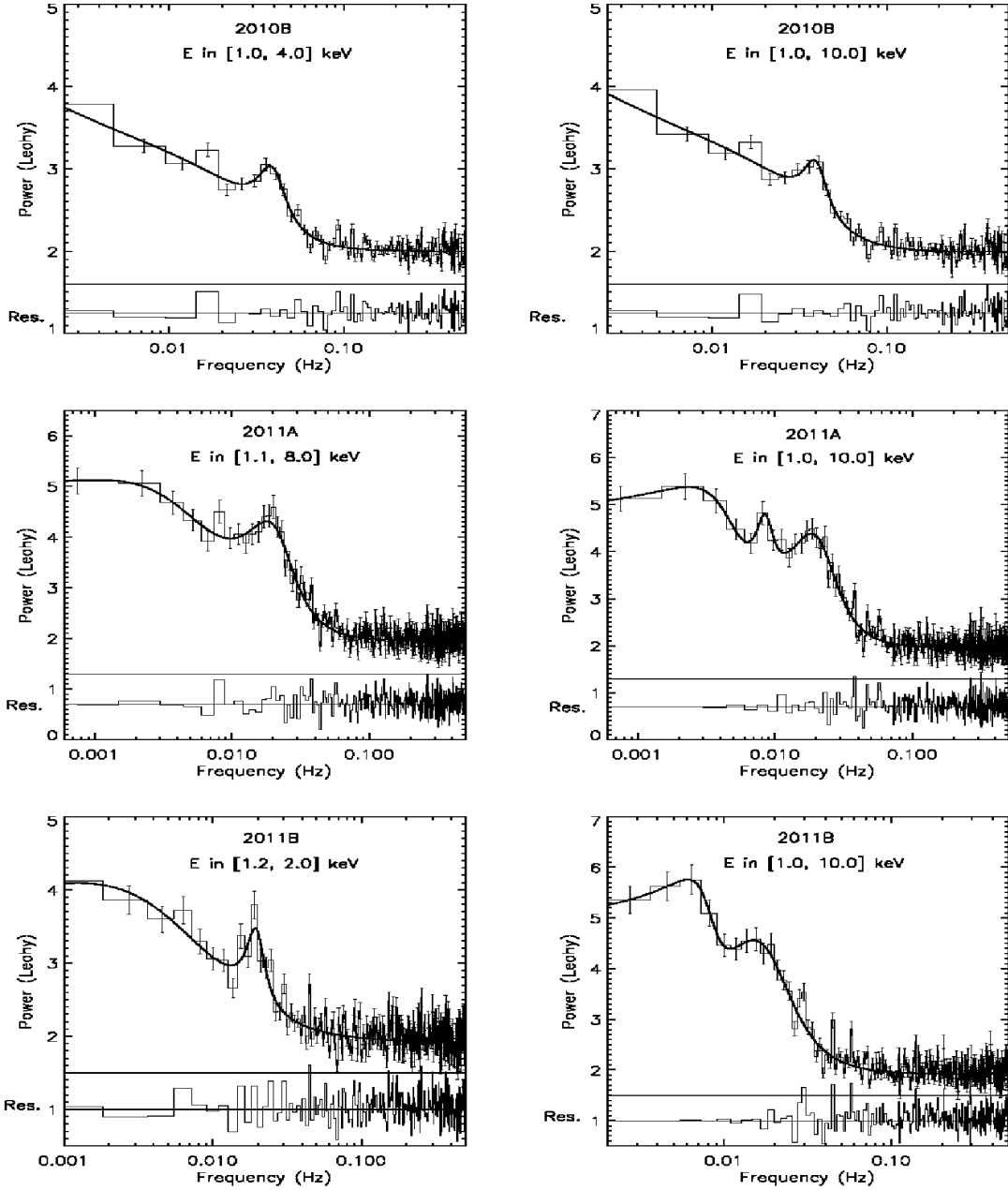


Figure 2.4: Shown are the power spectra derived from the last three of the six *XMM-Newton* observations (**2010B**, **2011A**, **2011B**: Table 2.1). For a given power spectrum, the strength of a QPO is dependent on the energy band under consideration. *Left Panels*: The power spectrum using an energy band (shown at the top of each plot) in which the QPO is clearly detected. Also shown are the error bars and the residuals (Data-Model) offset to an arbitrary value in each case. *Right Panels*: Same as the plots on the left panel. However, here we choose a fixed energy range of 1.0-10.0 keV. A consistent energy band across all the power spectra is required to unambiguously assess the behavior (especially, rms amplitude versus QPO centroid frequency: Fig.2.5) of these QPOs.

low. Nevertheless, for the purposes of analyzing the QPO properties and studying the overall qualitative nature of the power spectra, the fits are adequate. The best-fitting model parameters (derived from a fit in the frequency range 1.0 mHz - 0.5 Hz) for each observation are shown in Tables 2.2 & 2.3 for the two different energy bands (highlighted in the tables). Also shown are the χ^2 /degrees of freedom (dof) values for each of the fits along with the χ^2 /dof corresponding to the continuum model (in braces). The change in χ^2 serves as an indicator of the statistical significance of the QPOs. For a given observation, we choose two different energy bands: the first energy band (second row of Table 2.2) is the bandpass in which the QPO is detected with a very high confidence and the second bandpass of 1.0-10.0 keV was chosen to consistently compare the properties of the QPO across all the observations (overall variability is energy dependent). We confirm the overall qualitative nature of the power density spectrum, i.e., flat-topped noise breaking to a power law with a QPO on the power law portion (near the break). This is consistent with stellar-mass black holes showing type-C QPOs but with the characteristic frequencies scaled down by a factor of a few $\times 10$. This is in agreement with the results reported by Strohmayer et al. (2007) and Strohmayer & Mushotzky (2009), except with regard to possible close QPO pairs, as here all our power density spectra (Figure 2.3 & 2.4) are averaged to the extent of smearing out weak features (to clearly identify the strongest QPO). The effect of averaging is evident from the best-fit parameters of the QPOs (Tables 2.2 & 2.3). More specifically, since we have smeared out the possible close pair QPOs (as reported by Strohmayer et al. (2007) & Strohmayer & Mushotzky (2009) using the 2006 and the 2008 datasets, respectively) the average quality factors of the

Table 2.2: Summary of the best-fitting model parameters for the power density spectra of the ULX NGC 5408 X-1. Here, we use an energy band in which the QPO is detected with very high confidence.

Dataset	2006	2008	2010A	2010B	2011A	2011B
Exposure ^a (ksecs)	27.6×3	15.5×2	23.2×3	21.0×4	67.4×1	55.0×1
Energy Range ^b (keV)	0.30-2.0	1.0-10.0	0.85-10.0	1.0-4.0	1.10-8.0	1.20-2.0
Count rate ^c (cts s ⁻¹)	1.17 ± 0.03	0.43 ± 0.02	0.71 ± 0.02	0.50 ± 0.01	0.41 ± 0.02	0.23 ± 0.01
C*	1.95 ± 0.01	1.81 ± 0.02	1.95 ± 0.02	2.00 ± 0.01	1.95 ± 0.02	1.92 ± 0.02
A*	0.86 ± 1.05	3.39 ± 2.90	9.14 ± 17.90	(0.80 ± 2.30) × 10 ⁻⁰⁴	3.49 ± 10.61	(2.11 ± 3.47) × 10 ⁻⁰³
Γ _{Low} *	0.20 ± 0.19	0.09 ± 0.13	-0.25 ± 0.31	2.68 ± 0.98	-0.04 ± 0.42	1.45 ± 0.52
ν _{bend} * (mHz)	6.33 ± 0.75	6.34 ± 0.49	10.26 ± 6.03	30.63 ± 20.20	5.80 ± 4.84	7.15 ± 8.67
Γ _{High} *	6.74 ± 3.34	10.25 ± 5.60	1.60 ± 0.50	0.25 ± 0.17	1.98 ± 1.83	-0.09 ± 0.43
N _{QPO,1} †	1.88 ± 0.16	3.51 ± 1.69	0.63 ± 0.15	0.72 ± 0.21	2.10 ± 0.56	1.04 ± 0.29
ν _{0,1} † (mHz)	17.68 ± 0.77	10.28 ± 0.24	40.40 ± 2.93	38.81 ± 2.01	18.67 ± 2.20	19.43 ± 0.90
Δν ₁ † (mHz)	15.48 ± 2.05	1.28 ± 0.97	28.06 ± 11.96	18.75 ± 8.98	21.98 ± 6.23	7.08 ± 3.60
N _{QPO,2} †	-	1.91 ± 0.35	-	-	-	-
ν _{0,2} † (mHz)	-	15.05 ± 1.68	-	-	-	-
Δν ₁ † (mHz)	-	11.10 ± 3.05	-	-	-	-
χ ² /dof (continuum ^d)	309.83/208 (618.71/211)	753.75/764 (868.30/770)	178.14/137 (257.33/140)	128.05/97 (207.54/100)	327.11/329 (669.58/332)	268.86/267 (543.03/270)

^aThe good time intervals were broken into smaller intervals to improve the signal-to-noise in the power density spectra. For a given observation, the size of each segment×number of such segments is shown. ^bThe power spectrum was derived using all the photons in this energy range. For a given observation, this is an energy range in which the QPO was detected with a high significance. ^cThe count rate in the bandpass shown in the second row. ^{*}We fit the continuum with a bending power-law model described as follows:

$$Continuum = C + \frac{A\nu^{-\Gamma_{Low}}}{1 + \left(\frac{\nu}{\nu_{bend}}\right)^{\Gamma_{High} - \Gamma_{Low}}}$$

where, Γ_{Low} and Γ_{High} are the low and high frequency slopes, respectively, and ν_{bend} is the bend frequency.

†We model the QPOs with a Lorentzian. The functional form is as follows:

$$QPO = \frac{N_{QPO}}{1 + \left(\frac{2(\nu - \nu_0)}{\Delta\nu_0}\right)^2}$$

where, ν_0 is the centroid frequency and $\Delta\nu_0$ is the FWHM of the QPO feature. ^dThe χ^2 /dof for the continuum are shown in braces.

QPOs reported here are relatively lower than those typical of the type-C QPOs from stellar-mass black holes. Moreover, variation of the QPO centroid frequency over the timescale of the observation can further decrease its coherence. Furthermore, we analyzed the power density spectra of the backgrounds from each of the six observations and note that they are all consistent with a constant Poisson noise.

One of the main goals of the present work is to better characterize the mHz QPOs seen from NGC 5408 X-1 within the context of the known classes of low-frequency QPO seen in stellar-mass black holes (Casella et al. 2005). An important diagnostic for this purpose is the study of the variation of the rms amplitudes of these QPOs with their centroid frequency. In the case of low-frequency QPOs from stellar-mass black hole systems this behavior is fairly well-established (e.g., Revnivtsev et al. 2000; Sobczak et al. 2000a; Vignarca et al. 2003; McClintock & Remillard 2006). The typical behavior of the stellar-mass black hole low-frequency QPOs, in the energy range 2.0-20.0 keV (the nominal *RXTE* bandpass), can be described as follows: as the source evolves along the low/hard state towards the steep power-law state, the QPO frequency increases and the rms amplitude increases. Before reaching the steep power-law state, the source traverses an “intermediate” state in which the QPO frequency continues to increase, but the rms amplitude decreases. Upon reaching the steep power-law state the correlation tends to break down, showing more scatter in the rms amplitude (see Figure 11 in McClintock et al. 2009).

The X-ray variability of NGC 5408 X-1 is known to depend on energy (Middleton et al. 2011). The overall rms variability increases with an increase in the energy of the photons at least up to 2.5 keV (Given the poor signal-to-noise at higher

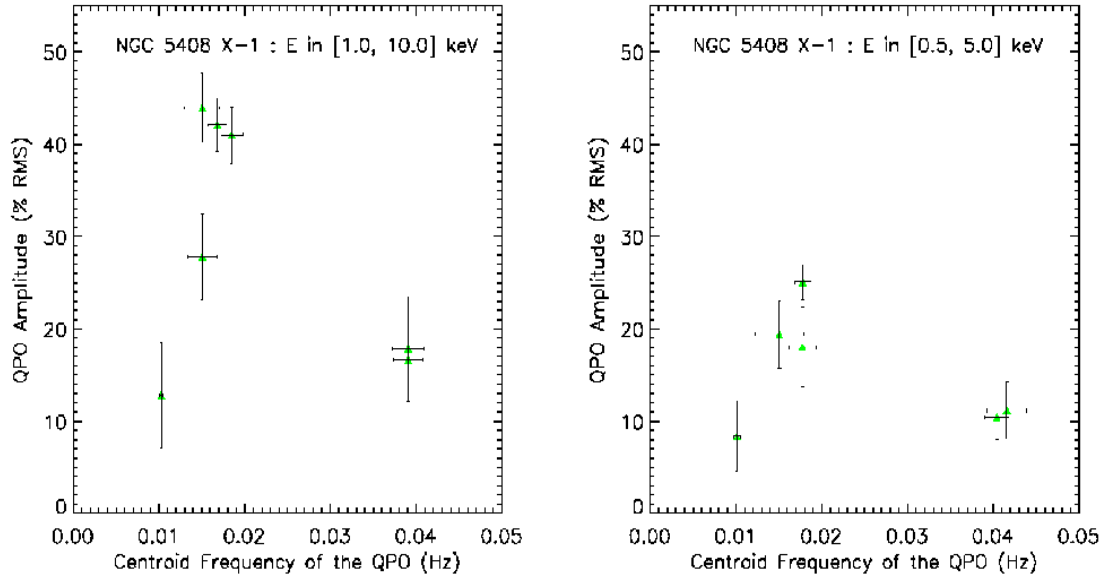


Figure 2.5: The rms amplitude of the mHz QPOs detected from NGC 5408 X-1 (Y-axis) is plotted against the QPO centroid frequency (X-axis). To study the dependence of this plot on the bandpass, we consider two different energy bands. *Left Panel:* Centroid frequency versus QPO amplitude using photons in the energy range from 1.0-10.0 keV. *Right Panel:* Same as the left panel, but a different band-pass of 0.5-5.0 keV was used. The qualitative nature of the behavior does not change with the energy band under consideration. However, the rms amplitude of a given QPO seems to increase with increasing energy (at least in the two energy bands considered), i.e., higher rms amplitude in 1.0-10.0 keV compared to 0.5-5.0 keV.

energies, it is not clear whether the variability strength levels off or decreases). This is similar to the energy dependence of the low-frequency QPO (\approx few Hz) detected from the galactic micro-quasar GRS 1915+105 (Rodriguez et al. 2004), where the QPO amplitude increases with energy, before rolling over. We used the QPO fit parameters from all the observations to explore the dependence of the QPO rms amplitude with centroid frequency. To be consistent across all the observations, we chose an optimum bandpass of 1.0-10.0 keV to ensure good statistics and significant detection of the variability (the variability of the source increases at higher energies

while the count rate decreases). In addition, to explore whether our results might depend on energy, we derived the QPO properties in a different energy band (though with some overlap of the optimum band defined above) of 0.5-5.0 keV. The rms amplitude versus QPO frequency results for the 1.0-10.0 keV and 0.5-5.0 keV are shown in the left and the right panels of Figure 2.5, respectively (compare with Figure 11 of McClintock et al. 2009). Given that the QPO amplitude is higher at higher energies (Middleton et al. 2011), not all power spectra derived from the lower energy band (0.5 - 5.0 keV) yielded statistically significant QPO features. This is why the right panel of Figure 2.3 has one less data point. Clearly, the variation is similar in both the energy bands. We further compare with the results from stellar-mass black holes in §2.5.

Another prime driver for the long observations of NGC 5408 X-1 was to search for high frequency QPO analogs of stellar-mass black holes. These QPOs are observed in the range from about 50 - 450 Hz in stellar-mass black holes (McClintock & Remillard 2006; Strohmayer 2001a). Simple mass scaling arguments would suggest that in intermediate-mass black holes they would be expected in the frequency range of 0.1-1 Hz, with a low rms amplitude of $\sim 2\%$. We do not detect any obvious QPO-like feature at these frequencies in any of the individual observations. Further, given that high-frequency QPOs appear to be reasonably stable in frequency in stellar-mass black holes (e.g., Strohmayer 2001b), we averaged the power spectra derived from the individual observations to improve the signal-to-noise, however, this did not lead to a detection. We estimate the upper limit on the rms amplitude of a QPO-like feature in the frequency range of 0.1-1.0 Hz to be $\sim 4\%$.

Table 2.3: Summary of the best-fitting model parameters for the power density spectra (using only photons in the energy range of 1.0-10.0 keV) of the ULX NGC 5408 X-1.

Dataset	2006	2008	2010A	2010B	2011A	2011B
Exposure ^a (ksecs)	27.6×3	15.5×2	23.2×3	21.0×4	67.4×1	55.0×1
Energy Range (keV)	1.0-10.0	1.0-10.0	1.0-10.0	1.0-10.0	1.0-10.0	1.0-10.0
Count rate ^b (cts s ⁻¹)	0.43 ± 0.01	0.43 ± 0.02	0.55 ± 0.02	0.53 ± 0.01	0.49 ± 0.02	0.49 ± 0.02
C*	2.00 ± 0.01	1.81 ± 0.02	1.90 ± 0.04	1.99 ± 0.01	1.94 ± 0.01	1.92 ± 0.01
A*	0.80 ± 0.89	3.39 ± 2.90	0.01 ± 0.01	(1.48 ± 3.88) × 10 ⁻⁰⁴	4.16 ± 11.49	2.96 ± 9.50
Γ _{Low} *	0.20 ± 0.17	0.09 ± 0.13	1.12 ± 0.30	2.65 ± 1.06	-0.072 ± 0.39	-0.05 ± 0.56
ν _{bend} * (mHz)	7.89 ± 0.73	6.34 ± 0.49	7.12 ± 6.13	36.39 ± 21.26	4.96 ± 1.48	8.30 ± 1.15
Γ _{High} *	10.02 ± 11.47	10.25 ± 5.60	-0.41 ± 0.46	0.25 ± 0.14	4.42 ± 7.78	9.87 ± 12.11
N _{QPO,1} [†]	2.49 ± 0.18	3.51 ± 1.69	0.64 ± 0.15	0.67 ± 0.21	2.40 ± 0.19	2.64 ± 0.27
ν _{0,1} [†] (mHz)	16.81 ± 1.05	10.28 ± 0.24	39.07 ± 1.70	39.07 ± 1.82	18.49 ± 1.28	15.04 ± 2.04
Δν ₁ [†] (mHz)	19.51 ± 2.16	1.28 ± 0.97	15.15 ± 6.44	16.04 ± 8.89	21.86 ± 2.60	22.83 ± 2.94
RMS _{QPO,1} [†]	42.12 ± 2.83	12.81 ± 5.75	16.64 ± 4.05	17.84 ± 5.68	41.00 ± 3.05	43.94 ± 3.72
N _{QPO,2} [†]	-	1.91 ± 0.35	-	-	1.31 ± 1.02	-
ν _{0,2} [†] (mHz)	-	15.05 ± 1.68	-	-	8.40 ± 1.22	-
Δν ₁ [†] (mHz)	-	11.10 ± 3.05	-	-	-	-
RMS _{QPO,2} [†]	-	27.82 ± 4.64	-	-	3.09 ± 4.32	-
χ ² /dof (continuum ^d)	268.34/208 (755.28/211)	753.75/764 (868.30/770)	200.60/137 (242.10/140)	135.27/97 (190.64/100)	350.16/326 (851.45/332)	291.45/266 (677.00/269)

^aThe good time intervals were broken into smaller intervals to improve the signal-to-noise in the power density spectra. For a given observation, the size of each segment×number of such segments is shown. Same time intervals as in Table 2.1 were used here. ^bTo systematically study the QPO properties, we reduced the power spectra in a consistent energy band of 1.0-10.0 keV. ^cThe count rate in the bandpass of 1.0-10.0 keV. *We fit the continuum with a bending power-law model described as follows:

$$Continuum = C + \frac{A\nu^{-\Gamma_{Low}}}{1 + \left(\frac{\nu}{\nu_{bend}}\right)^{\Gamma_{High} - \Gamma_{Low}}}$$

where, Γ_{Low} and Γ_{High} are the low and high frequency slopes, respectively, and ν_{bend} is the bend frequency. [†]We model the QPOs with a Lorentzian. The functional form is as follows:

$$QPO = \frac{N_{QPO}}{1 + \left(\frac{2(\nu - \nu_0)}{\Delta\nu_0}\right)^2}, \quad RMS_{QPO}(integrated\ from\ -\infty\ to\ +\infty) = \frac{\pi N_{QPO} \Delta\nu}{2} \times 100$$

where, ν₀ is the centroid frequency and Δν₀ is the FWHM of the QPO feature. ^dThe χ²/dof for the continuum are shown in braces.

Table 2.4: Summary of the energy spectral modeling of NGC 5408 X-1. *Top Panel:* Best-fitting parameters for the *tbabs*(diskpn+apec+pow)* model. *Bottom Panel:* Best-fitting parameters for the *tbabs*(bmc+apec)* model.

<i>tbabs*(diskpn+apec+pow)</i>							
Dataset	n_H^a	T_{max}^b	kT_{plasma}^c	Γ^d	$\text{Flux}_{0.3-10.0keV}^e$	Flux_{Disk}^f	χ^2/dof
2006	$14.21^{+0.87}_{-0.84}$	$0.141^{+0.005}_{-0.005}$	$1.00^{+0.04}_{-0.04}$	$2.66^{+0.04}_{-0.04}$	$4.03^{+0.17}_{-0.39} \times 10^{-12}$	$1.74^{+0.14}_{-0.28} \times 10^{-12}$	431.07/265
2008	$14.67^{+1.61}_{-1.48}$	$0.136^{+0.010}_{-0.009}$	$0.95^{+0.06}_{-0.06}$	$2.59^{+0.06}_{-0.06}$	$3.83^{+0.24}_{-0.68} \times 10^{-12}$	$1.56^{+0.24}_{-0.66} \times 10^{-12}$	227.40/210
2010A	$14.41^{+1.01}_{-0.96}$	$0.144^{+0.007}_{-0.006}$	$1.01^{+0.04}_{-0.04}$	$2.58^{+0.04}_{-0.04}$	$4.55^{+0.22}_{-0.43} \times 10^{-12}$	$1.72^{+0.08}_{-0.35} \times 10^{-12}$	403.69/277
2010B	$13.04^{+0.84}_{-0.80}$	$0.154^{+0.007}_{-0.007}$	$0.99^{+0.05}_{-0.05}$	$2.58^{+0.04}_{-0.04}$	$4.05^{+0.15}_{-0.33} \times 10^{-12}$	$1.33^{+0.11}_{-0.25} \times 10^{-12}$	429.91/288
2011A	$14.58^{+0.94}_{-0.90}$	$0.146^{+0.007}_{-0.006}$	$0.95^{+0.06}_{-0.07}$	$2.63^{+0.04}_{-0.04}$	$4.22^{+0.19}_{-0.37} \times 10^{-12}$	$1.59^{+0.17}_{-0.33} \times 10^{-12}$	430.67/267
2011B	$13.44^{+1.04}_{-0.99}$	$0.154^{+0.009}_{-0.008}$	$1.01^{+0.07}_{-0.07}$	$2.55^{+0.05}_{-0.05}$	$3.84^{+0.16}_{-0.38} \times 10^{-12}$	$1.41^{+0.15}_{-0.36} \times 10^{-12}$	326.50/256
<i>tbabs*(bmc+apec)</i>							
Dataset	n_H	kT_{disk}^g	$\alpha=\Gamma^h-1$	f^i	N_{BMC}^j	kT_{plasma}^c	χ^2/dof
2006	$9.47^{+1.04}_{-1.00}$	$0.116^{+0.004}_{-0.004}$	$1.68^{+0.04}_{-0.04}$	$0.40^{+0.05}_{-0.05}$	$3.12^{+0.31}_{-0.27} \times 10^{-5}$	$1.03^{+0.04}_{-0.04}$	342.95/265
2008	$10.79^{+1.89}_{-1.78}$	$0.110^{+0.007}_{-0.006}$	$1.59^{+0.06}_{-0.06}$	$0.39^{+0.10}_{-0.10}$	$3.10^{+0.63}_{-0.47} \times 10^{-5}$	$0.97^{+0.05}_{-0.05}$	210.30/210
2010A	$9.73^{+1.26}_{-1.22}$	$0.116^{+0.005}_{-0.005}$	$1.59^{+0.04}_{-0.04}$	$0.45^{+0.08}_{-0.08}$	$3.35^{+0.40}_{-0.33} \times 10^{-5}$	$1.03^{+0.04}_{-0.04}$	359.92/277
2010B	$7.90^{+1.09}_{-1.05}$	$0.121^{+0.005}_{-0.005}$	$1.60^{+0.03}_{-0.03}$	$0.52^{+0.09}_{-0.08}$	$2.75^{+0.26}_{-0.22} \times 10^{-5}$	$1.03^{+0.05}_{-0.04}$	364.36/288
2011A	$9.61^{+1.16}_{-1.11}$	$0.118^{+0.005}_{-0.005}$	$1.64^{+0.04}_{-0.04}$	$0.46^{+0.07}_{-0.07}$	$3.07^{+0.33}_{-0.28} \times 10^{-5}$	$0.99^{+0.05}_{-0.05}$	361.46/267
2011B	$8.69^{+1.32}_{-1.25}$	$0.121^{+0.006}_{-0.006}$	$1.57^{+0.04}_{-0.04}$	$0.47^{+0.08}_{-0.08}$	$2.74^{+0.33}_{-0.26} \times 10^{-5}$	$1.05^{+0.09}_{-0.06}$	299.37/256

^aTotal column density of hydrogen along the line of sight including the Galactic extinction (in units of 10^{20} cm^{-2}). We used the *tbabs* model in XSPEC. ^bAccretion disk temperature in keV. We used the *diskpn* model in XSPEC. The inner radius of the disk was fixed at $6GM/c^2$. ^cThe temperature of the surrounding plasma in keV. We used the *apec* model in XSPEC. The abundances were fixed at the solar value. ^dThe photon index of the power law. ^eThe total unabsorbed X-ray flux (in units of $\text{ergs cm}^{-2} \text{ s}^{-1}$) in the energy range of 0.3-10.0 keV. ^fThe disk contribution to the total X-ray flux (in units of $\text{ergs cm}^{-2} \text{ s}^{-1}$) in the energy range of 0.3-10.0 keV. ^gThe color temperature of the disk blackbody spectrum (in keV). ^hSpectral index of the power law portion of the energy spectrum. ⁱThe Comptonized fraction: fraction of the input blackbody photons that are Comptonized by the bulk motion of the in-falling material. ^jThe normalization of the disk blackbody spectrum (in units of $(L/10^{39} \text{ erg s}^{-1})/(d/10 \text{ kpc})^2$). This is an indicator of the disk flux.

2.4 Energy Spectral Analysis

We fit the X-ray spectra of NGC 5408 X-1 using the XSPEC (Arnaud 1996) spectral fitting package and the EPIC response files were generated using the *arfgen* and *rmfgen* tools which are part of the *XMM-Newton* Science Analysis System (SAS) software. Since, a primary goal of the present work is to search for timing - spectral correlations similar to those seen in accreting stellar-mass black holes, we began our analysis by characterizing the energy spectra using the same phenomenological models often used to describe the X-ray spectra of accreting stellar-mass black holes. In terms of XSPEC models, we used *diskpn + power-law*. We also explored the *bmc* model, Comptonization by bulk motion (Titarchuk et al. 1997), because it has been used to derive mass estimates from QPO frequency scaling arguments, and reference spectral - timing correlations have been derived for a significant sample of stellar-mass black holes using the parameters derived from this model (see Shaposhnikov & Titarchuk 2009). We start by describing some of the specifics of our data extraction and reduction methods.

Since we are interested in exploring the correlations between the timing and the spectral behavior, we elected to extract energy spectra from the same time intervals as those used to extract the power density spectra (see the first rows of Tables 2.2 & 2.3). Such synchronous measurements will tend to minimize any offsets that could be induced by variations in the system properties (both spectral and timing) within a given observation. In addition to the standard filters described in §2.2, the (*FLAG==0*) filter was imposed to get the highest quality spectra. The combined

(*pn+MOS*) average count rate of the source varied in the range 1.19 - 1.46 cts s⁻¹ over all the observations. Given such relatively low count rates, source pileup was not an issue in any of the six observations. Since we are using both the *pn* and the *MOS* data, we individually reduced the energy spectra from each of the detectors using the same good time intervals. This gave us three energy spectra (*pn*, *MOS1*, *MOS2*) for each of the six observations. A given model was fit simultaneously to all the three spectra to derive the tightest constraints on the best-fit parameters. The *pn* and the *MOS* spectra were binned to 1/3 of the FWHM of the *pn* and the *MOS* spectral resolution, respectively. We used the SAS task *specgroup* for this purpose. Given the high number of total counts ($\approx (6-12) \times 10,000$), this gave us high-quality spectra in each case.

We began by fitting the spectra with a multi-colored disk (*diskpn* in XSPEC, Gierlinski et al. 1999) + power law (*powerlaw* in XSPEC) + an X-ray hot plasma (*apec* in XSPEC) as in Strohmayer & Mushotzky (2009). We used the Tuebingen-Boulder ISM absorption model (*tbabs* in XSPEC) to account for interstellar absorption. The hydrogen column density was set as a free parameter. This model is very similar to that often used to model the spectra of stellar-mass black holes. Indeed, it is common to use this or similar phenomenological models to determine the spectral state of a stellar-mass black hole. However, here in addition to a thermal disk and a corona, there is an X-ray emitting plasma in the model. This was realized by Strohmayer et al. (2007) after identifying systematic emission-like features in the residuals of the *diskpn + power-law* fit to the 2006 data. We confirm their result that the χ^2 improves significantly (by $\sim 40-100$ over all the six observations)

Table 2.5: Summary of the energy spectral modeling of NGC 5408 X-1. Best-fitting parameters for the $tbabs*(diskpn+apec+cutoffpl)$ model are shown.

$tbabs*(diskpn+apec+cutoffpl)$						
Dataset	n_H^a	T_{max}^b	kT_{plasma}^c	Γ^d	$E_{rollover}^e$	χ^2/dof
2006	$12.03^{+0.97}_{-0.94}$	$0.153^{+0.006}_{-0.006}$	$1.03^{+0.05}_{-0.04}$	$1.88^{+0.20}_{-0.21}$	$3.80^{+1.23}_{-0.79}$	375.48/264
2008	$12.93^{+1.78}_{-1.66}$	$0.146^{+0.011}_{-0.010}$	$0.97^{+0.06}_{-0.06}$	$1.92^{+0.33}_{-0.37}$	$4.29^{+3.96}_{-1.51}$	214.02/209
2010A	$11.96^{+1.15}_{-1.10}$	$0.160^{+0.008}_{-0.008}$	$1.04^{+0.05}_{-0.05}$	$1.84^{+0.20}_{-0.22}$	$4.18^{+1.52}_{-0.93}$	357.17/276
2010B	$10.53^{+1.03}_{-0.99}$	$0.171^{+0.009}_{-0.008}$	$1.02^{+0.06}_{-0.06}$	$1.92^{+0.18}_{-0.20}$	$4.92^{+1.83}_{-1.11}$	385.27/287
2011A	$12.30^{+1.09}_{-1.05}$	$0.160^{+0.008}_{-0.008}$	$0.98^{+0.06}_{-0.07}$	$1.92^{+0.21}_{-0.23}$	$4.28^{+1.70}_{-1.01}$	389.94/266
2011B	$11.54^{+1.24}_{-1.18}$	$0.167^{+0.010}_{-0.009}$	$1.05^{+0.10}_{-0.08}$	$1.98^{+0.24}_{-0.26}$	$5.56^{+3.72}_{-1.69}$	307.22/255

^aTotal column density of hydrogen along the line of sight including the Galactic extinction (in units of 10^{20}cm^{-2}). We used the $tbabs$ model in XSPEC. ^bAccretion disk temperature in keV. We used the $diskpn$ model in XSPEC. The inner radius of the disk was fixed at $6\text{GM}/c^2$. ^cThe temperature of the surrounding plasma in keV. We used the $apec$ model in XSPEC. The abundances were fixed at the solar value. ^dThe photon index of the cutoff power law. ^eThe energy at which the exponential rollover of the spectrum occurs.

with addition of the $apec$ component to the standard *multi-colored disk + power-law* model. Such a feature is not exclusive to the ULX in NGC 5408, as NGC 7424 (Soria et al. 2006) and Holmberg II X-1 (Dewangan et al. 2004) also show evidence for the presence of an X-ray emitting plasma. In addition, the high-resolution VLA radio observations at 4.9 GHz of the counterpart of the X-ray source in NGC 5408 X-1 revealed a radio nebula of ≈ 40 pc extent (Lang et al. 2007). Based on the value of the power-law index of the radio spectrum, it was suggested that the radio emission is likely from an optically thin synchrotron emitting gas. Given this, it is possible that the putative X-ray hot plasma is coincident with the radio nebula. The best-fitting parameters of the above model for each of the six observations are

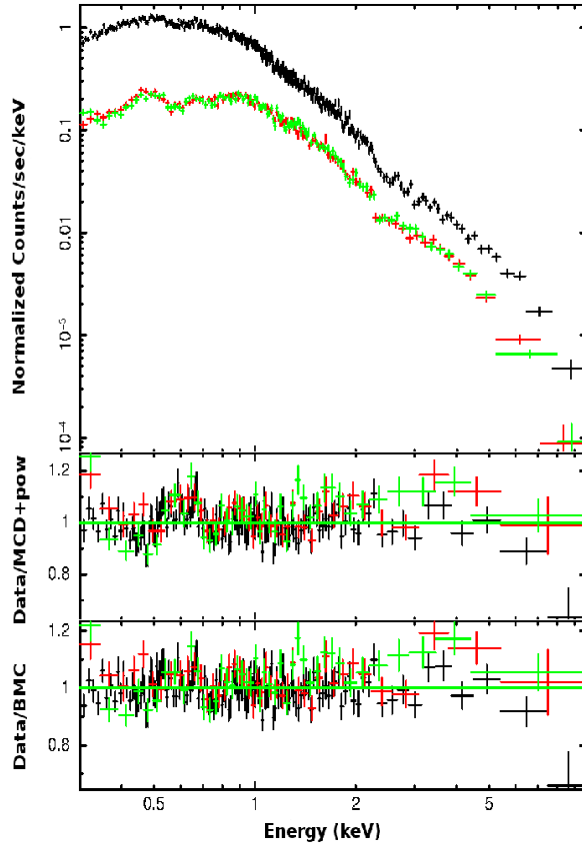


Figure 2.6: *Top Panel:* The X-ray energy spectrum (0.3-10.0 keV) of NGC 5408 X-1 derived from the 2010B observation (Table 2.1). The data from all the three detectors is shown. Black corresponds to EPIC-pn, while green and red represent data from the MOS1 and MOS2 detectors, respectively. The spectrum was re-binned for clarity to have a significant detection of at least 10σ . However, no more than 10 neighboring bins were combined to achieve this level of significance, i.e., *setplot rebin 10 10* in XSPEC. *Middle Panel:* The ratio of the data to the model defined by *tbabs*(diskpn + apec + powerlaw)* is shown. *Bottom Panel:* The ratio of the data to the model defined by *tabs*(bmc+apec)* is shown. Both the ratios were re-binned to have a detection significance of at least 20 with no more than 20 neighboring bins combined, i.e., *setplot rebin 20 20* in XSPEC.

shown in the top panel of Table 2.4. We note that the X-ray temperature of the plasma has remained constant across the suite of our *XMM-Newton* observations.

We also fit the spectra with a model based on Comptonization by bulk motion (Laurent & Titarchuk 1999, *bmc* in XSPEC). As mentioned above, this model has been used within the context of quantifying timing - spectral correlations in stellar-

mass black holes (Shaposhnikov & Titarchuk 2009). The underlying physical basis of this model is similar to that of the multi-colored disk + power-law model, i.e., the presence of a thermal disk and a hot electron corona. However, in this case the power-law is produced by the Comptonization of soft photons (from the disk) within a converging inflow onto the black hole. In this model, the normalization parameter derived from the fit mimics the disk flux from the *diskpn* component in the other model we have employed. We also include the *apec* component in this case. The best-fitting model parameters including the absorbing hydrogen column density using the *tbabs* in XSPEC for each of the six datasets are shown in the bottom panel of Table 2.4.

It can be noted straight away that, for a given observation, the plasma temperatures (*apec*) found from fitting the two spectral models are consistent with each other (within the error bars). The reduced χ^2 values for the *diskpn+powlaw+apec* and the *bmc+apec* model are in the range of 1.0-1.6 and 1.0-1.3 (~ 210 -290 degrees of freedom: last column of Table 2.4), respectively. Clearly, they both give acceptable values of reduced χ^2 . The latter model (*bmc+apec*) fits the data slightly better (see Table 2.4) than the simple *diskpn+apec+powlaw* model. However, the improvement in χ^2 is not statistically significant in all the cases and therefore it is not possible to rule out one model over the other based on the reduced χ^2 alone. A sample energy spectrum (using the 2010B data) is shown in Figure 2.6. Also shown in the figure are the ratios of the data to the folded model in the two cases (*diskpn+apec+powlaw* and *bmc+apec*). We use the spectral parameters derived here and the timing properties from the previous section to search for correlations between the two. The

results of which are presented in the next section.

It has been recently suggested (Gladstone et al. 2009) that the high-quality X-ray spectra of ULXs can be better characterized by complex comptonization models that predict a rollover at higher energies ($\gtrsim 3$ keV). A detailed study of the validity of such models in the case of NGC 5408 X-1 is beyond the scope of the present work, however, for the sake of completeness we also fit all our energy spectra with a cut-off power law component rather than just the simple power law model. In XSPEC we used the model, *tbabs*(diskpn+apec+cutoffpl)*. (the *cutoffpl* model describes a power law with a high energy exponential rollover.) The best fitting parameters for this model are shown in Table 2.5. We note that this model leads to a significant improvement in the χ^2 compared to the *tbabs*(diskpn+apec+pow)* model (compare the last column of Table 2.5 with the last column of Table 2.4). We also searched for possible timing-spectral correlations within the context of the *cutoff powerlaw* model, viz., QPO frequency vs the cutoff energy. We do not detect any clear correlation between the QPO frequency and the rollover energy. This is mainly due to poor statistics at the high end ($\gtrsim 5$ keV) of the energy spectra which result in large uncertainties on the rollover energies.

The measurement of fluorescent lines from elements like Fe, Ni, Cr, Ca etc. is another important probe of the vicinity of the X-ray emitting region. In principle, these reflection features can be produced by hard X-rays, presumably from the Comptonizing corona, irradiating cold material, e.g., in the disk. Among all such emission lines with their rest-frame energies in the *XMM-Newton* bandpass (0.2-10.0 keV), the iron feature is the most prominent (e.g., Matt et al. 1997). Given the

subtle changes in the energy spectra over the suite of observations (see Table 2.4), it does not seem unreasonable to combine all the data while searching for weak emission features. We searched for iron emission line features in the energy range of 6.0-7.0 keV, but did not detect any obvious features. Using an effective exposure of ≈ 540 ksecs (all datasets, see Table 2.1), we were able to place tight constraints on the equivalent width of any feature in the energy range of 6.0-7.0 keV. Assuming an unresolved narrow feature of width 10 eV, the upper limit (90% confidence) on the equivalent width of an emission line at 6.4 keV is 5.4 eV. We then check for the possibility of broad emission lines in the energy range 6.0-7.0 keV. The upper limits on the equivalent width assuming a broad emission line of width 0.3 keV and 1.0 keV are 11.6 eV and 11.0 eV, respectively.

The apparent weakness of iron emission from the disk can be due to a number of factors: an accretion disk that is completely ionized, scattering of the reflected iron-line photons in an optically thick corona (Matt et al. 1997), especially when the corona is a thin layer above the accretion disk or a low iron abundance in the accretion disk (Matt et al. 1997). Further, a high inclination angle for the accretion disk combined with one or more of the above factors can decrease the intensity of the iron-line. Recently, Gladstone et al. (2009) have analyzed energy spectra of a sample of ULXs (including NGC 5408 X-1) and have suggested that these sources might be operating in a new accretion state, with rollover at higher energies (> 2.0 keV) as a characteristic signature of such a state. Thus, the nature of the spectrum might be such that there are not enough photons at higher energies to generate a detectable iron-line fluorescent feature (Cole Miller, private communication).

Table 2.6: Comparing the power density spectral and the energy spectral properties of NGC 5408 X-1 with the steep power-law state in stellar-mass black holes

X-ray State	Definition ^a
Steep Power Law State	Presence of power-law component with $\Gamma > 2.4$ Power continuum: $r^b < 0.15$ Either disk fraction ^c $< 80\%$ and 0.1-30 Hz QPOs present with rms amplitude > 0.01 or disk fraction ^c $< 50\%$ with no QPOs present
X-ray State	Data from NGC 5408 X-1 ^d
Steep Power Law State ?	Presence of power-law component with Γ in the range 2.5-2.7 Power continuum: r^* in the range $\approx 0.36 - 0.43$ Disk fraction ^e in the range $\sim 30-50\%$ and 10-40 mHz QPOs present with rms amplitude in the range 0.10-0.45

^aIn case of stellar-mass black holes, the definition is using data in the energy range of 2-20 keV.

^bTotal rms power integrated over 0.1-10.0 Hz.

^cFraction of the total 2-20 keV unabsorbed flux.

^dIn case of NGC 5408 X-1, we use the *XMM-Newton* bandpass of 0.3-10.0 keV.

*We integrate the total power (continuum + QPOs) in the frequency range of 0.001 - 0.5 Hz (same as the frequency range used for power spectra fitting). The power spectra were derived using all the photons in the energy range of 1.0-10.0 keV (see Table 2.3 for the parameters).

^eFraction of the total 0.3-10 keV unabsorbed flux.

^fFraction of the total 0.3-10 keV unabsorbed flux.

2.5 Timing - Spectral Correlations

A primary goal of the new observations of NGC 5408 X-1 is to further test the preliminary classification of the mHz QPOs detected from NGC 5408 X-1 as the analogs of the 0.1-15 Hz Low-Frequency, type-C QPOs (low-frequency QPOs) detected from accreting stellar-mass black holes. If a strong connection can be demonstrated, then scaling of the characteristic frequencies (e.g., QPO centroid frequency) can be better justified to estimate the mass of the black hole within this source.

As mentioned earlier, scaling relations using the power density spectral break frequency have been successfully tested using power spectra of both stellar and super-massive black holes of known mass (McHardy et al. 2006 and K rding et al. 2007). Based on the qualitative nature of the power density spectra and the energy spectra derived using the 2006 and 2008 data, Strohmayer & Mushotzky (2009) suggested that the mHz QPOs from NGC 5408 X-1 may indeed be low-frequency QPO analogs. More specifically, they proposed that its X-ray state was analogous to that of a stellar-mass black hole in the so-called steep power-law state exhibiting type-C QPOs, but at the same time emitting a few $\times 10$ higher X-ray flux. Having analyzed the data from all six observations (§2.3 & 2.4) we confirm that the derived power- and energy-spectral parameters are qualitatively consistent with the source being in a steep power-law state exhibiting type-C QPOs (based on the state descriptions in McClintock & Remillard 2006). A summary of the working definition of the steep power-law state with type-C QPOs and the power density spectral &

energy spectral parameters of NGC 5408 X-1 are given in Table 2.6.

A further step in understanding the nature of these QPOs is to determine if they show the same evolutionary behavior in the QPO parameters as those exhibited by the stellar-mass black hole low-frequency QPOs. One such characteristic behavior is the QPO rms amplitude versus centroid frequency relationship. Our results for this relation from NGC 5408 X-1 are shown in the left and right panels of Figure 2.5 in two different energy bands (1.0-10.0 keV and 0.5-5.0 keV, respectively). Comparing these plots with those from stellar-mass black holes, as in Figure 11 of McClintock et al. (2009), the results appear to be at least qualitatively consistent with the behavior of steep power-law data from some stellar-mass black holes (see for example, the green triangles in Figure 11 of McClintock et al. 2009). However, because a tight correlation appears to break down in the steep power-law state it is hard to conclude definitively that the NGC 5408 X-1 behavior is exactly analogous.

Another important signature of the Type-C low-frequency QPOs in stellar-mass black holes is their dependence on the energy spectral features, i.e., the timing - spectral correlations. Using the X-ray state classifications as in McClintock et al. (2006), low-frequency QPOs in stellar-mass black holes are usually detected in the low/hard state, the steep power-law state and during the transition between these two states. Within the context of the multi-colored disk + power-law model parameters, it is known that the centroid frequency of these low-frequency QPOs is correlated with the disk flux and the photon index of the power-law component. In stellar-mass black holes, the typical behavior is that the QPO centroid frequency is positively correlated with the disk flux and the photon index of the power law.

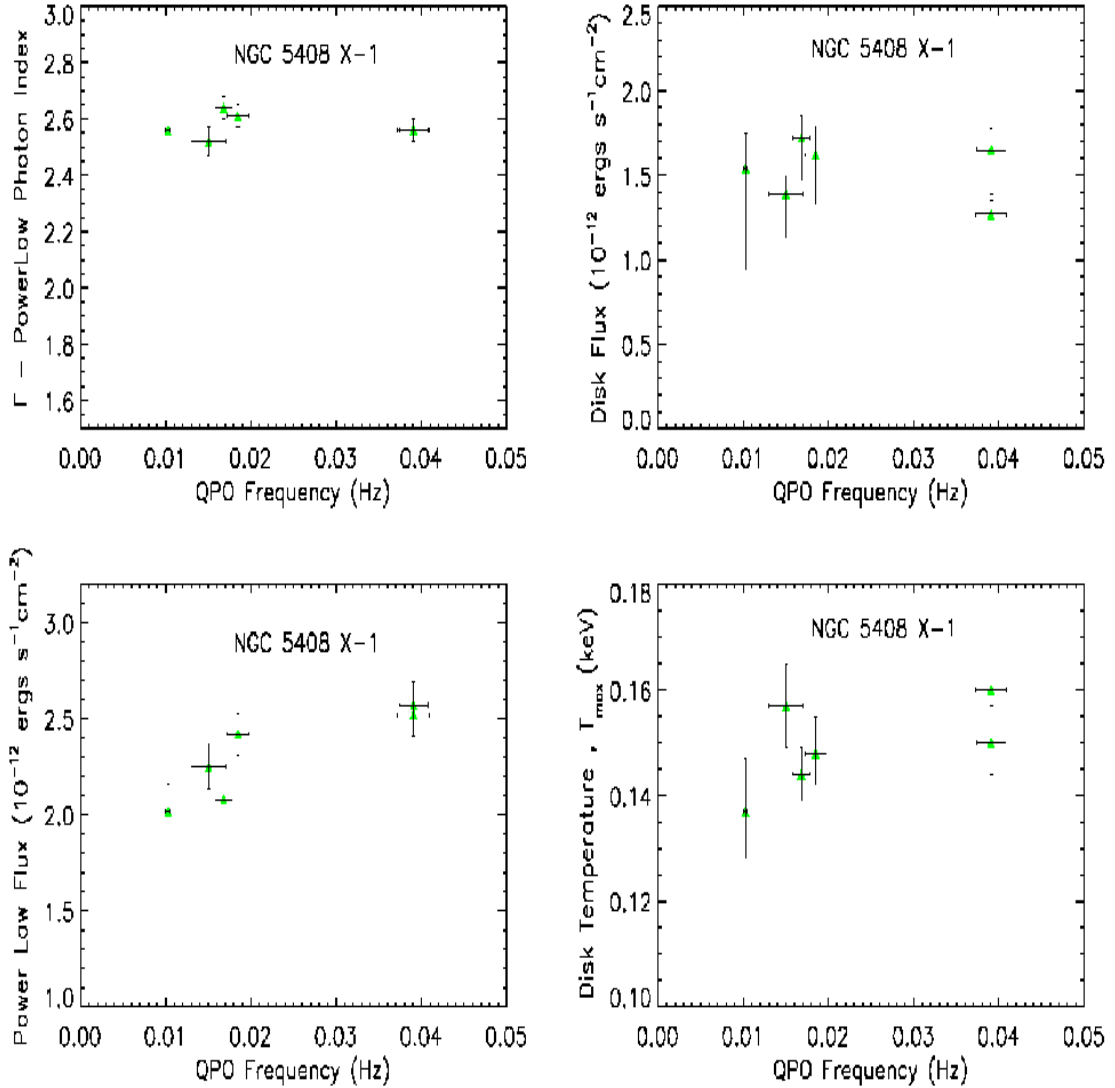


Figure 2.7: Timing-Spectral Correlations using the phenomenological model: diskpn + powerlaw. Six observations/data points were used to search for timing-spectral correlations. *Top Left Panel:* The photon index of the power-law (Y-axis) is plotted against the centroid frequency of the QPO (X-axis). *Top Right Panel:* The disk contribution to the total flux (Y-axis) in the energy range of 0.3-10.0 keV is plotted against the centroid frequency of the QPO. *Bottom Left Panel:* Flux from the power-law component (Y-axis) is plotted against the QPO centroid frequency (X-axis). *Bottom Right Panel:* For the sake of completeness, the disk temperature (Y-axis) is plotted against the QPO centroid frequency (X-axis). Within the present scheme of X-ray states in stellar-mass black holes, these results are qualitatively consistent with NGC 5408 X-1 being in the steep power law state exhibiting type-C QPOs, with the characteristic timescales scaled down by a factor of \approx a few $\times 10$.

At a certain higher QPO centroid frequency ($\approx 5\text{-}10$ Hz) the relationship seems to flatten (saturate) and even appears to start reversing in some cases (Vignarca et al. 2003). Furthermore, the correlation is not exactly the same for all stellar-mass black holes, i.e., the value of the slope of the correlation and the photon index/disk flux at saturation are different for different sources and can be different for the same source in a different outburst (Vignarca et al. 2003; Shaposhnikov & Titarchuk 2009). In Figure 2.7 we show plots of several derived spectral parameters and fluxes (using the *diskpn* + *power-law* fits) as a function of the QPO centroid frequency. These can be compared with similar plots derived from stellar-mass black hole systems (see, for example, Figures 8 & 9 in McClintock et al. 2009; Figure 10 of Vignarca et al. 2003). Again, there appears to be qualitative consistency between the behavior exhibited by NGC 5408 X-1 and stellar-mass black holes, but the full range of behavior is not yet seen, again because the range of spectral variations in NGC 5408 X-1 (most notably in the power-law index) is too modest. Additional measurements of QPO properties at lower values of the power-law photon index, for example, could provide a more definitive test.

One can also investigate the spectral - temporal correlations in the context of the spectral parameters derived using the *bmc* model. Indeed, Shaposhnikov & Titarchuk (2009) explored such correlations in detail for a sample of stellar-mass black holes using RXTE data. They also developed a set of fitting functions to quantify the observed correlations and used these to obtain mass estimates by scaling arguments. Figure 2.8 compares the results from NGC 5408 X-1 with those from stellar-mass black holes using the *bmc* spectral fits. We used the published data from

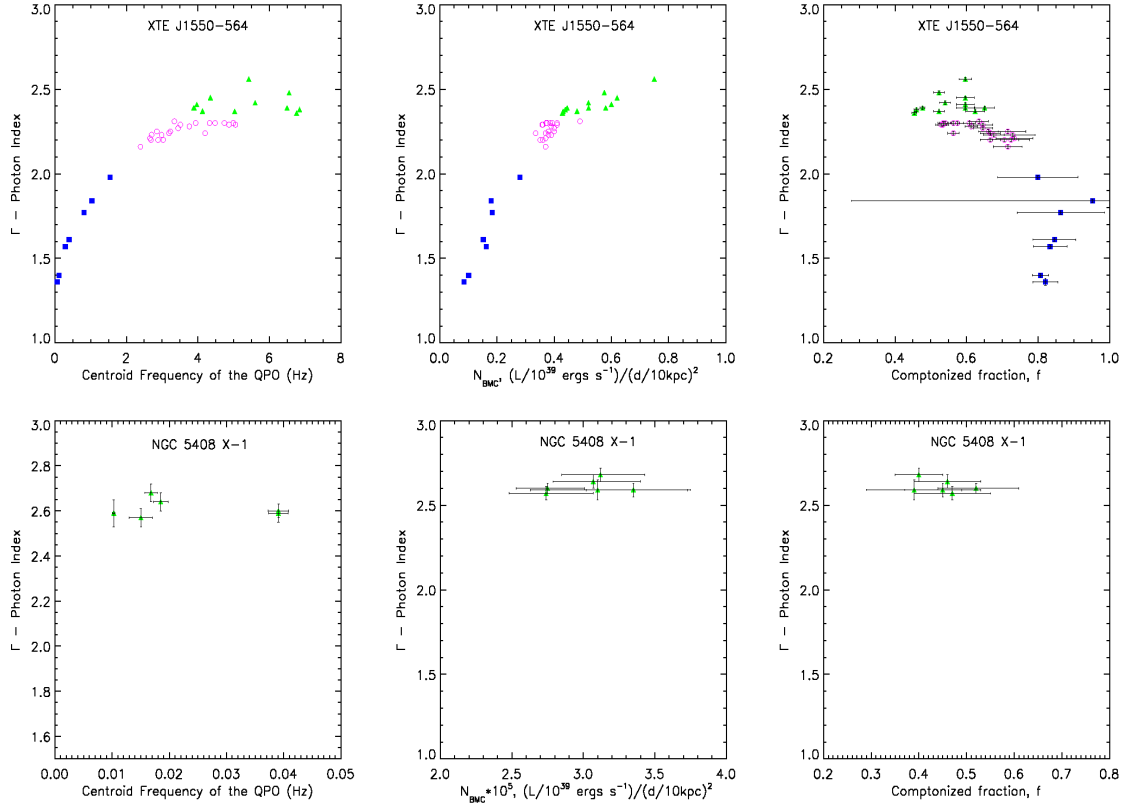


Figure 2.8: Timing-Spectral Correlations using the BMC model. *Top Panels:* The behavior of a typical stellar-mass black hole (1998 outburst of stellar-mass black hole XTE J1550-564) is shown (we plot data from Shaposhnikov & Titarchuk 2009). For clarity, the X-ray state of the source is highlighted using the following color scheme. Blue squares indicate the low/hard state, magenta corresponds to a state intermediate between the low/hard and the steep power-law state while the green triangles highlight the steep power-law state. From left to right, the dependence of the centroid frequency of the QPO, BMC normalization (disk flux) and the Comptonized fraction on the power law index are shown. The error bars are not indicated when their size is smaller than the size of the data point. *Bottom Panel:* Similar plots using the data from NGC 5408 X-1. The results from the ULX NGC 5408 X-1 are qualitatively consistent with the source being in an X-ray state very similar to the steep power-law state in stellar-mass black holes (Compare with the green triangles on the top panel).

Shaposhnikov & Titarchuk (2009) to produce representative plots for a stellar-mass black hole (XTE J1550-564, top panels). Shown from left to right are the QPO centroid frequency versus the power-law photon index (Γ), the *bmc* normalization (disk flux) versus Γ and the Comptonized fraction, f versus Γ , respectively. The

data points are color coded to highlight the low/hard state (blue) and the steep power-law state (green). We used the data from the 1998 outburst of XTE J1550-564 which clearly demonstrates the typical behavior of stellar-mass black holes (top panels). Comparisons of these plots with those in, for example, Shaposhnikov & Titarchuk (2009) lead to similar conclusions as with the results in Figure 2.7. There is qualitative consistency with the Type-C identification, but the classification is not definitive. In order to make a more secure association of the QPOs in NGC 5408 X-1 with Type-C (steep power-law state) QPOs in the stellar-mass black holes, we need, at a minimum, to obtain observations of the source over a greater range of power-law spectral indices.

2.6 Discussion

It has been established that black hole masses scale with the break frequency of their power density spectra (McHardy et al. 2006, Körding et al. 2007) and this relation is known to hold over 6 orders of magnitude in mass, i.e., from stellar-mass to super-massive black holes. Furthermore, at least in stellar-mass black holes, the break frequency of the power density spectra is known to strongly correlate with the centroid frequency of the low-frequency QPOs (Wijnands & van der Klis 1999). Therefore, it is reasonable to assume that the mass of the black hole scales with the centroid frequency of the low-frequency QPOs. This can be especially useful in cases where black hole mass measurements are otherwise difficult, viz., in ULXs. However, an important caveat is to ensure that the QPOs used for comparison are

similar in nature.

Our new results confirm the earlier result from Strohmayer & Mushotzky (2009) that the qualitative nature of the power density spectrum and the energy spectrum of NGC 5408 X-1 are very similar to that of stellar-mass black holes in the steep power-law state (see Table 2.6). At the same time, the characteristic timescales within the power density spectra are lower by a factor of ≈ 100 , while the X-ray luminosity is higher by a factor of a few $\times 10$, when compared to a typical stellar-mass black hole in such a state. However, based on the scaling between the break frequency of the power density spectrum and the centroid frequency of the low-frequency QPOs (Centroid frequency of low-frequency QPOs $\approx 12 \times$ break frequency of the power density spectra), the association of the mHz QPOs from NGC 5408 X-1 with the low-frequency QPOs from stellar-mass black holes has been questioned (Middleton et al. 2011)

A striking feature of the behavior of NGC 5408 X-1 is that the energy spectrum of the source has remained roughly constant over the current suite of observations, while the properties of the most prominent QPO (e.g., rms amplitude, centroid frequency) have changed significantly. These results appear consistent with the source being in a spectral state similar to the steep power-law state in stellar-mass black holes. More specifically, in stellar-mass black holes, certain spectral properties like the disk flux, the photon index of the power-law correlate positively with the QPO centroid frequency up to a certain frequency (≈ 2 -10 Hz) beyond which the relationship turns around or remains roughly constant. Detailed analysis of the timing - spectral correlations in stellar-mass black hole sources such as XTE J1550-564 and

H1743-322 has revealed a comprehensive picture (McClintock et al. 2009) of their behavior. Tracking these two sources as they evolved from the low/hard state into the steep power-law state, it was realized that the spectral properties like the disk flux and the power-law photon index are tightly correlated with the QPO centroid frequency during the low/hard state and during a transition phase intermediate between the low/hard and the steep power-law state; and the relationships seem to saturate/breakdown (spectral properties remain roughly constant with increase in the QPO frequency) as the sources entered the steep power-law state. It may be that we are in fact seeing NGC 5408 X-1 in a similar state, i.e., we may be seeing the “saturated” portion of the relation.

Given that the overall accretion timescales change with the mass of the black hole (timescales increase as the mass increases from stellar-mass black holes to super-massive black holes, e.g., McHardy et al. 2006), it is possible that we are seeing a similar timing - spectral behavior, and that the apparent longevity of the source in the steep power-law state might also be due to its having a higher mass. There may be a useful analogy to AGN in that their spectra are known to remain roughly constant on timescales of at least a few years (Markowitz et al. 2003) while transient stellar-mass black hole systems undergo strong energy spectral changes on timescales of the order of a few days (McClintock et al. 2006 and references therein). It could be that the persistence of NGC 5408 X-1 in the approximately same spectral state is related to it being of intermediate mass between stellar-mass black holes and AGN. Alternatively, perhaps the source is in an accretion state, like the so-called ultraluminous state of Gladstone et al. (2009), that is just not well sampled by

the behavior of Galactic stellar-mass black holes. We note that the indication for a rollover in the power-law at 4-5 keV (see §2.4 and Table 2.5) provides some support for this interpretation, in which case the spectral state of NGC 5408 X-1 may not be exactly analogous to the steep power-law state of stellar-mass black holes.

However, either conclusion will remain tentative until NGC 5408 X-1 is observed in a state with a lower value of the power-law photon index, i.e., a state similar to the low/hard state in stellar-mass black holes. Such an observation would clearly be important in order to make a more definitive identification of its QPOs in the context of those observed in stellar-mass black holes.

Assuming the constancy of the energy spectral features, i.e., disk flux, Γ , with the increasing QPO centroid frequency (see Figure 2.7) is analogous to the saturation observed in the timing - spectral correlations in stellar-mass black holes, one can estimate the minimum mass of the black hole in NGC 5408 X-1. If we are indeed seeing only the saturated portion of the complete timing - spectral correlation curve, then the minimum QPO frequency observed in NGC 5408 X-1 serves as an upper limit on the so-called transition frequency, i.e., the frequency beyond which the timing - spectral correlations tend to saturate. In order to derive a mass estimate, this particular frequency can be scaled to a reference stellar-mass black hole of known mass with a measured transition frequency (ν_{trans}). We can use the transition frequency as defined by Shaposhnikov & Titarchuk (2009) in their fits of QPO and spectral parameters. We find a sample of three stellar-mass black holes with mass and transition frequency measurements in Shaposhnikov & Titarchuk (2009) that are suitable for this purpose. Further, it is known that the

same source can exhibit different tracks (timing - spectral correlation curves), i.e., different transition frequencies, in various outburst episodes. Given that we are interested in a lower limit on the mass of the black hole in NGC 5408 X-1, we consider the lowest transition frequency for a given source. The minimum mass of the black hole in NGC 5408 X-1, can then be calculated as $\nu_{trans} \times \text{Mass}_{Reference} / (\text{minimum QPO frequency})$. The mass estimates using the three reference sources, GRO 1655-40, XTE J1550-564 and GX 339-4 are reported in Table 2.7 ($\sim 1000 M_{\odot}$), and show substantial overlap with those reported by Strohmayer & Mushotzky (2009).

2.7 Summary

The ULX in the irregular dwarf galaxy, NGC 5408 has been suggested to harbor an intermediate-mass black hole ($\text{Mass}_{BH} \approx 100 - \text{a few} \times 1000 M_{\odot}$) (Strohmayer & Mushotzky 2009). This mass estimate was strictly based on the assumption that the mHz QPOs seen from this source are the type-C analogs of the low-frequency QPOs (0.1-15 Hz) from stellar-mass black holes. Here we have presented results from new observations of NGC 5408 X-1 in which we searched for timing - spectral correlations similar to those often exhibited by the type-C low-frequency QPOs from stellar-mass black holes. Our analysis of multi-epoch *XMM-Newton* data from NGC 5408 X-1 reveals that certain characteristic features of the power spectra, especially the QPO centroid frequency, changed significantly. However, the energy spectrum has remained roughly constant. These results can be interpreted in two ways. This could be due to complete independence of the timing properties on the energy spec-

Table 2.7: Mass estimate of the black hole in NGC 5408 X-1

Reference	Mass (M_{\odot})	ν_{trans}^a (Hz)	Minimum Mass $_{5408}^b$ (M_{\odot})	References
GRO J1655-40	6.3 ± 0.5	3.0 ± 0.1	1720	1, 4
XTE J1550-564	9.5 ± 1.1	1.84 ± 0.07	1490	2, 4
GX 339-4	> 6	1.4 ± 0.2	820	3, 4

^aThe transition frequencies were estimated by Shaposhnikov & Titarchuk (2009). The fitting functions for the timing-spectral correlations are described therein.

^bMinimum mass of the black hole in the ULX =

$(\nu_{trans} \times \text{mass})_{Reference\ stellar-mass\ black\ hole} / 10.28$ mHz, where 10.28 mHz is the minimum QPO frequency detected from NGC 5408 X-1. We consider the error bars on the individual parameters and report the lower value of the mass.

References - (1) Greene et al. (2001) (2) Orosz et al. (2002) (3) Muñoz-Darias et al. (2008) (4) Shaposhnikov & Titarchuk (2009).

tra, unlike stellar-mass black holes, in which case mass scalings derived from the QPOs are likely to be problematic; or there is in fact a correlation, but we are seeing only the saturated part of the correlation behavior (constancy of the Γ /disk flux with increasing QPO frequency). Such saturation is often seen in stellar-mass black holes (e.g., Vignarca et al. 2003). Assuming we are seeing this saturated portion of the correlation curve, we estimate the lower limit on the mass to be $\approx 800 M_{\odot}$. At least one observation with the source in a low/hard-like state ($\Gamma < 2.0$) is necessary to resolve the issue of whether the timing and spectral properties are correlated as in stellar-mass black holes or not.

Chapter 3: On the Nature of the mHz X-ray QPOs from ULX M82

X-1: Search for Timing-Spectral Correlations

3.1 Introduction

In this chapter, we test the hypothesis that the mHz QPOs of ULX M82 X-1 are the analogs of the type-C low-frequency QPOs of stellar-mass black holes by investigating if its QPOs show the same characteristic behavior of type-C low-frequency QPOs of stellar-mass black holes, i.e., *whether M82 X-1's QPO frequency is correlated with the power-law index of its energy spectrum*. Similar attempts have been made earlier by Fiorito & Titarchuk (2004) for the case of M82 X-1 and Dheeraj & Strohmayer (2012) for the case of NGC 5408 X-1 (see Chapter 1). The work by Fiorito & Titarchuk (2004) considered only one *XMM-Newton* observation and three *RXTE*/PCA observations and was severely limited by the observed variability of M82 X-1's QPO frequencies, i.e., 50-100 mHz. In addition, they did not consider the contamination by a nearby bright X-ray source¹ in their spectral modeling. Here we include analysis using all of the archival *XMM-Newton* observations that show QPOs in the frequency range of 36 mHz (the lowest ever reported from M82 X-1)

¹This source is identified as source 5 by Matsumoto et al. (2001) and as X42.3+59 by Feng & Kaaret (2007)

to 210 mHz (the highest QPO frequency reported from M82 X-1).

This chapter is arranged as follows. In Section 3.2, we describe all the *XMM-Newton* observations used in the present study and carry out surface brightness modeling of their MOS1 images. In Section 3.3, we show results from our timing and energy-dependent surface brightness modeling analysis. We also show the two primary results of this chapter: (1) evidence for a correlation between the average count rate and the centroid frequency of the QPO and (2) no apparent correlation between the centroid frequency of the QPO and the hardness ratio which is an indicator of the power-law index of the energy spectrum. In Section 3.4, we compare these results with stellar-mass black holes with type-C QPOs. We discuss the implications of the observed correlations on the mass of the black hole within M82 X-1.

3.2 *XMM-Newton* observations and surface brightness modeling

Prior to the present work, QPOs have been reported from M82 X-1 using the *RXTE*/PCA (Strohmayer & Mushotzky 2003; Kaaret et al. 2006; Mucciarelli et al. 2006) and the *XMM-Newton*/EPIC data (Strohmayer & Mushotzky 2003; Mucciarelli et al. 2006; Dewangan et al. 2006). *RXTE*'s PCA is a non-imaging detector whose field of view includes various point sources nearby M82 X-1. Its data does not allow one to disentangle the contribution from the nearby bright sources. However, data acquired with *XMM-Newton* allows for surface brightness modeling that can help us understand M82 X-1's relative brightness with respect to the nearby sources.

Table 3.1: Resolved average count rates (3-10 keV) of M82 X-1 and source 5 derived from the surface brightness modeling of *XMM-Newton*'s MOS1 images.

ObsID ^a	Source 5 (counts s ⁻¹) ^b	M82 X-1 (counts s ⁻¹) ^b	χ^2/dof^c
0112290201	0.071 ± 0.003	0.041 ± 0.003	627/437
0206080101	0.011 ± 0.002	0.046 ± 0.002	509/437
0657800101	0.034 ± 0.003	0.037 ± 0.003	417/437
0657801901	0.015 ± 0.002	0.035 ± 0.002	400/437
0657802101	0.025 ± 0.003	0.040 ± 0.003	435/437
0657802301	0.047 ± 0.004	0.053 ± 0.004	571/437

^aThe *XMM-Newton* assigned observation ID.

^bThe count rates are calculated using the formula described in the text (see Section 2).

^cThe χ^2/dof was obtained by fitting two point spread functions to MOS1 images of size 21" × 21" binned to 1" × 1" and centered on M82 X-1.

Also, *XMM-Newton* observations have longer exposures which allow firm detection of the QPOs. Due to these reasons, we decided to use only *XMM-Newton* data. To date, *XMM-Newton* has observed M82 on twelve occasions. Three of these observations were severely effected by flaring. We analyzed the remaining nine observations to search for the presence of QPOs. We detected QPOs in six of them. Since the present work relies on searching for a correlation between the QPO frequency and the energy spectral power-law index, we only considered the observations with QPOs. The *XMM-Newton* assigned IDs of the six observations used in this chapter

are 0112290201, 0206080101, 0657800101, 0657801901, 0657802101 and 0657802301. The total observing times were 30 ksecs, 104 ksecs, 26 ksecs, 28 ksecs, 22 ksecs and 23 ksecs, respectively.

At *XMM-Newton*'s spatial resolution the flux from M82 X-1 is contaminated by the diffuse X-ray emission from the host galaxy (e.g., Strickland & Heckman 2007) and the nearby point sources (Matsumoto et al. 2001). Careful X-ray spectral modeling by various authors including Mucciarelli et al. (2006) and Caballero-García (2011) has shown that the diffuse component is dominant at energies below 3 keV. Therefore, to eliminate its contribution, we only included events in the energy range of 3.0-10.0 keV. Similar exclusions have been employed by Strohmayer & Mushotzky (2003), Fiorito & Titarchuk (2004) and Dewangan et al. (2006). The observations taken by the high-resolution camera on board *Chandra* have revealed that there are a total of nine point sources within the $10'' \times 10''$ region around M82 X-1 (Matsumoto et al. 2001). In principle, the flux contribution from all these point sources can bias the modeling of M82 X-1. Chiang & Kong (2011) have analyzed all of the archival *Chandra* observations of M82 to study the long-term (1999-2007) variability of the X-ray point sources within M82. They find that while the X-ray sources nearby M82 X-1 are variable, the maximum observed X-ray (0.3-8.0 keV) luminosity of these sources is $\lesssim 1/5^{th}$ the average luminosity of M82 X-1 (see Table 2 of Chiang & Kong 2011). However, source 5 (as defined in Matsumoto et al. 2001) is an exception. It can reach X-ray luminosities comparable to M82 X-1 (Feng & Kaaret 2007). Therefore, to estimate the amount of contamination by source 5 in each of the observations, we carried out surface brightness modeling of the images assuming

they are dominated by two point sources.

We used only the MOS1 data for the purposes of surface brightness modeling. This is because the MOS data offers the finest pixel size of 1.1" compared to the 4.1" of the EPIC-pn. Furthermore, the image resolution of EPIC-pn is close to the separation ($\approx 5''$) between source 5 and M82 X-1 (Feng & Kaaret 2007). We avoid MOS2 data because its point spread function (PSF) is non-axisymmetric at the core. The on-axis PSF of MOS1 can be adequately described by an axisymmetric 2D king model (*XMM-Newton* current calibration file release notes 167). Similar to the analysis of Feng & Kaaret (2007) (who also carried out surface brightness modeling of *XMM-Newton*'s MOS1 data of M82 using a king model), we used the *calview* tool with an EXTENDED accuracy level to extract an on-axis PSF at an energy of 3.0 keV. We then fit a king model² to this PSF. The best-fit values of the core radius and the index are 4.0" and 1.39, respectively. We note that these values are consistent with the best-fit parameters given in the calibration file XRT1_XPSF_0014.CCF and also with the values reported in the MOS calibration documentation (*XMM-Newton* current calibration file release notes 167).

From each of the six *XMM-Newton* observations, we extracted an exposure-corrected (using XMMSAS task *eeexpmap*) MOS1 image of size 21" \times 21" binned to 1" \times 1" (square pixels) and roughly centered on M82 X-1. The standard filters of *FLAG==0* and *PATTERN<=12* were applied. As mentioned earlier, all the images

²

$$PSF_{king} = \frac{N}{\left[1 + \left(\frac{r}{r_0}\right)^2\right]^\alpha}$$

where r_0 , α and N are the core radius, index and the normalization, respectively.

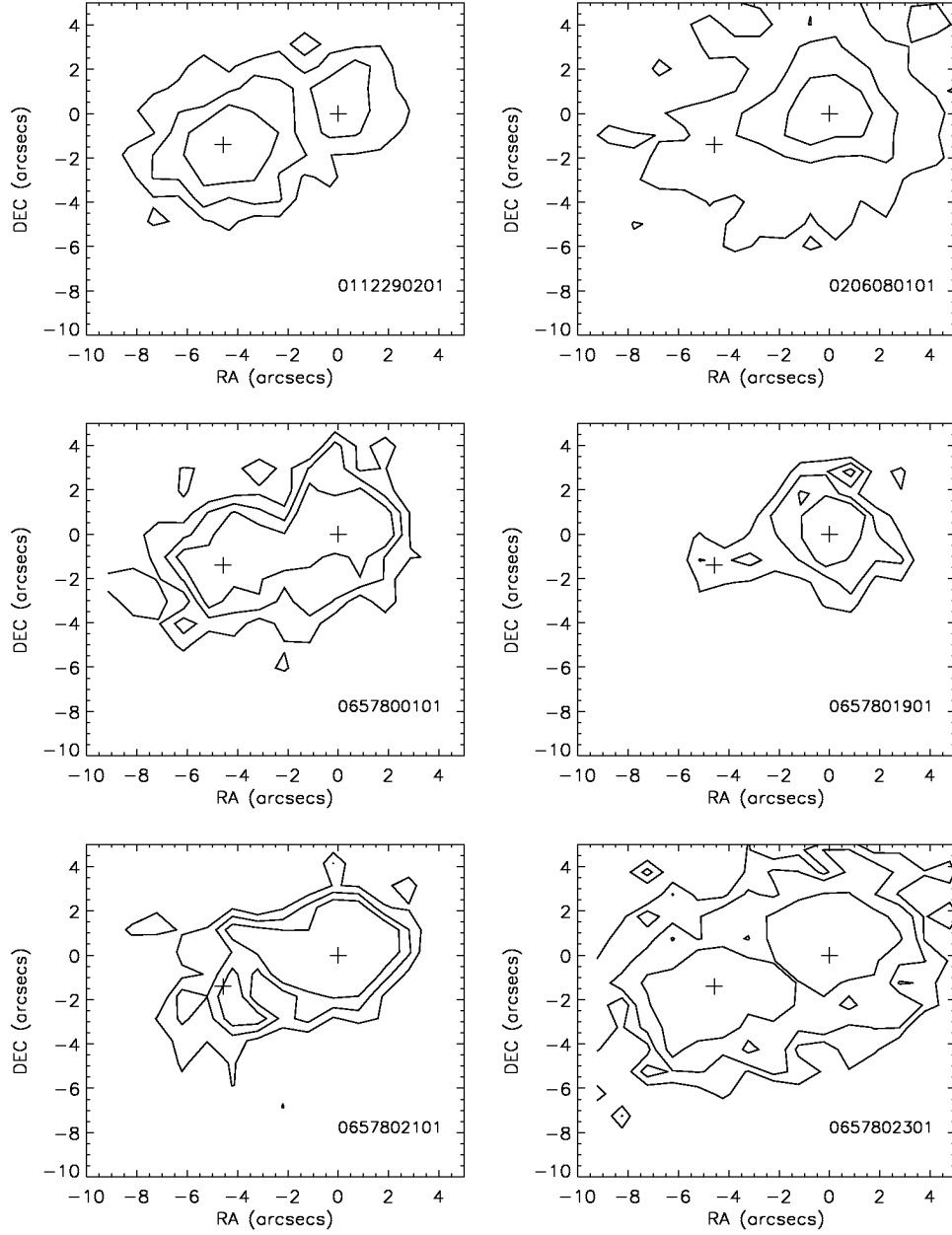


Figure 3.1: Surface brightness contour maps of the MOS1 images (3-10 keV) of M82 during six different epochs. The *XMM-Newton* assigned observation IDs are indicated at the bottom right of each panel. M82 X-1 is at the origin in all the plots and the best-fit positions of source 5 and M82 X-1 are represented by plus signs. Contour levels are different for different observations. *Top left panel:* The contour levels are 1.0, 1.75, 2.5 (10^{-3} counts s^{-1} arcsec $^{-2}$). *Top right panel:* The contour levels are 0.5, 1.0, 1.5 (10^{-3} counts s^{-1} arcsec $^{-2}$). *Middle left panel:* The contour levels are 0.75, 1.0, 1.25 (10^{-3} counts s^{-1} arcsec $^{-2}$). *Middle right panel:* The contour levels are 0.75, 1.0, 1.25 (10^{-3} counts s^{-1} arcsec $^{-2}$). *Bottom left panel:* The contour levels are 0.75, 1.0, 1.25 (10^{-3} counts s^{-1} arcsec $^{-2}$). *Bottom right panel:* The contour levels are 0.75, 1.0, 1.5 (10^{-3} counts s^{-1} arcsec $^{-2}$).

were extracted in the energy range of 3.0-10.0 keV to reduce the influence of the diffuse X-ray emission from the host galaxy. Each of these MOS1 images were then modeled with two PSFs to represent source 5 and M82 X-1. The core radius and the spectral index of the two PSFs were fixed at the best-fit values, i.e., 4.0" and 1.39, respectively. The centroids (x, y) and the normalizations of the two PSFs were allowed to vary. However, the distance between the two sources was fixed to the values found using the co-ordinates reported by Feng & Kaaret (2007). We ignore the background as it was negligible in all of the six observations. For bins with less than 5 counts, we assign error bars as derived by Gehrels (1986), i.e., $1.0 + \sqrt{\text{counts} + 0.75}$; And for bins with greater than 5 counts we assign Poisson errors of $\sqrt{\text{counts}}$. The model with two PSFs yielded acceptable values of χ^2 in all the six cases. The best-fit χ^2 value for each case is reported in the last column of Table 3.1. It should be noted that the effective exposure of all but observation ID 0206080101 are comparable. The observation length of 0206080101 is ≈ 100 ksecs while that of the rest of the observations is ≈ 25 ksecs. This dataset was also analyzed by Feng & Kaaret (2007) and they find that the long exposure causes the other dim sources nearby to be significant for surface brightness modeling. Therefore, to be consistent across all the observations we choose data from one of the good time intervals of MOS1 with an effective exposure of 30 ksecs. This is comparable to the exposure times of the other five observations. The X-ray (3-10 keV) surface brightness contour maps of all of the six observations are shown in Figure 3.1.

3.3 Results

3.3.1 Timing analysis

The following analysis was carried out primarily using the EPIC-pn data with events in the energy range of 3.0-10.0 keV. We used the standard Science Analysis System (SAS) version 12.0.1 to extract the filtered event lists and the light curves. The standard filters of ($FLAG==0$) and ($PATTERN<=4$) were applied to all the datasets. The source events were extracted from a circular region of $33''$ centered around the brightest pixel in each observation. This particular radius value was chosen to include roughly 90% of the light from the source (as estimated from the fractional encircled energy of the EPIC-pn instrument). The background events were extracted from a nearby circular region of radius $50''$ and free of other sources. We also removed episodes of high background flaring from our analysis.

We constructed PDS from each of the five observations. These datasets, excluding observation 0206080101, have not been analyzed earlier and became public only recently (December 7th 2012). The data from observation 0206080101 has already been analyzed by Mucciarelli et al. (2006) & Dewangan et al. (2006). We reanalyzed this observation to provide a consistent study of all the available data. All the PDS are shown in Figure 3.2 and Figure 3.3. All the power spectra shown here are so-called Leahy normalized where the Poisson noise level is equal to 2 (Leahy et al. 1983). It is clear that the overall behavior of all the PDS is the same. The power rises below ≈ 70 -400 mHz with evidence for a QPO in the range of ≈ 30 -220

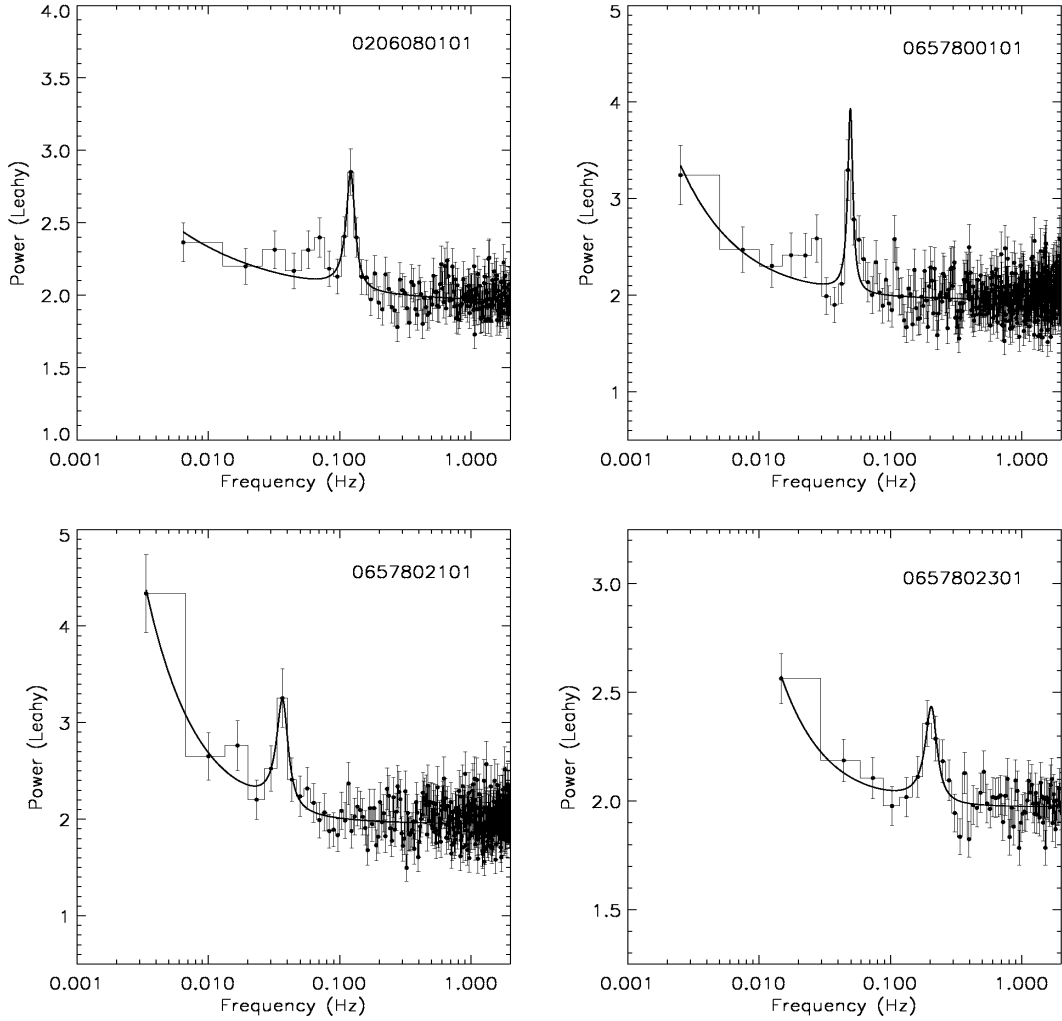


Figure 3.2: The EPIC-pn 3-10 keV power density spectra (*histogram*) and the best-fit model (*solid*) of four of the five *XMM-Newton* observations. The error bars are also shown. The *XMM-Newton* assigned observation IDs are shown on the top right of each panel.

mHz; And essentially Poisson noise at higher frequencies. To quantify this behavior, we fit a power law to the continuum and a Lorentzian to model the QPO (Belloni et al. 2002). The mathematical representation of the model can be found within the index of Table 3.2. This model fits adequately in all the cases with reduced χ^2 in the range of 0.9-1.2. The best-fitting model parameters (derived from a fit in

the frequency range of 0.001 Hz - 2.0 Hz) for each of the observation are shown in Table 3.2. We also indicate the χ^2/dof (degrees of freedom) values for each of the fits along with the χ^2/dof corresponding to the continuum model (in braces). The change in the χ^2 serves as an indicator of the statistical significance of the QPOs.

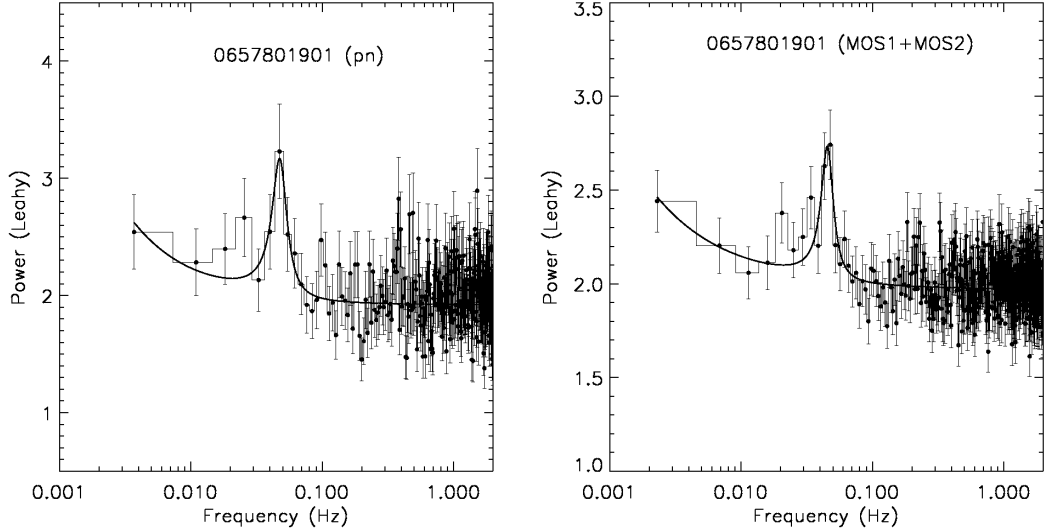


Figure 3.3: *Left Panel:* The EPIC-pn 3-10 keV power density spectrum (*histogram*) and the best-fit model (*solid*) of the observation ID 0657800101. *Right Panel:* The combined EPIC-MOS1 and EPIC-MOS2 3-10 keV power density spectrum (*histogram*) and the best-fit model (*solid*) of the same observation. In the EPIC-pn data the QPO is significant at only 3σ level. However, in the combined MOS power density spectrum the QPO is significant at 5σ level.

We estimated the individual average count rates of source 5 and M82 X-1 as follows. First, we estimated the total counts from a given source by integrating its best-fit PSF until the core radius. We then divide this by the total exposure time to calculate an average count rate. The formula for the count rate is therefore:

$$\text{count rate} = \frac{1}{T} \times \left(\int_0^{r_0} \frac{N}{\left[1 + \left(\frac{r}{r_0}\right)^2\right]^\alpha} 2\pi|r| dr \right)$$

where r is the radial distance from the centroid of the source and is defined as:

$$r = \sqrt{(x - x_0)^2 + (y - y_0)^2}$$

where (x_0, y_0) is the best-fit centroid position of a given source. N is the best-fit value of the normalization of a given source. T is the effective exposure time. The count rates of source 5 and M82 X-1 estimated with the method described above are shown in the second and the third columns of Table 3.1, respectively. In observation 0112290201, source 5 clearly dominates the overall X-ray flux from M82. However in the rest of the observations M82 X-1's flux is greater than the flux from source 5. To minimize the contamination, we only considered observations in which M82 X-1's flux is \gtrsim source 5 flux. This filtering criterion resulted in a total of five observations (excluding observation 0112290201) to test for the timing-spectral correlation. We present the timing (PDS analysis) and the spectral analysis (energy-dependent surface brightness modeling) of these datasets in the following section.

The longest available EPIC-pn good time interval during the observation 0657801901 was only 8.8 ksecs. The significance (f_{test}) of the QPO detected in the PDS extracted from this short exposure was $\approx 3\sigma$. Fortunately, long uninterrupted data of duration ≈ 24 ksecs each was available from the MOS detectors. Therefore, to confirm the presence of the QPO, we extracted a PDS from the combined MOS data. The QPO is clearly evident in the MOS data with a detection significance of $\approx 5\sigma$. The 3-10 keV EPIC-pn and combined EPIC-MOS PDS are shown in the left

Table 3.2: Summary of the 3-10 keV power spectral modeling.

ObsID	0206080101	0657800101	0657801901 ^c (pn)	0657801901 ^c (MOS)	0657802101	0657802301
Exposure ^a (ksecs)	60.0	22.0	8.8	24.2	17.4	17.0
A*	1.94 ± 0.04	1.96 ± 0.01	1.92 ± 0.02	1.97 ± 0.02	1.95 ± 0.01	1.97 ± 0.01
B*	0.03 ± 0.03	0.01 ± 0.01	0.01 ± 0.01	0.01 ± 0.01	0.01 ± 0.01	0.01 ± 0.01
Γ*	0.55 ± 0.23	1.09 ± 0.29	0.92 ± 0.64	0.76 ± 0.30	1.12 ± 0.22	1.28 ± 0.52
N _{QPO} [†]	0.81 ± 0.16	1.25 ± 0.29	1.19 ± 0.39	0.71 ± 0.18	1.13 ± 0.31	0.44 ± 0.18
ν ₀ [†] (mHz)	121.4 ± 2.9	49.3 ± 1.5	47.4 ± 2.5	45.4 ± 1.3	36.7 ± 2.1	204.8 ± 6.3
Δν [†] (mHz)	23.15 ± 6.22	8.6 ± 2.6	15.3 ± 6.8	12.0 ± 4.5	9.2 ± 3.6	51.8 ± 31.7
χ ² /dof (continuum ^b)	137/150 (181/153)	381/338 (409/341)	310/269 (329/272)	442/434 (478/437)	317/294 (338/297)	53/62 (78/65)
Significance (ftest)	> 5σ	≈ 3.9σ	≈ 3σ	≈ 5σ	> 3σ	≈ 3.9σ

^aThe effective exposure used for extracting the power density spectra.

*We fit the continuum with a power-law model described as follows:

$$Continuum = A + B\nu^{-\Gamma}$$

where, Γ is the power-law index of the continuum.

[†] We model the QPOs with a Lorentzian. The functional form is as follows:

$$QPO = \frac{N_{QPO}}{1 + \left(\frac{2(\nu - \nu_0)}{\Delta\nu}\right)^2}$$

where, ν₀ is the centroid frequency and Δν is the FWHM of the QPO feature.

^bThe χ²/dof for the continuum are shown in braces.

^cOwing to only 8.8 ksecs of available good time interval, the significance of the QPO in the pn data was only 3σ. To confirm the presence of the QPO, we extracted a power density spectrum from combined MOS data.

and the right panels of Figure 3.3, respectively. Finally, we analyzed the PDS of the backgrounds from each of the six datasets (five pn and one MOS) and note that they all are consistent with a constant Poisson noise.

3.3.1.1 Origin of the mHz QPOs

As mentioned earlier, the source region of M82 X-1 – used for constructing the PDS – is contaminated by the nearby point sources. The major source of contamination is source 5 which can reach flux levels comparable to M82 X-1. Therefore it is a concern as to which source (M82 X-1 or source 5) produces the QPOs. Work by Feng & Kaaret (2007) has clearly shown that the $\text{few} \times 10$ mHz QPOs originate from M82 X-1. More specifically, they demonstrate that the 54 mHz QPO during the observation 0112290201 and the ≈ 120 mHz QPO during the observation 0206080101 originate from M82 X-1. Furthermore, Feng et al. (2010) used the high angular resolution observations by *Chandra* to construct a clean PDS of source 5. They find that in the frequency range of ≈ 30 -220 mHz the PDS of source 5 is essentially noise (see Figure 1 of Feng et al. 2010), suggesting that the power spectral contamination by source 5 is negligible. It is therefore likely that all the QPOs reported here (36-210 mHz) originate from M82 X-1.

To confirm that M82 X-1 is indeed the origin of the mHz QPOs reported here, we carried out the same analysis as Feng & Kaaret (2007). For each observation, we divided the source region into two semi-circles, one containing the majority of the flux from M82 X-1 (region A of the top panel of Figure 3.4) and the other dominated

by the flux from source 5 (region B of the top panel of Figure 3.4). We then extracted the PDS from each of these individual half-circles. The PDS using only events from region A and from region B of observation 0657802301 (with the 210 mHz QPO) are shown in the middle and the bottom panel of Figure 3.4, respectively. It is clear that the QPO is evident in region A which is dominated by flux from M82 X-1. We found this to be the case in all the five observations. This analysis suggests that M82 X-1 is indeed the source of the mHz QPOs.

3.3.2 Spectral analysis: Energy-dependent surface brightness modeling

Due to contamination by point sources within the PSF of EPIC data a clean energy spectrum of M82 X-1 cannot be extracted. Energy spectral modeling of the previous high resolution *Chandra* observations of M82 X-1 suggests that its X-ray spectrum can be modeled by a simple power-law (see Kaaret et al. 2006). Furthermore, work by Feng & Kaaret (2007) indicates that the absorbing column towards the source does not change significantly between observations that are randomly spread in time. Therefore, assuming the 3-10 keV X-ray spectrum of M82 X-1 can be modeled with a simple power-law, its hardness ratio (say ratio of the count rates in 3-5 keV and the 5-10 keV bands) will suffice as an indicator of the energy spectral power-law index. Therefore, we extracted the hardness ratio from each of the five observations by first carrying out the surface brightness modeling – using the procedure described in Section 3.2 – in the soft (3-5 keV) X-ray band and then in

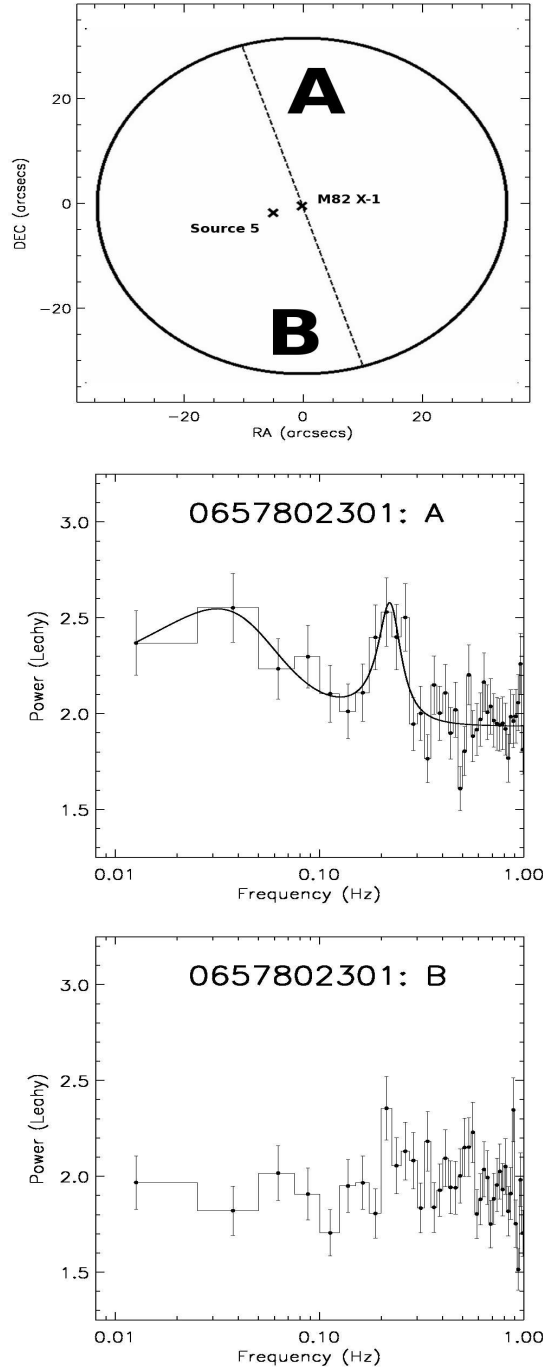


Figure 3.4: *Top Panel:* A circular source extraction region (radius of $33''$ and centered on M82 X-1) demarcated as region A (not containing source 5) and region B (containing source 5). Similar to Feng & Kaaret (2007), the dashed line is perpendicular to the line connecting M82 X-1 and source 5. *Middle Panel:* 3-10 keV EPIC-pn power density spectrum of region A. A best-fit model (bending power-law for the continuum and a Lorentzian for the QPO) is also shown (*solid*). *Bottom Panel:* 3-10 keV EPIC-pn power density spectrum of region B (*histogram*). This analysis shows that M82 X-1 is the source of the mHz QPOs.

the hard band (5-10 keV). The resolved soft and hard count rates of M82 X-1 are indicated in the second and the fourth columns of Table 3.3. The corresponding hardness ratios are also shown.

Furthermore, we ran simulations in *XSPEC* (Arnaud 1996) to constrain M82 X-1's spectral shape, i.e., the value of its power-law index. Our procedure is described as follows. First, using the *fakeit* command in *XSPEC*, we simulated a number of energy spectra (1000 in our case) each of which was described by a simple power-law modified by absorption, i.e., *phabs*pow* in *XSPEC*. We used the MOS1 responses generated using the *arfgen* and the *rmfgen* tasks for this purpose. These energy spectra spanned a wide range of power-law indices (1-4) and normalizations (0.0001-0.01) with exposure time equal to the observing time of a given dataset. In essence, we generated a set of energy spectra as observed by EPIC-MOS1 and each prescribed by a power-law model with index and the normalization values in the range of 1-4 and 0.0001-0.01, respectively. From each of the five *XMM-Newton* observations (see Table 3.3), we calculated the MOS1 count rate of M82 X-1 in seven energy bands (3-10 keV, 3-9 keV, 3-8 keV, 3-7 keV, 3-6 keV, 3-5 keV and 3-4 keV) using surface brightness modeling technique described earlier. Within the suite of simulated spectra, we searched for the energy spectra whose count rates in the above bands are equal to the measured values (within the error bars) from surface brightness modeling of the real image. We find that the power-law index of M82 X-1 measured this way is only weakly constrained with a value in the range of 1.3-1.8. Note that this is consistent with the previous *Chandra* measurement of 1.67 (Kaaret et al. 2006).

3.3.3 Timing-Spectral correlations

The primary goal of the present work is to understand the nature of the mHz QPOs from ULX M82 X-1 by testing for a timing-spectral correlation similar to that seen in stellar-mass black holes with type-C low-frequency QPOs. The basic correlation that is characteristic of type-C low-frequency QPOs in stellar-mass black holes is the dependence of the power-law index of the energy spectrum on the centroid frequency of the strongest QPO. Using all of the archival *XMM-Newton* observations we detected QPOs at five distinct frequencies from ULX M82 X-1 (see Section 3.3.1). Since a clean energy spectrum cannot be extracted with the present data we used the hardness ratio to represent the power-law index in each of these cases (see Section 3.2). Compiling all the results, we find that the hardness ratio shows no apparent dependence on the centroid frequency of the QPO. We find that as the centroid frequency of the QPO increases the hardness ratio appears to be constant. This is shown in the right panel of Figure 3.5. In addition, we plot the resolved MOS1 X-ray (3-10 keV) count rate of M82 X-1 against the centroid frequency of the QPO. We find a strong correlation with a Pearson's correlation coefficient of +0.97. We find that as the count rate of the source increases, the centroid frequency of the QPO also increases. This correlation is shown in the left panel of Figure 3.5.

3.4 Discussion

The so-called type-C low-frequency QPOs of stellar-mass black holes are known to occur in the frequency range of ~ 0.2 -15 Hz. They are characterized by high qual-

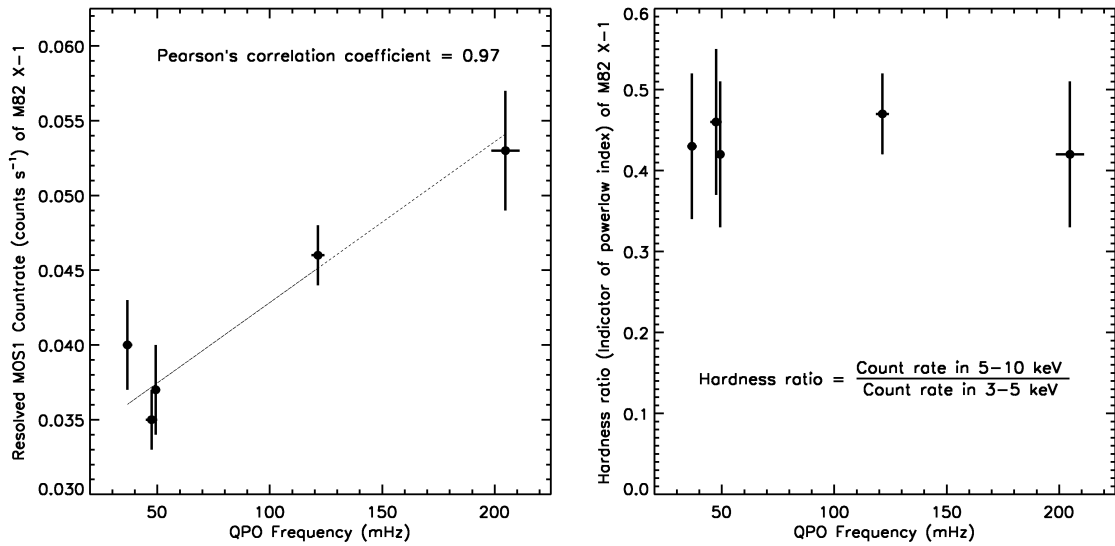


Figure 3.5: Timing-Spectral correlations. *Left Panel:* The correlation between the resolved MOS1 3-10 keV count rate of M82 X-1 (*Y-axis*) and the centroid frequency of the QPO (*X-axis*). The error bars are also shown. The value of the Pearson's correlation coefficient, which measures the significance of the correlation, is indicated at the top of the panel. The best-fit straight line (*dashed*) is also shown. *Right Panel:* The dependence of the hardness ratio of M82 X-1 (*Y-axis*) on the centroid frequency of the QPO (*X-axis*). The error bars are also shown. Using *XMM-Newton* data it is not possible to extract a clean energy spectrum, therefore, we use the hardness ratio instead which serves as an indicator of the power-law index of the energy spectrum. Compare with Figure 5 of Dheeraj & Strohmayer (2012).

ity factors ($Q = \text{centroid frequency}/\text{FWHM}$) of ~ 7 -12 and high fractional RMS amplitudes of ~ 7 -20% (see Table 1 of Casella et al. 2005, Table 2 of Remillard et al. 2002b and Table 1 of McClintock et al. 2009). Another distinct feature of the type-C low-frequency QPOs of stellar-mass black holes is that their centroid frequency is tightly correlated with the power-law index of the X-ray energy spectrum (Sobczak et al. 2000a; Vignarca et al. 2003). The relationship can be described as an increase in the power-law index with the QPO frequency with evidence for either a turn-over or constancy (saturation) beyond some higher value of the QPO

Table 3.3: Summary of energy-dependent surface brightness modeling. We modeled all the MOS1 images in two energy bands: the soft (3-5 keV) and the hard (5-10 keV) X-ray bands.

ObsID ^a	3-5 keV ^b count rate (cts s ⁻¹)	χ^2/dof^c	5-10 keV ^d count rate (cts s ⁻¹)	χ^2/dof^e	Hardness ^f ratio
0206080101	0.030 ± 0.002	392/437	0.014 ± 0.001	233/437	0.47 ± 0.05
0657800101	0.026 ± 0.003	352/437	0.011 ± 0.002	219/437	0.42 ± 0.09
0657801901	0.024 ± 0.002	293/437	0.011 ± 0.002	140/437	0.46 ± 0.09
0657802101	0.028 ± 0.003	362/437	0.012 ± 0.002	156/437	0.43 ± 0.09
0657802301	0.036 ± 0.003	432/437	0.015 ± 0.003	280/437	0.42 ± 0.09

^aThe *XMM-Newton* assigned observation ID.

^bResolved 3-5 keV MOS1 count rate of ULX M82 X-1. All the count rates are calculated using the formula described in the text (see Section 2).

^cThe best-fit $\chi^2/\text{degrees of freedom (dof)}$ from the surface brightness modeling using only the photons in the energy band of 3-5 keV.

^dResolved 5-10 keV MOS1 count rate of ULX M82 X-1.

^eThe best-fit $\chi^2/\text{degrees of freedom (dof)}$ from the surface brightness modeling using only the photons in the energy band of 5-10 keV.

^fHardness ratio of ULX M82 X-1 defined as the count rate in 5-10 keV over the count rate in 3-5 keV band.

frequency, i.e., beyond a certain high QPO frequency ($\sim 5\text{-}10$ Hz) the power-law spectral index either decreases or remains constant (saturates) with increasing QPO frequency. The turn-over/saturation is known to hold over a small range ($\sim 5\text{-}15$ Hz) of QPO frequencies (see Figure 10 of Vignarca et al. 2003). This general behavior has now been observed from various stellar-mass black holes including XTE J1550-564 (Sobczak et al. 2000a; Vignarca et al. 2003; Shaposhnikov & Titarchuk

2009; McClintock et al. 2009), GX 339-4 (Revnivtsev et al. 2001; Shaposhnikov & Titarchuk 2009; Stiele et al. 2013), GRO J1655-40 (Sobczak et al. 2000a; Vignarca et al. 2003; Shaposhnikov & Titarchuk 2009), Cygnus X-1 (Shaposhnikov & Titarchuk 2007, 2009), H1743-322 (Shaposhnikov & Titarchuk 2009; McClintock et al. 2009; Stiele et al. 2013), 4U 1543-475 (Shaposhnikov & Titarchuk 2009) and GRS 1915+105 (Vignarca et al. 2003; Titarchuk & Seifina 2009). While the slope of the correlation is different for different sources and sometimes different for the same source in a different outburst, the overall trend is the same.

It is interesting to note that the hardness ratio of M82 X-1, an estimator of the energy spectral power-law index, remains constant over a wide range of QPO frequencies (36-210 mHz). There are two ways to interpret this result: (1) the mHz QPOs of M82 X-1 are indeed the analogs of type-C low-frequency QPOs of stellar-mass black holes with the observed relationship representing the saturation portion of the trend or (2) the mHz QPOs of M82 X-1 are fundamentally different from the type-C low-frequency QPOs of stellar-mass black holes as they show no apparent dependence on the power-law spectral index which is different from the positive correlation seen in stellar-mass black holes. Assuming the former to be the case, one can estimate the mass of the black hole in M82 X-1 by simply scaling the turn-over frequency of M82 X-1 (≈ 40 mHz) to the turn-over frequency observed in various stellar-mass black holes (≈ 5 -10 Hz). Under the assumption that the turn-over frequency scales inversely with the mass of the black hole, the mass of the black hole in M82 X-1 can be estimated to be in the range of ≈ 500 -1000 M_{\odot} , i.e., an intermediate-mass black hole. But on the other hand, saturation of the power-law

index with the QPO frequency has never been seen over such a wide range of QPO frequencies in stellar-mass black holes. In stellar-mass black holes such a saturation is known to hold for QPO frequency changes of a factor of ≈ 1.5 -3 (see Figure 10 of Vignarca et al. 2003; Shaposhnikov & Titarchuk 2009). The QPOs observed from M82 X-1 occur in the frequency range of 36-210 mHz. This represents a factor of ≈ 6 change in the centroid frequency of the QPOs. Given such a large range in the QPO frequencies, it seems unlikely that the observed relationship represents the saturated portion of the type-C low-frequency QPOs of stellar-mass black holes. In other words, *the mHz QPOs of M82 X-1 may be fundamentally different compared to the type-C low-frequency QPOs of stellar-mass black holes.* This is not surprising as similar dependence has now been seen from another ULX NGC 5408 X-1 (Dheeraj & Strohmayer 2012).

Furthermore, mHz QPOs in the range of ≈ 2 -300 mHz (a frequency range comparable to the QPOs of M82 X-1) have been observed from various stellar-mass black holes. These include GRO J0422+32 (QPOs with centroid frequencies of 300 mHz, 230 mHz and 200 mHz using Granat/SIGMA (40-150 keV), OSSE (35-60 keV) and BATSE (20-100 keV), respectively: Vikhlinin et al. 1995; Grove et al. 1998; van der Hooft et al. 1999), GRO J1719-24 (QPOs with centroid frequencies as low as 40 mHz and 300 mHz using BATSE (20-100 keV): van der Hooft et al. 1996), XTE J1118+480 (70-150 mHz QPOs detected using the USA experiment and RXTE: Wood et al. 2000; Revnivtsev et al. 2000), GX 339-4 (90-660 mHz QPOs using *RXTE*/PCA: Revnivtsev et al. 2001), GRO J1655-40 (100 mHz QPO using *RXTE*/PCA: Remillard et al. 1999), XTE J1550-564 (80-300 mHz QPOs

using *RXTE*/PCA: Remillard et al. 2002b; Cui et al. 1999), GRS 1915+105 (2-160 mHz QPOs using *RXTE*/PCA: Morgan et al. 1997), Cygnus X-1 (40-70 mHz QPOs using Granat/SIGMA: Vikhlinin et al. 1994) and H1743-322 (11 mHz QPO using *RXTE* and *Chandra*: Altamirano & Strohmayer 2012). Moreover, the overall PDS of M82 X-1 show similarities with the PDS of GRS 1915+105 when it exhibits a few \times 10 mHz QPOs and XTE J1550-564 when it shows a few \times 10 mHz QPOs (compare Figure 3.2 & 3.3 with Figure 2 of Morgan et al. 1997 and Figure 2 of Cui et al. 1999). The continuum of the PDS of these three sources appear to be a simple power-law or a bending power-law. It is therefore possible that the mHz QPOs of M82 X-1 may be similar to the mHz QPOs of stellar-mass black holes and we are not able to observe the “higher-frequency” QPOs (\sim 1-15 Hz) owing to very low count rate of M82 X-1 (Heil et al. 2009). If that were the case, the accreting black hole within M82 X-1 can be of stellar-mass. The large X-ray output may then be produced via some sort of a super-Eddington mechanism (see, for example, Begelman 2002).

On the other hand it is interesting to note that the X-ray intensity of the source correlates with the QPO centroid frequency. Such a dependence has been observed from some stellar-mass black holes exhibiting type-C low-frequency QPOs. These sources include XTE J1550-564 (see Figure 7 of Vignarca et al. 2003 and Table 1 of Sobczak et al. 2000b) and GRS 1915+105 (Figure 1 of Munro et al. 1999; Figure 1 of Reig et al. 2000; see Figure 2 & 3 of Rodriguez et al. 2002). In addition, the constancy of the hardness ratio indicates that the energy spectral power-law index remains the same across these observations. Assuming that the 3-10 keV

X-ray spectrum can be described by a simple power-law (previous high-resolution *Chandra* observations suggest this may be the case: see Kaaret et al. 2006) the X-ray count rate is directly proportional to the total X-ray/power-law flux. In which case, the left panel of Figure 3.5 is indicating a positive correlation between the X-ray/power-law flux and the QPO centroid frequency.

Finally, we would like to point out that the implied spectral indices are in the range of 1.3-1.8, which is within the range that low-frequency QPO frequency increases with the spectral index in stellar-mass black holes (see, for example, Shaughnessy & Titarchuk 2009). In other words, there could be an increase in the spectral index of M82 X-1 with the mHz QPO frequency but the hardness ratio constraints are just not precise enough to show it. An effective way to know for certain if the QPO centroid frequency of ULX M82 X-1 is correlated or not correlated with its power-law spectral index is through joint *Chandra/XMM-Newton* observations; Where the *Chandra* data can be used to extract clean energy spectra of M82 X-1 and the *XMM-Newton* data can be used to estimate the QPO parameters of the source.

Chapter 4: Discovery of a 7 mHz X-ray Quasi-periodic Oscillation
from the most Massive Stellar-mass Black Hole IC 10
X-1

4.1 Introduction

The X-ray light curves of numerous accreting neutron star and stellar-mass black holes show evidence for the presence of quasi-periodic oscillations (QPOs), which appear as finite-width peaks in their power density spectra (PDS) (see van der Klis 2006 and McClintock & Remillard 2006 for reviews of neutron star and stellar-mass black hole QPOs). While it is known that QPOs occur with a wide range of centroid frequencies—a few mHz to above a kHz in neutron stars and a few mHz to a few hundred Hz in the case of stellar-mass black holes—the exact nature of the physical processes producing such oscillations is still a mystery.

Based on the observed properties, i.e., their centroid frequencies, widths, amplitudes, and the overall nature of their power spectra, etc., QPOs have been categorized into different groups. In neutron star binaries the QPO phenomenon constitutes the *kilohertz* QPOs (centroid frequencies in the range of 300-1200 Hz: see the review by van der Klis 2000) seen from over two dozen sources (e.g., Méndez et

al. 2001; Barret et al. 2008 and references therein), the *hertz* QPOs (~ 100 -300 Hz: e.g., van Straaten et al. 2003; Altamirano et al. 2008a) seen predominantly in a special class (atoll) of neutron star binaries, the low-frequency QPOs (0.01-50 Hz: e.g., van Straaten et al. 2003), the 1 Hz QPOs observed in two accreting millisecond X-ray pulsars (e.g., Wijnands 2004), the $\approx 0.6 - 2.4$ Hz QPOs observed only from dipping (high-inclination) neutron star binaries (e.g., Homan et al. 1999; Jonker et al. 1999, 2000) and the very low-frequency 7-15 mHz QPOs observed from at least three systems (e.g., Revnivtsev et al. 2001, Altamirano et al. 2008b).

Similarly, black holes also show a variety of QPOs (McClintock & Remillard 2006). They can be broadly classified into two categories: (1) high-frequency QPOs with centroid frequencies in the range of a few \times (10-100) Hz (e.g., Miller et al. 2001; Strohmayer 2001a, b; Remillard et al. 2006; Belloni & Altamirano 2013) and (2) low-frequency QPOs that occur in the range of 0.1-15 Hz (e.g., Casella et al. 2005). Based on their broadband properties, viz., shape, fractional amplitude of the PDS and the QPOs, etc., the low-frequency QPOs have been further subdivided into type-A, B and C (e.g., Homan et al. 2001; Remillard et al. 2002a). In addition to the high-frequency QPOs and the low-frequency QPOs of stellar-mass black holes, two black hole sources, GRS 1915+105 and IGR J17091–3624, show so-called “heartbeat” QPOs which occur in the mHz frequency regime (e.g., Belloni et al. 2000; Altamirano et al. 2011). Furthermore, as described in this thesis, some ULXs show a few \times 10 mHz QPOs (e.g., Dewangan et al. 2006; Pasham & Strohmayer 2013b). More recently, an 11 mHz X-ray QPO and the recurrence of a few \times mHz QPOs were detected from the black hole candidates H1743–322 and

Cygnus X-3, respectively (Koljonen et al. 2011; Altamirano & Strohmayer 2012).

IC 10 X-1 is an eclipsing, Wolf-Rayet binary. Current evidence suggests that it contains a massive stellar-mass black hole with an estimated mass of 23-34 M_{\odot} (Prestwich et al. 2007; Silverman & Filippenko 2008). The presence of an eclipse suggests that the system is highly inclined, i.e., close to edge-on. This source was observed previously with *XMM-Newton* (ID: 0152260101) for a duration of roughly 45 ksecs. After accounting for background flaring only a mere 15 ksecs of useful data was available, analysis of which showed some evidence—although at modest statistical significance—for the presence of a QPO at ≈ 7 mHz. Motivated by this, and to carry out eclipse mapping, a long *XMM-Newton* observation was proposed to confirm the presence of this mHz QPO (ID: 0693390101; PI: Strohmayer). Here we present results from our timing analysis of this new data set and confirm the presence of the QPO at 7 mHz.

4.2 *XMM-Newton* observations

Beginning 2012 August 18 at 22:05:46 (UTC) *XMM-Newton* observed IC 10 X-1 for roughly 135 ksecs, a duration approximately equal to its orbital period (34.93 hrs: Prestwich et al. 2007; Silverman & Filippenko 2008). For our study we only used the EPIC data (both pn and MOS). We used the standard analysis system version 13.0.0 for extracting the images and the event lists. The source was easily identifiable and there were no source confusion problems (see Figure 4.1). The source events were extracted from a circular region of radius 33'' centered around the source

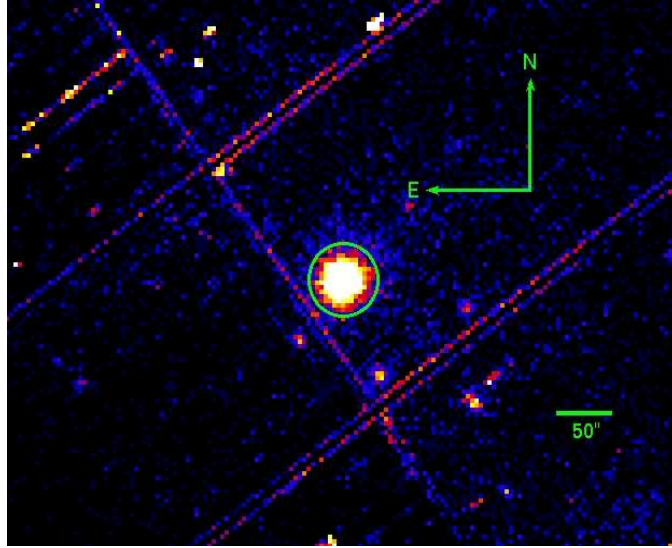


Figure 4.1: EPIC-pn X-ray (0.3-10.0 keV) image of IC 10 X-1. Clearly there is only one point source, IC 10 X-1, and no obvious evidence for source contamination. The extraction region of radius $33''$ is indicated by a green circle.

and the background events were extracted from a nearby circular region of the same size. The observation was affected by flaring only briefly at the very beginning and the end of the pointing. These epochs were removed from our analysis.

The combined pn and MOS 0.3-10.0 keV light curve of IC 10 X-1 is shown in Figure 4.2 (*black*) along with the background (*red*). Also overlaid are the good time intervals (GTIs) during which a given EPIC instrument (pn/MOS1/MOS2) was continuously active for more than 5 ksecs. For a given instrument the horizontal line, which is offset to an arbitrary value, indicates the active time, while a vertical line marks the beginning or the end of a continuous GTI. It is clear that EPIC-pn has three GTIs of duration roughly 23 ksecs, 75 ksecs and 27 ksecs, while MOS1 has two GTIs of length 30 ksecs and 99 ksecs and MOS2 has one long GTI of 130 ksecs.

4.3 Results

It is clear even by eye that the source varies significantly. Since the pn detector offers the highest effective area among the three EPIC instruments, we started our analysis with its longest available GTI of ≈ 75 ksecs (between hour 8.5 to 29.5 in Figure 4.2). Using all the 0.3-10.0 keV photons we constructed a Leahy-normalized PDS where the Poisson noise equals 2 (Leahy et al. 1983). This is shown in the top left panel of Figure 4.3 (*histogram*). It is evident that the overall power spectrum can be described by a simple power-law noise at the lowest frequencies with a QPO-like feature around 7 mHz and essentially Poisson noise at frequencies above $\gtrsim 0.02$ Hz. In order to test the significance of the QPO we followed a rigorous Monte Carlo approach described below.

First, we fit the continuum of the PDS using a model consisting of a power-law plus a constant. While modeling the continuum we used the frequency range 0.0001 (the lowest that can be probed) - 0.1 Hz and excluded the region containing the apparent QPO feature, i.e., 5-9 mHz. The best-fit continuum model parameters are shown in the first column of Table 4.1. Thereafter, following the prescription described by Timmer & Koenig (1995), we simulated a large number of light curves (and their corresponding PDS) that have the same shape, i.e., same parameters, as in the 1st column of Table 4.1, and the same frequency resolution as the spectrum used for obtaining the best-fit continuum parameters. A sample PDS simulated with the above technique (*red*) along with the real PDS (*black*) is shown in the top right panel of Figure 4.3. We simulated 370 such power spectra and found the

maximum value in each frequency bin. This gave us the 99.73% (3σ) significance within that particular bin. A similar estimate for each frequency bin gave us the complete confidence curve. Similarly we simulated 10000 PDS and estimated the 99.99% (3.9σ) confidence curve. It should be noted that the confidence curves are sensitive to the chosen values of the continuum model parameters. Given the error on each of the individual model parameters, i.e., best-fit power-law normalization and the power-law index, we estimated the 99.73% and the 99.99% curves for various combinations of the power-law normalization and the index within the error bars quoted in column 1 of Table 4.1. To be conservative we picked the maximum of these curves. These confidence levels are overlaid in the figure. It is clear that the QPO feature is significant at the 99.99% level.

To further confirm the presence of this QPO feature we extracted another PDS using the combined MOS data. For this purpose we used the longer GTI of roughly 95 ksecs (from hour 8.5 to hour 34.5 in Figure 4.2). The 0.3-10.0 keV combined MOS PDS is shown in the bottom left panel of Figure 4.3. The QPO feature is again evident at 7 mHz. To quantify the variability we first modeled the PDS with a power-law plus a constant. This gave a χ^2 of 245 with 192 degrees of freedom (dof). We then added a Lorentzian component to model the QPO feature at 7 mHz. This improved the χ^2 by 28 with an addition of three parameters, i.e., a χ^2 of 217 with 189 dof (see the second column of Table 4.1). This decrease in χ^2 serves as a further indicator of the significance of the QPO component. Using the F-test this corresponds to a single-trial significance of 4×10^{-5} . Note that we essentially searched in a known narrow frequency range of ≈ 5 -10 mHz (from the

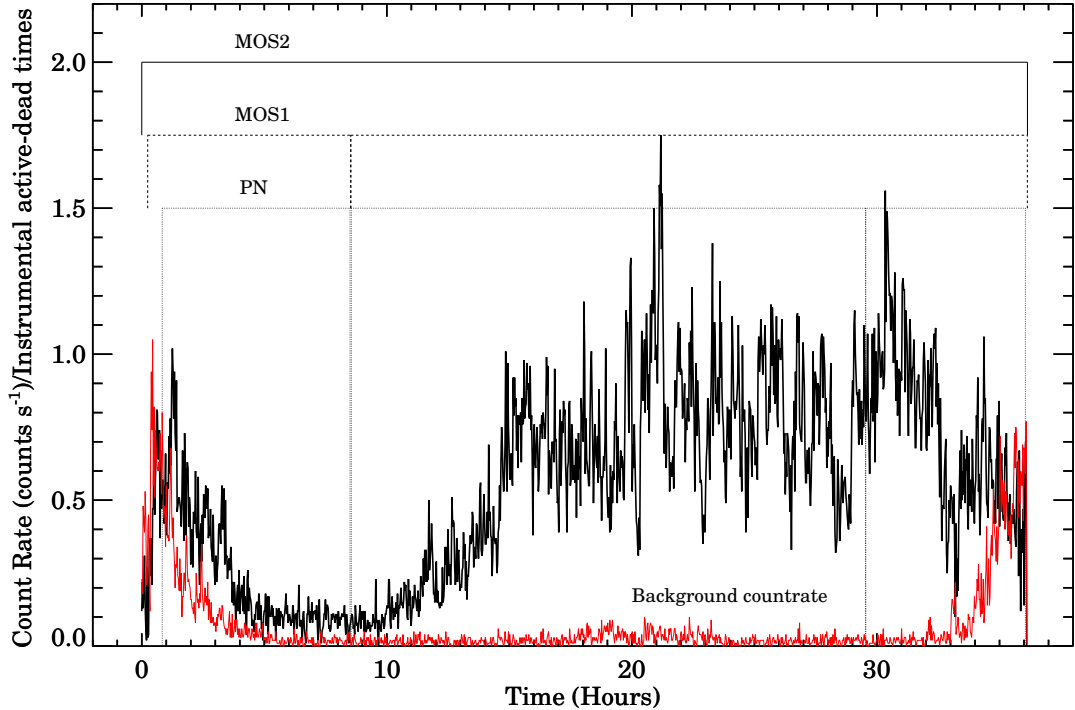


Figure 4.2: The combined, background-subtracted EPIC X-ray (0.3-10.0 keV) light curve of IC 10 X-1 (*black*) along with the background light curve (*red*). Time zero corresponds to 4.6171485×10^8 secs since 50814.0 (Modified Julian Date). Both the light curves were binned to 100 seconds. The start and end times of all the GTIs greater than 5 ksecs are indicated by vertical lines (see text).

prior *XMM-Newton* observation), and thus the effective number of trials is ~ 1 .

It is clear that the QPO is present in two independent detectors at $> 3.5\sigma$ confidence level in each case. The chance probability of two independent 3σ detections alone is 4.33σ . Given the 3.5σ detections in two separate measurements, we conclude that the observed 7 mHz QPO of IC 10 X-1 is statistically highly significant.

In addition, we studied the energy dependence of the fractional RMS amplitude of the QPO. For this purpose, we extracted the PDS of the source in seven energy bands. Owing to the low count rate we fixed the upper bound of the bandpass at 10

Table 4.1: Summary of power spectral modeling.

Parameter	EPIC-pn (Continuum)	Combined MOS (0.3-10.0 keV)	Combined MOS (0.6-10.0 keV)	Combined MOS (0.9-10.0 keV)	Combined MOS (1.2-10.0 keV)	Combined MOS (1.5-10.0 keV)
$N(\times 10^{-7})^a$	143 ± 125	1.6 ± 1.7	1.8 ± 1.9	1.3 ± 1.5	3.2 ± 3.5	1.2 ± 1.5
Γ^a	1.9 ± 0.1	2.4 ± 0.2	2.4 ± 0.2	2.5 ± 0.2	2.3 ± 0.2	2.4 ± 0.2
C^a	1.9 ± 0.1	1.9 ± 0.1	1.9 ± 0.1	1.9 ± 0.1	1.9 ± 0.1	1.9 ± 0.1
N_{QPO}^b	$-^e$	1.5 ± 0.4	1.5 ± 0.4	1.4 ± 0.4	1.4 ± 0.4	1.0 ± 0.4
$\nu_0(\text{mHz})^b$	$-^e$	6.3 ± 0.2	6.3 ± 0.2	6.2 ± 0.2	6.3 ± 0.2	6.3 ± 0.2
$\Delta\nu(\text{mHz})^b$	$-^e$	1.5 ± 0.5	1.5 ± 0.5	1.7 ± 0.6	1.6 ± 0.6	1.5 ± 0.7
Q^c	$-^e$	4.2	4.2	3.7	3.9	4.2
RMS_{QPO}^d	$-^e$	11.1 ± 2.5	11.2 ± 2.5	11.9 ± 2.7	12.6 ± 2.9	12.0 ± 3.5
χ^2/dof	354/284	216/189	219/189	215/189	243/189	220/189

^aWe fit the continuum with a power-law model described as follows:

$$\text{Continuum} = N\nu^{-\Gamma} + C$$

where, Γ is the power-law index of the continuum. ^bWe modeled the QPOs with a Lorentzian. The functional form is as follows:

$$QPO = \frac{N_{QPO}}{1 + \left(\frac{2(\nu - \nu_0)}{\Delta\nu}\right)^2}$$

where, ν_0 is the centroid frequency and $\Delta\nu$ is the full-width-half-maximum (FWHM) of the QPO feature. ^cThe quality factor of the QPO defined as $\nu_0/\Delta\nu$. ^dThe fractional RMS amplitude of the QPO (see text). ^eIn this case we only modeled the continuum.

keV and varied the lower limit from 0.3 to 1.5 keV and constructed a PDS in each case using the combined MOS data. Each of these PDS were then modeled with a power-law plus constant for the continuum and a Lorentzian for the QPO (best-fit model parameters shown in Table 4.1). The fractional RMS amplitude of the QPO is:

$$RMS\ amplitude\ (\%) = 100 \left(\sqrt{\frac{\pi NW}{2C}} \right)$$

where N and W are the normalization and the width of the QPO (Lorentzian), respectively, while C is the mean count rate of the source. The dependence of the RMS amplitude of the QPO as a function of the lower limit of the band pass is shown in the bottom right panel of Figure 4.3. There is a very weak dependence of the QPO's amplitude on the energy from 0.3-1.5 keV. Four of the five PDS used for this analysis are shown in Figure 4.4. At energies greater than 1.5 keV the low signal to noise ratio of the data does not allow us to detect the QPO.

4.3.1 Search for a power spectral break

Numerous X-ray binaries and also AGN show evidence for the presence of a break in their PDS (e.g., McHardy et al. 2006; Markowitz & Edelson 2004). We searched for a spectral break in IC 10 X-1 using the data from the longest GTI outside the eclipse, i.e., hour 15.5 to 33.5 in Figure 4.2. Note that the presence of an eclipse in the data adds red noise to the power spectrum that is not intrinsic to the source variability. We constructed the combined MOS 0.3-10.0 keV PDS and did not find any obvious evidence for a PDS break down to frequencies as low as

0.0001 Hz. Note that a single PDS is noisy, with error in a particular bin equal to the value of that bin (van der Klis 1989). Therefore, averaging (say, by combining neighboring bins) is necessary to reduce the noise in the PDS. Hence, even though the lowest sampled frequency is $\approx 10^{-5}$ Hz (1/total length) averaging reduces the lowest effective frequency to roughly 0.0001 Hz in this case. It remains possible that a break may exist at $\lesssim 0.0001$ Hz. Moreover, we modeled this PDS with a power-law and a Lorentzian. We find that the best-fit continuum can be described by a power-law of index ≈ -2 .

4.4 Discussion

The frequency of the high-frequency QPOs of stellar-mass black holes (\sim a few 100 Hz) and the *hertz* QPOs of neutron stars (~ 100 -300 Hz) are roughly constant in frequency for a given source (van der Klis 2006). They are thought to have a common origin (e.g., Abramowicz et al. 2003) and it has been proposed that the QPO frequency may scale inversely with the mass of the compact object (e.g., see Figure 4.17 of McClintock & Remillard 2006). With a mass of 23-34 M_{\odot} IC 10 X-1's high-frequency QPOs, if any, are expected to occur in the range of a few 10s of Hz. Clearly the 7 mHz QPO of IC 10 X-1 is orders of magnitude slower than this and is very likely not a high-frequency QPO phenomenon.

The typical values of the centroid frequency, RMS amplitude and the quality factor ($Q = \text{centroid-frequency}/\text{QPO-width}$) of type-A low-frequency QPOs are ~ 8 Hz, $\lesssim 3$ and $\lesssim 3$, respectively (e.g., Casella et al. 2005). The respective values for

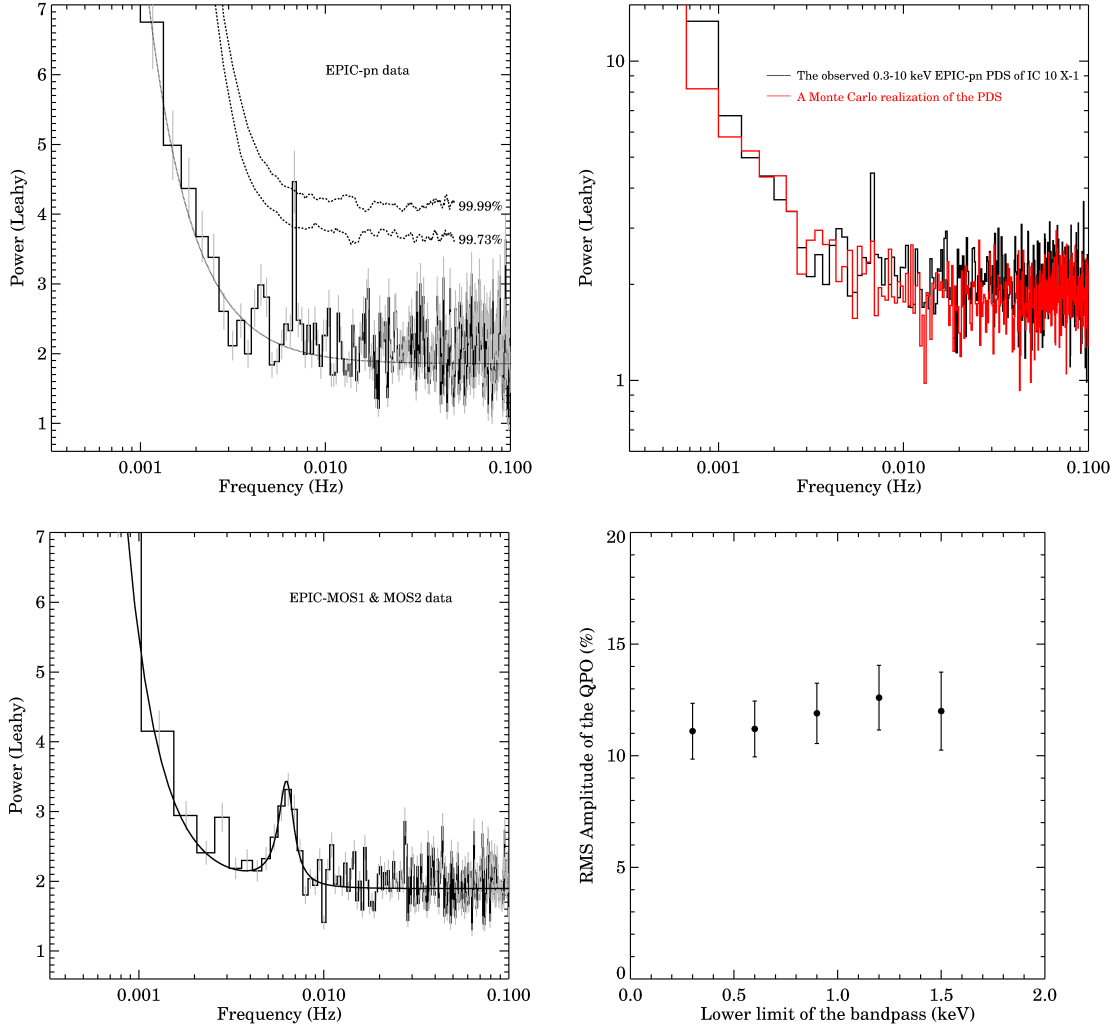


Figure 4.3: *Top Left panel:* The EPIC-pn PDS of IC 10 X-1 using the longest GTI of 75 ksecs (*black histogram*) along with the best-fit power-law model for the continuum (*solid*). The 99.73% and the 99.99% Monte Carlo simulated confidence contours are also shown (*dashed*). The QPO at 7 mHz is evident. *Top Right panel:* The observed EPIC-pn PDS of IC 10 X-1 (*black*: same as the figure on the left) and a sample Monte Carlo simulated PDS (*red*). *Bottom Left panel:* The combined 0.3-10.0 keV EPIC-MOS PDS of IC 10 X-1 using the longest common GTI of 95 ksecs (*histogram*). The best-fit model is also shown (*solid*). Again the feature at 7 mHz is evident. *Bottom Right panel:* The fractional RMS amplitude of the QPO versus the lower bound of the band pass used for constructing the PDS. The upper limit was fixed at 10 keV (see text).

type-B low-frequency QPOs are $\sim 5 - 6$ Hz, $\sim 2 - 4$ and $\gtrsim 6$. Lastly, type-C QPOs occur in a wider range of frequencies – 0.1-15 Hz – and have RMS amplitudes of

3-20 with Q factors of $\sim 7 - 12$. The overall nature of the PDS accompanying type-A, B, and C QPOs can be described as weak red noise, weak red noise and strong flat-topped noise, respectively. Although the continuum of the PDS of IC 10 X-1 is similar to that accompanying type-A or B QPOs, its QPO frequency, RMS amplitude and Q value are quite different (compare values in Table 4.1 with Table 1 of Casella et al. 2005). On the other hand, the centroid frequency of IC 10 X-1's QPO is much lower compared to a typical type-C QPO.

The mHz QPOs (frequency range of ~ 10 -200 mHz) of ULXs have been argued to be the analogs of the type-C low-frequency QPOs of stellar-mass black holes but occurring at a lower frequency (a few 10s of mHz compared to the few Hz of stellar-mass black holes) due to the presence of intermediate-mass black holes (mass of a few $\times (100$ -1000) M_{\odot}) within these systems. While the centroid frequency, the RMS amplitude and the Q value of the 7 mHz QPO of IC 10 X-1 are comparable to the mHz QPOs of ULXs (e.g., Dheeraj & Strohmayer 2012), there are two aspects that are dissimilar. (1) We do not detect a break in the PDS of IC 10 X-1 whereas breaks have been seen in all the ULXs (e.g., Dewangan et al. 2006). It is known that the break frequency scales with the QPO frequency as $\nu_{break} \sim \nu_{QPO}/9$ (Wijnands & van der Klis 1999). If that were the case for IC 10 X-1, the expected break is at ~ 0.7 mHz. It is thus possible that we are unable to detect the break due to our inability to sample variability at very low ($\lesssim 0.7$ mHz) frequencies, or the effects of the eclipse. (2) The RMS amplitude—at least in the case of the ULX NGC 5408 X-1—is known to increase with energy from 0.3-2.0 keV (Strohmayer et al. 2007; Middleton et al. 2011). However, we do not find evidence for such behavior in IC

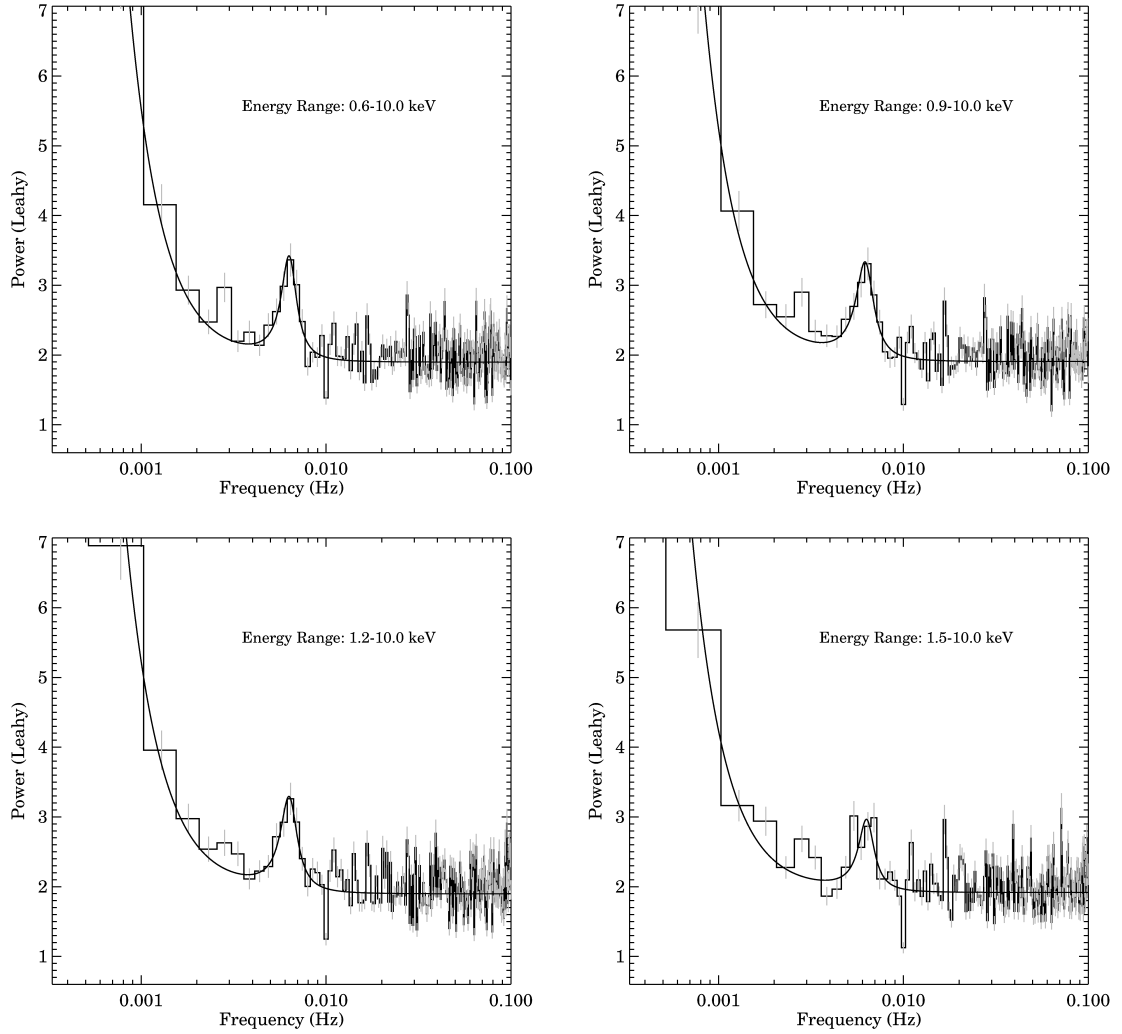


Figure 4.4: Combined MOS PDS of IC 10 X-1 in various energy bands. The energy band used for the PDS is indicated at the top-right of each panel. The best-fit model (see Table 4.1) is also overlaid (*solid*) in each case.

10 X-1 (see the bottom right panel of Figure 4.3).

Two black hole sources, GRS 1915+105 and IGR J17091–3624, show mHz QPOs in the so-called “heartbeat” state or the ρ state (e.g., Greiner et al. 1996; Morgan et al. 1997; Belloni et al. 2000; Altamirano et al. 2011). These QPOs are thought to be the result of a radiation pressure instability causing quasi-periodic evaporation followed by refilling of the inner regions of the accretion disk (Lightman

& Eardley 1974, Belloni et al. 1997; Neilsen 2011). These mHz QPOs occur at relatively high luminosities ($\sim 10^{38}$ erg s $^{-1}$) and at least in GRS 1915+105 appear to be energy-independent in the band pass from 2-30 keV (see Figure 8 of Morgan et al. 1997). Given the similar frequency, comparable RMS amplitude (e.g., Altamirano et al. 2011), energy independence (although here energy independence is seen over a different X-ray band pass) and similar X-ray luminosity¹ (see also Wang et al. 2005) it is possible that the 7 mHz QPO of IC 10 X-1 is related to the “heartbeat” QPOs. Given its low count rate it is, however, not possible to resolve IC 10 X-1’s light curve to the same level as GRS 1915+105 or IGR J17091–3624. It will require instruments with larger collecting area to test this hypothesis.

The 7 mHz QPO of IC 10 X-1 is likely not related to the 1 Hz QPOs of accreting millisecond X-ray pulsars (AMXPs) or the 7-15 mHz QPOs seen in some neutron star systems (e.g., Revnivtsev et al. 2001, Altamirano et al. 2008b). The 1 Hz QPO phenomenon in AMXPs is thought to be due to disk instabilities within the boundary layer of the accretion disk and neutron star magnetosphere (Patruno et al. 2009). Moreover, the 1 Hz QPOs are seen at low luminosities ($< 10^{36}$ erg s $^{-1}$) and can have RMS amplitudes as large as 100% (Patruno et al. 2009). Given the high RMS amplitude, and that they are likely related to the beginning of the propeller regime, they are probably different from the QPO seen in IC 10 X-1. The 7-15 mHz oscillations in some neutron stars are linked to marginally stable burning

¹The X-ray (0.3-10.0 keV) energy spectrum of IC 10 X-1 outside the eclipse can be fit with a canonical model consisting of a disk-blackbody and a power-law plus a Gaussian to model the emission feature at ≈ 0.9 keV. This model gives an acceptable fit with a χ^2 of 165 for 125 degrees of freedom. A detailed spectral analysis is not the subject of this work. Nevertheless, assuming this simple model, the inferred 2-10 keV luminosity at a distance of 0.66 Mpc is $\sim 10^{38}$ ergs s $^{-1}$.

of light elements on the surface of the neutron star (e.g., Heger et al. 2007), a process unique to neutron stars.

On the other hand, the 7 mHz QPO may be connected to the 0.6-2.4 Hz “dipper QPOs” of high-inclination neutron stars in the sense that IC 10 X-1 is also highly inclined (see the eclipse in Figure 4.1 and Silverman & Filippenko 2008). The so-called “dipper QPOs” are only seen from X-ray dipping sources. The dipping is presumably due to obscuration associated with the high inclination (Parmar & White 1988). Their RMS amplitudes are $\sim 10\%$ and are energy-independent in the range of 2-30 keV (see, for example, Figure 4 of Homan et al. 1999). With the present *XMM-Newton* data a similar energy range cannot be probed. However, we note that the QPO’s RMS amplitude is comparable to those of “dipper QPOs” and appears to be independent of energy in the range from 0.3-1.5 keV. More recently Altamirano & Strohmayer (2012) reported the discovery of an 11 mHz QPO from a black hole candidate H1743-322 (likely highly inclined: Homan et al. 2005) and suggested this could be the first detection of a “dipper QPO” analog in a black hole (candidate) system. The centroid frequency of the “dipper QPOs” is roughly constant over time. If the 7 mHz QPO is indeed a “dipper QPO” then it’s centroid frequency should also remain more or less constant. This can be tested with multi-epoch observations of IC 10 X-1 to search for QPO variability.

Finally, we note that the overall PDS and the QPO properties of IC 10 X-1 are also similar to that of Cygnus X-3 (van der Klis & Jansen 1985). They both have the same power-law like noise at low frequencies—each with roughly the same slope of -2 —with a QPO in the mHz regime and barely any power above 0.1 Hz (see

the bottom panels of Figure 2 of Koljonen et al. 2011). In addition the QPOs in both cases have comparable frequencies, RMS amplitudes and coherences (van der Klis & Jansen 1985). The mHz oscillations of Cygnus X-3 are likely associated with major radio flaring events (Koljonen et al. 2011; see, for example, Lozinskaya & Moiseev (2007) and references therein for radio studies of IC 10 X-1). Simultaneous radio and X-ray observations in the future can test whether jet ejection is related to the QPO in IC 10 X-1.

Chapter 5: Evidence for Quasi-periodic X-ray Dips from an Ultraluminous X-ray Source: Implications for the Binary Motion

5.1 Introduction & Background

There are now three detections of periodicities from long term (\sim a few hundred days) X-ray monitoring of ULXs which may reflect the orbital motion of these systems: a 62 day modulation in M82 X-1 detected with *RXTE* (Kaaret et al. 2007), a 375 day period in HLX ESO 243-39 (e.g., Servillat et al. 2011) and a 115.5 day period in NGC 5408 X-1 obtained from *Swift* data (Strohmayer 2009). The main results of Strohmayer (2009) are: (a) the discovery of a quasi-sinusoidal modulation of the X-ray flux with a period of 115.5 ± 4 days and (b) that the modulation amplitude decreases with increasing energy. The present work utilizes additional data acquired by *Swift* over a much longer temporal baseline (more than twice as long as used by Strohmayer 2009) and can be regarded as an extension of the work by Strohmayer (2009).

The phenomenon of periodic orbital X-ray modulations within the context of galactic X-ray binaries has been well-studied for over 30 years now (e.g., White & Holt 1982; Mason 1986). The basic idea is that there is a distribution of obscuring

material around the X-ray emitting region and as the X-ray source orbits the center of mass of the binary, our line of sight intercepts varying amounts of the intervening material resulting in the observed modulation (e.g., Parmar & White 1988; Armitage & Livio 1998). In addition, these X-ray variations are expected to recur with the orbital period of the binary. However, due to the turbulent nature of the accretion process and irregularities within the material surrounding the X-ray source, these modulations may not be strictly periodic (see, for example, Smale et al. 1988; Barnard et al. 2001; Kuulkers et al. 2012). Nevertheless, they provide an excellent means to track the orbital motion of the X-ray source.

Moreover, the nature of the obscuring medium, i.e., its distribution around the X-ray source as well as its density and ionization state, dictates the observed modulation profiles. In the case of the high-inclination ($\gtrsim 60^\circ$) low-mass X-ray binaries, periodic decreases in the X-ray flux (X-ray dips) extending over 10-30% of their orbital phase have been observed (e.g., White et al. 1995). In these cases it is generally accepted that the X-ray variations are due to absorption in the “bulge” at the edge of the accretion disk, where the accretion stream from the Roche-lobe filling companion star impacts the accretion disk (White & Holt 1982; Bisikalo et al. 2005). Such variations have been predominantly observed in the X-ray light curves of high-inclination neutron star low-mass X-ray binaries, viz., XB 1916-053 (e.g., Boirin et al. 2004), XB 1254-690 (e.g., Smale et al. 2002), EXO 0748-676 (Church et al. 1998).

On the other hand, sharp drops in the X-ray flux lasting less than one percent of the orbital phase have been observed in a small sample of accreting black hole

binaries. These include the low-mass X-ray binary GRO J1655-40 (Kuulkers et al. 1998, 2000) and the high-mass X-ray binary Cygnus X-1 (Balucińska-Church et al. 2000; Feng & Cui 2002). In the case of GRO J1655-40 the sharp dips last a very small fraction of the orbital period (a few minutes compared to its orbital period of 2.62 days) and are confined between the orbital phases of 0.7 and 0.9 (phase 0 corresponds to the superior conjunction of the X-ray source, i.e., when the companion star is in front of the black hole with respect to our line of sight). The short duration of these dips suggests that the absorbing medium is likely filamentary in nature. Based on 3-dimensional numerical simulations of the accretion stream impacting the disk in compact binaries (Armitage & Livio 1998), Kuulkers et al. (2000) suggested that the likely scenario operating in GRO J1655-40 is that the accretion stream from the Roche lobe overflow of the stellar companion splashes onto the disk rim, creating a local distribution of material above and below the plane of the disk. Also, the numerical work by Armitage & Livio (1998) predicts that the sharp dips should occur preferentially around the orbital phase of 0.8 (the stream-disk impact site), similar to those observed in GRO J1655-40 (Kuulkers et al. 2000). This suggested that the absorber in the case of GRO J1655-40 is a local distribution (between orbital phases of 0.7-0.9) of clumps above and below the accretion disk and is then somewhat different compared to the dipping in neutron star low-mass X-ray binaries.

The high-mass X-ray binary Cygnus X-1 exhibits two types of “sharp” X-ray dips (type-A and type-B as classified by Feng & Cui 2002). The type-A dips are energy-dependent, i.e., accompanied by an increase in the hardness ratio while

the type-B dips are energy-independent, i.e., no evidence for an increase in the hardness ratio. While the type-A dips are preferentially distributed roughly about the superior conjunction of the X-ray source, type-B dips occur randomly over the binary orbit. The type-A dips are attributed to being produced due to absorption by density enhancements (clumps or “blobs,” in the vernacular) in an inhomogeneous wind from the companion star. On the other hand, type-B dips are suggested to be caused by partial covering of an extended X-ray source by an opaque screen (Feng & Cui 2002). Numerical simulations of the accretion flow of wind-fed systems including high-mass X-ray binaries have shown that the tidal force from the compact object can distort the companion star and give rise to a focused wind in the direction of the compact source (Blondin et al. 1991). This tidal wind then develops into a Roche lobe overflow as the surface of the stellar companion reaches its equipotential surface. The Coriolis force deflects the accretion stream such that it does not directly impact the compact companion but goes around it (see Figure 7 of Blondin et al. 1991). The density in these tidal streams can be as high as 20-30 times the ambient density and therefore, in principle, can serve as an opaque absorber of the X-rays (see also, Balucińska-Church et al. 2000). Furthermore, these simulations predict that systems with dominant tidal streams should show evidence for pronounced dipping around the orbital phase of 0.6. A study of the distribution of the sharp X-ray dips from Cygnus X-1 as a function of orbital phase has shown that there are indeed two peaks: the primary peak corresponds to phase 0, i.e., superior conjunction of the X-ray source and a secondary peak at a phase of 0.6 (Balucińska-Church et al. 2000).

In summary, two types (based on the duration of the individual dips) of periodic/quasi-periodic X-ray modulations have been observed in accreting X-ray binaries: 1) broad dips lasting 10-30% of the orbital period have been seen in a sample of neutron star low-mass X-ray binaries and 2) sharp dips lasting less than one percent of the orbital period have been observed from the black hole low-mass X-ray binary and high-mass X-ray binary, GRO J1655-40 and Cygnus X-1, respectively. It is important to note that the location of the absorber is different in the neutron star low-mass X-ray binaries (bulge at the edge of the accretion disk) compared with GRO J1655-40 (clumps above the accretion disk) and Cygnus X-1 (accretion stream).

In this chapter we report on a study of the X-ray monitoring data from NGC 5408 X-1 obtained with the *Swift* X-Ray Telescope (XRT). In particular, we present evidence for sharp dips in the X-ray light curve and interpret the observed variability in the context of binary motion. The chapter is arranged as follows. In Section 5.2 we discuss the details of the *Swift*/XRT data used for this work. In Section 5.3 we study the long-term (\sim a few hundred days) timing behavior of the source. In particular, we report the detection of the quasi-periodic, sharp X-ray dips along with the smooth, quasi-sinusoidal X-ray modulation. Both modulations are consistent with the dipping phenomena seen in accreting galactic X-ray binaries. However, to avoid confusion and to be able to clearly distinguish between the two kinds of modulations we will refer to the sharp X-ray dips as simply dips or sharp dips while we refer to the smooth component as the smooth quasi-sinusoidal X-ray modulation. In Section 5.4 we present spectral evidence for a change in the physical properties of

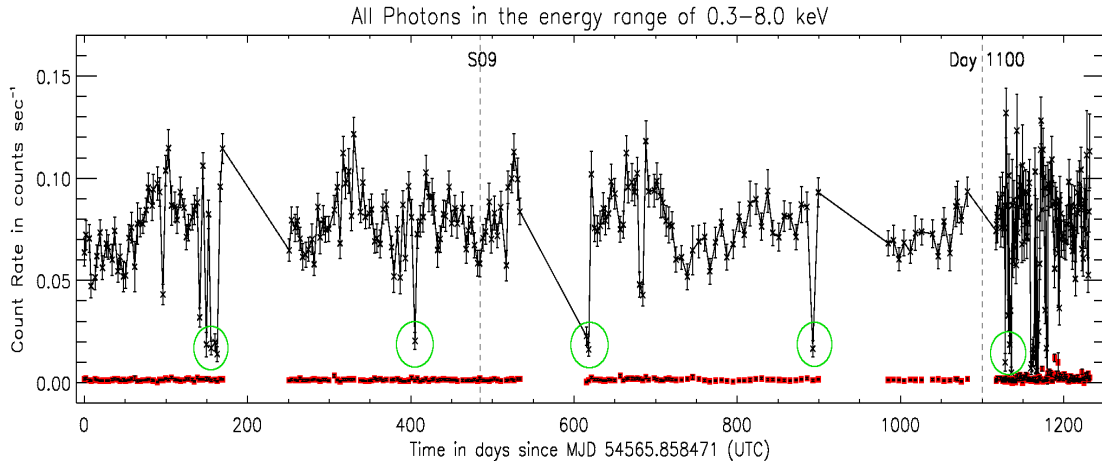


Figure 5.1: *Swift*/XRT X-ray light curve of the ULX NGC 5408 X-1 in the 0.3–8.0 keV energy band. The background count rates with their respective error bars are also shown (red points and black error bars within). The most prominent feature of the light curve is the quasi-periodic recurrence of the dips. These are highlighted with green circles. The vertical line labeled as Strohmayer (2009) marks the last observation used by Strohmayer (2009). The vertical line labeled as “day 1100” corresponds to the approximate epoch at which the physical properties of the system may have changed (see §5.4.1). Time zero corresponds to MJD 54565.85847 (UTC).

the system. We also study the spectral differences between the sharp dips and the other portions of the data. We discuss the implications of our results on the orbital motion of the X-ray source in Section 5.5. We summarize this work in Section 5.6.

5.2 *Swift*/XRT Observations

The X-ray Telescope (XRT) on board *Swift* began monitoring the ULX NGC 5408 X-1 in 2008 April as part of an approved Cycle 4 program (PI: Strohmayer). We include in our analysis all the observations obtained since the beginning of that program through 2011 August 30. The observing cadence has varied over this timespan of ≈ 3.4 yrs (1240 days), but on average the source was observed,

when viewable, for a few ksecs once every 4 days. Gaps in the coverage due to *Swift* observing constraints occurred from 2008 September 26 - 2008 December 16 (81 days), 2009 September 25 - 2009 December 15 (81 days), 2010 September 26 - 2009 December 20 (85 days) and 2011 March 27 - 2011 May 1 (35 days). This provided a total of 305 pointed observations with a cumulative exposure of ≈ 500 ksecs distributed over a temporal baseline of ≈ 1240 days.

All the observations were carried out in the photon counting (PC) data mode. We began our analysis with the level-1 raw XRT event files (data as stored in the *Swift* archive). Each of the event files was reduced with the standard *xrtpipeline* data reduction tool. One crucial consideration during the reduction process was to mitigate the impact of bad pixels/columns on the XRT CCD. When a source is positioned on such pixels, it can lead to an incorrect measurement of the flux. Furthermore, the bad pixels can result in an erroneous estimate of the response (effective area) of the instrument. The University of Leicester's XRT data analysis web page (<http://www.swift.ac.uk/analysis/xrt/exposuremaps.php>) provides a detailed discussion of this problem. The solution is to create exposure maps that account for the presence of bad pixels. We used *xrtexpomap* (*xrtpipeline* with the qualifier *xrtexpomap = yes*) to create exposure maps for each of the individual observations. These exposure maps were then used to correct the light curves (using *xrtlccorr*) and the ancillary response files (effective area) (using *xrtmkarf*) of each of the observations.

As recommended in the XRT's user guide, we only used events with grades 0 - 12 for further processing. We then used *XSELECT* to extract light-curves and

spectra from the individual observations. We extracted source light-curves and spectra from a circular region of radius 47.1" centered around the source. This particular value was chosen to include roughly 90% (at 1.5 keV) of the light from the source (estimated from the fractional encircled energy of the XRT). A background region, free of other sources, was extracted in a nearby region. Given the low individual exposure times, to better estimate the background, we chose a circular region of twice the radius of the source, i.e., four times the source area. The same source and background region was used for all the 305 observations. We present results from detailed timing and spectral analysis in the following sections.

5.3 Results: Timing Analysis

This section is divided into four parts: (1) we show the complete (≈ 1240 day temporal baseline) *Swift*/XRT X-ray (0.3-8.0 keV) light curve of NGC 5408 X-1, highlighting the most prominent features, (2) we compute periodograms (Lomb-Scargle) of two different portions of this complete light curve (one with strong quasi-sinusoidal X-ray modulation and the other with apparently weaker modulation), (3) we estimate the distribution of dips with orbital phase and also construct an epoch folded light curve and finally, (4) we study the energy dependence of the quasi-sinusoidal modulation and the dips.

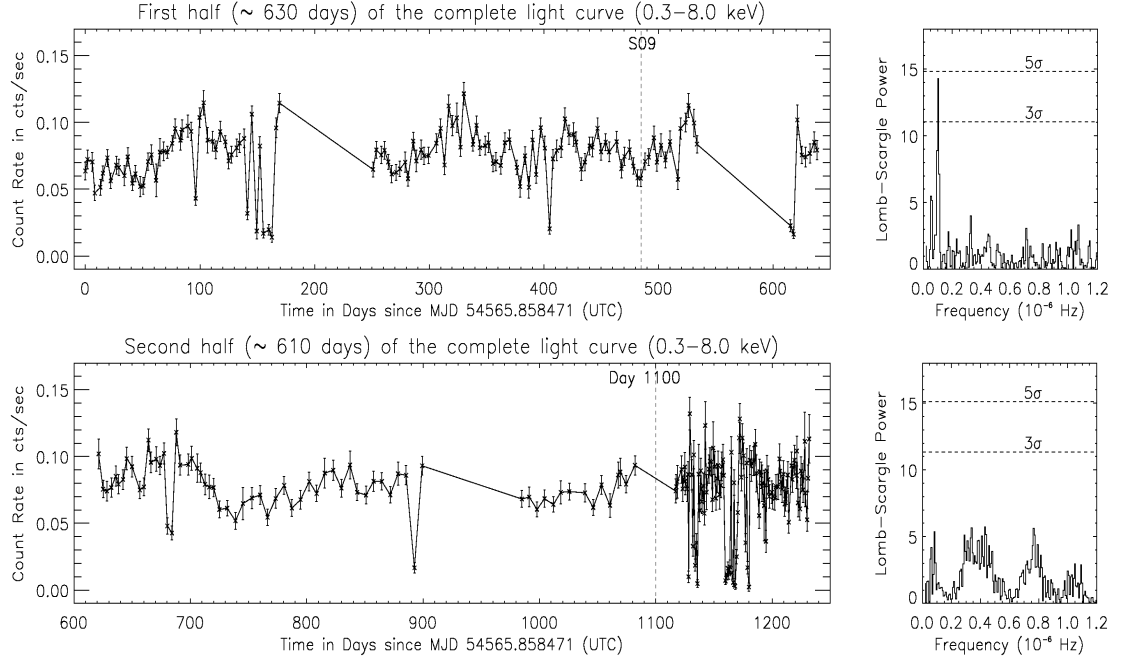


Figure 5.2: *Top Left Panel:* First half (≈ 630 days) of the complete *Swift*/XRT X-ray light curve of the ULX NGC 5408 X-1 in the energy range 0.3–8.0 keV. *Top Right Panel:* The Lomb-Scargle periodogram of the first half of the *Swift*/XRT X-ray light curve of NGC 5408 X-1 (top left panel). The highest peak corresponds to 112.6 ± 4 days. *Bottom Left Panel:* Second half (≈ 610 days) of the *Swift*/XRT X-ray light curve of the ULX NGC 5408 X-1 in the energy range 0.3–8.0 keV. Note the erratic dipping in the last continuous segment of the data. *Bottom Right Panel:* The Lomb-Scargle periodogram of the second half of the complete *Swift*/XRT X-ray light curve of NGC 5408 X-1 (bottom left panel). Note the difference between the two periodograms: there is no statistically significant period detected during the second half of the light curve.

5.3.1 X-ray Light Curve

For each observation, we combined all the data to obtain an average source and background count rate. The light curve of NGC 5408 X-1 in the 0.3–8.0 keV energy range is shown in Figure 5.1. The background count rate in the same energy range is also shown (red data points with black error bars). The background is almost always negligible compared to the source count rate. Roughly 40% of these

observations, i.e., the first 113 observations of the present dataset, were analyzed by Strohmayer (2009). The vertical line marked as Strohmayer (2009) indicates the end of the observations used by Strohmayer (2009) (see Figure 5.1). Strohmayer (2009) reported a 115.5 day period in this data and concluded that it likely represents the orbital period of the binary. The additional data provides new insights about the system. A prominent feature of the full light curve is the quasi-periodic recurrence of deep, sharp X-ray dips (though with non-zero X-ray intensity during the dip minima). These dips are highlighted with green circles in Figure 5.1. With the available temporal baseline of ≈ 1240 days, we detected five epochs of dips that recur roughly every 243 days. The approximate time intervals between the dips are 251 days, 211 days, 276 days and 235 days.

5.3.2 Timing Evidence for weakening of the 115 day modulation

In this section we present evidence for weakening of the 115.5 day quasi-sinusoidal X-ray modulation during the second half (\approx last 600 days) of the light curve shown in Figure 5.1. We started our analysis by dividing the light curve into roughly two equal segments. We then directly compared the Lomb-Scargle periodograms (Scargle 1982; Horne & Baliunas 1986) of the two segments. We used all the photons in the 0.3 - 8.0 keV energy range for this analysis. The two periodograms with their respective light curves are shown in Figure 5.2. The top left panel of the plot shows the light curve of the first half of the complete light curve (first half of Figure 5.1) and the top right panel shows the Lomb-Scargle periodogram of this

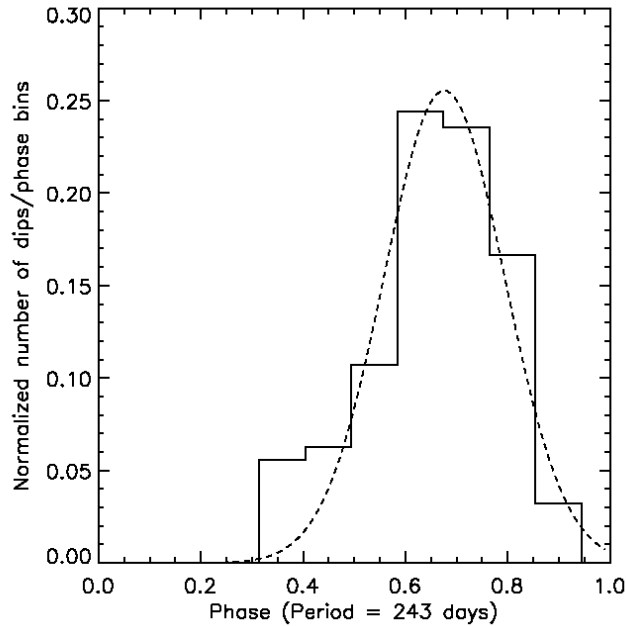


Figure 5.3: Frequency of the sharp dips as a function of the orbital period (243 days). It is normalized by dividing each value by the number of times each phase bin was observed. A total of 27 dips were detected. 11 phase bins were used for the above distribution. The best-fit Gaussian is also shown with a dashed line.

segment with confidence limits overlaid. The bottom left panel shows the light curve of the second half of Figure 5.1 (note the x-axis) and the bottom right panel shows the periodogram of the second half of the complete light curve. The highest peak in the periodogram of the first half of the light curve (top right panel of Figure 5.2) corresponds to a period of 112.6 ± 4 days. This is consistent with the value reported by Strohmayer (2009) (also see Han et al. 2012). Furthermore, such a peak is not evident in the periodogram of the second half of the data. We note that the reason for this difference is unlikely to be purely statistical as the two portions of the light curve have comparable signal-to-noise ratios, temporal baseline (≈ 600 days each) and sampling rate (with the exception of the last continuous segment of the light

curve which has a higher sampling rate of \approx once per day). It is very likely that the drop in the amplitude of the modulation in the second half of the light curve is physical.

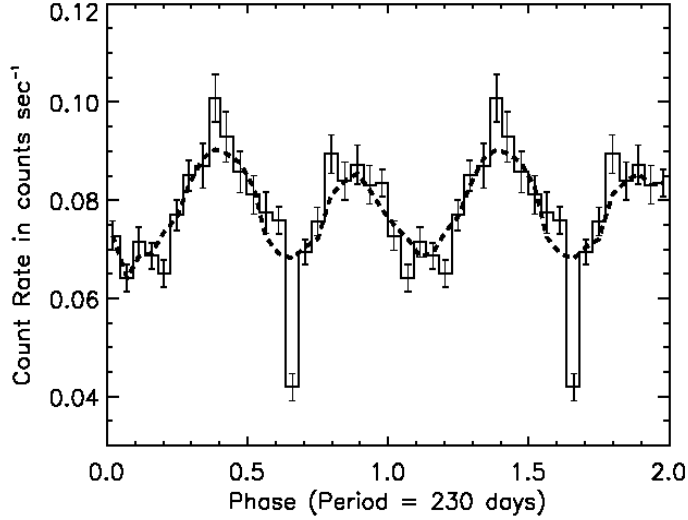


Figure 5.4: The epoch folded (period = 230 days) X-ray (0.3-8.0 keV) light curve of NGC 5408 X-1. A total of 22 phase bins per cycle were used and two cycles are shown for clarity. Also overplotted is a running average curve to guide the eye. Each point is an average of 5 neighboring bins. Both the smooth components (period of 115.5 days) and the sharp dips (quasi-period of 243 ± 23 days) can be clearly seen.

5.3.3 Dip distribution and the folded light curve

We have detected a total of 27 dips (see Figure 5.1). Each of these dips was assigned a phase assuming a period of 243 days, the average time interval between successive epochs of dipping. A normalized distribution of the phases of these dips is shown in Figure 5.3. A normalized distribution was obtained by dividing each value by the number of times each phase bin was observed. This was done to eliminate the bias of preferentially sampling certain phase bins. Since the absolute orbital phase

of the system is not known we arbitrarily assign the zero phase to correspond to the start of the monitoring observations. One can see that the dip phase distribution is roughly Gaussian with a width (FWHM) of ≈ 0.24 .

Another analysis tool to understand the nature of the modulations is epoch folding of the light curve. In the case of NGC 5408 X-1, we have detected five epochs of sharp dips. If these are associated with the orbital period of the binary then the implied period is likely in the range 243 ± 23 days. The variance (23 days) on this value is rather large, thus, the precise value of the orbital period to use for folding the data is not known. Therefore, we used values between 220 - 270 days and then chose the value that resulted in the highest modulation amplitude. This value is 230 days. Furthermore, it was noted previously that the smooth, quasi-sinusoidal modulation disappears/weakens in the latter half of the data. Therefore, we used only the portion of the complete light curve that shows strong evidence for both components, i.e., the first ≈ 700 days of the data. The epoch folded light curve using all the photons in the 0.3-8.0 keV X-ray band is shown in Figure 5.4, and one can clearly see both modulations.

5.3.4 Energy dependence of the X-ray modulations

5.3.4.1 Energy-dependent quasi-sinusoidal modulation

Using only part of the present dataset, Strohmayer (2009) reported that the amplitude of the quasi-sinusoidal X-ray modulation was energy dependent, with the modulation amplitude decreasing with increasing energy. Here we attempt to

systematically quantify the variability as a function of energy. The procedure we carry out is as follows. We obtain folded light curves in different energy bands. More specifically, keeping the upper limit of the bandpass constant at 8.0 keV, we vary the lower limit of the bandpass from 0.3 to 2.0 keV. Again, since the 115.5 day modulation weakens during the later half of the monitoring we used only the first ≈ 700 days of data. A few folded profiles along with the best-fitting model (solid line) are shown in Figure 5.5. Two cycles are shown for clarity. Here we used only 13 phase bins per cycle as our goal is to model only the overall quasi-sinusoidal modulation and not to study the subtle features within the modulation profiles.

To each of these profiles we fit a model that includes two Fourier components (the fundamental and the first harmonic), i.e., $I = A + B\sin 2\pi(\phi - \phi_0) + C\sin 4\pi(\phi - \phi_1)$. All the fits give acceptable values of reduced χ^2 (≈ 1 with 8 degrees of freedom). The fractional amplitude for such a model is defined as $f_{amplitude} = (max(I) - min(I))/(max(I) + min(I))$, and is an indicator of the amount of variability in the source in the given energy range. Figure 5.6 shows the variation of the fractional amplitude (y-axis) as a function of the lower limit of the bandpass considered (x-axis). Clearly, the fractional amplitude of the X-ray modulation is dependent on the energy range under consideration. The amplitude decreases with increasing energy. These results are consistent with those reported by Strohmayer (2009).

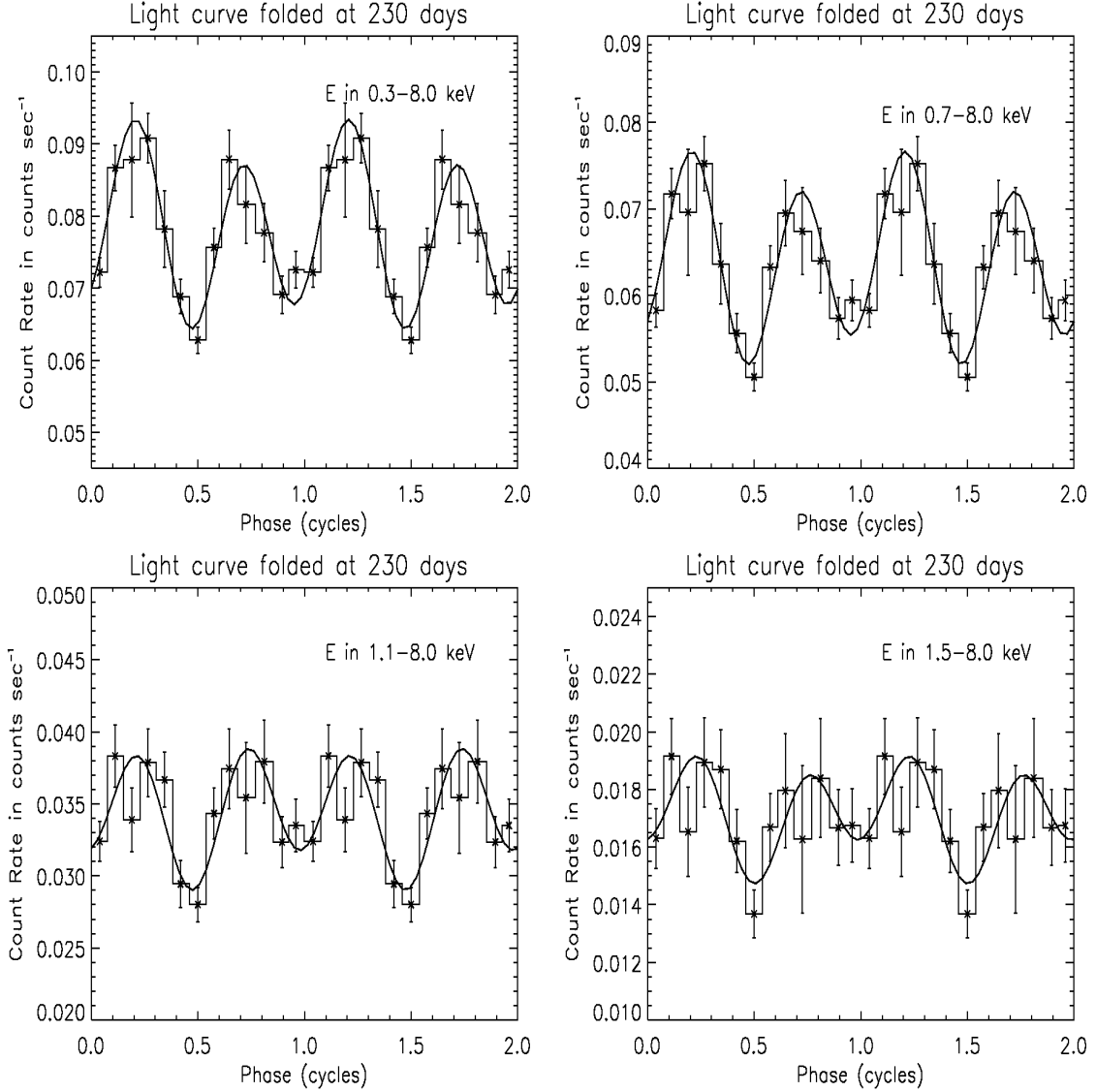


Figure 5.5: The epoch folded light curves of NGC 5408 X-1 in varying energy bands. The light curves in the energy range 0.3-8.0 keV, 0.7-8.0 keV, 1.1-8.0 keV and 1.5-8.0 keV are shown in the top left, top right, bottom left and the bottom right panels, respectively. In each case, we used 13 phase bins per cycle and two cycles are shown for clarity. To each of these profiles we fit a model that includes two Fourier components (the fundamental and the first harmonic), i.e., $I = A + B\sin 2\pi(\phi - \phi_0) + C\sin 4\pi(\phi - \phi_1)$. The best fitting curve is overlaid (solid curve). Clearly, the modulation amplitude decreases with increasing energy.

5.3.4.2 Energy independent or dependent sharp dips?

To study the energy dependence of the dips, we first extracted the hardness ratio during these dips and elsewhere. We define this as the ratio of the count rate in the hard band (1.0-8.0 keV) to the soft band (0.3-1.0 keV). The top panel of Figure 5.7 shows the hardness ratio as a function of time (in days). The middle and the bottom panels show the light curves in the soft (0.3-1.0 keV) and the hard (1.0-8.0 keV) bands, respectively. Owing to the lower count rates during the dips, the error bars on the hardness ratio are large. It is not clear from these plots alone whether the dips from NGC 5408 X-1 are energy dependent. To explore further we obtained an average hardness ratio of the dips before and after day 1100. These values are 1.18 ± 0.17 and 0.95 ± 0.19 , respectively. Within the error bars they are not only consistent with each other, but are also consistent with the average value of the non-dip observations. This suggests that the X-ray dips are largely energy-independent.

5.4 Results: Spectral analysis

This section is divided into two parts: (1) we investigate the differences in the spectra derived from two different portions of the complete light curve, providing evidence for a change in the spectrum of the source and (2) we compare the average X-ray spectrum of the dips with the spectra derived from the rest of the observations.

Table 5.1: Summary of the best-fitting model parameters of the X-ray modulation profiles of NGC 5408 X-1

Bandpass (keV)	A ¹ (10 ⁻²)	B ¹ (10 ⁻²)	ϕ_0^1	C ¹ (10 ⁻²)	ϕ_1^1	$f_{amplitude}^2$	χ^2/dof
0.3-8.0	7.82 ± 0.09	3.57 ± 0.13	0.88 ± 0.05	-1.20 ± 0.13	1.34 ± 0.01	0.184 ± 0.021	11.6/8
0.5-8.0	7.55 ± 0.09	3.76 ± 0.14	0.91 ± 0.05	-1.25 ± 0.13	0.84 ± 0.01	0.196 ± 0.021	13.4/8
0.7-8.0	6.40 ± 0.09	2.87 ± 0.11	0.86 ± 0.07	-1.03 ± 0.12	0.84 ± 0.01	0.191 ± 0.023	11.7/8
0.9-8.0	4.89 ± 0.08	1.71 ± 0.08	0.79 ± 0.11	0.68 ± 0.11	1.09 ± 0.01	0.163 ± 0.025	7.9/8
1.1-8.0	3.45 ± 0.06	1.40 ± 0.07	0.70 ± 0.11	0.41 ± 0.08	0.60 ± 0.01	0.144 ± 0.028	12.7/8
1.3-8.0	2.39 ± 0.05	1.21 ± 0.05	0.71 ± 0.10	0.28 ± 0.07	0.60 ± 0.02	0.147 ± 0.032	9.8/8
1.5-8.0	1.71 ± 0.04	0.08 ± 0.04	0.81 ± 0.12	-0.16 ± 0.06	-0.13 ± 0.03	0.130 ± 0.039	8.5/8
1.7-8.0	1.29 ± 0.04	0.08 ± 0.04	0.81 ± 0.11	-0.12 ± 0.05	-1.13 ± 0.03	0.139 ± 0.045	6.3/8
2.0-8.0	0.90 ± 0.03	0.07 ± 0.03	0.78 ± 0.10	0.07 ± 0.03	0.61 ± 0.04	0.132 ± 0.050	6.9/8

¹We fit the X-ray modulation profiles with a model consisting of two Fourier components. The mathematical form of the model is shown below:

$$I = A + B\sin 2\pi(\phi - \phi_0) + C\sin 4\pi(\phi - \phi_1)$$

where, A is the mean count rate while B and C are the amplitudes of the fundamental and the first harmonics, respectively.

²This parameter is the fractional modulation amplitude and gives a quantitative measure of the amount of variation in the pulse profile. This is defined as follows:

$$f_{amplitude} = \frac{I_{max} - I_{min}}{I_{max} + I_{min}}$$

5.4.1 Spectral evidence for a change in the absorption

In this section we investigate the differences in the average spectra of the source before and after day 1100. We chose this epoch because of the apparent increase in the frequency of dips compared to the earlier parts of the light curve. For this purpose we used all but the dip observations, i.e., the observations with count rate (0.3-8.0 keV) lower than $0.045 \text{ counts sec}^{-1}$ were excluded. The number of counts in any individual observation is too low (a few 10s of counts) to extract a meaningful spectrum. This necessitated combining the individual observations to obtain an average spectrum. We did this for all observations both preceding and following day 1100, resulting in two spectra for comparison. We used the FTOOL *sumpha* to combine the individual spectra. The two spectra in the X-ray energy range of 0.5-8.0 keV are shown in Figure 5.8. The average spectrum prior to day 1100 is shown in black while the data from after day 1100 is shown in red. Both these spectra were binned to ensure a minimum of 50 counts in each spectral bin.

To quantify the spectra we fit them with a model that is often used to describe the X-ray spectra of accreting black hole binaries: a multi-colored disk and a power law, all modified by photoelectric absorption. This same model has been used to fit the high-resolution ($\approx 100,000$ counts) *XMM-Newton* spectra of NGC 5408 X-1 (Strohmayer et al. 2007; Dheeraj & Strohmayer 2012). We used the XSPEC (Arnaud 1996) spectral fitting package to fit all our spectra. In terms of XSPEC models, we used *phabs*(diskpn+pow)*. The X-ray spectrum of the dips (green points in Figure 5.8) suffers from significant statistical uncertainty below 0.6 keV. Therefore, we

used the energy range of 0.6-8.0 keV for its spectral modeling. To be consistent across all the X-ray spectra (as we will be comparing them directly with each other) we chose the same energy range to model the two average, non-dip spectra. The results of the spectral fits are summarized in Table 5.2.

Even without detailed modeling it can be seen straightaway that there are significant differences between the two spectra below 1.5 keV (black and red symbols in Figure 5.8). A closer look at the unfolded spectra reveals that the disk black body component dominates at energies below 2 keV while the powerlaw component dictates the nature of the spectrum at higher energies; and the photoelectric absorption is stronger at lower energies. Therefore, the apparent differences between the two spectra can either be due to a change in the absorption column density (*phabs*) or to changes in the disk properties, viz., the disk temperature, and/or the disk normalization. The quality of the data does not allow us to independently constrain each model's parameters. To break this degeneracy, either one of the *diskpn* model parameters (the disk temperature or the disk normalization) or the column density had to be frozen. A careful analysis of the spectra reveals stronger statistical evidence for a varying column density than varying disk properties.

To illustrate this we simultaneously, but independently, fit the model to both the spectra (without freezing any model parameters except for the inner radius of the accretion disk). We then obtain confidence contours (χ^2) between the column densities, the disk temperatures and the disk normalizations of the spectra before and after day 1100. These confidence contours are shown in Figure 5.9. The top panel shows the confidence contours between the column density of hydrogen prior

Table 5.2: Summary of the spectral modeling of NGC 5408 X-1. Best-fitting parameters for the *phabs*(diskpn+pow)* model are shown.

<i>phabs*(diskpn+pow)</i> [†]							
Dataset	n_H^a	$N_{disk}^b (\times 10^{-2})$	Γ^c	$N_{pow}^d (\times 10^{-4})$	$\text{Flux}_{0.6-8keV}^e$	Flux_{Disk}^f	χ^2/dof
Average Spectrum Before day 1100	$0.30^{+0.02}_{-0.02}$	$1.57^{+0.22}_{-0.27}$	$2.96^{+0.07}_{-0.07}$	$7.69^{+0.49}_{-0.48}$	$3.68^{+0.21}_{-0.23} \times 10^{-12}$	$1.69^{+0.29}_{-0.33} \times 10^{-12}$	233/179
Average Spectrum After day 1100	$0.44^{+0.04}_{-0.04}$	$4.27^{+0.83}_{-0.86}$	$2.97^{+0.17}_{-0.15}$	$8.64^{+1.42}_{-1.19}$	$6.71^{+0.70}_{-0.77} \times 10^{-12}$	$4.35^{+0.89}_{-0.77} \times 10^{-12}$	112/87
Average Dip Spectrum	$0.31^{+0.15}_{-0.18}$	$0.45^{+0.54}_{-0.42}$	$2.92^{+0.61}_{-0.53}$	$1.78^{+1.05}_{-0.70}$	$0.96^{+0.62}_{-0.48} \times 10^{-12}$	$0.51^{+0.82}_{-0.82} \times 10^{-12}$	17/17

^aTotal column density of hydrogen along the line of sight including the Galactic extinction (in units of 10^{22}cm^{-2}). We used the *phabs* model in XSPEC. ^bThe normalization of the disk component. We used the *diskpn* model in XSPEC. The inner radius of the disk was fixed at $6GM/c^2$. The disk temperature was fixed at 0.149 keV to avoid parameter degeneracy (see text). ^cThe photon index of the power law. ^dThe normalization of the power law component. We used *pow* model in XSPEC. ^eThe total unabsorbed X-ray flux (in units of $\text{ergs cm}^{-2} \text{s}^{-1}$) in the energy range of 0.6-8.0 keV. ^fThe disk contribution to the total X-ray flux (in units of $\text{ergs cm}^{-2} \text{s}^{-1}$) in the energy range of 0.6-8.0 keV.

to day 1100 (X-axis) and after day 1100 (Y-axis). Similarly, the bottom left and the bottom right panels show the contours between the disk temperatures and the disk normalizations, respectively. In all the cases, the black, the red and the green represent the 1σ , 2σ and the 3σ confidence contours, respectively. In each case, the diagonal line shows the locus of points where the value on the X-axis equals the value on the Y-axis.

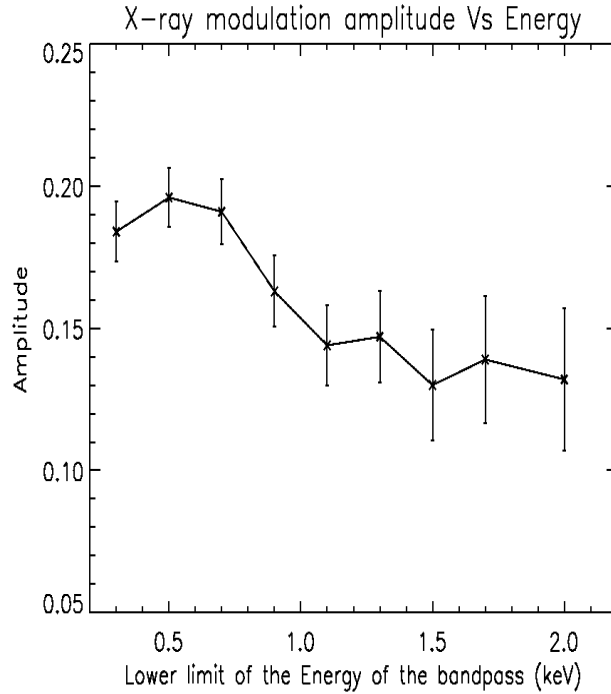


Figure 5.6: The fractional amplitude of the smooth component of the X-ray modulation as a function of the lower limit of the band pass is shown. The upper limit of the bandpass was fixed at 8 keV. The fractional amplitude of the mathematical form used to model the epoch folded light curves of NGC 5408 X-1 (Figure 5.4) is defined as $f_{amplitude} = (max(I) - min(I))/(max(I) + min(I))$, where I is the X-ray count rate.

The amount of deviation of the confidence contours from this line indicates the significance of the variation of a given parameter between the two epochs. In other words, the larger the deviation the stronger is the evidence for a change in

the given parameter. Clearly, the statistical evidence for an increase in the column density after day 1100 is very strong (top panel: strong deviation from the straight line) compared to that for changes in the disk temperature (bottom left panel) and the disk normalization (bottom right panel). In addition, the source has been observed on multiple occasions with *XMM-Newton* over the past ten years. The disk temperature on those occasions has remained roughly constant (Soria et al. 2004; Strohmayer & Mushotzky 2009; Dheeraj & Strohmayer 2012). Furthermore, in accreting galactic black hole binaries, changes in the accretion disk temperature are often accompanied by significant variations in the X-ray light curve (McClintock & Remillard 2006). Clearly, this is not seen in the light curve of NGC 5408 X-1. These arguments suggest that the disk temperature has likely remained constant. Therefore, for subsequent analysis we assumed a constant disk temperature of 0.149 keV, the average value reported from the analysis of the high-quality *XMM-Newton* data (Dheeraj & Strohmayer 2012). The model then gives a reasonable fit in both cases (before and after day 1100) with reduced χ^2 of 1.3 (179 degrees of freedom) and 1.3 (87 degrees of freedom). The best-fitting model parameters for the two average spectra are shown in the first and the second row of Table 5.2, respectively.

The most prominent difference between the two spectra is the amount of photoelectric absorption. The total hydrogen column density before and after day 1100 was $0.30_{-0.02}^{+0.02} \times 10^{22} \text{cm}^{-2}$ and $0.44_{-0.04}^{+0.04} \times 10^{22} \text{cm}^{-2}$, respectively. That is, the latter X-ray spectrum is more absorbed than the former. The estimated total unabsorbed flux in the 0.6-8.0 keV range before and after day 1100 is $3.7_{-0.2}^{+0.2} \times 10^{-12} \text{ergs cm}^{-2} \text{s}^{-1}$ and $6.7_{-0.8}^{+0.7} \times 10^{-12} \text{ergs cm}^{-2} \text{s}^{-1}$, respectively. This suggests a factor of 2 in-

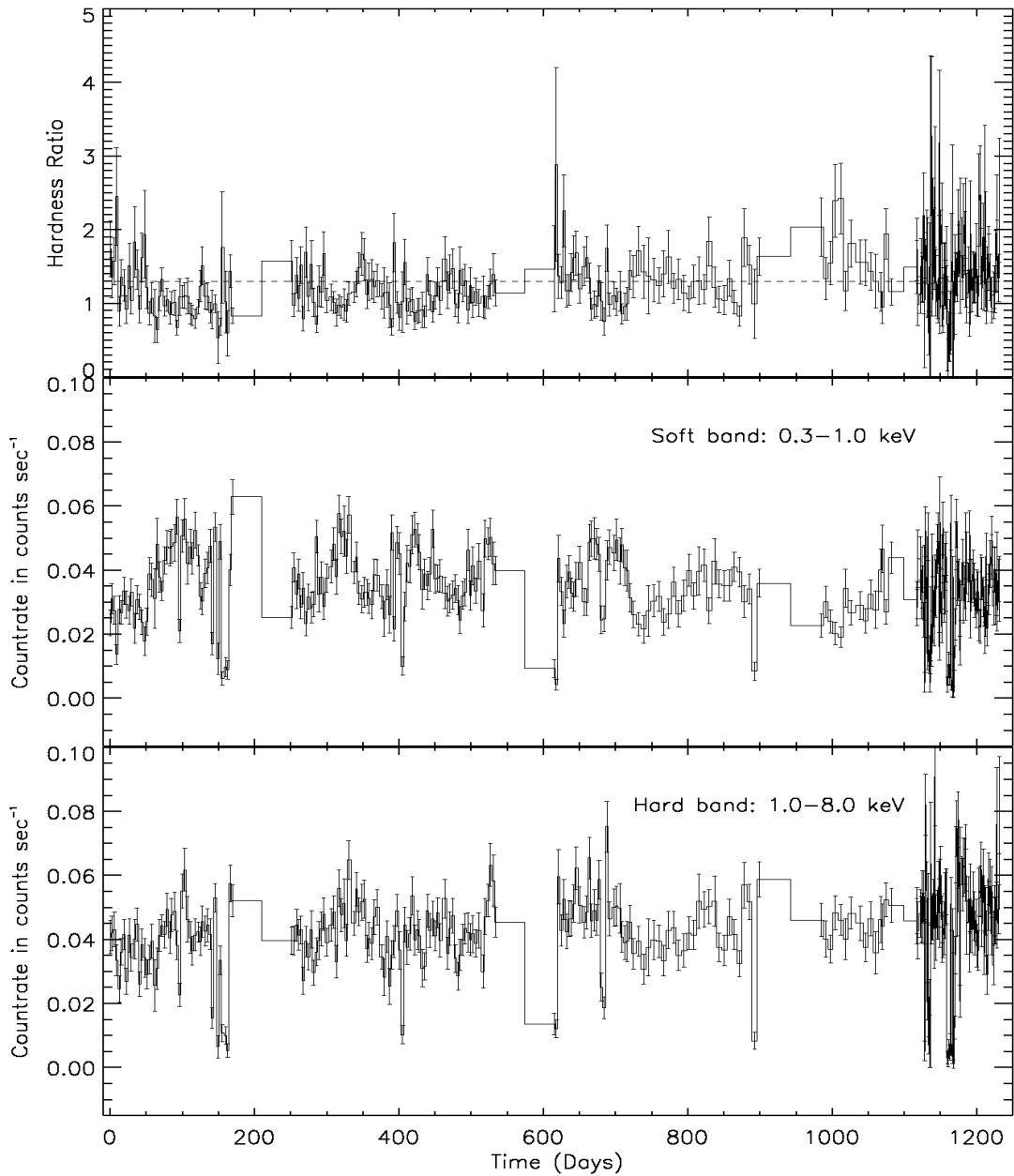


Figure 5.7: *Top panel:* Time history of the hardness ratio (ratio of the count rate in the hard band (1.0-8.0 keV) to the soft band (0.3-1.0 keV)). The mean value is indicated by the dashed line. *Middle panel:* The light curve of the source in the soft band, i.e., 0.3-1.0 keV. *Bottom panel:* The light curve of the source in the hard band, i.e., 1.0-8.0 keV.

crease in the unabsorbed X-ray flux during the last continuous segment of the light curve. Another important thing to note is the fraction of the disk contribution to the total flux before and after day 1100. The values are $1.7_{-0.3}^{+0.3} \times 10^{-12} \text{ergs cm}^{-2} \text{s}^{-1}$ and $4.6_{-0.8}^{+0.9} \times 10^{-12} \text{ergs cm}^{-2} \text{s}^{-1}$, respectively. This implies that the disk fraction of the total X-ray flux (0.6-8.0 keV) before and after day 1100 is $46 \pm 9\%$ and $68 \pm 15\%$, respectively. In other words, the latter spectrum appears more disk-dominated.

5.4.2 Spectra during the sharp dips versus elsewhere

The dips detected here occur both prior to and after day 1100 (see Figure 5.1); and the individual dip observations have too few counts (a few 10s) to extract meaningful spectra. However, it was noted earlier that the average hardness ratio of both the dips before and after day 1100 are comparable, suggesting a plausible common physical origin. Therefore, we combined all the dip observations (both prior to and after day 1100) and obtained an average dip spectrum. This is shown in Figure 5.8 (green data points) along with the two other average spectra. The spectrum was binned to ensure a minimum of 25 counts in each spectral bin.

We began by fitting the dip spectrum with the same model (*phabs*(diskpn+pow)*) used to fit the two spectra described in the previous section. This model gives a good fit with a reduced χ^2 of 1.0 (17 degrees of freedom). The best-fit parameters are shown in the last row of Table 5.2. We find that the best-fit parameters of the dip spectrum are consistent with the values for the two average non-dip spectra derived earlier. This is also consistent with

the simpler hardness ratio analysis, i.e., the dips are consistent with being energy independent.

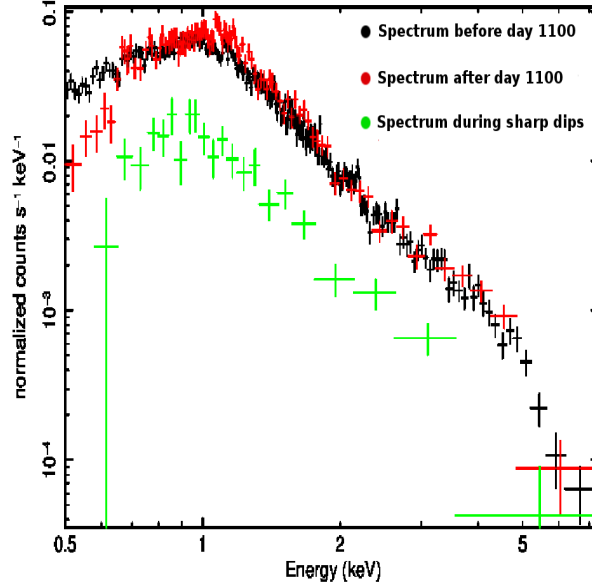


Figure 5.8: The *Swift*/XRT spectra of NGC 5408 X-1 in the energy range 0.5-8.0 keV. The *black* points show the average spectrum prior to day 1100 (as marked by the vertical line in Figure 5.1). Shown in *red* is the average spectrum of the source after day 1100 epoch. There are clear differences between the two spectra, especially at lower energies (below 1.5 keV). The *green* data points denote the average spectrum during the sharp dips. The two spectra, i.e., the spectra before and after day 1100, are binned to ensure a minimum of 50 counts per spectral bin, while the dip-spectrum is binned to ensure a minimum of 25 counts per spectral bin.

The dip spectra of X-ray binaries are often characterized using more complex models involving either an absorbed-plus-unabsorbed (hereafter, A+U) approach (e.g., Parmar et al. 1986, Courvoisier et al. 1986) or a progressive covering approach (e.g., Church et al. 1997, 1998, 2001). To explore the A+U approach we used the following model in *XSPEC*, $phabs1*const1*(diskpn+powerlaw) + phabs2*const2*(diskpn+powerlaw)$, where the first and second terms represent the unabsorbed and absorbed components, respectively. In this case the only free

parameters are the two normalization constants (*const1* and *const2*) and the column density associated with *phabs2*. The parameters describing the shape of the spectrum are all fixed at the average best-fit values derived from the two non-dip spectra (first and second rows of Table 5.2). This model gives an acceptable fit with a reduced χ^2 of 0.9 with 19 degrees of freedom. The best-fit values of the normalization of the unabsorbed component, normalization of the absorbed component and the column density of the absorbed component are 0.2, 4.1×10^{-4} and $2.7 \times 10^{22} \text{cm}^{-2}$, respectively. A simple interpretation in the context of this model is that during dips the direct X-ray emission is completely obscured/absorbed, and what remains is largely scattered (in an energy independent fashion) into our line of sight from more extended regions around the source.

Partial covering models have been quite successful in describing the spectral evolution with intensity during dipping (see for example Church et al. 1998). In this approach the spectral evolution as dipping becomes stronger is accounted for by the progressive covering of, typically, one of the spectral components. The implication is that the progressively covered component is spatially extended compared to the other component. A perceived strength in favor of these models is that scattering—the details of which are not often specified in the A+U approach—is not required. In the case of low-mass X-ray binary neutron star dippers it is the coronal (power-law) component that is progressively covered, whereas in some black hole systems successful modeling requires partial covering of the thermal (disk black body) component (Church 2001). We found that the dip spectrum of NGC 5408 X-1 could not be well described by progressive covering of either spectral component by itself, but

that progressive covering of the sum of both components provided as good a fit as the A+U modeling. The reason for this is two-fold, 1) the dip spectrum is consistent with being energy independent, that is, it has the same shape as the non-dip spectra, and 2) both spectral components contribute a comparable amount to the total flux. Thus, it is very difficult to partially cover only one component and still maintain the same spectral shape. Partial covering of just the power-law component does a better job than covering of only the *diskpn* component, but in each case the fits are not as good as the A+U case. Covering of the sum of the components provides a good fit. The implication in this case is that the emission components are extended but co-spatial. The dipping then corresponds to complete obscuration of about 4/5 of the extended source (in an average sense over all dips).

The conclusion from either modeling framework is that an absorbed component is not seen directly, only an unabsorbed component. Finally, we note that due to the limited statistical quality of the dip spectrum and the fact that only a single dip spectrum could be meaningfully extracted, it is difficult to be more precise about the exact physical nature of the dipping.

5.5 Discussion

In this chapter we have studied the long-term X-ray variability of the ULX NGC 5408 X-1 using 1240 days of *Swift*/XRT monitoring data. In addition to the periodic (115.5 days), smooth modulation reported by Strohmayer (2009), the source also exhibits quasi-periodic sharp dips that occur on average every 243 ± 23

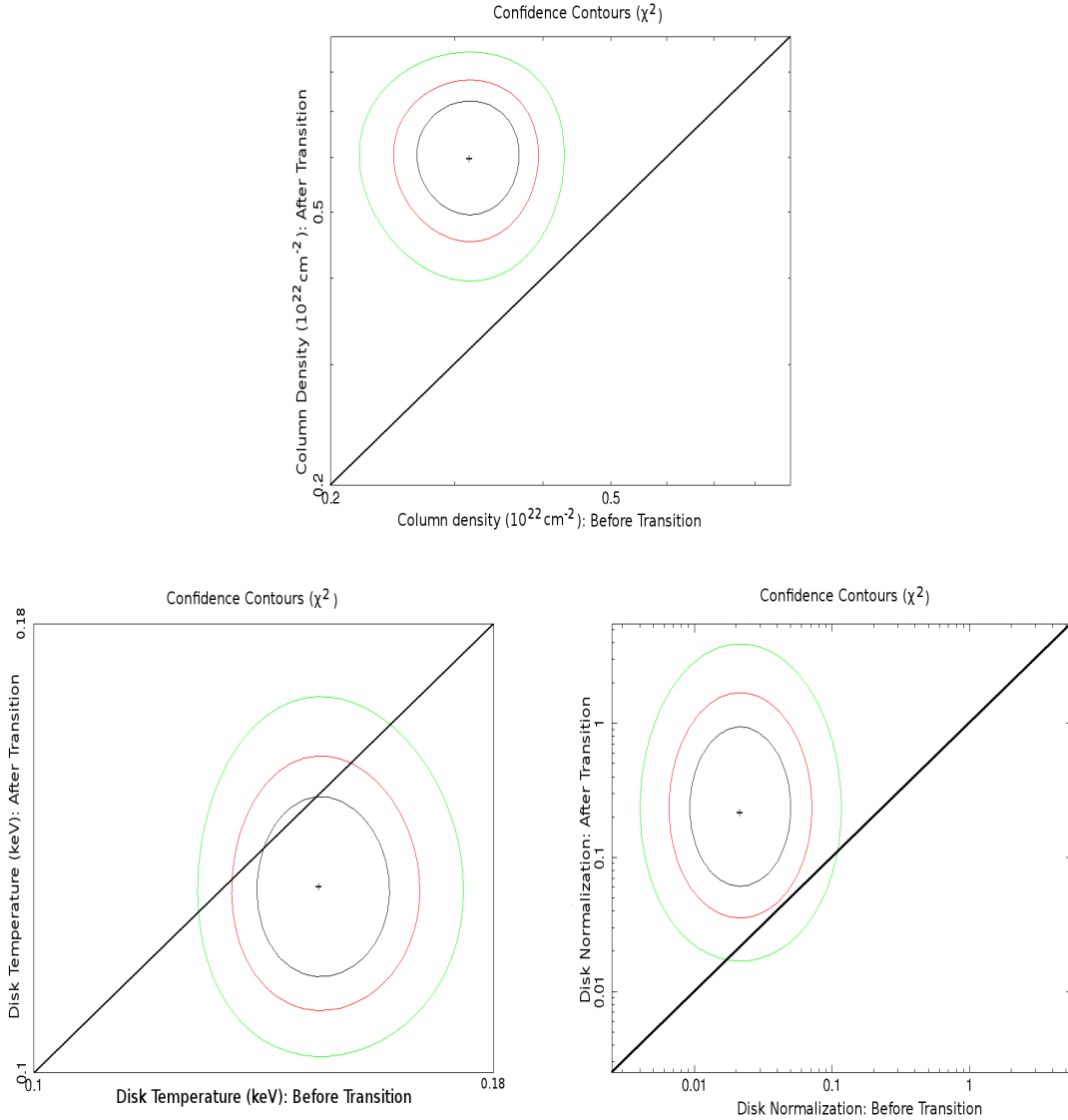


Figure 5.9: *Top Panel:* The confidence contours of the total hydrogen column densities along the line of sight (n_H) before (X-axis) and after (Y-axis) day 1100. *Bottom Left Panel:* The confidence contours of the disk temperatures before (X-axis) and after (Y-axis) day 1100. *Bottom Right Panel:* The confidence contours of the disk normalizations before (X-axis) and after (Y-axis) day 1100. The black, red and the green curves in each panel represent the 1σ , 2σ and the 3σ confidence contours. Contours were obtained from fits to the non-dip spectra in both cases. The straight line in each case represent the locus of all points with $X = Y$. For a given parameter, if the contours do not overlap with this line then that is a strong indication for a change in the parameter value.

days, roughly twice the 115.5 day period. As discussed in §1, such orbit-phase dependent X-ray dipping has been well-studied in the case of accreting X-ray binaries and is usually ascribed to periodic obscuration of the X-ray source by an intervening medium, viz., a bulge at the edge of the accretion disk, the wind from the companion star or the accretion stream. In those cases, dipping has been shown to be an excellent tracer of the orbital motion of the binary. Given that NGC 5408 X-1 is very likely an accreting black hole system, it is conceivable that a similar phenomenon causes the observed dipping. If that were indeed the case, then the detected period of 243 ± 23 days likely represents the orbital motion of the X-ray binary.

NGC 5408 X-1 is the only known ULX system that exhibits two types of dipping behavior, smooth & sharp, simultaneously. The basic properties of the smooth component are: 1) it occupies a significant portion ($\approx 50\%$) of the putative orbital cycle of 243 ± 23 days (see Figure 5.4), 2) it is energy-dependent with the modulation amplitude decreasing with increasing energy (see Figures 5.5 & 5.6) and 3) the modulation amplitude is variable, i.e., the smooth component modulation is weaker during the second half of the *Swift* monitoring data (see Figure 5.2). On the other hand, the sharp X-ray dips detected from NGC 5408 X-1 are not strictly periodic and are distributed over an orbital phase of ≈ 0.24 (see Figure 5.3). In addition, they are consistent with being energy-independent (see Figure 5.8 & Table 5.2). We now discuss these observed properties within the framework of an accreting X-ray binary scenario.

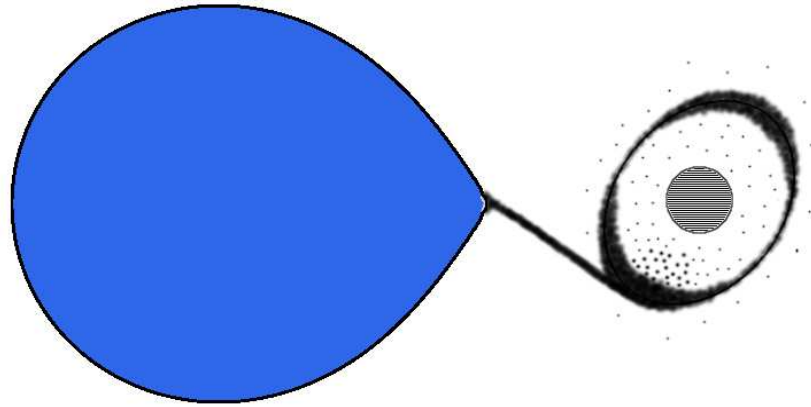
5.5.1 Roche Lobe Accretion: Eccentric accretion disk and stream-disk interaction

Assuming that the recurrence period of the X-ray dips is close to the orbital period of a Roche-lobe filling binary, the density of the companion star in NGC 5408 X-1 can be constrained using the formula, $\rho \simeq 0.2(P_{days})^{-2} \text{ g cm}^{-3}$ (Frank et al. 2002). For a period (P_{days}) of 243 days, this would imply that the companion star has a mean density of $3.4 \times 10^{-6} \text{ g cm}^{-3}$. This value is consistent with a recent study by Grisé et al. (2012), who extracted the UV/optical/NIR spectral energy distribution (SED) of the optical counterpart of NGC 5408 X-1. They find that the SED is consistent with a massive B0I super-giant star. Numerical hydrodynamical simulations of stream-fed accretion in low mass ratio binaries show that the accretion disk can be tidally distorted (Armitage & Livio 1996). This leads to the formation of a secondary bulge in the disk in addition to the primary bulge at the stream-disk impact site. In other words, tidal effects can lead to the formation of two broad bulges above the disk mid-plane along the outer rim of the accretion disk, separated by an orbital phase of ≈ 0.5 (see Figure 5 of Armitage & Livio 1996). This process may explain the observed modulations in NGC 5408 X-1. The modulation profile of the smooth component, including the phase separation between the two peaks, is in accord with the predicted X-ray variations from high inclination X-ray binaries (see the right panels of Figure 6 of Armitage & Livio 1996). Similar double-peaked modulation profiles have also been observed from neutron star low-mass X-ray binaries including X 1916-053 (Smale et al. 1988; Homer et al. 2001),

X 0748-676 (Parmar et al. 1988) and 4U 1822-37 (White & Holt 1982). Again, in those cases the presence of a secondary bulge, presumably due to the tidal effects of the companion, has been suggested. In this context the nature of the accretor (neutron star or black hole) is largely irrelevant, it is simply the tidal effects on the disk that are important in producing a secondary bulge.

Further simulations by Armitage & Livio (1998) show that the fate of the material in the accretion stream after it impacts the disk depends on the cooling efficiency within the shock-heated gas created by the impact. If the cooling is efficient, which is generally the case for low mass accretion rates ($\lesssim 10^{-9} M_{\odot} \text{ yr}^{-1}$) (see Armitage & Livio 1998 for details), the material continues to freely overflow above and below the accretion disk. This ballistic stream will reimpact the disk near the point of its closest approach to the compact source where it forms an obscuring bulge (see also Frank et al. 1987; Lubow 1989). However if the cooling is inefficient which is thought to be the case for high mass accretion rates, the stream-disk interaction leads to a flow that is better described as an “explosion” at the point of the impact, and leads to a more vertically extended distribution of scattered material (clumps: see the bottom panel of Figure 7 of Armitage & Livio 1998). Such clumps could account for the sharp dips observed in NGC 5408 X-1. Given its high luminosity and hence high inferred accretion rate (average X-ray luminosity of $\approx 10^{40} \text{ ergs s}^{-1}$) it is plausible that the cooling at the stream-disk impact site is inefficient. Therefore, one would expect a distribution of splashed material (clumps) around the primary bulge. This is in reasonable agreement with the modulation profile of NGC 5408 X-1 where the sharp dips occur predominantly

Top View



Edge-On View

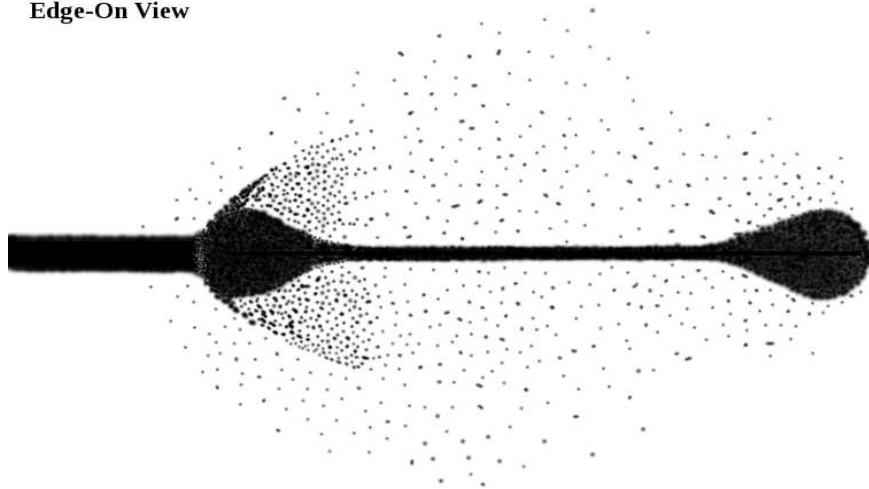


Figure 5.10: An idealized depiction of a possible accretion geometry for NGC 5408 X-1. *Top Panel:* A face-on (top) view of the binary system. The optical star (possibly a B0I supergiant, [Grisé et al. 2012](#)) is shown in blue (left), while the eccentric accretion disk with two obscuring regions is shown on the right hand side. The X-ray source is indicated by a circular region at the center of the disk. *Bottom Panel:* An edge-on view of the accretion disk. The accretion stream from the companion approaches from the left hand side. Again the two bulges are shown. The “clumps”, produced due to the splashing of the accretion stream at the edge of the disk, are also shown (scattered black points). See also Figure 5 of [Armitage & Livio \(1996\)](#) and the bottom panel of Figure 7 of [Armitage & Livio \(1998\)](#).

at one of the minima which is consistent with the phase of the stream-disk impact site (primary bulge).

In summary, the observed modulation profile of NGC 5408 X-1 appears consistent with the predicted variations from Roche-lobe accreting binaries with low mass ratios, $q = M_{donor}/M_{accretor}$ (Armitage & Livio 1996, 1998). The smooth component is produced by absorption/obscuration by the two spatially distinct bulges along the outer rim of the accretion disk while the sharp dips are possibly produced due to absorption by clumps of material produced by the stream-disk impact. A schematic depiction of a possible source geometry for NGC 5408 X-1 based on this scenario is shown in Figure 5.10. The top panel shows the distribution of material in the binary viewed from above (face on) while the bottom panel shows the accretion disk viewed edge-on.

The sharp dips seen in NGC 5408 X-1 appear similar to those observed in the black hole low-mass X-ray binary GRO J1655-40 (Kuulkers et al. 2000), however, GRO J1655-40 does not show a smooth periodic modulation as in NGC 5408 X-1. This may be due to the inclination of GRO J1655-40 ($i = 70.2 \pm 2^\circ$: Greene et al. 2001), as simulations show that the bulge material has a limited extent above the disk. However, stream material splashing on to the edge of the accretion disk is able to reach higher above the plane of the accretion disk (higher than the bulges) so that in principle sharp dips can still occur away from the plane of the accretion disk (Armitage & Livio 1998). While the morphology of the sharp X-ray dips in NGC 5408 X-1 somewhat resembles partial eclipse profiles, we note that this is unlikely to be the case because the sharp dips are not strictly periodic. That is, the large

variance on the dip period (see Figure 5.3) strongly indicates that we are not seeing eclipses.

If these two arguments are correct then a rough constraint on the inclination angle can be derived, as the inclination angle has to be less than some upper limit so that eclipses are not seen but must be large enough so that the absorbing/obscuring effects of the disk bulges are not completely eliminated. Assuming the donor star fills its Roche lobe, an upper limit on the inclination angle (such that eclipses are not seen) can be derived that depends on the orbital period and the mass ratio of the binary (see Eggleton 1983; Rappaport & Joss 1986 for the appropriate formulae). For an orbital period of 243 days with a B0I donor of $\approx 10M_{\odot}$, the upper limits on the inclination are 75° and 85° assuming the compact source is a massive stellar-mass black hole (mass $\approx 50M_{\odot}$: Middleton et al. 2011) or an intermediate-mass black hole (mass $\approx 1000M_{\odot}$: Strohmayer et al. 2009), respectively. If we further assume that the absence of a smooth modulation in GRO J1655-40 provides a rough lower limit of 70° , we obtain an inclination angle for NGC 5408 X-1 in the range from $70 - 85^{\circ}$. While this is based on a number of assumptions we note that it is broadly consistent with inclination angles inferred for other dipping binaries (see Ritter & Kolb 2003).

Finally, we note that while the sharp dips seen in NGC 5408 X-1 are similar to the Type-B dips observed in Cygnus X-1 (see §1 for details on the sharp dips from Cygnus X-1), the high X-ray luminosity and thus high inferred mass accretion rate, is much easier to accommodate via Roche overflow than wind-fed accretion.

5.5.2 Alternative Scenarios

Alternatively, it could be that the observed X-ray modulations from NGC 5408 X-1 are not due to the orbital motion of the X-ray source in a binary (Foster et al. 2010). X-ray modulations on “super-orbital” periods (periods longer than the binary orbital period) of the order of a few days to a few hundred days have been reported from accreting X-ray binaries (e.g., Wen et al. 2006; Sood et al. 2007). In a sub-sample of these sources consisting of Her X-1 ($P_{Superorbit} = 35$ days), SS 433 ($P_{Superorbit} = 164$ days), LMC X-4 ($P_{Superorbit} = 30.4$ days) and SMC X-1 ($P_{Superorbit} \approx 55$ days), it is likely that the observed X-ray modulation is due to the periodic obscuration of the central X-ray source by a tilted, precessing accretion disk. The basic idea here is that the accretion disk is tilted or warped with respect to the orbital plane of the binary. The tidal effects of the companion star then force the accretion disk to precess about an axis normal to the binary orbit. As the tilted disk precesses, the effective area of the disk obscuring the central X-ray source can vary, producing modulations at or near the precession period. Furthermore, the radiation force from the X-ray source can warp the outer regions of the accretion disk (Ogilvie & Dubus 2001; Ogilvie 2002) leading to two spatially distinct density enhancements. This might possibly account for the twin-peaked X-ray modulation curve of NGC 5408 X-1. In summary, the theory of tilted, warped accretion disks may be adaptable to the present scenario to perhaps explain the observed properties.

5.6 Summary

We have presented results from long-term X-ray (0.3-8.0 keV) monitoring of the ULX NGC 5408 X-1 using *Swift*/XRT. Our primary results are: (1) the discovery of sharp, energy-independent dips (a total of 5 dip epochs) in the X-ray intensity that recur roughly every 243 days and (2) the detection of a smooth, quasi-sinusoidal modulation of the X-rays which appears to weaken during the second half of the monitoring program. We interpret these findings in the context of orbital motion in a Roch-lobe overflow binary with a period comparable to the dip-recurrence period (243 ± 23 days; see Figure 5.10), however, it is also possible that a precessing accretion disk (a “super-orbital” phenomenon) can cause a similar X-ray modulation. Further X-ray monitoring of NGC 5408 X-1 with *Swift* is warranted to more firmly establish that the X-ray dips are indeed associated with the orbital period of the binary.

Chapter 6: Can the 62 day X-ray Period of the Ultraluminous X-ray Source M82 X-1 be due to a Precessing Accretion Disk?

6.1 Introduction

With a maximum X-ray luminosity of approximately 10^{41} ergs s^{-1} (Kaaret et al. 2009) M82 X-1 is a remarkably bright ULX. Its average X-ray luminosity of roughly 5×10^{40} ergs s^{-1} combined with quasi-periodic oscillations (QPOs) in the frequency range of 0.04-0.2 Hz suggests that it may contain an intermediate-mass black hole of roughly 100-1000 M_{\odot} (Strohmayer & Mushotzky 2003; Hopman et al. 2004; Portegies Zwart et al. 2005; Dewangan et al. 2006; Mucciarelli et al. 2006; Pasham & Strohmayer 2013b). In addition, as mention earlier in chapter 5, its X-ray intensity varies regularly with a period of 62 days (Kaaret et al. 2006; Kaaret & Feng 2007, KF07 hereafter). This period has been claimed to be the orbital period of the black hole binary system (KF07). Here, we study the properties of this period using new data and present evidence that this modulation may instead be due to the precessing accretion disk of the black hole.

6.2 Data Primer

The data used herein was obtained with the Rossi X-ray Timing Explorer's (*RXTE*'s) proportional counter array (PCA) operating in the *GoodXenon* data acquisition mode. We used data from the monitoring program beginning 2004 September 2 until 2009 December 30 (1945 days), during which M82 was observed roughly once every three days (2-3 ksecs per observation).

We used data from all active proportional counter units (PCUs). For faint sources (net count rates $\lesssim 20$ counts sec^{-1}) like M82, the PCA data analysis guide provided by *RXTE*'s Guest Observer Facility (GOF, <http://heasarc.nasa.gov/docs/xte/recipes/layers.html>) suggests using only the top Xenon layer to maximize the signal to noise ratio. Therefore, we screened our data to include only events from the top layer (layer-1) with both anode chains (Left and Right). In addition, we imposed the following standard filter on the data: $\text{ELV} > 10.0 \ \&\& \ \text{OFFSET} < 0.02 \ \&\& \ (\text{TIME_SINCE_SAA} < 0 \ || \ \text{TIME_SINCE_SAA} > 30) \ \&\& \ \text{ELECTRON2} < 0.1$. Finally, we used the latest SAA history and background model files for our analysis. The screening criteria used here is discussed in detail on NASA/HEASARC's Web page <http://heasarc.nasa.gov/docs/xte/abc/screening.html>.

The PCA observations were divided amongst six proposals (*RXTE* proposal IDs: P20303, P90121, P90171, P92098, P93123, P94123). We used the *rex* script provided by *RXTE*'s GOF to extract individual light curves and energy spectra of the source as well as the background. In addition to the filters described above we

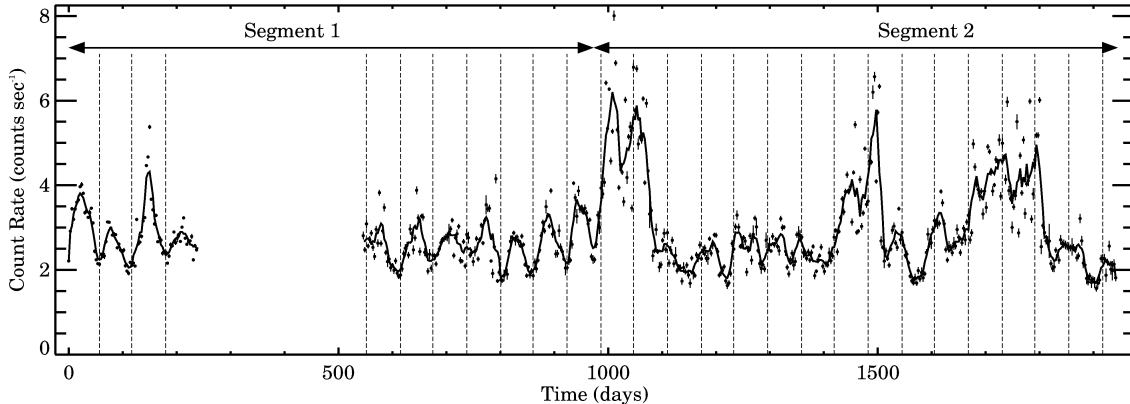


Figure 6.1: Complete *RXTE*/PCA binned X-ray (3-15 keV) light curve of M82 (*solid points*) along with the running average (*solid curve*) that traces the overall X-ray variability of M82. The error bars on the individual data points are also shown. The start time of the light curve is 2004 September 2, 14:26:14.757 UTC. The bin size is 3 days. The vertical lines show the expected minima of the X-ray modulation assuming the 62 day period remains constant throughout the data. The two segments represent data before and after the first major flare that occurs around day 1000.

only used data from channels 0-35 which translates to X-ray events in the energy range 3-15 keV.

6.3 Results

6.3.1 Timing Analysis

From each individual observation we extracted an average¹, background-subtracted, count rate. This resulted in a total of 810 measurements distributed over 1945 days. The complete *RXTE*/PCA 3-15 keV light curve of M82 is shown in Figure 6.1. While the earlier work by KF07 used only the data from day 0 until roughly day 900, i.e., essentially segment 1 of Figure 6.1, this work includes the

¹The mean was taken over all active PCUs using PCU normalizations given by the *RXTE* data analysis guide: http://heasarc.nasa.gov/docs/xte/recipes/pcu_combine.html.

entire *RXTE*/PCA monitoring data of M82.

As an initial test for the stability of the period, we over-plotted vertical lines uniformly separated by 62 days² and coincident with the expected minima of the light curve assuming this period is constant (dashed vertical lines in Figure 6.1). It is clear even by eye that while the vertical lines are coincident with the light curve's minima until the large flare occurring around day 1000, they are offset thereafter. The location of the minima were estimated as follows. We folded the first four cycles of the data at a period of 62 days, i.e., data from day 0 - day 240. We then fit this folded light curve with a model that includes two Fourier components (the fundamental and first harmonic), i.e., $I = A + B\sin 2\pi(\phi - \phi_0) + C\sin 4\pi(\phi - \phi_1)$. The folded light curve (*solid points*) along with the best-fit function (*solid curve*) is shown in the left panel of Figure 6.2. The best-fit model parameters are $A = 2.74 \pm 0.01$, $B = 0.38 \pm 0.01$, $\phi_0 = 1.14 \pm 0.01$, $C = 0.12 \pm 0.01$, $\phi_1 = 1.04 \pm 0.01$ while the best-fit χ^2 value was 1.4 for 1 degree of freedom. If the 62 day modulation were constant throughout the monitoring program then the minima of the best-fit model should track the light curve's minima.

Another way to assess this phase change is to separately fold the segments of the light curve before and after the first large flare (segment 1 and 2 as indicated in Figure 6.1), at the period of 62 days. Therefore, we divided the complete light curve into two segments: 1) prior to the large flare and 2) after the large flare excluding the data during flares. For the first segment we used data from day 0 to day 976 where day 976 represents roughly the epoch of the onset of the flare (see Figure

²The best-fit period reported by KF07 was 62 ± 0.3 days.

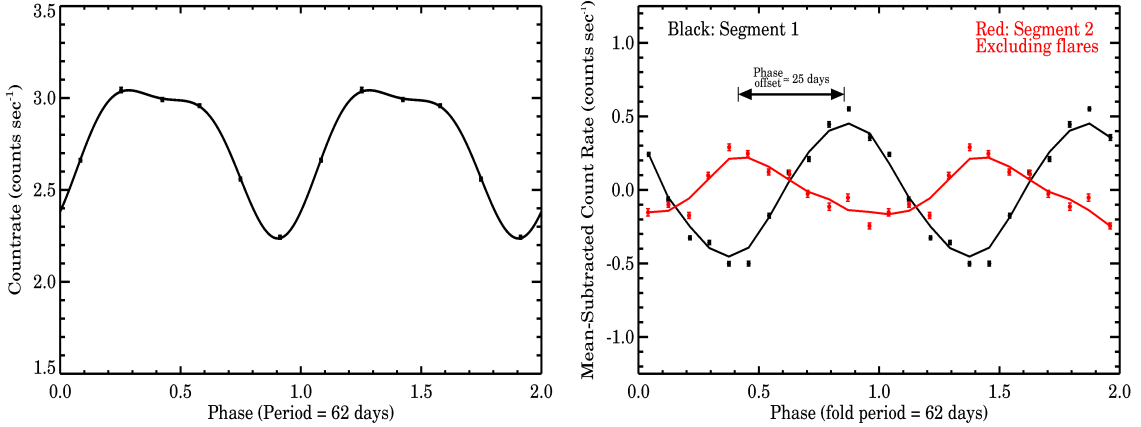


Figure 6.2: *Left Panel:* Folded X-ray (3-15 keV) light curve of M82 (*solid points*) along with the best-fit sinusoid curve (*solid curve*) using only data from day 0 until day 240 (see text). 6 bins per cycle were used and two cycles are shown to guide the eye. *Right Panel:* Mean-subtracted, folded X-ray (3-15 keV) light curves of M82 during segment 1 (black) and segment 2 excluding the flares (red). In each case a total of 12 bins per cycle were used and two cycles are shown for clarity. The error bars on the individual phase bins are also shown. The solid curves represent the running average over three neighboring bins. A phase offset of ≈ 25 days between the two portions of the light curve is evident.

6.1). For the second segment we used all the data from day 976 until the end of the light curve except for the flares. We then transformed the two segments of the light curve to have the same start time. This is essential as a phase difference between the start times of the two segments can manifest as an offset between their folded light curves. We then folded the two segments separately at a period of 62 days³ as found in the earlier work by KF07. The two folded light curves (offset to have zero mean) are shown in the right panel of Figure 6.2. Clearly there is a significant phase offset of roughly 0.4 cycles – equivalent to $0.4 \times 62 \text{ days} \approx 25 \text{ days}$ – between the two portions of the light curve.

³Note that we have constructed a Lomb-Scargle periodogram (Scargle 1982; Horne & Baliunas 1986) of segment 2 and find evidence – although weaker compared to segment 1 – for a power spectral peak that is consistent with a period of 62 days.

It is possible that this phase difference is due to an incorrect choice of the fold period. Considering the uncertainty in the period reported by KF07, the actual value of the period can be in the range (90% confidence) 62 ± 0.3 days. Therefore, we repeated the analysis using various fold periods between 61.7 and 62.3 days. We find that the lag is significant in all the cases with the lag varying from roughly 20 to 30 days (see Figure 6.3). However, if we relax the confidence interval on the best-fit period, we find that one can obtain essentially zero lag between the two segments with a fold period of 60.6 days. We note that this value is 4.7 times the quoted uncertainty, that is, $(1.4/0.3) = 4.7$, away from the best-fit period of 62 days. Since a 90% confidence region is $\approx 1.6\sigma$ (assuming gaussian statistics) from the best value, then one has to go $1.6 \times 4.7 = 7.5\sigma$ from the best period (62 days) in order to cancel the inferred lag. This supports the presence of a real phase shift, but due to the relatively modest number of overall cycles present in the data, a confirmation of a varying period would still be important.

6.3.2 Energy Spectral Analysis

For the purposes of extracting phase-resolved energy spectra we used only data from day zero until prior to the first large flare around day 1000, i.e., segment 1 of Figure 6.1. We made this choice for the following reasons: (1) the 62 day modulation is highly coherent during this portion of the data and (2) the flaring in the second segment likely introduces additional state-related spectral variations (Feng & Kaaret 2010) which could mask any purely phase-related changes.

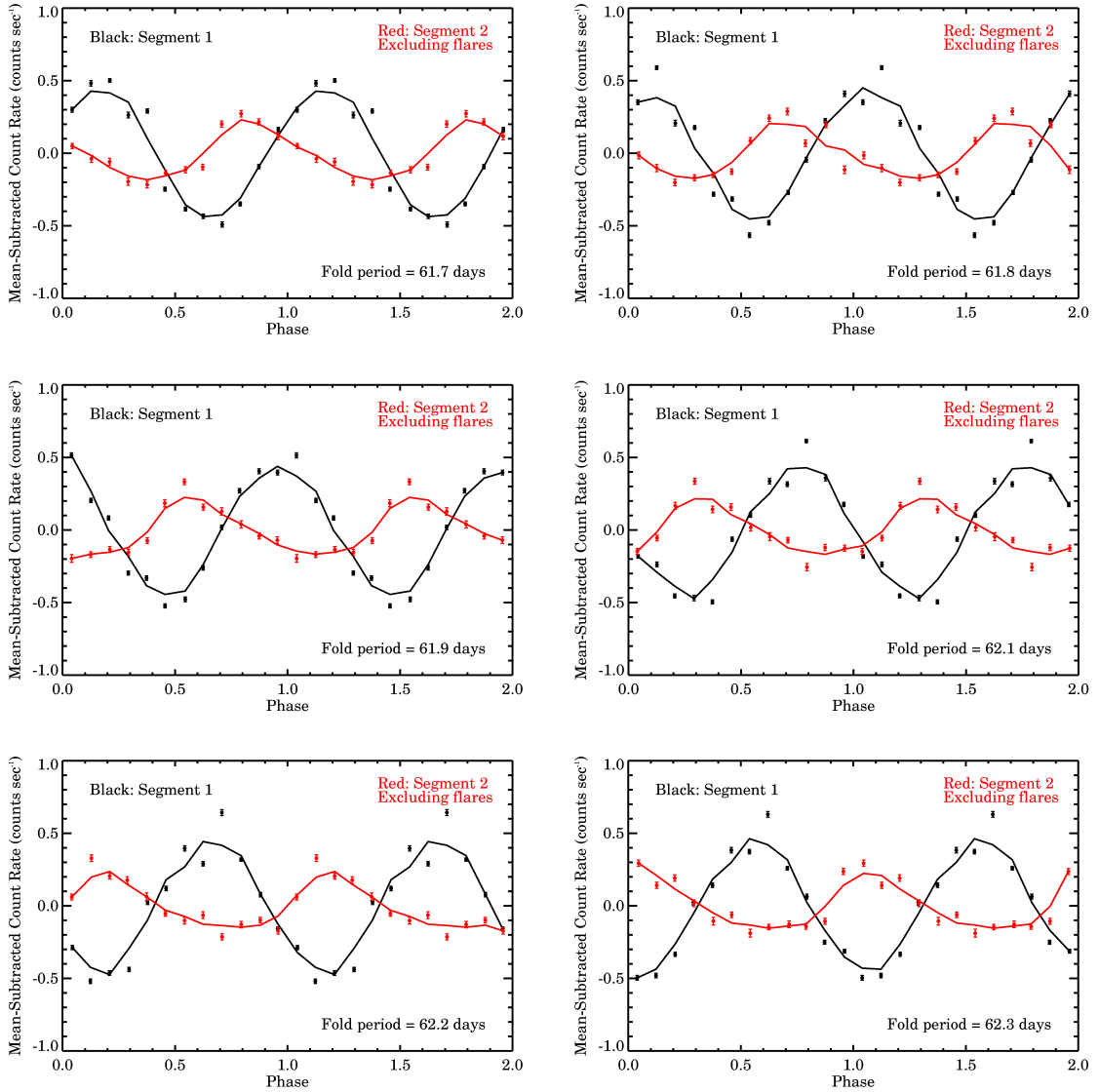


Figure 6.3: Same as the right panel of Figure 6.2 but using various fold periods within the error bar reported by Kaaret & Feng (2007). The fold period used is indicated in each panel (bottom-right). A significant “phase-offset” is evident in each case.

We then extracted the energy spectra of the source and background from each observation in segment 1. Using the tool *pcarsp* we created responses separately for each observation. If multiple PCUs were active in any given observation, we first obtained the source, the background spectra and the responses from individual

PCUs and then combined them to have a single source spectrum, a background spectrum and a response (the individual PCU responses were weighted according to the background-subtracted source counts) per observation. We then divided these observations into six equal-sized phase bins of size 1/6 using a period of 62 days. Using the FTOOL *sumpha* we combined all the source and the background energy spectra in a given phase bin to obtain six average phase-resolved source and background energy spectra. Similarly using the FTOOLS *addrmf* and *addarf*, we created six weight-averaged response matrices and the ancillary response functions, respectively. For each of these twelve response files (six RMFs and six ARFs) weights were assigned according to the total number of background-subtracted counts in a given observation. We then binned the energy spectra to ensure a minimum of 30 counts in each spectral bin.

We modeled each energy spectrum with a blackbody disk, a power-law model, and a gaussian component to account for the weakly broadened Fe K α line. We used the *XSPEC* (Arnaud 1996) spectral fitting package to fit the spectra. In terms of *XSPEC* models, we used *phabs*(diskpn + gauss + pow)*. The spectral resolution of the data does not allow us to constrain the Gaussian parameters but it is required for a good fit. Therefore, we fixed the centroid energy and the width of the iron line at 6.55 keV and 0.33 keV, respectively. We obtained these values from earlier work using high-resolution *Suzaku* and *XMM-Newton* observations of M82 X-1 (Strohmayer & Mushotzky 2003; Caballero-García 2011). We find that in the energy range 3-15 keV this model fits the data well, giving reduced χ^2 values in the range of 0.5-1.1 for 23 degrees of freedom. All the best-fit model parameters are

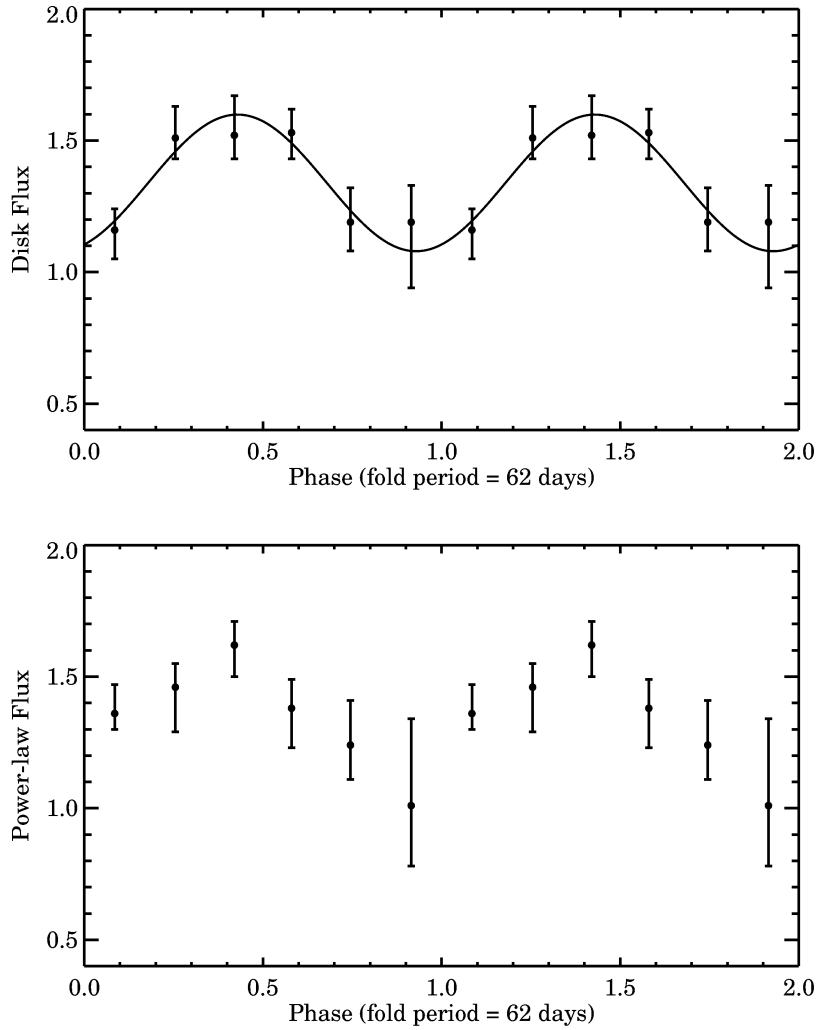


Figure 6.4: The phase-resolved X-ray (3-15 keV) disk flux (*y-axis* in the top panel) and the power-law flux (*y-axis* in the bottom panel) as a function of the 62 day phase (*x-axis*). The flux units are 10^{-11} ergs s^{-1} cm^{-2} . In each case two cycles are shown for clarity. In order to guide the eye, the best-fitting sinusoid curves (*solid*) defined as $A + B \cdot \sin[2\pi(\text{phase} - \text{constant}_0)]$ are also indicated in the top panel. The error bars represent 1σ uncertainty on the flux. Clearly, the disk component is strongly modulated. There is only weak evidence for power-law modulation.

indicated in Table 6.1. Figure 6.4 shows the value of the disk and the power-law fluxes as a function of the phase. Clearly, the disk flux varies with phase.

Table 6.1: Summary of the phase-resolved energy spectral modeling of M82. Best-fitting parameters using the *phabs*(diskpn+gauss+pow)* model are shown.

<i>phabs*(diskpn+gauss+pow):</i>						
Phase ^a	0.085	0.255	0.420	0.58	0.745	0.915
T_{max}^b	$2.2^{+0.2}_{-0.2}$	$2.1^{+0.2}_{-0.1}$	$2.1^{+0.2}_{-0.1}$	$2.2^{+0.2}_{-0.2}$	$2.4^{+0.3}_{-0.2}$	$2.8^{+0.2}_{-0.4}$
N_{disk}^c	$5.7^{+2.7}_{-1.8}$	$9.1^{+3.6}_{-2.7}$	$10.0^{+3.9}_{-2.9}$	$7.5^{+3.0}_{-2.2}$	$4.1^{+2.0}_{-1.2}$	$2.0^{+1.0}_{-0.5}$
N_{gauss}^d	$3.9^{+0.7}_{-0.7}$	$4.1^{+0.8}_{-0.8}$	$4.4^{+0.8}_{-0.8}$	$4.2^{+0.8}_{-0.8}$	$3.9^{+0.7}_{-0.7}$	$4.3^{+0.8}_{-0.8}$
Γ^e	$2.0^{+0.2}_{-0.2}$	$1.8^{+0.2}_{-0.2}$	$1.8^{+0.2}_{-0.2}$	$1.8^{+0.2}_{-0.2}$	$2.1^{+0.2}_{-0.2}$	$2.5^{+0.6}_{-0.3}$
N_{powlaw}^e	$5.4^{+1.6}_{-1.5}$	$3.8^{+1.6}_{-1.6}$	$4.6^{+1.7}_{-1.7}$	$4.1^{+1.6}_{-1.5}$	$6.3^{+1.9}_{-1.6}$	$9.6^{+6.6}_{-2.6}$
F_X^f	$2.60^{+0.02}_{-0.07}$	$3.10^{+0.02}_{-0.06}$	$3.22^{+0.05}_{-0.11}$	$2.98^{+0.03}_{-0.11}$	$2.48^{+0.02}_{-0.13}$	$2.26^{+0.06}_{-0.05}$
F_{Disk}^f	$1.16^{+0.08}_{-0.11}$	$1.51^{+0.12}_{-0.08}$	$1.52^{+0.15}_{-0.09}$	$1.53^{+0.09}_{-0.10}$	$1.19^{+0.13}_{-0.11}$	$1.19^{+0.14}_{-0.25}$
F_{Power}^f	$1.36^{+0.11}_{-0.06}$	$1.46^{+0.09}_{-0.17}$	$1.62^{+0.09}_{-0.12}$	$1.38^{+0.11}_{-0.15}$	$1.24^{+0.17}_{-0.13}$	$1.01^{+0.33}_{-0.23}$
χ^2/dof	14/23	11/23	18/23	24/23	21/23	18/23

^aWe obtained six phase-resolved energy spectra where each spectrum is an average of all data within 1/6th of the phase bin. ^bAccretion disk temperature in keV. The inner disk radius was fixed at 6GM/c². ^cNormalization ($\times 10^{-7}$) of the *diskpn* component. ^dNormalization ($\times 10^{-5}$) of the *gaussian* component (Fe K α emission line). ^eIndex (Γ) and the normalization ($\times 10^{-3}$) of the power-law component of the energy spectrum. ^fTotal X-ray flux (F_X), Disk flux (F_{Disk}) and the power-law flux (F_{Power}) of the energy spectrum in the energy range of 3-15 keV (units are 10^{-11} ergs s⁻¹ cm⁻²). The column density of hydrogen along the line of sight was fixed at 1.1×10^{22} cm⁻² – the best-fitting value found by Feng & Kaaret (2010) using the high spatial resolution *Chandra* data.

6.4 Discussion

The phase offset noted above (≈ 0.4 cycles or about 25 days) occurs over roughly 1000 days. This corresponds to a characteristic timescale of $1/(0.4/1000)$ or ~ 10 yrs. This is unusually fast for an orbital phenomenon. The typical values of evolution timescales of orbits of accreting compact binaries (neutron star or black hole binaries) are a few $\times 10^6$ yrs (e.g., Verbunt 1993; Levine et al. 2000; Wolff et al. 2009; Jain et al. 2010 and references therein). This suggests that the evolutionary timescale of the phenomenon associated with the 62 day period may be $\sim 10^5$ times faster than typical. Periods longer than the orbital period have been detected from numerous compact binaries (e.g., Kotze & Charles 2012, KC12 hereafter; Wen et al. 2006, W06 hereafter). These are known as super-orbital periods and are ascribed to disk precession (e.g., Katz 1973; Pringle 1996; Ogilvie & Dubus 2001) in addition to several other mechanisms (e.g., KC12). A characteristic feature of super-orbital periods is that they are often accompanied by sudden changes in coherence, either in the period or the phase, similar to the suggested behavior reported here from M82 (e.g., Clarkson et al. 2003; KC12).

On the other hand, numerous systems exhibit relatively stable super-orbital periods. These include Her X-1 with a period between 33-37 days (e.g., Leahy & Igna 2010; Figure 16 of KC12), LMC X-4 with ~ 30 days (W06; Figure 5 of KC12), and SS433 with a period of ~ 162 days (W06; Figure 7 of KC12). 2S 0114+650 also shows a stable super-orbital period (Figure 8 of KC12) but this may not be due to a precessing accretion disk (e.g., Farrell et al. 2006). At least in Her X-1 phase shifts

are known to occur (see, for example, Figure 9 of Clarkson et al. 2003) just before the onset of the so-called anomalous low state.

Moreover, if this modulation is indeed due to a precessing accretion disk one expects the X-ray flux originating from the disk to vary with a period of 62 days. This is simply because as the accretion disk precesses its projected area on the sky varies with the phase of the precession period. The observed dependence of the disk flux with the phase of the 62 day period is consistent with this idea (see Figure 6.4).

As discussed earlier in chapter 3, it is still unclear whether M82 X-1 hosts an intermediate-mass or a stellar-mass black hole. If the 62 day period is indeed due to relatively stable precession of the accretion disk – perhaps due to radiation induced warping – then probing the warp structure can, in principle, give us some insight into the mass question. Given the accretion efficiency of the black hole (ϵ) and the ratio of the viscosity in the normal to the planar direction (η), Pringle (1996) derived the radius R beyond which the disk warps,

$$\frac{R}{R_s} \geq \left(\frac{2\sqrt{2}\pi\eta}{\epsilon} \right)^2 \quad (6.1)$$

where R_s is the Schwarzschild radius ($2GM/c^2$). The value of η is ~ 1 (Pringle 1996). As noted earlier, M82 X-1 has an average luminosity of 5×10^{40} ergs s^{-1} . Assuming isotropic emission the relation connecting the mass of the black hole (M), the accretion efficiency (ϵ) and the luminosity (L) is,

$$L = 1.38 \times 10^{38} \times \frac{\epsilon M}{M_\odot} \text{ ergs } s^{-1} \quad (6.2)$$

where M has units of M_{\odot} . Now, if M82 X-1 were an intermediate mass black hole of, say, a few 1000 M_{\odot} , the value of ϵ is of order 0.1. The radii at which the disk warps is then \sim a few 1000 R_s . On the other hand, if the source were a stellar-mass black hole, say of 20 M_{\odot} , the value of ϵ is about 10 which results in warping at radii of a few R_s , i.e., the innermost regions of the disk.

The majority of the disk flux is emitted from its innermost regions (\sim a few 10 R_s), by the gravitational energy loss of the in-falling material. As noted above there are two possible disk structures: (1) where the inner disk is warped while the outer disk remains flat (stellar-mass black hole scenario) or (2) the outer disk is warped with the inner disk remaining flat (intermediate-mass black hole scenario). In the first case, as the innermost disk precesses the X-ray disk flux originating from this region will also modulate at the precession period thus naturally explaining the observed disk modulation (Figure 6.4). In the second case the direct disk emission is expected to remain constant with the precession period. However, the disk photons can reflect off the warp in the outer disk and this reflected component will modulate at the precession period. In this case the reflection can also produce emission features, viz., Fe $k\alpha$. The strength of the reflection is proportional to the projected surface area of the warped disk where reflection occurs. Therefore any such emission lines would be expected to vary periodically with the phase of the precession period. The quality of the current data (Table 6.1) does not allow us to solve this problem, however, this should be possible in the near future using phase-resolved X-ray spectroscopy.

6.5 Orbital Scenario and caveats

While our results show that the 62 day period of M82 X-1 may be due to a precessing accretion disk they do not yet rule out an orbital nature. In the standard picture of periodic X-ray modulations from X-ray binaries, obscuration by, for example, a hot spot at the edge of the accretion disk (accretion stream interaction site: see Parmar & White 1988; Armitage & Livio 1998) is thought to produce the regular variations at the orbital period (see chapter 5 for a detailed discussion). It is interesting to note that the phase offset appears to occur just prior to the large flare occurring around day 1000. If the standard hot spot model is at play here, it is conceivable that a sudden influx in the accreting material may have shifted the hot spot and caused an apparent phase shift. Furthermore, the flux from M82 (Figure 6.1) is a combination of multiple sources within *RXTE*'s field-of-view (see Figure 1 of Matsumoto et al. 2001). If the power-law component were dominated by the contaminating sources one expects it to remain constant with phase. But, given the fact that there is some evidence for a varying power-law flux with phase (bottom panel of Figure 6.4) it is likely that part of the power-law contribution comes from M82 X-1. This can be tested with future *NuStar* observations. While *NuStar* will not be able to spatially resolve M82 X-1, energy-dependent surface brightness modeling similar to that reported by Pasham & Strohmayer (2013b) can, in principle, constrain its high-energy X-ray spectrum. On the other hand, the assumption of a thermal accretion disk and a power-law corona for the X-ray energy spectra of ULXs has been questioned (e.g., Gladstone et al. 2009).

In summary, our results suggest that the 62 day X-ray period of M82 X-1 may be due to a precessing accretion disk. This hypothesis would be greatly strengthened if a variation in the observed periodicity can be confirmed. This can be explored with future monitoring observations using instruments such as the X-ray telescope on board *Swift*.

Chapter 7: Evidence for a 3:2 High Frequency QPO Pair in an Ultraluminous X-ray Source: a 400 Solar Mass Black Hole in M82

7.1 Introduction

One criticism of the ULX mass estimates based on scaling of QPO frequencies has been simply the plethora of QPO types observed in stellar-mass black holes, i.e., what QPO type is actually being observed in the ULXs, and is it the same as that of the stellar-mass black hole to which it is being compared? Moreover, the QPOs of a given type in stellar-mass black holes can be observed over a rather broad range of frequencies. Because of this, there remains ambiguity with respect to what QPO frequency should be used to obtain a mass scaling estimate. Thus, the correct identification of the mHz QPOs observed in M82 X-1 (and other ULXs) is critical to a reliable mass estimate.

The most distinct type of QPO appears to be the so-called high-frequency QPOs which occur in the frequency range of 100 - 450 Hz range in stellar-mass black holes (e.g., Morgan et al. 1997, Remillard et al. 1999, 2002a,b, Strohmayer 2001a,b, Belloni et al. 2012). In contrast to the Type-C low-frequency QPOs, these

oscillations appear to have quite stable frequencies, and they have been observed to occur in pairs with frequency ratios of 3:2 (McClintock & Remillard 2006). The centroid frequencies of these high-frequency QPOs are higher than the Type-C low-frequency QPOs by a factor of 30-40 with typical rms amplitudes of $\approx 3\text{-}5\%$ (see Table 2 of Belloni et al. 2012). Thus, the detection of high-frequency QPOs in a ULX together with lower frequency QPOs would provide a means to confidently identify the low-frequency QPO type as well as setting the overall frequency scale of the power spectrum for comparison with that of stellar-mass black holes of known mass, therefore facilitating an accurate measurement of the mass of the ULX black hole.

M82 X-1's current mass estimates of a few hundred solar masses combined with the type-C identification of its mHz QPOs suggest that 3:2 twin-peak high-frequency QPOs analogous to those seen in stellar-mass black holes, if present, should be detectable in the frequency range of a few Hz (Abramowicz et al. 2004). The detectability (statistical significance, n_σ) of a QPO feature can be expressed as,

$$n_\sigma = \frac{1}{2} r^2 \frac{S^2}{(S+B)} \sqrt{\frac{T}{\Delta\nu}}, \quad (7.1)$$

where r , S , B , T , and $\Delta\nu$ are the rms (root-mean-squared) amplitude of the QPO, the source count rate, the background count rate, the exposure time, and the width of the QPO, respectively (van der Klis 1989). Assuming an rms amplitude of a few percent—similar to that seen in stellar-mass black holes—and using the mean *RXTE*/PCA source and background rates obtained from prior observa-

tions (Pasham & Strohmayer 2013c), we found that the wealth of publicly available, archival *RXTE*/PCA monitoring data (≈ 1 Megasecond) spread across a timespan of ≈ 6 years would provide a sensitive search for high-frequency QPOs in M82 X-1. Here we present the results of this search and the evidence of a 3:2 QPO pair (3.3 and 5 Hz) in the combined *RXTE*/PCA data from M82 which we argue are the high-frequency QPO analogs of stellar-mass black holes seen for the first time in a ULX.

7.2 *RXTE*/PCA observations

M82 was monitored with the Rossi X-ray Timing Explorer’s (*RXTE*’s) proportional counter array (PCA) between 1997 February 2 until 1997 November 25 (296 days) and 2004 September 2 until 2009 December 30 (1945 days). All the PCA observations were carried out in the *GoodXenon* data acquisition mode. The average observing cadence during the monitoring program was once every three days for a duration of 0.5-2 ksecs per observation. The total number of monitoring observations was 867, which were divided amongst six proposals (*RXTE* proposal IDs: P20303, P90121, P90171, P92098, P93123, P94123).

As recommended by the data analysis guide provided by the *RXTE*’s Guest Observer Facility (GOF, <https://heasarc.gsfc.nasa.gov/docs/xte/abc/screening.html>), we first screened the data to only include time intervals that satisfy the following criteria: $ELV > 10.0$ && $OFFSET < 0.02$ && $(TIME_SINCE_SAA < 0 \ || \ TIME_SINCE_SAA > 30)$

&& ELECTRON2 < 0.1. In addition to the above standard filters, we only used X-ray events within the energy range of 3-13 keV which translates to PCA channels 7-32. This energy range is comparable to the bandpass in which high-frequency QPOs have been reported from stellar-mass black holes. Moreover, beyond 13 keV the background dominates the overall count rate by a factor greater than 10. For each observation we used all active proportional counter units (PCUs) in order to maximize the counting rate, and thus the sensitivity to QPOs.

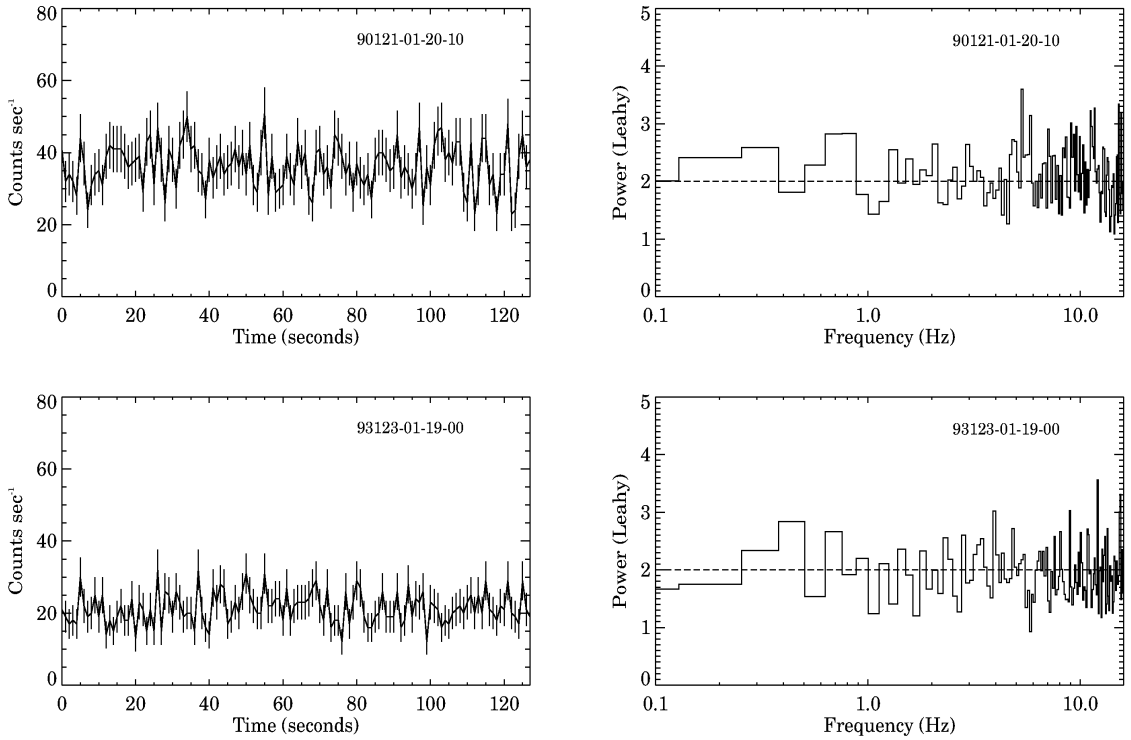


Figure 7.1: Sample 128-second *RXTE*/PCA X-ray (3-13 keV) light curves (left panels) and their corresponding power spectra (right panels) of M82. The corresponding observation IDs are shown in the top right of each panel. The light curves have a bin size of 1 second while the power spectra have a frequency resolution of 0.125 Hz.

7.3 Results

We started our analysis by first extracting individual light curves (using a bin size of 1 second) from all the observations. Through manual inspection we removed a small number of observations affected by flares, as these are attributed to background events not associated with the source, for example, gamma-ray bursts. We then divided all the remaining data into 128-second segments and extracted their light curves with a time resolution of 1/32 seconds. We then constructed a Leahy normalized power density spectrum (PDS) (where the Poisson noise level is 2; Leahy et al. 1983) from each of these 128-second light curves. Two sample light curves and their corresponding PDS are shown in the left and the right panels of Figure 7.1, respectively. All the power spectra were then combined to obtain a six-year averaged PDS of M82 (7362 individual power spectra). This PDS—rebinned further in frequency by a factor of 16—is shown in the top left panel of Figure 7.2. For direct comparison with stellar-mass black holes, M82’s broad band PDS showing the lower-frequency mHz QPO—extracted using the longest continuous *XMM-Newton/EPIC* (both pn and mos) exposure of ≈ 100 ksecs (*XMM-Newton* observation ID: 0206080101)—is shown in the bottom panel of the Figure.

In order to estimate the statistical significance of any features in the 1-16 Hz range of the six-year averaged PDS, we first ensured that the local mean was equal to 2, the value expected from a purely Poisson (white noise) process. We then computed the probability, at the 99.73% (3σ) and the 99.99% (3.9σ) confidence levels, of obtaining the power, $P = P_* \times 7362 \times 16$ from a χ^2 distribution with

$2 \times 7362 \times 16$ degrees of freedom. P_* is the power value of a statistical fluctuation at a given confidence level. We used this χ^2 distribution because we averaged in frequency by a factor of 16 and averaged 7362 individual power spectra. Considering the total number of trials (frequency bins within 1-16 Hz) we computed the 99.73% ($1/(371 \times \text{trials})$) and the 99.99% ($1/(10000 \times \text{trials})$) confidence limits (dotted lines). We detect two power spectral peaks at 3.32 ± 0.06 Hz (coherence, $Q = \nu/\Delta\nu > 27$) and 5.07 ± 0.06 Hz ($Q > 40$) significant at the 2×10^{-4} (3.7σ) and 6×10^{-3} (2.75σ) levels, respectively, assuming both features were searched for independently. However, it should be realized that after identifying a feature at 3.3 Hz, if we are searching for features with a 3:2 ratio, then the search from there on does not include all the frequency bins, but only the bins nearby $3/2$ or $2/3$ of 3.3 Hz. If this is taken into consideration the significance of the 5 Hz feature increases due to the smaller number of trials to 5×10^{-4} or 3.5σ . In order to further test the significance of the 5 Hz feature, we extracted an average PDS using all the data with segments longer than 1024 seconds. The averaged PDS of all 1024-second segments (total of 363 PDS)–frequency re-binned further by a factor of 64–is shown in the top right panel of Figure 7.2. The 5 Hz feature ($Q = 80$) is clearly detected at the 1.5×10^{-4} confidence level or 3.8σ , considering a full search between 1-16 Hz.

It is important to realize that the combined probability of two independent chance fluctuations – in the 3:2 frequency ratio – one at the 3.7σ level (3.3 Hz feature) and the other at the 2.75σ level (5 Hz feature) is greater than 4.7σ . Therefore, the observed 3:2 ratio QPO pair in M82 is highly statistically significant.

The very presence of these two features in the six-year averaged power spec-

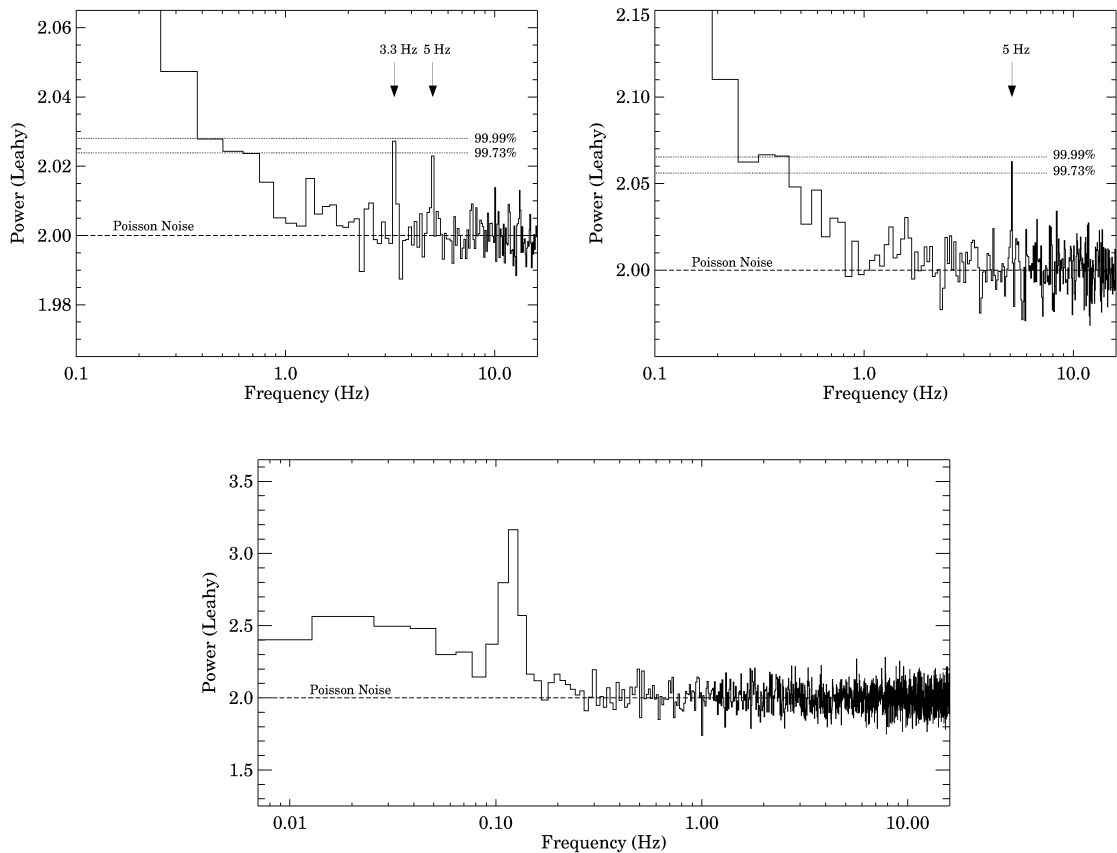


Figure 7.2: *Top-Left Panel:* six-year average X-ray (3-13 keV) power density spectrum of M82 (frequency resolution of 0.125 Hz) using 128-second individual light curves. The two strongest features in the power spectrum occur at 3.32 ± 0.06 and 5.07 ± 0.06 Hz consistent with a 3:2 frequency ratio. *Top-Right Panel:* Same as the left panel except here 1024-second long light curves were used. The frequency resolution is 0.0625 Hz. The strongest feature is at 5 Hz (see text). *Bottom Panel:* Broadband power density spectrum of M82 showing the low-frequency QPO at 120 mHz in addition to the high-frequency QPO pair in the top panels. This spectrum was obtained using the longest *XMM-Newton*/EPIC exposure of ≈ 100 ksecs.

trum suggests that they are stable on this timescale. In order to further rule out the possibility that these oscillations are due to a single or small number of particular observations, we constructed two dynamic average power spectra, one for the 128-second segments (dynamic PDS#1) and another for the 1024-second segments (dynamic PDS#2). These track the evolution of the average PDS as a function

of the total number of individual power spectra used in constructing the average. The two dynamic PDS clearly suggest that the power in these two features builds-up gradually as more data is being averaged, as opposed to a sudden appearance, which would be expected if a single or a small number of observations were contributing all the signal power. In addition, dynamic PDS#1 clearly shows that while the 5 Hz feature is stronger during the earlier stages of the monitoring program the 3.3 Hz feature is stronger during the later observations. Longer exposures of the order of 1-2 ksecs were carried out during the earlier stage of the monitoring program, which explains the higher significance of the 5 Hz feature in the average PDS of the 1024-second segments.

To calculate the rms variability amplitude of these QPOs we first determined the mean net count rate (source + background) of all the light curves used to extract the average power spectra. The values were equal to 29.9 counts s^{-1} and 35.2 counts s^{-1} for the 128-second and the 1024-second segment power spectra, respectively. The rms amplitudes of the 3.3 Hz and the 5 Hz QPOs, not correcting for the background, were estimated to be $1.1\pm 0.1\%$ and $1.0\pm 0.1\%$, respectively. Similarly, the rms amplitude of the 5 Hz feature within the 1024 segment PDS was estimated to be $1.1\pm 0.1\%$. We then estimated the mean background count rate from the *Standard2* data utilizing the latest PCA background model. The mean background rates during the 128-second and the 1024-second segments were estimated to be 18.9 counts s^{-1} and 24.0 counts s^{-1} , respectively. After accounting for the X-ray background we find that the rms amplitudes of the 3.3 Hz and the 5 Hz features—averaged over the entire data—are $3.0\pm 0.4\%$ and $2.7\pm 0.4\%$, respectively

while the amplitude of the 5 Hz feature within the 1024-second PDS was estimated to be $3.5 \pm 0.4\%$.

Furthermore, the source count rates estimated above (*net minus background*) represent the combined contribution from all the X-ray point sources within the PCA's 1° (FWHM) field of view. Thus, the QPO rms amplitudes are underestimated. A study using the high-resolution camera (HRC) on board *Chandra* suggests that there are multiple point sources within the $1' \times 1'$ region around M82 X-1 (Matsumoto et al. 2001, Chiang & Kong 2011). Tracking the long-term variability of these sources suggests that the maximum luminosity reached by any of these sources—except for source 5 (as defined by Matsumoto et al. 2001; see chapter 3 for details on this source and a discussion on source contamination)—is less than $1/5^{\text{th}}$ of the average luminosity of M82 X-1 (Chiang & Kong 2011). Source 5 is a highly variable transient ULX with its 2-10 keV luminosity varying between 10^{37-40} ergs s^{-1} (see Figure 5 of Feng & Kaaret 2007 and the middle left panel of Figure 1 of Chiang & Kong 2011). The QPOs reported here are most likely produced from M82 X-1, which has persistently been the brightest source of any in the immediate vicinity of M82 X-1 (see below). Although a precise value of the rms amplitude cannot be evaluated using the current data, we estimate an absolute upper limit by calculating the inverse of the fraction of the count rate contribution from M82 X-1, assuming all the remaining contaminating sources are at their brightest ever detected. This scenario is highly unlikely but will serve as an absolute upper bound to the rms amplitude of the QPOs, assuming they are from M82 X-1. Using the values reported by Chiang & Kong (2011) and Pasham & Strohmayer (2013b) the

fraction is roughly 1.8. Thus the true rms amplitudes of the 3.3 Hz and the 5 Hz QPOs are estimated to be in the range of 3-5%.

Also, *XMM-Newton*'s EPIC pn instrument – with an effective area of $\approx 1/5^{\text{th}}$ of *RXTE*'s PCA albeit with lower background – observed M82 on multiple epochs, with a total effective exposure of ≈ 350 ksecs. These observations were taken in the so-called full-frame data acquisition mode with a time resolution of 73.4 ms or a Nyquist frequency of 6.82 Hz. This value is close to the QPO frequencies of interest and causes some signal suppression. Nevertheless, we extracted an average 3-10 keV PDS with 128-second data segments using all the observations (2718 individual power spectra). We do not detect any statistically significant features nearby 3.3 and 5 Hz, however, we estimate a QPO upper limit (3σ confidence) of 5.2 and 6.2% rms (using Eq. 4.4 and Eq. 4.10 of van der Klis 1989) at 3.3 and 5 Hz, respectively, which are roughly twice the rms values of the QPOs detected in the PCA data.

7.4 Discussion

The remarkable stability of the two QPOs on timescales of a few years strongly suggests they are not low-frequency QPOs from a stellar-mass black hole in the PCA's field of view. Low-frequency QPOs of stellar-mass black holes, such as the Type-C QPOs discussed earlier, have typical centroid frequencies of a few Hz with rms amplitudes of 5-25%, but are known to vary in frequency by factors of 8-10 over time scales of days (see, for example, Figure 1 of Wood et al. 2000, Figure 2 of Rodriguez et al. 2004). This would lead to very broad features in the kind

of average power spectrum we have computed from the M82 PCA observations. Moreover, among the plethora of low-frequency QPOs currently known there is no indication of them preferentially occurring with a 3:2 frequency ratio. Furthermore, the average luminosity of the QPOs reported here is $\approx 0.03 \times$ (the average luminosity of all the sources observed by the PCA in the 3-13 keV band) which is $\approx 0.03 \times 5 \times 10^{40}$ ergs $s^{-1} = 1.5 \times 10^{39}$ ergs s^{-1} (see Table 1 of Pasham & Strohmayer 2013c). This is comparable to or more than the peak X-ray luminosities of the contaminating sources, except for source 5 and source 9 (as defined by Matsumoto et al. 2001; See Table 2 of Chiang & Kong 2011). However, a more careful look at the long-term light curve of source 9 suggests its typical luminosity is of the order of 10^{39} ergs s^{-1} (see Figure 2 of Jin et al. 2010). Therefore, if these features were simply low-frequency QPOs produced by any of these contaminating sources— except for source 5—their X-ray flux would have to be modulated at almost 100%, which is not plausible for the typical amplitudes of low-frequency QPOs.

On the other hand, source 5 which is a ULX can in principle be the origin of these 3:2 ratio QPOs. However, 3-4 mHz QPOs have been discovered from this source and have been identified as Type-A/B QPO analogs of stellar-mass black holes (Feng et al. 2010). Such a characterization for the mHz QPOs suggests that the ULX might host a black hole with a mass of 12,000-43,000 M_{\odot} (Feng et al. 2010). If that were the case, the expected frequency range of high-frequency QPO analogs for a few 10,000 M_{\odot} black hole would be a few 100s of mHz. The detected frequencies of 3.3 and 5 Hz are a factor of 10 higher, suggesting that the 3.3 and 5 Hz QPOs are less likely to be the high-frequency QPO analogs of source 5. This

leaves M82 X-1 as the most likely source associated with the 3:2 ratio QPO pair.

An X-ray pulsar might, in principle, produce a periodic signal, however, a pulsar origin for the QPO signals is very unlikely for several reasons. First, a pulsar signal would be much more coherent than that of the observed QPO signals, which clearly have a finite width. Second, it is extremely implausible based on the observed high QPO luminosities. For example, rotation-powered pulsars can be strongly excluded, they simply cannot provide the required luminosity. A neutron star’s rotational energy loss rate can be expressed in terms of its moment of inertia, I , spin period P , and period derivative, \dot{P} as,

$$\dot{E}_{rot} = \frac{2\pi^2 I \dot{P}}{P^3}. \quad (7.2)$$

No known pulsar has a spin-down luminosity comparable to the estimated QPO X-ray luminosity. For example, the energetic Crab pulsar has $\dot{E} \approx 2 \times 10^{38}$ erg s⁻¹, and only a fraction of a pulsar’s spin-down power typically appears as X-ray radiation. This rules out rotation-powered pulsars. As M82 is a starburst galaxy it likely hosts a population of accreting X-ray pulsars. Such accretion-powered pulsar systems are typically limited by the Eddington limit of $\approx 2 \times 10^{38}$ ergs s⁻¹ for a “canonical” neutron star. Useful comparisons can be made with the population observed with the *RXTE*/PCA in the Small Magellanic Cloud (SMC, see Laycock et al. 2005). These authors present pulsed luminosities for the SMC pulsar population, and none is larger than $\approx 2 - 3 \times 10^{38}$ erg s⁻¹. Again, this is much smaller than the inferred QPO luminosities. Moreover, such pulsars are variable, and their time-

averaged luminosities would be reduced further by their outburst duty cycles. At present the only pulsar that is known to reach luminosities of $\sim 10^{40}$ ergs s^{-1} for brief periods of time is GRO J1744-28—the so-called bursting pulsar (Giles et al. 1996; Jahoda et al. 1999, Sazonov et al. 1997). This object has a 2.1 Hz spin frequency and was discovered during an outburst that spanned the first 3 months of 1996 (we note that a few months prior to the time of writing the source was detected in outburst again, suggesting a duty cycle of about 18 years, ATel #5790, #5810, #5845, #5858, #5883, #5901). Its peak persistent luminosity (assuming a distance close to that of the Galactic center) was $\approx 7 \times 10^{38}$ erg s^{-1} . With a pulsed amplitude of about 10% this would still give a pulsed luminosity much less than the inferred QPO luminosities. The Type II–accretion driven–bursts from this source could reach about 10^{40} erg s^{-1} (Kommers et al. 1997), and with a 10% pulsed amplitude this could give an instantaneous luminosity close to that of the average QPO luminosities. However, the bursting intervals make up less than 1% of the total time, and thus this small duty cycle will reduce the average pulsed luminosity due to the bursts to a level substantially below that of the observed QPOs. We conclude that the observed QPOs cannot be associated with accreting pulsars in M82.

The only X-ray oscillations from black holes that are known to be stable on timescales of a few years and that occur in a 3:2 frequency ratio are the so-called high-frequency QPOs. Their remarkable stability combined with the fact that their frequencies/timescales are comparable to the Keplerian orbital periods in the inner few gravitational radii of the accretion disk strongly suggest a dependence on both

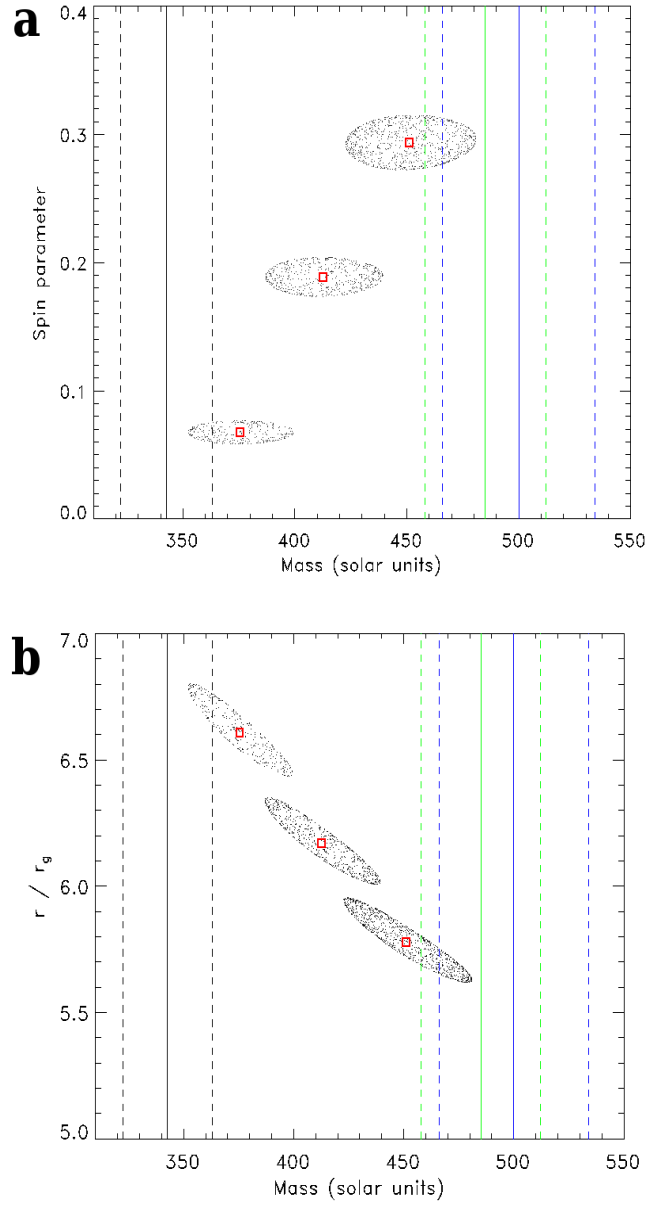


Figure 7.3: *Top Panel:* Contours (90% confidence) of M82 X-1’s mass as a function of the spin parameter under the relativistic precession model (RPM). The three contours correspond to the three low-frequency values (37 mHz, 120 mHz and 210 mHz) with the mass increasing as the oscillation frequency increases. *Bottom Panel:* Contours of M82 X-1’s mass as a function of the radius of the origin of these oscillations (in units of $r_g = GM/c^2$, where G , M , c are the Gravitational constant, the black hole mass and the speed of light, respectively). In both the panels the vertical lines (solid: solution; dashed: upper-lower limits) represent M82 X-1’s mass estimates assuming a simple $1/M$ scaling for the high-frequency quasi-periodic oscillations. The three colors correspond to scalings using the three microquasars (green: GRO J1655-40 (Beer & Podsiadlowski 2002); blue: XTE J1550-64 (Orosz et al. 2011); black: GRS 1915+105 (Steghs et al. 2013)).

the mass and the spin of the black hole. The exact physical mechanism producing these QPOs is currently uncertain, however in one of the earliest proposed QPO models, the so called relativistic precession model (RPM), the upper harmonic of the high-frequency QPO is associated with the Keplerian frequency at some inner radius while the lower harmonic of the high-frequency QPO and the type-C QPO are associated with the periastron and nodal precession frequencies, respectively, at the same radius. Recently, Motta et al. (2014a) have applied this model to GRO J1655-40 which exhibits both the low-frequency and the high-frequency QPOs and has a very accurate mass measurement of $5.4 \pm 0.3 M_{\odot}$ (Beer & Podsiadlowski 2002). They find that the black hole mass evaluated from the RPM analysis agrees nicely with its dynamical mass estimate. Given this promise of the RPM, we estimated the mass and spin of M82 X-1's black hole using this model. Note that the RPM analysis requires that the three QPOs, the two high-frequency QPOs and a low-frequency QPO, be observed simultaneously. This is however not the case for the M82 observations. While the combined six-year *RXTE*/PCA data shows the twin high-frequency QPO pair, individual *XMM-Newton* observations randomly dispersed over the same epoch as the *RXTE* monitoring have shown mHz low-frequency QPOs with frequencies in the range of 37-205 mHz (see Table 2 of Pasham & Strohmayer 2013b, Caballero-García et al. 2013). Thus, we carried out the RPM analysis for three separate values of the low-frequency QPOs, the lowest and the highest values of 37 mHz and 210 mHz, respectively, as well as a mean QPO frequency of 120 mHz. This enables us to set limits on the mass and spin. The RPM solutions for the three values of the QPOs are shown in the top (mass - spin contours) and the bottom panels

(radius-mass contours) of Figure 7.3, respectively, and suggests that the mass of the black hole in M82 X-1 is $428 \pm 105 M_{\odot}$. Further, the dimensionless spin parameter is constrained to the range $0.06 < a < 0.31$, and the inferred radius, r , in the disk is in the range $5.53 < r/r_g < 6.82$, where $r_g = GM/c^2$.

In general, any GR induced oscillation has its frequency varying as $1/M$ (e.g., Abramowicz & Kluźniak 2004). Using the masses and the frequencies of the three known stellar-mass black holes which show the 3:2 high-frequency QPO pair (McClintock & Remillard 2006, Steeghs et al. 2013) and assuming similar spins, we estimated the mass of M82 X-1 by simply scaling the observed frequencies. These values along with their uncertainties are indicated by vertical solid and dashed lines, respectively, in the left and the right panels of Figure 7.3. Note that these estimates are also consistent with measurements from the RPM analysis.

Interestingly, these measurements are consistent with estimates obtained from scaling the mHz QPOs of M82 X-1 to the low-frequency QPOs of stellar-mass black holes (see, for example, Dewangan et al. 2006, Mucciarelli et al. 2006). The apparent detection of high-frequency QPOs in M82 X-1 separated from the low frequency, mHz QPOs by a factor consistent with the high to low frequency QPO spacing in stellar-mass black holes, supports the interpretation of the mHz QPOs in X-1 as Type-C QPOs. Also, a thorough modeling of the X-ray energy spectra of the source during the thermal-dominant state using a fully relativistic multi-colored disk model suggests that it hosts an intermediate-mass black hole with mass in the range 200-800 M_{\odot} and that it is accreting near the Eddington limit (Feng & Kaaret 2010). The mass estimates from the X-ray variability plane also suggest a black

hole mass of 100-1300 M_{\odot} (Casella et al. 2008). Our result is not only consistent with all the previous mass estimates of M82 X-1 but it represents the most accurate black hole mass measurement of M82 X-1 to-date. It also suggests that the physical phenomenon causing high-frequency QPOs in stellar-mass black holes also scales to intermediate-mass black holes.

Finally, the average 2-10 X-ray luminosity of the source is 5×10^{40} ergs s^{-1} which combined with the measured mass suggests that the source is accreting close to the Eddington limit with an accretion efficiency of 0.8 ± 0.2 . The key to understanding ULXs has been to know whether they are super-Eddington stellar-mass black holes or sub-Eddington intermediate-mass black holes. Our results strongly suggest that M82 X-1 hosts an intermediate-mass black hole.

Chapter 8: Conclusions & Future Work

This thesis demonstrates the importance of time variability studies for understanding the physical environments of ULXs (Chapter 5 & 6) and enabling accurate mass estimates of their black holes in some cases (Chapter 7). While this dissertation gives important insights into some of the physical characteristics of variable ULXs, it also opens up more questions that will be the subject of future studies. For instance, in our work involving the search for timing-spectral correlations in ULXs NGC 5408 X-1 and M82 X-1 (Chapters 2 & 3) it is still unclear whether a correlation between the mHz QPO frequency and the energy spectral power-law index exists. In the case of NGC 5408 X-1 this is owing to the limited energy spectral variability of the source, while in the case of M82 X-1 this is due to source confusion within the *XMM-Newton* images. The issue with NGC 5408 X-1 can be resolved by observing the source when it undergoes an energy spectral change. On the other hand, simultaneous *Chandra* and *XMM-Newton* observations of M82 X-1 can facilitate an unbiased test for a correlation where *Chandra*—with its superior spatial resolution—can be used to extract a clean energy spectrum while *XMM-Newton*, with a large collecting area, can provide a more sensitive power density spectrum. In addition, while our analysis of the 62-day period of M82 X-1 (Chapter 6) suggests that this

period may not represent the orbital period of the system, a more straightforward way to ascertain this claim would be to detect a clear change in this periodicity. This can be tested with further monitoring of M82 with, for example, *Swift*. Also, it would be interesting to observe M82 with *Nustar* (Nuclear Spectroscopic Telescope Array) to see if the 3:2 high-frequency QPOs are detected. Although it should be pointed out that *Nustar* has slightly lower effective area in the 3-13 keV X-ray band than *RXTE*. One can also observe the source with *XMM-Newton* in a high-time resolution mode (previous observations were limited to a Nyquist frequency of 6.82 Hz), although it would require much longer exposures to build up the same signal-to-noise ratio as presented in Chapter 7 (see Eq. 8.3). Furthermore, some ULX sources can be observed with NASA's upcoming mission *NICER* to search for high-frequency QPO signatures (see section 8.3). In the following sections, I will discuss new methods that can be used to explore the field of intermediate-mass black holes and ULXs.

8.1 X-ray–Optical Reverberation Mapping of ULXs: Search for and Measure X-ray – Optical Time Lags

It is now known that a significant fraction of the optical emission from accreting X-ray binaries is due to X-ray reprocessing in the surrounding accretion disk (van Paradijs & McClintock 1994; Reynolds & Miller 2013), and current evidence suggests that this may be the case in some ULXs (Tao et al. 2011). In simple models of this process the optical emission results from X-ray irradiation of the outer portions

of the disk by the central continuum. The optical emission is thus correlated with the X-ray emission but delayed by the light travel time effects. Measurement of the time delay (τ) will provide a direct probe of the accretion disk's (and hence the binary's) size ($R \approx c\tau$, where c is the speed of light). A mass estimate can follow in a manner analogous to AGN reverberation mapping (Peterson & Wandel 2000). The difference is that in ULXs the optical flux reverberates in response to the variations in the central X-ray flux while in AGN the optical broad-line flux responds to changes in the optical continuum. Nevertheless, a lag measurement gives a size scale of the accretion disk which can then be combined with measured line widths due to the Keplerian motions in the disk. Line widths of $\Delta v \approx 750 \text{ km s}^{-1}$, attributable to the disk, have been measured for some ULXs (e.g., Cseh et al. 2011, 2013). If these are indeed due to disk motion, then a mass estimate of $M_{\text{ULX}} \approx R\Delta v^2/G$ follows (G is the Gravitational constant).

To test our methodology we have successfully proposed for joint *XMM-Newton* (X-ray: 2×33 ksecs) and Very Large Telescope (optical: 4 half nights) observations of our highest priority target ULX NGC 5408 X-1. But owing to observing constraints only 20 ksecs of simultaneous X-ray/Optical data were acquired.

A preliminary analysis indicates that the optical emission from the source is quite variable. This is shown along with the X-ray light curve in Figure 8.1 where 10 ksecs of the simultaneous X-ray-Optical data is shown. The next obvious step is to test if the optical emission is correlated with the X-ray band. This will be the subject of study soon after completing my thesis.

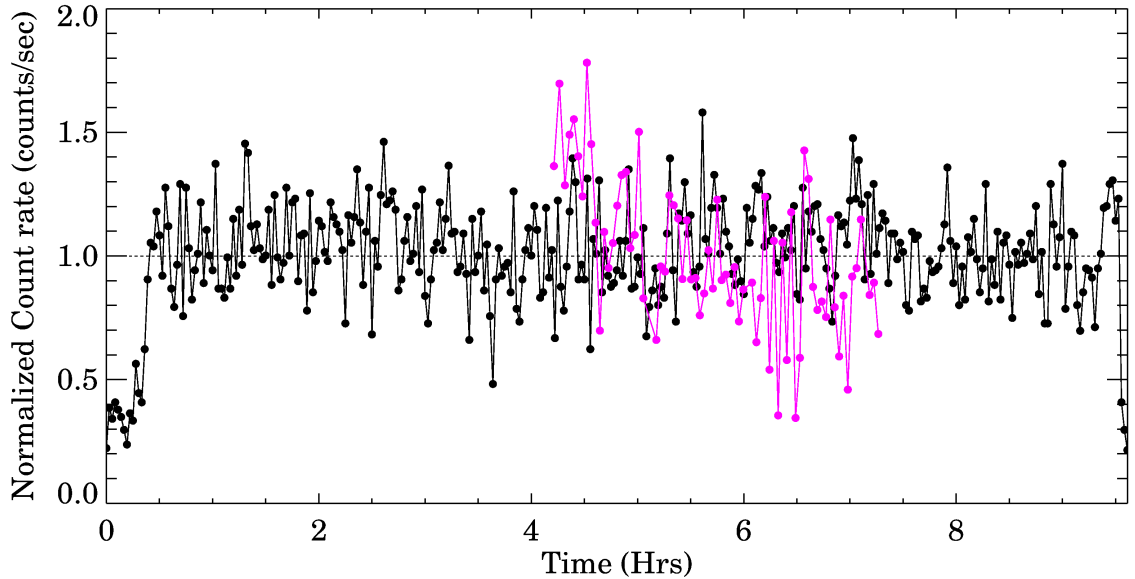


Figure 8.1: The X-ray (0.2-12 keV: black) and the optical (400-550 nm: magenta) light curve of NGC 5408 X-1 obtained using *XMM-Newton* and the FOCal Reducer Spectrograph (FORS2) on the Very Large Telescope, respectively. Both the light curves are normalized such that their mean is unity. The X-ray light curve is uniformly sampled with a bin size of 100 sec while the optical is irregularly sampled with a mean cadence of one image per every 143 seconds (120 sec exposure + 23 sec of CCD readout).

8.2 Searches for Tidal Disruption Signatures of a Star by an intermediate-mass black hole

When a star orbits close enough to a massive black hole ($\gtrsim 10^4 M_\odot$) such that its periastron distance is less than the tidal radius of the black hole—and if the tidal forces exceed the self-binding energy of the star—it will be disrupted and cause what is commonly referred to as a tidal disruption event (TDE). A fraction of the stellar debris is expected to fallback and accrete onto the black hole (while a significant fraction escapes the black hole), causing a tidal disruption flare (Rees 1988). To

the zeroth order, the mass accretion rate and hence the bolometric luminosity is expected to decay as $t^{-5/3}$, where t is the time since the peak luminosity (Evans & Kochanek 1989, Phinney 1989). The fallback material also forms an accretion disk whose emission peaks in the hard UV/soft X-rays and is observed as a black body spectrum (Ulmer 1999).

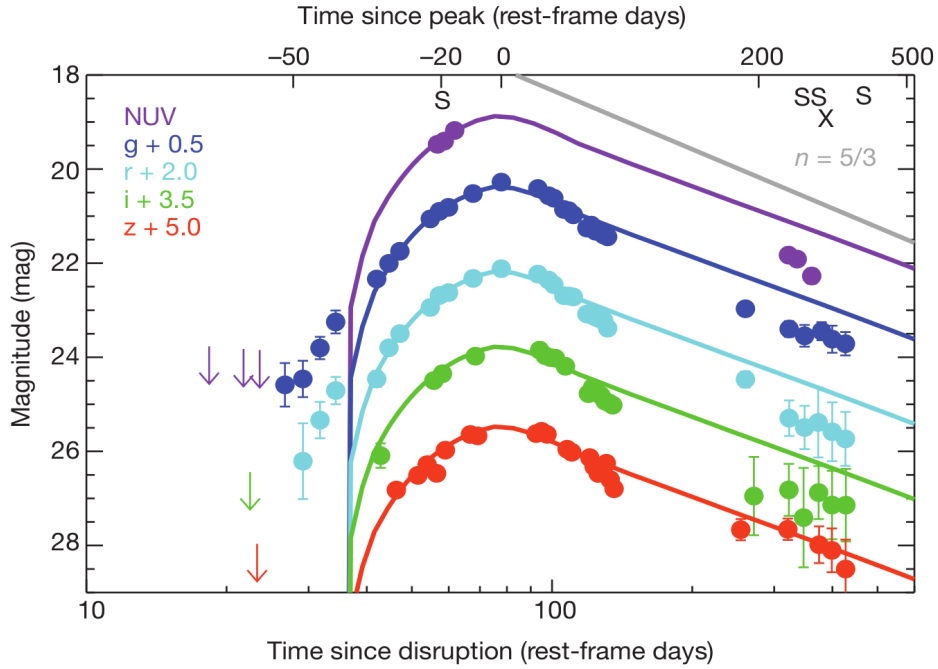


Figure 8.2: UV and Optical light curve of TDE PS1-10jh (Gezari et al. 2012). The data (filled circles) in various UV, optical filters are indicated by different colors (see legend). The solid curves are the best-fits using the numerical model of Lodato et al. (2009).

While many of the finer details still remain uncertain, the basic theoretical framework for understanding TDEs is well-established. The central black hole masses can be accurately derived using parameters measured from observed light curves and multi-wavelength spectral energy densities (SEDs). For example, the fallback time, i.e., time between the disruption (t_D) and the peak luminosity (t_0),

can be expressed as

$$t_{fallback} = t_0 - t_D = 0.11k^{-3/2}M_6^{1/2}\beta^{-3}r_*^{3/2}m_*^{-1} \text{ yrs} , \quad (8.1)$$

where k ranges from 1 for a non-rotating star to 3 for a maximally spun-up star near its point of disruption. M_6 is the mass of the black hole in units of $10^6 M_\odot$. β is known as the penetration factor and is defined as the ratio of the tidal and the peristron radii of the black hole ($\beta \leq 1$). $r_* = R_*/R_\odot$ and $m_* = M_*/M_\odot$ where R_* and M_* are the radius and the mass of the star being disrupted, respectively. Furthermore, for main-sequence stars with masses $< 1 M_\odot$ and $> 1 M_\odot$ the term $r_*^{3/2}m_*^{-1}$ reduces to $m_*^{1/2}$ and $m_*^{1/8}$, respectively (Ulmer 1999). Thus, if one can obtain a well-sampled light curve of a TDE the mass of the black hole can be directly obtained using the above equation.

The temperature of the fallback accretion disk (T_{disk}) can also be expressed in terms of the mass of the black hole, the radius and the mass of the star and is given as,

$$T_{disk} = 2.5 \times 10^5 M_6^{1/12} r_*^{-1/2} m_*^{-1/6} (r/R_t)^{-1/2} \text{ K} , \quad (8.2)$$

where r is the radius of the disk and R_t is the tidal radius of the star that is being disrupted. A multi-wavelength SED of the TDE at late times (after the formation of the disk) can thus allow another independent measure of the black hole mass. These mass estimates can be further improved by directly fitting the observed light curve profiles to numerical simulations varying appropriately only a few parameters:

black hole mass, radius and mass of the star, penetration factor, and the polytropic exponent of the star (Lodato et al. 2009, Guillochon et al. 2014). An example of such numerical fits (solid curves) to the observed data is shown in Figure 8.2.

Recent general relativistic magneto-hydrodynamic simulations of the accretion flow around black holes suggest that the interplay between the disk and the jet can excite quasi-periodic oscillations (QPOs; McKinney et al. 2012). This is especially relevant in the context of TDEs where both an accretion disk and a jet are known to form as the stellar debris accretes onto the black hole (Zauderer et al. 2011, Bloom et al. 2011, Burrows et al. 2011). Observationally, an X-ray QPO with a frequency of 4.8 mHz has been detected from one TDE, Swift J1644+57 (Reis et al. 2012). Assuming this frequency corresponds to the orbital period of a test particle at the innermost stable circular orbit, the mass of this source was estimated to be in the range of $10^{5-6} M_{\odot}$. Thus, the detection of X-ray QPOs in TDEs can also serve as a tool to measure the black hole mass, provided high timing-mode observations are made by prompt follow-up with either *XMM-Newton*, *Chandra* or *NuStar*.

TDEs by themselves are a spectacular phenomenon but they are also very important for many physical reasons. For example, it is estimated that only a fraction of all the super-massive black holes can be observed while the rest lie dormant at the centers of quiescent galaxies (e.g., McConnell & Ma 2013). TDEs provide a one-time opportunity to detect these systems and study the onset of accretion and the formation of accretion disks and jets, which are currently only poorly understood.

There are now only about a dozen transients (including detections in the X-ray, UV and optical bands) classified as TDEs (Gezari et al. 2006, 2008). A sub-sample

of these are characterized as possible intermediate-mass black hole TDEs. These include Swift J1644+57 (Krolik & Piran 2011), GRB060218 (Shcherbakov et al. 2012) and GRB 060614 (Lu et al. 2008) and the flare from the elliptical galaxy NGC 1399 (Irwin et al. 2010) where it is hypothesized that a white dwarf is being tidally disrupted by an intermediate-mass black hole with a mass of $10^{3-4} M_{\odot}$. Another candidate is a serendipitously discovered bright point-source flare in the Abell cluster A1795 which is consistent with being tidal disruption of a star by an \approx a few $\times 10^5 M_{\odot}$ intermediate-mass black hole (Donato et al. 2014, Maksym et al. 2013).

Currently, some of the most promising new targets for the detection of intermediate-mass black hole TDEs are the centers of dwarf galaxies. Wang & Merritt (2004) estimate the expected event rate per galaxy as a function of the black hole mass. These are shown in the left panel of Figure 8.3. Clearly, the estimated tidal capture rates increase with decreasing mass (assuming, of course, that a certain dwarf galaxy contains a central compact source).

8.2.1 Expected Results: Coordinated *Swift* and Ground-based UV/Optical/IR Observations

Emission from TDEs is observed in various wavebands including the optical, UV (e.g., van Velzen et al. 2011, Gezari et al. 2006), X-rays (e.g., Maksym, Ulmer & Eracleous 2010) and radio (e.g., Zauderer et al. 2013). However, the X-ray band is the best place to detect the $t^{-5/3}$ “smoking gun” behavior of a TDE (Lodato &

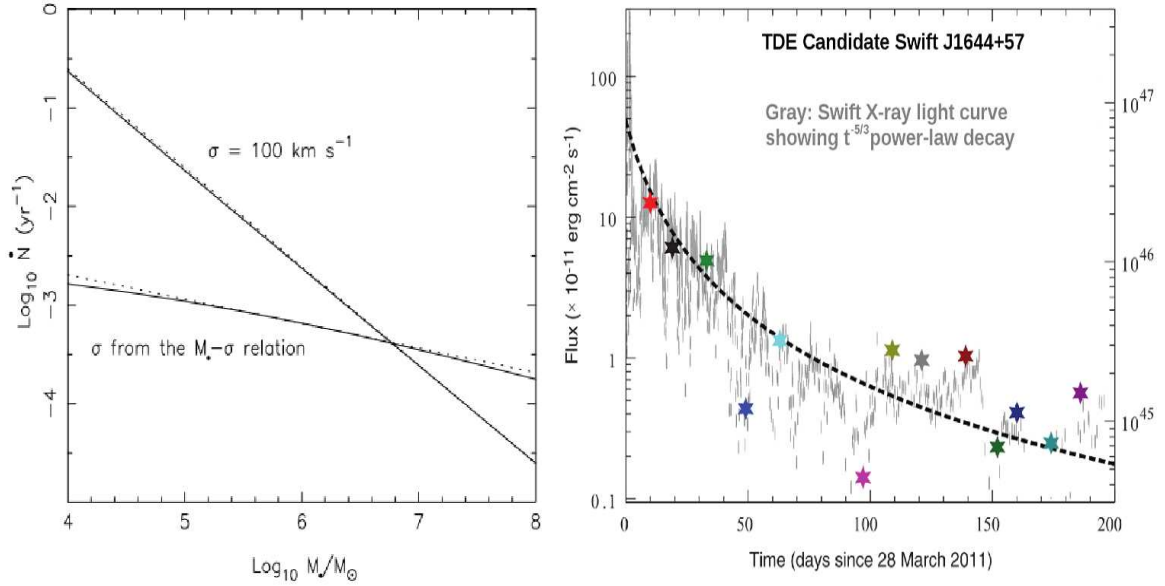


Figure 8.3: *Left Panel:* Expected TDE rates per galaxy as a function of black hole mass assuming the $M - \sigma$ relation of super-massive black holes extends to intermediate-mass black holes (lower curve) and assuming the $M - \sigma$ relation flattens (saturates) to a $\sigma = 100 \text{ km s}^{-1}$ (upper curve) as derived by Wang & Merritt (2004). Clearly, in both cases the expected TDE rates increase with decreasing black hole mass. *Right Panel:* *Swift* X-ray light curve of the TDE Sw J1644+57 along with the expected $t^{-5/3}$ power-law decay (dashed). The filled stars indicate *XMM-Newton* observations (Reis et al. 2012). The luminosity of the source is also indicated on the right hand side of the panel.

Rossi 2011). Currently, *Swift* is the only X-ray observatory capable of monitoring TDEs. An example of this behavior can be seen in the right panel of Figure 8.3 where the long-term X-ray light curve of Swift J1644+57 is shown (Reis et al. 2012). Evans et al. (2014) have recently reduced every image taken by the *Swift-XRT* in its 8 years of operation and cataloged 151,524 X-ray point sources. Reaching a sensitivity level of $\approx 3 \times 10^{-13} \text{ erg cm}^{-2} \text{ s}^{-1}$ (0.3-10 keV), they identified $\sim 30,000$ variable X-ray point sources. This archive is the richest and the most expedient resource for assimilation of TDE candidates. Furthermore, this automated pipeline

will soon be applied to real-time data—which will be extremely valuable for timely identification of TDE-candidates.

As predicting the location of the next TDE in the sky is obviously not possible, the only practical means to progress on this front is via periodic all-sky surveys. Currently, one of the best resources in this regard is the intermediate Palomar Transient Factory (iPTF), a wide-field (7.8 deg^2) optical survey aimed at identifying transients. My future collaborator for this proposed project, Dr. Brad Cenko, is a member of the PTF collaboration and hence will have prompt access to the data from all the transients. A similar sky survey is the La Silla-Quest (LSQ) variability survey (4 deg^2) which is also aimed at studying the transient optical sources. All the data from this survey will be immediately made public after an initial pipeline processing. Furthermore, a team comprised of members from NASA Goddard, University of Maryland College Park and NOAO have proposed an optical monitoring campaign (PI: Brad Cenko) using the Dark Energy Camera (DECam) on the 4-m Blanco telescope. If approved, this dataset is expected to detect several tens of TDEs per year. Of the dozen or so TDE candidates currently known, five events are classified as plausibly due to an intermediate-mass black hole. Assuming the campaign does detect a few tens of TDEs, forty percent or so of them should be intermediate-mass black hole candidates. Even assuming this to be a severe over-estimate, if even a single intermediate-mass black hole TDE can be detected and studied it will have important implications.

8.3 ULX High-Frequency QPOs using *NICER*

The Neutron star Interior Composition Explorer (*NICER*) is an upcoming NASA mission with an expected launch in December 2016. While *NICER* will primarily focus on neutron star observations, given its superior timing, fast maneuverability, large collecting area and high sensitivity, it will be an ideal instrument for detecting high-frequency QPO analogs from ULXs—similar to the ones reported in Chapter 7 of this dissertation.

8.3.1 Expected results with *NICER*

The detectability (quantified by statistical significance, n_σ) of a QPO feature can be expressed as,

$$n_\sigma = \frac{1}{2} r^2 \frac{S^2}{(S+B)} \sqrt{\frac{T}{\Delta\nu}}, \quad (8.3)$$

where r , S , B , T , and $\Delta\nu$ are the rms (root-mean-squared) amplitude of the QPO, the source count rate, the background count rate, the exposure time, and the width of the QPO, respectively (van der Klis 1989). The combined significance of the detected features from M82 using ≈ 1 Megasecond of *RXTE*/PCA data was 4.7σ (Pasham et al. 2014, accepted). For the low flux rates ($\lesssim 10^{-11}$ ergs s $^{-1}$ cm $^{-2}$) expected from ULXs, PCA suffers from high X-ray background. However, *NICER* will have the advantage of significantly less background than *RXTE* though with a lower effective source count rate. Based on the expected effective area of *NICER* and the observed rms amplitude of the high-frequency QPOs of M82 X-1, *NICER*

will be able to detect these oscillations—at the same combined significance—with \lesssim 150 ksecs of effective exposure.

Currently, it is not clear which ULX targets *NICER* should observe and for how long. My work on M82 X-1 will be critical in this regard as one can estimate—using the above equation—the required exposure times assuming that the expected QPO rms from ULXs are comparable to those detected from M82 X-1. There is also a wealth of archival X-ray observations from *XMM-Newton* and *Suzaku* on ULXs, including Holmberg IX X-1, M81 X-6, NGC 1313 X-1, NGC 1313 X-2, Holmberg II X-1 and M33 X-8. Analysis of this complete sample will result in more high-frequency QPO detections or upper limits thereof, either of which would provide extremely valuable guidance for scheduling observations with *NICER*.

Bibliography

- [1] Abramowicz, M. A., Bulik, T., Bursa, M., & Kluźniak, W. 2003, *A&A*, 404, L21
- [2] Abramowicz, M. A., Kluźniak, W., McClintock, J. E., & Remillard, R. A. 2004, *ApJL*, 609, L63
- [3] Abramowicz, M. A., & Kluźniak, W. 2004, *X-ray Timing 2003: Rossi and Beyond*, 714, 21
- [4] Altamirano, D., van der Klis, M., Méndez, M., et al. 2008a, *ApJ*, 687, 488
- [5] Altamirano, D., van der Klis, M., Wijnands, R., & Cumming, A. 2008b, *ApJL*, 673, L35
- [6] Altamirano, D., Belloni, T., Linares, M., et al. 2011, *ApJL*, 742, L17
- [7] Altamirano, D., & Strohmayer, T. 2012, *ApJL*, 754, L23
- [8] Amaro-Seoane, P., Miller, M. C., & Freitag, M. 2009, *ApJL*, 692, L50
- [9] Armitage, P. J., & Livio, M. 1996, *ApJ*, 470, 1024
- [10] Armitage, P. J., & Livio, M. 1998, *ApJ*, 493, 898
- [11] Arnaud, K. A. 1996, *Astronomical Data Analysis Software and Systems V*, 101, 17
- [12] Bałucińska-Church, M., Church, M. J., Charles, P. A., et al. 2000, *MNRAS*, 311, 861

- [13] Barnard, R., Balucińska-Church, M., Smale, A. P., & Church, M. J. 2001, *A&A*, 380, 494
- [14] Barret, D., Boutelier, M., & Miller, M. C. 2008, *MNRAS*, 384, 1519
- [15] Beer, M. E., & Podsiadlowski, P. 2002, *MNRAS*, 331, 351
- [16] Begelman, M. C. 2002, *ApJL*, 568, L97
- [17] Belloni, T., Mendez, M., King, A. R., van der Klis, M., & van Paradijs, J. 1997, *ApJL*, 479, L145
- [18] Belloni, T., Klein-Wolt, M., Méndez, M., van der Klis, M., & van Paradijs, J. 2000, *A&A*, 355, 271
- [19] Belloni, T., Psaltis, D., & van der Klis, M. 2002, *ApJ*, 572, 392
- [20] Belloni, T. M., Sanna, A., & Méndez, M. 2012, *MNRAS*, 426, 1701
- [21] Belloni, T. M., & Altamirano, D. 2013, *MNRAS*, 432, 10
- [22] Bisikalo, D. V., Kaigorodov, P. V., Boyarchuk, A. A., & Kuznetsov, O. A. 2005, *Astronomy Reports*, 49, 701
- [23] Blondin, J. M., Stevens, I. R., & Kallman, T. R. 1991, *ApJ*, 371, 684
- [24] Bloom, J. S., Giannios, D., Metzger, B. D., et al. 2011, *Science*, 333, 203
- [25] Bolton, C. T. 1972, *Nature*, 235, 271
- [26] Burrows, D. N., Kennea, J. A., Ghisellini, G., et al. 2011, *Nature*, 476, 421
- [27] Caballero-García, M. D. 2011, *MNRAS*, 418, 1973
- [28] Caballero-García, M. D., Belloni, T., & Zampieri, L. 2013, *MNRAS*, 436, 3262
- [29] Casella, P., Belloni, T., & Stella, L. 2005, *ApJ*, 629, 403
- [30] Casella, P., Ponti, G., Patruno, A., et al. 2008, *MNRAS*, 387, 1707
- [31] Chakrabarti, S. K., & Manickam, S. G. 2000, *ApJL*, 531, L41

- [32] Charles, P., Clarkson, W., Cornelisse, R., & Shih, C. 2008, *New Astro. Rev.*, 51, 768
- [33] Chiang, Y.-K., & Kong, A. K. H. 2011, *MNRAS*, 414, 1329
- [34] Church, M. J., Dotani, T., Balucinska-Church, M., et al. 1997, *ApJ*, 491, 38
- [35] Church, M. J., Parmar, A. N., Balucinska-Church, M., et al. 1998, *A&A*, 338, 556
- [36] Church, M. J. 2001, *Advances in Space Research*, 28, 323
- [37] Clarkson, W. I., Charles, P. A., Coe, M. J., & Laycock, S. 2003, *MNRAS*, 343, 1213
- [38] Colbert, E. J. M., & Mushotzky, R. F. 1999, *ApJ*, 519, 89
- [39] Courvoisier, T. J.-L., Parmar, A. N., Peacock, A., & Pakull, M. 1986, *ApJ*, 309, 265
- [40] Cseh, D., Grisé, F., Corbel, S., & Kaaret, P. 2011, *ApJL*, 728, L5
- [41] Cseh, D., Grisé, F., Kaaret, P., et al. 2013, *MNRAS*, 435, 2896
- [42] Cui, W., Zhang, S. N., Chen, W., & Morgan, E. H. 1999, *ApJL*, 512, L43
- [43] Dewangan, G. C., Miyaji, T., Griffiths, R. E., & Lehmann, I. 2004, *ApJL*, 608, L57
- [44] Dewangan, G. C., Titarchuk, L., & Griffiths, R. E. 2006, *ApJL*, 637, L21
- [45] Dheeraj, P. R., & Strohmayer, T. E. 2012, *ApJ*, 753, 139
- [46] Doeleman, S. S., Fish, V. L., Schenck, D. E., et al. 2012, *Science*, 338, 355
- [47] Donato, D., Cenko, S. B., Covino, S., et al. 2014, *ApJ*, 781, 59
- [48] Eddington, A. S. 1924, *MNRAS*, 84, 308
- [49] Eggleton, P. P. 1983, *ApJ*, 268, 368
- [50] Evans, C. R., & Kochanek, C. S. 1989, *ApJL*, 346, L13

- [51] Evans, P. A., Osborne, J. P., Beardmore, A. P., et al. 2014, *ApJS*, 210, 8
- [52] Fabbiano, G. 1989, *ARA&A*, 27, 87
- [53] Farrell, S. A., Sood, R. K., & O'Neill, P. M. 2006, *MNRAS*, 367, 1457
- [54] Feng, Y. X., & Cui, W. 2002, *ApJ*, 564, 953
- [55] Feng, H., & Kaaret, P. 2007, *ApJ*, 668, 941
- [56] Feng, H., & Kaaret, P. 2010, *ApJL*, 712, L169
- [57] Feng, H., & Soria, R. 2011, *New A Rev.*, 55, 166
- [58] Feng, H., Rao, F., & Kaaret, P. 2010, *ApJL*, 710, L137
- [59] Ferrarese, L., & Ford, H. 2005, *SSR*, 116, 523
- [60] Ferrarese, L., & Merritt, D. 2000, *ApJL*, 539, L9
- [61] Fiorito, R., & Titarchuk, L. 2004, *ApJL*, 614, L113
- [62] Foster, D. L., Charles, P. A., & Holley-Bockelmann, K. 2010, *ApJ*, 725, 2480
- [63] Frank, J., King, A. R., & Lasota, J.-P. 1987, *A&A*, 178, 137
- [64] Frank, J., King, A., & Raine, D. J. 2002, *Accretion Power in Astrophysics*, by Juhan Frank and Andrew King and Derek Raine, pp. 398. ISBN 0521620538. Cambridge, UK: Cambridge University Press, February 2002.,
- [65] Gebhardt, K., Bender, R., Bower, G., et al. 2000, *ApJL*, 539, L13
- [66] Gehrels, N. 1986, *ApJ*, 303, 336
- [67] Gezari, S., Martin, D. C., Milliard, B., et al. 2006, *ApJL*, 653, L25
- [68] Gezari, S., Dessart, L., Basa, S., et al. 2008, *ApJL*, 683, L131
- [69] Gezari, S., Chornock, R., Rest, A., et al. 2012, *Nature*, 485, 217
- [70] Ghez, A. M., Salim, S., Hornstein, S. D., et al. 2005, *ApJ*, 620, 744

- [71] Ghez, A. M., Salim, S., Weinberg, N. N., et al. 2008, *ApJ*, 689, 1044
- [72] Gierliński, M., Zdziarski, A. A., Poutanen, J., et al. 1999, *MNRAS*, 309, 496
- [73] Giles, A. B., Swank, J. H., Jahoda, K., et al. 1996, *ApJL*, 469, L25
- [74] Gladstone, J. C., Roberts, T. P., & Done, C. 2009, *MNRAS*, 397, 1836
- [75] Greiner, J., Morgan, E. H., & Remillard, R. A. 1996, *ApJL*, 473, L107
- [76] Greene, J., Bailyn, C. D., & Orosz, J. A. 2001, *ApJ*, 554, 1290
- [77] Grimm, H.-J., Gilfanov, M., & Sunyaev, R. 2003, *MNRAS*, 339, 793
- [78] Grisé, F., Kaaret, P., Corbel, S., et al. 2012, *ApJ*, 745, 123
- [79] Grove, J. E., Strickman, M. S., Matz, S. M., et al. 1998, *ApJL*, 502, L45
- [80] Guillochon, J., Manukian, H., & Ramirez-Ruiz, E. 2014, *ApJ*, 783, 23
- [81] Gültekin, K., Richstone, D. O., Gebhardt, K., et al. 2009, *ApJ*, 698, 198
- [82] Han, X., An, T., Wang, J.-Y., et al. 2012, *Research in Astronomy and Astrophysics*, 12, 1597
- [83] Heger, A., Cumming, A., & Woosley, S. E. 2007, *ApJ*, 665, 1311
- [84] Heil, L. M., Vaughan, S., & Roberts, T. P. 2009, *MNRAS*, 397, 1061
- [85] Homan, J., Jonker, P. G., Wijnands, R., van der Klis, M., & van Paradijs, J. 1999, *ApJL*, 516, L91
- [86] Homan, J., Wijnands, R., van der Klis, M., et al. 2001, *ApJS*, 132, 377
- [87] Homan, J., Miller, J. M., Wijnands, R., et al. 2005, *ApJ*, 623, 383
- [88] Homer, L., Charles, P. A., Hakala, P., et al. 2001, *MNRAS*, 322, 827
- [89] Hopman, C., Portegies Zwart, S. F., & Alexander, T. 2004, *ApJL*, 604, L101
- [90] Horne, J. H., & Baliunas, S. L. 1986, *ApJ*, 302, 757

- [91] Immler, S., & Lewin, W. H. G. 2003, *Supernovae and Gamma-Ray Bursters*, 598, 91
- [92] Irwin, J. A., Brink, T. G., Bregman, J. N., & Roberts, T. P. 2010, *ApJL*, 712, L1
- [93] Jahoda, K., Stark, M. J., Strohmayer, T. E., et al. 1999, *Nuclear Physics B Proceedings Supplements*, 69, 210
- [94] Jain, C., Paul, B., & Dutta, A. 2010, *MNRAS*, 409, 755
- [95] Jin, J., Feng, H., & Kaaret, P. 2010, *ApJ*, 716, 181
- [96] Jonker, P. G., van der Klis, M., & Wijnands, R. 1999, *ApJL*, 511, L41
- [97] Jonker, P. G., van der Klis, M., Homan, J., et al. 2000, *ApJ*, 531, 453
- [98] Kaaret, P., Simet, M. G., & Lang, C. C. 2006, *ApJ*, 646, 174
- [99] Kaaret, P., & Feng, H. 2007, *ApJ*, 669, 106
- [100] Kaaret, P., & Feng, H. 2007, *ApJ*, 669, 106
- [101] Kaaret, P., Feng, H., & Gorski, M. 2009, *ApJ*, 692, 653
- [102] Katz, J. I. 1973, *Nature Physical Science*, 246, 87
- [103] King, A. R., Davies, M. B., Ward, M. J., Fabbiano, G., & Elvis, M. 2001, *ApJL*, 552, L109
- [104] Koljonen, K. I. I., Hannikainen, D. C., & McCollough, M. L. 2011, *MNRAS*, 416, L84
- [105] Kommers, J. M., Fox, D. W., Lewin, W. H. G., et al. 1997, *ApJL*, 482, L53
- [106] Körding, E. G., Migliari, S., Fender, R., Belloni, T., Knigge, C., & McHardy, I. 2007, *MNRAS*, 380, 301
- [107] Körding, E., Falcke, H., & Markoff, S. 2002, *A&A*, 382, L13
- [108] Kotze, M. M., & Charles, P. A. 2012, *MNRAS*, 420, 1575

- [109] Krolik, J. H., & Piran, T. 2011, ApJ, 743, 134
- [110] Kuulkers, E., Wijnands, R., Belloni, T., et al. 1998, ApJ, 494, 753
- [111] Kuulkers, E., in't Zand, J. J. M., Cornelisse, R., et al. 2000, A&A, 358, 993
- [112] Kuulkers, E., Kouveliotou, C., Belloni, T., et al. 2012, arXiv:1204.5840
- [113] Lang, C. C., Kaaret, P., Corbel, S., & Mercer, A. 2007, ApJ, 666, 79
- [114] Laurent, P., & Titarchuk, L. 1999, ApJ, 511, 289
- [115] Laycock, S., Corbet, R. H. D., Coe, M. J., et al. 2005, ApJs, 161, 96
- [116] Leahy, D. A., Darbro, W., Elsner, R. F., et al. 1983, ApJ, 266, 160
- [117] Leahy, D. A., & Igna, C. D. 2010, ApJ, 713, 318
- [118] Levine, A. M., Rappaport, S. A., & Zojcheski, G. 2000, ApJ, 541, 194
- [119] Lightman, A. P., & Eardley, D. M. 1974, ApJL, 187, L1
- [120] Liu, J., Orosz, J., & Bregman, J. N. 2012, ApJ, 745, 89
- [121] Lodato, G., King, A. R., & Pringle, J. E. 2009, MNRAS, 392, 332
- [122] Lodato, G., & Rossi, E. M. 2011, MNRAS, 410, 359
- [123] Lozinskaya, T. A., & Moiseev, A. V. 2007, MNRAS, 381, L26
- [124] Lubow, S. H. 1989, ApJ, 340, 1064
- [125] Lu, Y., Huang, Y. F., & Zhang, S. N. 2008, ApJ, 684, 1330
- [126] Lu, R.-S., Broderick, A. E., Baron, F., et al. 2014, arXiv:1404.7095
- [127] Makishima, K., Kubota, A., Mizuno, T., et al. 2000, ApJ, 535, 632
- [128] Maksym, W. P., Ulmer, M. P., & Eracleous, M. 2010, ApJ, 722, 1035
- [129] Maksym, W. P., Ulmer, M. P., Eracleous, M. C., Guennou, L., & Ho, L. C. 2013, MNRAS, 435, 1904

- [130] Madau, P., & Rees, M. J. 2001, *ApJL*, 551, L27
- [131] Magorrian, J., Tremaine, S., Richstone, D., et al. 1998, *AJ*, 115, 2285
- [132] Markowitz, A., Edelson, R., & Vaughan, S. 2003, *ApJ*, 598, 935
- [133] Markowitz, A., & Edelson, R. 2004, *ApJ*, 617, 939
- [134] Mason, K. O. 1986, *The Physics of Accretion onto Compact Objects*, 266, 29
- [135] Matsumoto, H., Tsuru, T. G., Koyama, K., et al. 2001, *ApJL*, 547, L25
- [136] Matt, G., Fabian, A. C., & Reynolds, C. S. 1997, *MNRAS*, 289, 175
- [137] McClintock, J. E., & Remillard, R. A. 2006, *Compact stellar X-ray sources*, 157
- [138] McClintock, J. E., Remillard, R. A., Rupen, M. P., et al. 2009, *ApJ*, 698, 1398
- [139] McConnell, N. J., & Ma, C.-P. 2013, *ApJ*, 764, 184
- [140] McHardy, I. M., Koeding, E., Knigge, C., Uttley, P., & Fender, R. P. 2006, *Nature*, 444, 730
- [141] McKinney, J. C., Tchekhovskoy, A., & Blandford, R. D. 2012, *MNRAS*, 423, 3083
- [142] Méndez, M., van der Klis, M., & Ford, E. C. 2001, *ApJ*, 561, 1016
- [143] Middleton, M. J., Roberts, T. P., Done, C., & Jackson, F. E. 2011, *Astronomische Nachrichten*, 332, 388
- [144] Middleton, M. J., Roberts, T. P., Done, C., & Jackson, F. E. 2011, *MNRAS*, 411, 644
- [145] Miller, J. M., Wijnands, R., Homan, J., et al. 2001, *ApJ*, 563, 928
- [146] Miller, J. M., Fabian, A. C., & Miller, M. C. 2004, *ApJL*, 614, L117
- [147] Miller, J. M., Walton, D. J., King, A. L., et al. 2013, *ApJL*, 776, L36
- [148] Miller, M. C., & Hamilton, D. P. 2002, *MNRAS*, 330, 232

- [149] Miller, M. C., & Colbert, E. J. M. 2004, *International Journal of Modern Physics D*, 13, 1
- [150] Morgan, E. H., Remillard, R. A., & Greiner, J. 1997, *ApJ*, 482, 993
- [151] Motta, S. E., Belloni, T. M., Stella, L., Muñoz-Darias, T., & Fender, R. 2014a, *MNRAS*, 437, 2554
- [152] Motta, S. E., Muñoz-Darias, T., Sanna, A., et al. 2014b, *MNRAS*, L7
- [153] Mucciarelli, P., Casella, P., Belloni, T., Zampieri, L., & Ranalli, P. 2006, *MNRAS*, 365, 1123
- [154] Munoz, M. P., Morgan, E. H., & Remillard, R. A. 1999, *ApJ*, 527, 321
- [155] Muñoz-Darias, T., Casares, J., & Martínez-Pais, I. G. 2008, *MNRAS*, 385, 2205
- [156] Neilsen, J., Remillard, R. A., & Lee, J. C. 2011, *ApJ*, 737, 69
- [157] Ogilvie, G. I., & Dubus, G. 2001, *MNRAS*, 320, 485
- [158] Ogilvie, G. I. 2002, *MNRAS*, 330, 937
- [159] Orosz, J. A., Groot, P. J., van der Klis, M., et al. 2002, *ApJ*, 568, 845
- [160] Orosz, J. A. 2003, *A Massive Star Odyssey: From Main Sequence to Supernova*, 212, 365
- [161] Parmar, A. N., & White, N. E. 1988, *Mem. Soc. Astron. Italiana*, 59, 147
- [162] Parmar, A. N., White, N. E., Giommi, P., & Gottwald, M. 1986, *ApJ*, 308, 199
- [163] Pasham, D. R., & Strohmayer, T. E. 2013a, *ApJ*, 764, 93
- [164] Pasham, D. R., & Strohmayer, T. E. 2013b, *ApJ*, 771, 101
- [165] Pasham, D. R., Strohmayer, T. E., & Mushotzky, R. F. 2013, *ApJL*, 771, L44
- [166] Pasham, D. R., & Strohmayer, T. E. 2013c, *ApJL*, 774, L16

- [167] Patruno, A., Watts, A., Klein Wolt, M., Wijnands, R., & van der Klis, M. 2009, *ApJ*, 707, 1296
- [168] Peterson, B. M., & Wandel, A. 2000, *ApJL*, 540, L13
- [169] Phinney, E. S. 1989, *The Center of the Galaxy*, 136, 543
- [170] Portegies Zwart, S. F., Dewi, J., & Maccarone, T. 2005, *Ap&SS*, 300, 247
- [171] Poutanen, J., Lipunova, G., Fabrika, S., Butkevich, A. G., & Abolmasov, P. 2007, *MNRAS*, 377, 1187
- [172] Prestwich, A. H., Kilgard, R., Crowther, P. A., et al. 2007, *ApJL*, 669, L21
- [173] Pringle, J. E. 1996, *MNRAS*, 281, 357
- [174] Rao, F., Feng, H., & Kaaret, P. 2010, *ApJ*, 722, 620
- [175] Rees, M. J. 1988, *Nature*, 333, 523
- [176] Reig, P., Belloni, T., van der Klis, M., et al. 2000, *ApJ*, 541, 883
- [177] Reis, R. C., Miller, J. M., Reynolds, M. T., et al. 2012, *Science*, 337, 949
- [178] Remillard, R. A., Morgan, E. H., McClintock, J. E., Bailyn, C. D., & Orosz, J. A. 1999, *ApJ*, 522, 397
- [179] Remillard, R. A., Munro, M. P., McClintock, J. E., & Orosz, J. A. 2002a, *ApJ*, 580, 1030
- [180] Remillard, R. A., Sobczak, G. J., Munro, M. P., & McClintock, J. E. 2002b, *ApJ*, 564, 962
- [181] Remillard, R. A., McClintock, J. E., Orosz, J. A., & Levine, A. M. 2006, *ApJ*, 637, 1002
- [182] Revnivtsev, M., Sunyaev, R., & Borozdin, K. 2000, *A&A*, 361, L37
- [183] Revnivtsev, M. G., Trudolyubov, S. P., & Borozdin, K. N. 2000, *MNRAS*, 312, 151
- [184] Revnivtsev, M., Gilfanov, M., & Churazov, E. 2001, *A&A*, 380, 520

- [185] Revnivtsev, M., Churazov, E., Gilfanov, M., & Sunyaev, R. 2001, *A&A*, 372, 138
- [186] Reynolds, M. T., & Miller, J. M. 2013, *ApJ*, 769, 16
- [187] Ritter, H., & Kolb, U. 2003, *A&A*, 404, 301
- [188] Rodriguez, J., Durouchoux, P., Mirabel, I. F., et al. 2002, *A&A*, 386, 271
- [189] Rodriguez, J., Corbel, S., Hannikainen, D. C., et al. 2004, *ApJ*, 615, 416
- [190] Rodriguez, J., Corbel, S., Kalemci, E., Tomsick, J. A., & Tagger, M. 2004, *ApJ*, 612, 1018
- [191] Roberts, T. P., Gladstone, J. C., Goulding, A. D., Swinbank, A. M., Ward, M. J., Goad, M. R., & Levan, A. J. 2011, *Astronomische Nachrichten*, 332, 398
- [192] Sazonov, S. Y., Sunyaev, R. A., & Lund, N. 1997, *Astronomy Letters*, 23, 286
- [193] Scargle, J. D. 1982, *ApJ*, 263, 835
- [194] Schnittman, J. D., Homan, J., & Miller, J. M. 2006, *ApJ*, 642, 420
- [195] Servillat, M., Farrell, S. A., Lin, D., et al. 2011, *ApJ*, 743, 6
- [196] Shcherbakov, R. V., Pe'er, A., Reynolds, C. S., et al. 2013, *ApJ*, 769, 85
- [197] Shakura, N. I., & Sunyaev, R. A. 1973, *A&A*, 24, 337
- [198] Shaposhnikov, N., & Titarchuk, L. 2007, *ApJ*, 663, 445
- [199] Shaposhnikov, N., & Titarchuk, L. 2009, *ApJ*, 699, 453
- [200] Silverman, J. M., & Filippenko, A. V. 2008, *ApJL*, 678, L17
- [201] Smale, A. P., Mason, K. O., White, N. E., & Gottwald, M. 1988, *MNRAS*, 232, 647
- [202] Smale, A. P., Church, M. J., & Bałucińska-Church, M. 2002, *ApJ*, 581, 1286
- [203] Sobczak, G. J., McClintock, J. E., Remillard, R. A., et al. 2000a, *ApJ*, 531, 537

- [204] Sobczak, G. J., McClintock, J. E., Remillard, R. A., et al. 2000b, *ApJ*, 544, 993
- [205] Sood, R., Farrell, S., O'Neill, P., & Dieters, S. 2007, *Advances in Space Research*, 40, 1528
- [206] Soria, R., Motch, C., Read, A. M., & Stevens, I. R. 2004, *A&A*, 423, 955
- [207] Soria, R., Kuncic, Z., Broderick, J. W., & Ryder, S. D. 2006, *MNRAS*, 370, 1666
- [208] Stiele, H., Belloni, T. M., Kalemci, E., & Motta, S. 2013, *MNRAS*, 496
- [209] Strickland, D. K., & Heckman, T. M. 2007, *ApJ*, 658, 258
- [210] Strohmayer, T. E. 2001a, *ApJL*, 552, L49
- [211] Strohmayer, T. E. 2001b, *ApJL*, 554, L169
- [212] Strohmayer, T. E., & Mushotzky, R. F. 2003, *ApJL*, 586, L61
- [213] Strohmayer, T. E., Mushotzky, R. F., Winter, L., Soria, R., Uttley, P., & Cropper, M. 2007, *ApJ*, 660, 580
- [214] Strohmayer, T. E. 2009, *ApJL*, 706, L210
- [215] Strohmayer, T. E., & Mushotzky, R. F. 2009, *ApJ*, 703, 1386
- [216] Swartz, D. A., Ghosh, K. K., Tennant, A. F., & Wu, K. 2004, *ApJS*, 154, 519
- [217] Swartz, D. A., Soria, R., Tennant, A. F., & Yukita, M. 2011, *ApJ*, 741, 49
- [218] Tao, L., Feng, H., Grisé, F., & Kaaret, P. 2011, *ApJ*, 737, 81
- [219] Timmer, J., & Koenig, M. 1995, *A&A*, 300, 707
- [220] Titarchuk, L., Mastichiadis, A., & Kylafis, N. D. 1997, *ApJ*, 487, 834
- [221] Titarchuk, L., & Osherovich, V. 2000, *ApJL*, 542, L111
- [222] Titarchuk, L., & Fiorito, R. 2004, *ApJ*, 612, 988

- [223] Titarchuk, L., & Seifina, E. 2009, *ApJ*, 706, 1463
- [224] Ulmer, A. 1999, *ApJ*, 514, 180
- [225] van der Hooft, F., Kouveliotou, C., van Paradijs, J., et al. 1996, *ApJL*, 458, L75
- [226] van der Hooft, F., Kouveliotou, C., van Paradijs, J., et al. 1999, *ApJ*, 513, 477
- [227] van der Klis, M., & Jansen, F. A. 1985, *Nature*, 313, 768
- [228] van der Klis, M. 1989, *Timing Neutron Stars*, 27
- [229] van der Klis, M. 2000, *ARA&A*, 38, 717
- [230] van der Klis, M. 2006, *Compact stellar X-ray sources*, 39
- [231] van Straaten, S., van der Klis, M., & Méndez, M. 2003, *ApJ*, 596, 1155
- [232] van Velzen, S., Farrar, G. R., Gezari, S., et al. 2011, *ApJ*, 741, 73
- [233] Verbunt, F. 1993, *ARA&A*, 31, 93
- [234] Vignarca, F., Migliari, S., Belloni, T., Psaltis, D., & van der Klis, M. 2003, *A&A*, 397, 729
- [235] Vikhlinin, A., Churazov, E., Gilfanov, M., et al. 1994, *ApJ*, 424, 395
- [236] Vikhlinin, A., Churazov, E., Gilfanov, M., et al. 1995, *ApJ*, 441, 779
- [237] Volonteri, M., Haardt, F., & Madau, P. 2003, *ApJ*, 582, 559
- [238] Wagoner, R. V. 1999, *Phys. Rep.*, 311, 259
- [239] Walton, D. J., Roberts, T. P., Mateos, S., & Heard, V. 2011, *MNRAS*, 416, 1844
- [240] Wang, J., & Merritt, D. 2004, *ApJ*, 600, 149
- [241] Wang, Q. D., Whitaker, K. E., & Williams, R. 2005, *MNRAS*, 362, 1065
- [242] Webster, B. L., & Murdin, P. 1972, *Nature*, 235, 37

- [243] Wen, L., Levine, A. M., Corbet, R. H. D., & Bradt, H. V. 2006, *ApJS*, 163, 372
- [244] White, N. E., & Holt, S. S. 1982, *ApJ*, 257, 318
- [245] White, N. E., Nagase, F., & Parmar, A. N. 1995, *X-ray Binaries*, 1
- [246] Wijnands, R., & van der Klis, M. 1999, *ApJ*, 514, 939
- [247] Wijnands, R. 2004, *Nuclear Physics B Proceedings Supplements*, 132, 496
- [248] Wolff, M. T., Ray, P. S., Wood, K. S., & Hertz, P. L. 2009, *ApJS*, 183, 156
- [249] Wood, K. S., Ray, P. S., Bandyopadhyay, R. M., et al. 2000, *ApJL*, 544, L45
- [250] Zauderer, B. A., Berger, E., Soderberg, A. M., et al. 2011, *Nature*, 476, 425
- [251] Zauderer, B. A., Berger, E., Margutti, R., et al. 2013, *ApJ*, 767, 152